

OPTICAL AND ELECTRONIC PROCESSES IN ORGANIC PHOTOVOLTAIC DEVICES

By

JASON DAVID MYERS

A DISSERTATION PRESENTED TO THE GRADUATE SCHOOL
OF THE UNIVERSITY OF FLORIDA IN PARTIAL FULFILLMENT
OF THE REQUIREMENTS FOR THE DEGREE OF
DOCTOR OF PHILOSOPHY

UNIVERSITY OF FLORIDA

2011

© 2011 Jason David Myers

To Anne

ACKNOWLEDGMENTS

This research and my graduate studies were only possible because of contributions from many incredible people in my life. First, I extend my gratitude to my PhD advisor, Dr. Jianguo Xue. Dr. Xue taught the best course I had while I was completing my undergraduate degree at the University of Florida and I was happy to join his group. My years working with him have been challenging and fruitful and I feel I'm leaving UF prepared to handle the rigors of a career in research. I also wish to thank Dr. Susan B. Sinnott for accepting me as an undergraduate research assistant, and especially for sending me to the 2005 AVS International Symposium to present my research. Exposure to the wider scientific research community was a major influence on my decision to continue my schooling and obtain a doctorate. Your patience and concern for your students are an inspiration. I also acknowledge my other advisory committee members, Drs. Franky So, Elliot Douglas, and Jing Guo for their time and interest.

This research could not have been completed without the help of my current and former labmates. To the more senior members of the Xue research group: your experience and instruction were invaluable to my research. I owe my initial training to Teng-Kuan Tseng, Ying Zheng was a great sounding board for ideas and guidance, and it was a pleasure collaborating with Sang-Hyun Eom on my microlens research. I especially thank Bill Hammond, who was a great partner in the trenches as the years went on. To my other group members, Yixing Yang, Weiran Cao, Renjia Zhou, Ed Wrzesniewski, John Mudrick, Nate Shewmon, and Matt Rippe, you have all contributed to my success as a graduate student. I specifically acknowledge Weiran for his

collaboration in our optical management projects and John for being an apt pupil and shouldering responsibility in maintaining the lab. I also thank the undergraduate students who worked with me, Vincent Cassidy and Erik Klump.

My research has been made possible by partial financial support from the National Science Foundation CAREER Fellowship, the Department of Energy Solar Energy Technologies Program, the Florida Energy Systems Consortium, and the University of Florida Alumni Fellowship. I also thank Karl Zawoy and the University of Florida Office of Technology Licensing for their financial support and assistance in moving forward with patenting this work.

My most profound gratitude is extended to my friends and family. This long journey would not have been possible without you all. I was grateful to be able to share my experiences as a graduate student with my brother, Daniel. I especially thank my parents, Judy and Phil, and my wife's parents, Keith and Becky, for their constant support, encouragement, and interest in my results and progress. Finally, I thank my wife, Anne. Anne, you've been there from the time I was a nervous undergrad looking for a summer research opportunity to now, when I'm leaving school with my doctorate. This work is dedicated to you.

TABLE OF CONTENTS

	<u>page</u>
ACKNOWLEDGMENTS.....	4
LIST OF TABLES.....	9
LIST OF FIGURES.....	10
LIST OF ABBREVIATIONS.....	15
ABSTRACT.....	18
CHAPTER	
1 INTRODUCTION TO ORGANIC SEMICONDUCTORS	20
1.1 Overview.....	20
1.2 Classification of Organic Materials.....	21
1.3 Electrical and Excitonic Properties of Organic Semiconductors.....	23
1.3.1 Origin of Electronic Structure.....	24
1.3.2 Transport Behavior.....	26
1.3.3 Excitons.....	28
1.4 Processing Techniques of Organic Semiconductors.....	31
1.4.1 Small Molecule Purification	32
1.4.2 Vacuum Thermal Evaporation	34
1.4.3 Spin Coating.....	37
1.4.4 Emerging Techniques.....	39
1.5 Common Organic-Based Devices.....	40
1.5.1 Organic Photovoltaics.....	40
1.5.2 Organic Light Emitting Devices	42
1.6 Research Scope	43
2 INTRODUCTION TO ORGANIC PHOTOVOLTAIC DEVICES.....	46
2.1 Basic Concepts.....	46
2.2 Overview and History.....	50
2.3 Operation Principles.....	52
2.3.1 Basic Processes.....	52
2.3.2 Fundamental Limitations	56
2.4 Progress in Organic Photovoltaic Device Performance	57
2.4.1 Small Molecule Organic Photovoltaic Devices	58
2.4.2 Polymer-Based Organic Photovoltaic Devices	61
2.4.3 Tandem Organic Photovoltaic Devices.....	64
2.4.4 Optical Management	66

3	ORGANIC OPTOELECTRONIC DEVICE CHARACTERIZATION	69
3.1	Chapter Overview	69
3.2	Organic Photovoltaics	69
3.2.1	Calibration, Spectral Mismatch, and Current-Voltage Measurement	69
3.2.2	Quantum Efficiency	75
3.2.3	Synchronous Photocurrent	78
3.3	Organic Light Emitting Diodes	81
4	OPTICAL SIMULATION OF ORGANIC PHOTOVOLTAIC DEVICES	85
4.1	Monte Carlo-Based Ray Optics Modeling	85
4.1.1	Basic Implementation Scheme	88
4.1.2	Simulation of Optical Structures	92
4.1.3	Quantitative Significance and Verification	96
4.2	Transfer Matrix Wave Optics	99
4.2.1	Concept	99
4.2.2	Optical Field Calculation	100
4.2.3	Photocurrent Calculation	108
4.3	Review of Optical Simulation Techniques	110
5	PHOTOCURRENT GENERATION AND TRANSPORT BEHAVIOR IN ORGANIC PHOTOVOLTAIC DEVICES	112
5.1	Overview	112
5.2	Effect of Heterojunction Architecture	112
5.3	Wavelength-Dependent Photocurrent Behavior in Mixed Heterojunction Devices	119
5.4	Exciton Dissociation Behavior in Bilayer Organic Photovoltaics	125
5.5	Review	130
6	OPTICAL MANAGEMENT IN ORGANIC PHOTOVOLTAIC DEVICES	133
6.1	Introduction and Background	133
6.2	Microlens Array Fabrication	137
6.3	Enhancement Characteristics	139
6.4	Optical Field Optimization	144
6.4.1	Bilayer Heterojunction Devices	144
6.4.2	Bulk Heterojunction Devices	150
6.5	Geometric Effects	153
6.6	Ideal Architectures for Enhancement	163
6.7	Review	164
7	BIFUNCTIONAL ORGANIC OPTOELECTRONIC DEVICES	166
7.1	Fundamentals of Organic Bifunctional Devices	166
7.2	Novel Device Architectures for Phosphorescent Bifunctional Devices	169
7.3	Requirements for Efficient Bifunctional Device Design	178

8	CONCLUSIONS AND FUTURE WORK	181
	8.1 Photocurrent Generation and Transport	181
	8.2 Optical Management in Organic Photovoltaic Devices	183
	8.3 Bifunctional Organic Optoelectronic Devices	187
	8.4 Afterword	189
	LIST OF REFERENCES	191
	BIOGRAPHICAL SKETCH.....	207

LIST OF TABLES

<u>Table</u>		<u>page</u>
1-1	Structures and optical properties of the polyacene family.	26
3-1	Spectral mismatch factor M for various devices	72
6-1	Performance characteristics for several different device architectures and active layer materials with and without microlens arrays.	144

LIST OF FIGURES

<u>Figure</u>		<u>page</u>
1-1	Examples of different categories in the spectrum of organic materials.	22
1-2	Molecular structures of several organic small molecules and polymers used in this work.....	23
1-3	Diagram of σ - and π -bonding within an ethane molecule.....	24
1-4	Schematic energy level diagram of a discrete organic molecule.	25
1-5	Schematic representation of different classes of excitons.	29
1-6	Gradient zone sublimation, with colors approximating that of CuPc during high vacuum purification.	33
1-7	A representative vacuum thermal evaporation (VTE) system.....	34
1-8	Diagram of shadow mask geometry.	36
1-9	Stages of spin coating.	38
1-10	Examples of organic photovoltaic devices.....	41
1-11	Examples of commercial OLED products.	43
2-1	Current-voltage characteristics of a representative photovoltaic device.	47
2-2	Equivalent photovoltaic device circuit and typical schematic of an organic photovoltaic device.	49
2-3	Basic processes in power generation in a bilayer organic photovoltaic device...	53
2-4	Optical absorption spectra for several organic photovoltaic materials.....	54
2-5	HOMO and LUMO energy levels for several common OPV materials.....	56
2-6	Representations of unoptimized and nanoscale phase-segregated bulk heterojunction OPV microstructures with two constituent materials.	59
2-7	Ideal interdigitated heterojunction for organic photovoltaics.	59
2-8	Typical device structure and optical field plot for a tandem organic photovoltaic device.	66
2-9	Three previous examples of optical enhancement techniques.	67

3-1	Reference solar spectra.	70
3-2	Reference AM1.5 Global and simulated Xe-arc lamp spectra.	71
3-3	Arrangement of the solar simulator and associated optical components.	73
3-4	Optical intensity distribution over a calibrated 100 mW/cm ² white light beam. ...	74
3-5	External quantum efficiency characterization system based on the ASTM E1021 standard.	76
3-6	External quantum efficiency spectrum and current-voltage curve for a rubrene/C ₆₀ (35/25 nm) device.	78
3-7	Example photocurrent data.	79
3-8	Irradiance spectra of two different white light bias lamps compared to the absorption spectra of three representative OPV materials within the visible region.	80
3-9	OLED current-voltage and luminance characterization system.	82
4-1	Schematic diagram of light propagation via ray optics.	86
4-2	Simplified flow chart of a Monte Carlo ray optics simulator.	89
4-3	Typical simulated stack.	90
4-4	Typical simulated device structure with a convex microlens array.	92
4-5	Simulated microlens arrays.	93
4-6	Concept and mathematical details to simulate lenses of different contact angles.	94
4-7	Simulated lens arrays with contact angles of 90° and 30°.	95
4-8	Verification of basic simulator functions.	97
4-9	Simulated air mass 1.5G solar spectrum and active layers absorption coefficients for various material systems.	98
4-10	Calculated transmission, absorption, and reflection of a multilayer CuPc/C ₆₀ structure.	103
4-11	Transfer matrix-calculated optical fields.	106
4-12	Exciton generation plots in two different bilayer CuPc/C ₆₀ devices.	107

4-13	Transfer-matrix calculated short circuit current in a 20 nm CuPc/ x nm C ₆₀ device.	109
5-1	Three different small molecule device architectures.	113
5-2	Example photocurrent characteristics for three different device architectures..	116
5-3	Relative contributions of drift and diffusion currents to the net photocurrent at a small forward bias for two different device architectures.	117
5-4	Relative contributions of drift and diffusion currents to the net photocurrent at a large forward bias for two different device architectures.	118
5-5	Photocurrent measurements of a 90 nm 1:1 CuPc:C ₆₀ device at various wavelengths.	120
5-6	Measured photocurrent values for two different mixed layer thicknesses at different wavelengths.	121
5-7	V ₀ vs. wavelength for three different CuPc:C ₆₀ (1:1) layer thicknesses.	122
5-8	Experimental V ₀ vs. wavelength data and transfer matrix-calculated charge generation fields for three different CuPc:C ₆₀ (1:1) active layer thicknesses.	123
5-9	V ₀ vs. wavelength for three different P3HT:PCBM devices.	125
5-10	Measured photocurrent characteristics for planar heterojunction devices at different wavelengths.	126
5-11	Transfer matrix optical simulations for three different bilayer devices.	127
5-12	Inversion voltage and exciton generation profiles for CuPc/C ₆₀ planar devices with different thicknesses.	128
5-13	The drift, diffusion, and net photocurrent for excitons dissociated by either the interface or the electric field.	129
6-1	Schematic diagram of light interaction and path length through the active layer in a device with and without a microlens array.	135
6-2	Processing steps in microlens array fabrication.	138
6-3	Current-voltage and external quantum efficiency characteristics of a SubPc/C ₆₀ (12/40 nm) device with and without a microlens array.	140
6-4	Current-voltage and quantum efficiency characteristics for a high efficiency PBnDT-DTffBT:PCBM OPV.	142

6-5	Current-voltage characteristics of hybrid PCPDTBT:CdSe polymer:inorganic nanoparticle devices with and without a ZnO optical spacing layer.	143
6-6	Calculated optical fields for SubPc/C ₆₀ (12/60 nm) OPVs at normal (0°) and 30° incidence.	145
6-7	Effect of varied C ₆₀ thickness on J_{SC} and η_P enhancement for a SubPc/C ₆₀ (12/y nm) device with and without a microlens array.	147
6-8	Distributions of light incident angle upon the active layer in SubPc:C ₆₀ (1:4 by weight) films calculated by ray optics simulations.	148
6-9	Power conversion efficiency η_P for SubPc/C ₆₀ (12/y nm) with and without a microlens array.	149
6-10	Short-circuit current enhancements for P3HT:PCBM bulk heterojunction devices with and without a microlens array.	150
6-11	Effect of ZnO optical spacer thickness on mixed P3HT:PCBM devices.	152
6-12	Effect of device active area on relative enhancement with SubPc/C ₆₀ (12 nm/60 nm) devices.	154
6-13	Simulation results of different geometric arrangements.	156
6-14	Effect of device spacing on simulated absorption enhancement in a 70 nm-thick SubPc:C ₆₀ (1:4) device.	158
6-15	Effect of contact angle variations on simulated enhancements in 70 nm-thick SubPc:C ₆₀ (1:4) films.	159
6-16	Performance of 1 cm ² SubPc/C ₆₀ (12/40 nm) devices under 5 mW/cm ² white light illumination with a variable incident angle.	161
7-1	Basic OPVs and OLEDs device architectures, with charge carrier behavior diagrammed.	166
7-2	Auger up-conversion process for half-gap electroluminescence in rubrene/C ₆₀ BFDs.	168
7-3	Effect of an NPB electron blocking layer on a rubrene/C ₆₀ BFD.	170
7-4	BFDs using a doped phosphorescent emissive layer.	172
7-5	Jablonski diagram of exciton energies for a system containing NPB, PtOEP, and rubrene.	173
7-6	Ir(ppy) ₃ phosphorescent BFD architecture and emission spectra for devices with and without doping into NPB.	174

7-7	Adjusted phosphorescent BFD architecture.	175
7-8	Photovoltaic and LJV characteristics of phosphorescent BFDs.....	176
7-9	Light emitting characteristics of phosphorescent BFDs.	177
8-1	Device schematics for concave and convex microlens array rear reflectors. ...	186
8-2	Schematic diagram of localized effects of ferroelectric nanoparticles polarization on the potential barrier for electron injection at a rubrene/C ₆₀ interface.....	188

LIST OF ABBREVIATIONS

Alq3	aluminum tris(8-hydroxyquinoline)
AM1.5G	Air Mass 1.5 Global
AMU	Atomic mass unit
ASTM	American Society for Testing and Materials
BCP	Bathocuproine, or 2,9-dimethyl-4,7-diphenyl-1,10-phenanthroline
BFD	Bifunctional device
CBP	4,4'-N,N'-dicarbazole-biphenyl
CIGS	$\text{CuIn}_x\text{Ga}_{(1-x)}\text{Se}_2$, copper indium gallium diselenide
ClAlPc	Chloroaluminum phthalocyanine
ClInPc	Chloroindium phthalocyanine
CRZ	Carrier recombination zone
CT	Charge transfer
CuPc	Copper phthalocyanine
EQE	External quantum efficiency
F8TBT	poly((9,9-dioctylfluorene)-2,7-diyl-alt-[4,7-bis(3-hexylthien-5-yl)-2,1,3-benzothiadiazole]-2',2"-diyl)
FDTD	Finite difference time domain
FF	Fill factor
HJ	Heterojunction
HOMO	Highest occupied molecular orbital
IQE	Internal quantum efficiency
$\text{Ir}(\text{ppy})_3$	<i>fac</i> -tris-(phenylpyridine) iridium
ITO	Indium tin oxide

LED	Light emitting diode
LUMO	Lowest unoccupied molecular orbital
MDMO-PPV	poly(2-methoxy-5-(3,7-dimethyloctyloxy)-1,4-phenylene-vinylene)
MEH-PPV	poly(2-methoxy-5-(2'-ethyl-hexyloxy)-1,4-phenylene vinylene)
MFP	Mean free path
MLA	Microlens array
MO	Molecular orbital
NPB	N, N'-bis(naphthalen-1-yl)-N,N'-bis(phenyl)-benzidine
OLED	Organic light emitting diode
OPV	Organic photovoltaic
OVJP	Organic vapor jet printing
OVPD	Organic vapor phase deposition
P3HT	poly(3-hexylthiophene)
PBC	Periodic boundary conditions
PBnDT-DTffBT	poly(benzo[1,2-b:4,5-b']dithiophene)-(5,6-difluoro-4,7-dithien-2-yl-2,1,3-benzothiadiazole)
PbPc	Lead phthalocyanine
PCBM	[6,6]-phenyl C ₆₁ -butyric acid methyl ester
PCDTBT	poly[N-9''-hepta-decanyl-2,7-carbazole-alt-5,5-(4',7'-di-2-thienyl-2',1',3'-benzothiadiazole)
PCPDTBT	poly[2,6-(4,4-bis-[2-ethylhexyl]-4H-cyclopenta[2,1-b;3,4-b]-dithiophene)-alt-4,7-(2,1,3-benzothiadiazole)]
PDMS	poly(dimethylsiloxane)
PEDOT:PSS	poly(3, 4-ethylenedioxythiophene):poly(styrenesulfonate)
PPV	poly(1,4-phenylene-vinylene)
PTCBI	3,4,9,10-perylene tetracarboxylic-bis-benzimidazole

PtOEP	Platinum octaethylporphine
QTH	Quartz tungsten halogen
SnPc	Tin phthalocyanine
SubPc	Boron subphthalocyanine chloride
TPyP	5,10,15,20-tetra(3-pyridyl)porphyrin
VMD	Visual Molecular Dynamics
VTE	Vacuum thermal evaporation
ZnPc	Zinc phthalocyanine

Abstract of Dissertation Presented to the Graduate School
of the University of Florida in Partial Fulfillment of the
Requirements for the Degree of Doctor of Philosophy

OPTICAL AND ELECTRONIC PROCESSES IN ORGANIC PHOTOVOLTAIC DEVICES

By

Jason David Myers

August 2011

Chair: Jiangeng Xue

Major: Materials Science and Engineering

Organic photovoltaic devices (OPVs) have become a promising research field. OPVs have intrinsic advantages over conventional inorganic technologies: they can be produced from inexpensive source materials using high-throughput techniques on a variety of substrates, including glass and flexible plastics. However, organic semiconductors have radically different operation characteristics which present challenges to achieving high performance OPVs.

To increase the efficiency of OPVs, knowledge of fundamental operation principles is crucial. Here, the photocurrent behavior of OPVs with different heterojunction architectures was studied using synchronous photocurrent detection. It was revealed that photocurrent is always negative in planar and planar-mixed heterojunction devices as it is dominated by photocarrier diffusion. In mixed layer devices, however, the drift current dominates except at biases where the internal electric field is negligible. At these biases, the diffusion current dominates, exhibiting behavior that is correlated to the optical interference patterns within the device active layer.

Further, in an effort to increase OPV performance without redesigning the active layer, soft-lithographically stamped microlens arrays (MLAs) were developed and

applied to a variety of devices. MLAs refract and reflect incident light, giving light a longer path length through the active layer compared to a device without a MLA; this increases absorption and photocurrent. The experimentally measured efficiency enhancements range from 10 to 60%, with the bulk of this value coming from increased photocurrent. Additionally, because the enhancement is dependent on the substrate/air interface and not the active layer, MLAs are applicable to all organic material systems.

Finally, novel architectures for bifunctional organic optoelectronic devices (BFDs), which can function as either an OPV or an organic light emitting device (OLED), were investigated. Because OPVs and OLEDs have inherently opposing operation principles, BFDs suffer from poor performance. A new architecture was developed to incorporate the phosphorescent emitter platinum octaethylporphine (PtOEP) into a rubrene/C₆₀ bilayer BFD to make more efficient use of injected carriers. While the emission was localized to a PtOEP emitter layer by an electron permeable exciton blocking layer of N, N'-bis(naphthalen-1-yl)-N,N'-bis(phenyl)-benzidine (NPB), total performance was not improved. From these experiments, a new understanding of the material requirements for BFDs was obtained.

CHAPTER 1

INTRODUCTION TO ORGANIC SEMICONDUCTORS

1.1 Overview

This Chapter introduces the reader to the electrical and physical properties of organic semiconductors to better understand their application to optoelectronic devices. As a class, organic semiconductors have fueled much interest in the scientific community for over three decades. They have the potential to revolutionize several aspects of society: ubiquitous photovoltaic power, transparent displays, efficient and inexpensive solid-state white lighting, and truly flexible and rugged electronics are merely a few examples¹⁻⁷.

Interest in these materials is driven by their intrinsic advantages over inorganic semiconductors such as Si or GaAs. Organic materials are generally inexpensive and compatible with large area, low cost and low temperature manufacturing techniques. Many of these manufacturing techniques are compatible with high-throughput roll-to-roll processing. Further, while most inorganic devices require high-purity crystalline substrates, organic devices can be produced on glass, plastic films, or metal foils without concern of lattice matching or strain-induced defect states.

However, organic materials suffer from low charge carrier mobilities due to weak intermolecular interactions, which lower their performance relative to inorganic devices. Additionally, most organic materials are damaged by exposure to oxygen and water vapor, requiring extensive environmental encapsulation to achieve acceptable device lifetimes. The purity of organic materials is also much less than inorganics, introducing electronic defect states that further reduce performance.

Section 1.2 covers the basic definition and classification of organic materials. Their electronic nature is discussed in Section 1.3, along with an introduction to excitons. Processing techniques are covered in Section 1.4, and a brief introduction to different organic electronic devices is in Section 1.5.

1.2 Classification of Organic Materials

In the broadest sense, “organic” materials are materials primarily based around carbon atoms. For the purposes of this research, organic materials are restricted to those that have conjugated molecular structures and exhibit semiconducting properties. In strong contrast to conventional inorganic semiconductors based on covalently-bonded silicon or III-V, organic materials are loosely bound molecular solids held together by weak van der Waals interactions; this has a profound effect on their electrical properties.

Organic materials can be further subdivided into three categories based on complexity: discrete small molecules, polymers, and biological molecules (Figure 1-1). The most complex organic molecules known are biological, such as the absorbing chromophore antenna of *Rhodospseudomonas acidophila*, a purple-colored photosynthetic bacterium⁸. Biological molecules have not been incorporated into organic electronic devices.

The current field of organic photovoltaics is instead centered on the first two classes of materials, small molecules and polymers. This work has made extensive use of both types of materials.

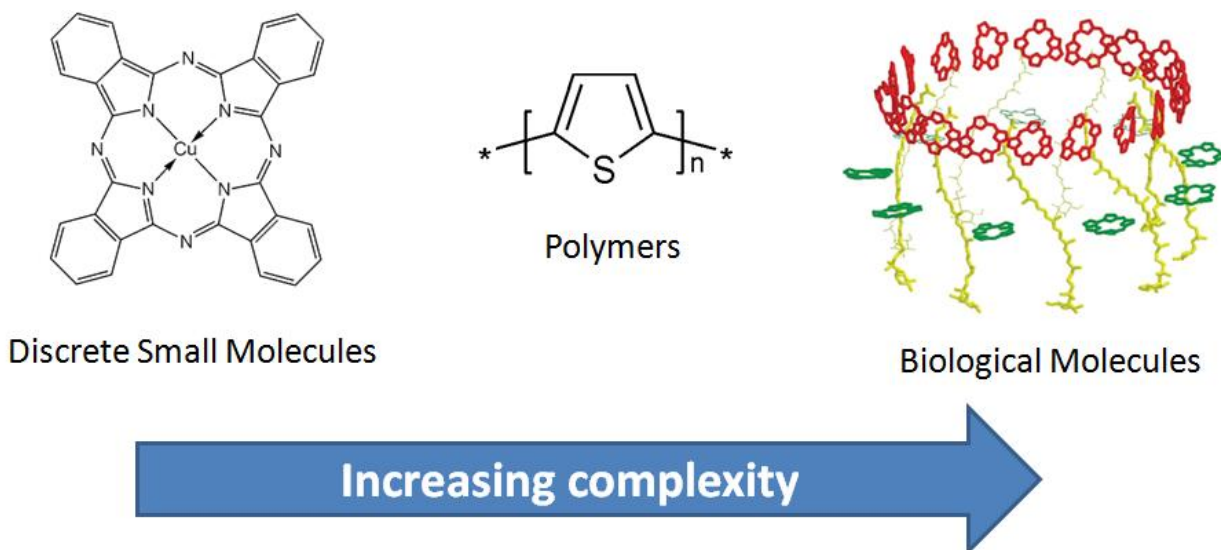


Figure 1-1. Examples of different categories in the spectrum of organic materials.

Small molecules are the simplest type of organic solid and, despite their moniker, can be relatively massive, with typical masses of several hundred atomic mass units (AMU). Regardless of their size, all small molecules are distinct units. The bulk of the organic materials considered in this work fall into this category. Moving up the complexity scale, one arrives at polymers, long chains of repeating units based on a backbone of carbon-carbon bonds. Polymer masses can vary greatly, ranging from tens to thousands of repeating units, with masses up to a million AMU. The complexity of semiconducting polymers also varies greatly, from relatively simple polythiophenes to intricate donor-acceptor complexes.

Several examples of organic small molecules and polymers used in this work are shown in Figure 1-2.

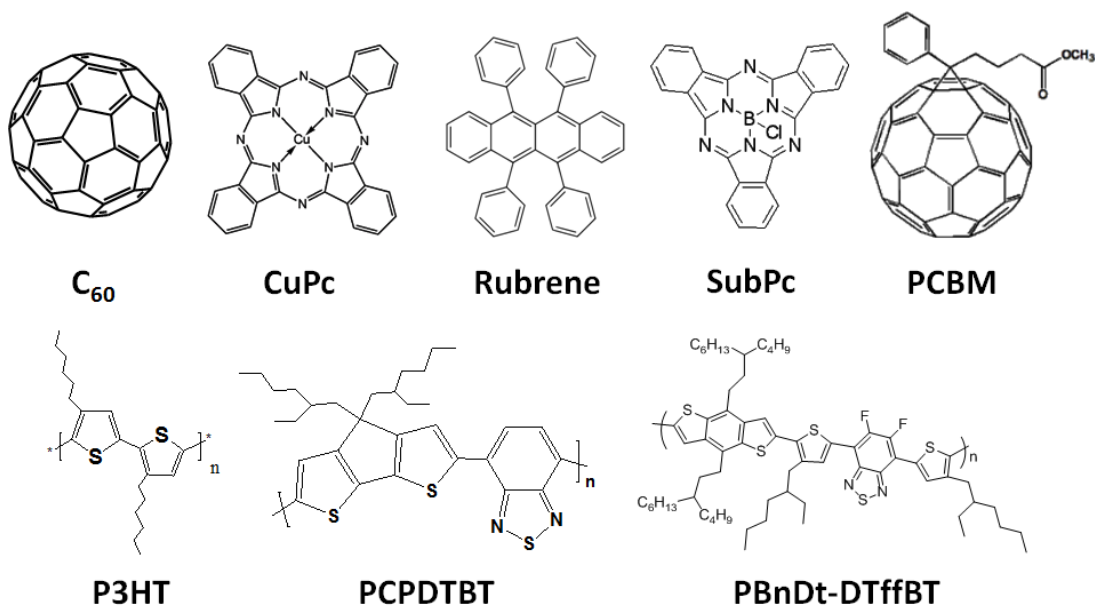


Figure 1-2. Molecular structures of several organic small molecules (top row) and polymers (bottom row) used in this work.

1.3 Electrical and Excitonic Properties of Organic Semiconductors

As a class, organic semiconductors have very different electrical properties when compared to traditional, inorganic semiconductors. In this section, a brief overview of the electronic structure and charge carrier behavior of an organic semiconductor will be discussed. Additionally, excitons, which couple optical and electronic processes in organics, are introduced. Consequently, optoelectronic devices based on excitonic semiconductors have different operation principles and design requirements compared to those based on traditional inorganic materials. An understanding of organic charge transport and exciton formation is therefore crucial in effective device design and optimization.

1.3.1 Origin of Electronic Structure

All organic semiconducting materials, whether they are small molecules, polymers, or more complex structures, rely on conjugated π -electron systems for conduction. Systems are considered π -conjugated when alternating carbon-containing single and double bonds are present in their molecular structure. A straightforward example of this system is an ethene molecule, C_2H_4 (Figure 1-3).

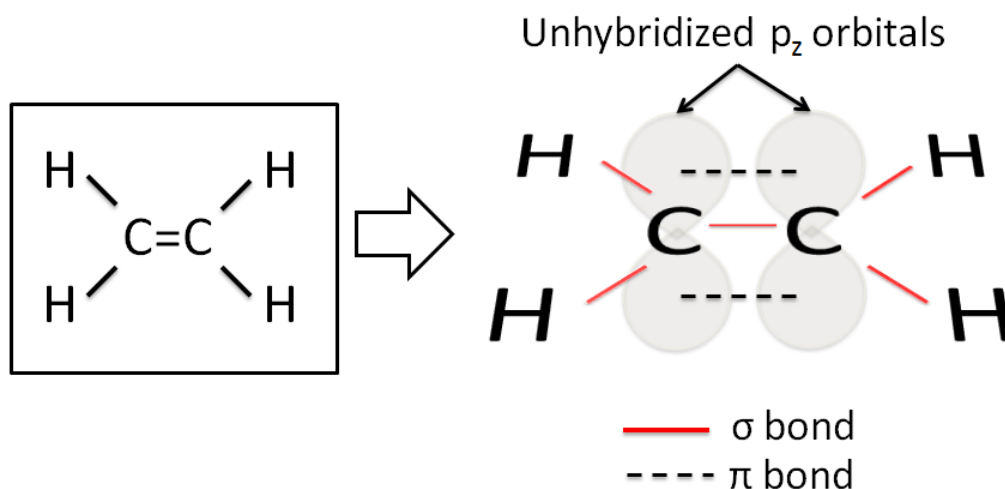


Figure 1-3. Diagram of σ - and π -bonding within an ethane molecule.

Each carbon atom in ethane is sp^2 hybridized, with three sp^2 orbitals created per atom and one leftover unhybridized p_z orbital. The six sp^2 orbitals result in five strong σ -bonds within the system (four C-H bonds and one C-C), with the leftover dumbbell-shaped p_z orbitals around each carbon atom forming a C-C π -bond. Due to the shape of the p_z orbitals, the C-C π -bond has weak interaction due to small electron cloud overlap above and below the molecular plane.

The strength of the overlapping σ -bonds leads to strong bonding (σ) and antibonding (σ^*) molecular orbitals (MOs). The weaker interactions of the parallel p_z

orbitals give correspondingly weaker bonding (π) and antibonding (π^*) MO energy levels, making the π - π^* transition the smallest possible electronic excitation within the molecule. This is schematically represented in Figure 1-4. Because of the importance of the π - π^* transition as the lowest-energy option in a π -conjugated system, the π -bonding MO is dubbed the “highest occupied molecular orbital (HOMO)” and the π^* -antibonding MO is named the “lowest unoccupied molecular orbital (LUMO).” The HOMO and LUMO, respectively, are analogous to the valence and conduction bands in inorganic semiconducting materials.

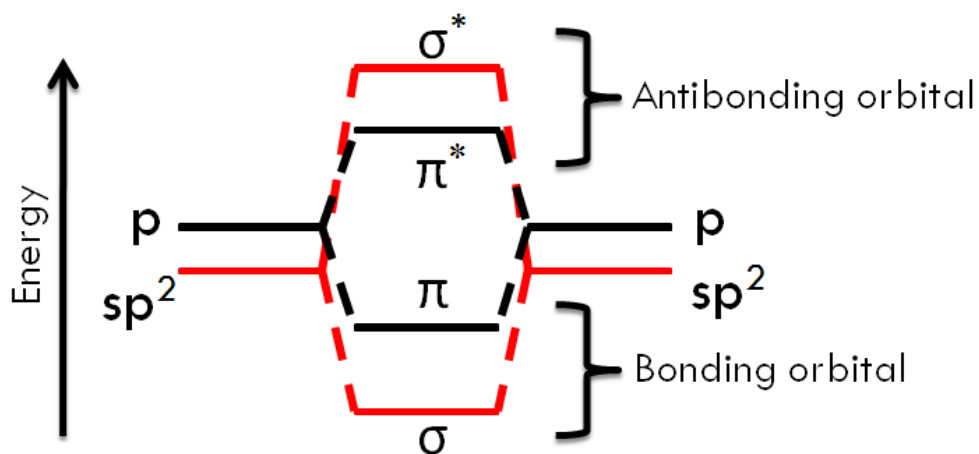
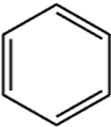
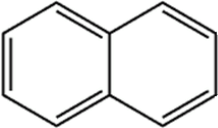
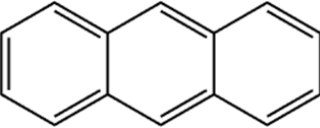
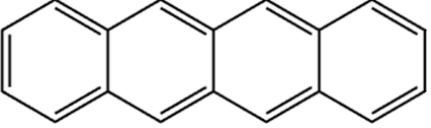
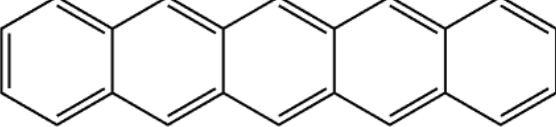


Figure 1-4. Schematic energy level diagram of a discrete organic molecule. The electronic band gap (HOMO-LUMO) is taken as the π - π^* gap.

The degree of π -conjugation within an organic solid has a large impact on its electrical properties. Increased conjugation length causes a greater degree of electron delocalization, increasing the mobility of charges through the π -bonding system. Similarly, short conjugation length localizes electrons, reducing their ability to freely move about a system. This is reflected archetypically in the polyacenes, conjugated systems of conjoined benzene rings (Table 1-1). Increased conjugation (more

conjoined benzene rings) corresponds with red-shifted absorption spectra caused by decreasing HOMO-LUMO separation⁹. This illustrates a prime strength of organic semiconductors: simple changes to a base molecule can alter its electronic transport and optical properties.

Table 1-1. Structures and optical properties of the polyacene family.

Molecule	Structure	Absorption Maximum
Benzene		255 nm
Napthalene		315 nm
Anthracene		380 nm
Tetracene		480 nm
Pentacene		580 nm

1.3.2 Transport Behavior

Charge transport within organic-based materials is a combination of two processes: intramolecular carrier movement and intermolecular charge transfer. Within a molecule, π -conjugation enables charge carriers to move freely. In organic materials, transport is limited by the weak van der Waals intermolecular coupling, drastically

lowering charge carrier mobility to typical values of 10^{-5} to 10^{-2} cm^2/Vs within the photovoltaic materials of interest¹⁰⁻¹².

Because of the weak coupling, charge carriers are strongly localized on individual molecules, preventing continuous band transport. Intermolecular transport typically occurs through a hopping process as a charge carrier overcomes an energy barrier to move from one molecule to the next. The mobility in this situation is dependent on the energy barrier height, electric field, and temperature according to

$$\mu(F, T) \propto \exp\left(\frac{-E_A}{k_B T}\right) \cdot \exp\left(\frac{-\beta\sqrt{F}}{k_B T}\right),$$

where k_B is the Boltzmann constant, F is the electric field, T is the temperature, E_A is the energy barrier height, and β is a material-dependent constant. The situation can change substantially based on the degree of interaction between adjacent molecules.

The van der Waals interaction force can be approximated by

$$U(r) = \frac{A}{r^{12}} - \frac{B}{r^6}$$

where A and B are empirically-derived constants, r is the distance between molecules, and U is the interaction potential energy. This relationship is known as the Lennard-Jones potential and is used widely in molecular dynamics simulations¹³. In this relationship, small deviations in r can have large effects on the degree of interaction within the solid, increasing coupling between molecules, decreasing charge carrier localization, and lowering the energy barrier for hopping transport. In a highly-ordered molecular crystal charge carriers are sufficiently delocalized that band transport is realized, much like in inorganic semiconductors. Charge mobility in highly pure crystals of 5,6,11,12-tetraphenylnaphthacene (rubrene) has reached values of 1-40 cm^2/Vs ¹⁴⁻¹⁷.

1.3.3 Excitons

Bound electron-hole pairs, or excitons, are crucial to the operation of optoelectronic organic devices, including organic photovoltaics and organic light emitting devices^{9,18}. In OPVs, excitons are the byproduct of photon absorption, where an electron is excited to the LUMO level of the molecule and coulombically binds with the hole left behind in the HOMO to slightly lower the total system energy. The exciton must then be broken back into free charge carriers (dissociated) to extract power from the device. In organic light emitting devices, injected charge carriers form excitons in an emissive layer, which then recombine to emit a photon. In either case, an electron and hole are separated by a distance r_c based on the coulombic attraction force and dielectric constant of the material. The material will form a tightly-bound exciton if r_c is larger than the Bohr radius r_B of the material, as in

$$\gamma = \frac{r_c}{r_B} = \left(\frac{q^2}{4\pi\epsilon_0 k_B r_0 m_e} \right) \left(\frac{m_{eff}}{\epsilon^2 T} \right),$$

where q is the elementary charge, k_B is the Boltzmann constant, m_e and m_{eff} are the standard and effective electron masses, and r_0 is the Bohr radius of hydrogen, 0.53 Å. If the ratio $\gamma > 1$, the semiconductor is excitonic; $\gamma < 1$ is a traditional inorganic semiconductor. A semiconductor is also excitonic if the critical radius is larger than the particle itself, as in inorganic quantum dots¹⁹.

Based on the spin of the electron and hole, the exciton can either be classified as a triplet (total spin = 1) or a singlet (total spin = 0), so named because triplets are created at a 3:1 ratio relative to singlets²⁰. Direct recombination of a triplet exciton is forbidden by spin conservation, giving it a much longer lifetime than a singlet, on the order of 10^{-6} s vs. 10^{-9} s^{21,22}. Exciton type is seldom considered in organic photovoltaic

devices, but huge advances in light emission efficiency have resulted by forcing recombination to occur in the lower energy triplet state using phosphorescent emitters, giving internal quantum efficiencies approaching 100%²³⁻²⁶.

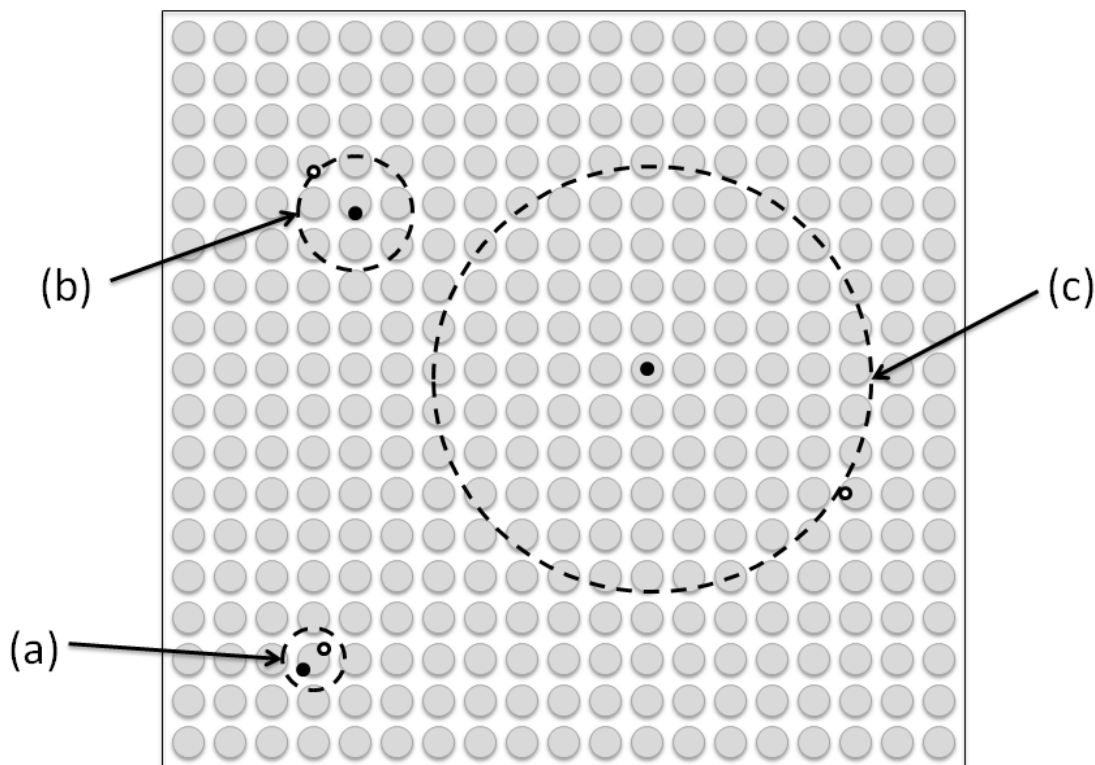


Figure 1-5. Schematic representation of different classes of excitons: (a) Frenkel (b) charge-transfer and (c) Wannier-Mott, with varying degrees of delocalization indicated.

There are three types of excitons that have been observed: Frenkel, charge-transfer (CT), and Wannier-Mott (Figure 1-5). Frenkel excitons are formed with the electron-hole binding distance smaller than a single molecule or (in the case of inorganics) the lattice constant of the crystallographic unit cell. CT excitons occur when the bound carriers are delocalized over adjacent molecules. The third class, Wannier-Mott excitons, are found in inorganic semiconductors, where the large dielectric constant screens the coulombic attraction of the electron and hole and allows them to

delocalize over a long distance. Binding energies of Frenkel and CT excitons are greater than 0.1 eV; Wannier-Mott binding energies are only a few meV. At room temperatures, Wannier-Mott excitons are dissociated by thermal energy – consequently, inorganic photovoltaics are not considered “excitonic” as any excitons formed upon photon absorption are immediately dissociated into free charge carriers.

While bound, excitons can move throughout a solid much like other fundamental particles. Because excitons are charge neutral, applied electric fields do not control their motion. Excitons instead diffuse through a material either in a band-to-band direct energy transfer method (Förster transfer), or in a molecule-to-molecule hopping process (Dexter transfer). In the former, temporary electric dipoles are formed in a molecule’s π -electrons upon initial excitation, which induce sympathetic dipoles in an adjacent molecule. When the first molecule’s dipole begins to relax, its energy is transferred to the second molecule. This can be thought of as a photon emission-and-absorption process, where the first molecule relaxes to the ground state and simultaneously excites the second molecule, though no photon is actually emitted. This process is highly dependent on both the spectral absorption overlap of the two molecules and the distance between them. In Dexter transfer, an excited electron moves directly to the LUMO of the acceptor molecule and an electron of the opposite spin is transferred from the acceptor to the donor HOMO. Förster transfer occurs at distances up to 10 nm²⁷, while Dexter transfer happens at shorter distances, typically 5-10 Å. Much as is the case with charge carrier transport, the weak intermolecular interactions in organic solids limit exciton mobilities and diffusion lengths; most excitons in organic solids can diffuse

on the order of 10 nm prior to recombination²⁷⁻²⁹, though micrometer diffusion lengths have been observed in highly pure rubrene crystals³⁰.

The large binding energy of Frenkel and CT excitons does not lend itself to easy dissociation. Thermal dissociation is not practical due to the low decomposition temperatures of organic materials. Excitons can be dissociated by application of an electric field, but the field strength must be in excess of 10^6 V/m, a prohibitively large value. The preferred route to induce exciton dissociation is the introduction of a heterojunction between organic materials with differing electron affinities and ionization potentials. When an exciton encounters such an interface, provided that the offset between the HOMO and LUMO levels is greater than the exciton binding energy, it is energetically favorable for that exciton to dissociate back into free charge carriers. This process will be discussed in detail in Section 2.3.1.

1.4 Processing Techniques of Organic Semiconductors

One of the most distinct differences between inorganic and organic semiconductors is the processing techniques required with each. Inorganic semiconductors are produced on expensive, highly pure crystalline substrates with high temperature, low throughput techniques. In contrast, organic semiconductors can be produced on inexpensive substrates such as glass, plastic, and metal foil, and their molecular nature allows for solution-based techniques. Prior to device fabrication, most small molecule materials are purified using multiple rounds of gradient zone sublimation^{31,32}. The concept and practical application of gradient zone sublimation are discussed in Section 1.4.1.

Two film deposition techniques are used extensively in this research: vacuum thermal evaporation and spin coating, respectively covered in Sections 1.4.2 and 1.4.3. Thin, high quality films can be produced with either of these techniques. There are a variety of other techniques for both polymers and small molecules that are promising for industrial production of organic electronics. These will be briefly highlighted in Section 1.4.4.

1.4.1 Small Molecule Purification

As purchased, most small molecule source materials are of insufficient purity for use in electronic devices. Listed material purities are typically in excess of 99% based on residual metal content. However, as electronic transport and quenching can be dominated by a small minority of defects and recombination centers, additional purification is required to obtain electronically acceptable source material. Materials will typically be purified from one to four times, depending on the quality of the source material. High purity crystalline yields for each purification are 25-75% of the source material mass, varying greatly based on the source material quality.

Materials can either be purified under high vacuum or under an inert gas flow, such as nitrogen or argon. The sublimation procedure occurs within a ~1.5" diameter quartz tube heated by a multi-zone furnace; prior to purification, the tube is cleaned under high vacuum at high temperatures (600-700°C) to eliminate all residual organic material. Several grams of source material are then added within a smaller inner quartz sleeve and placed in the hottest zone of the furnace. Two additional quartz collection sleeves are also added to the main tube to serve as high and low purity collection tubes. Finally, a plug of quartz wool is used to prevent excessive material contamination of the

vacuum pumps and a mesh screen prevents stray quartz wool fibers from collecting in the pumping chamber and damaging the high vacuum turbo pump. The system is then sealed and pumped to the desired pressure ($< 10^{-5}$ Torr for high vacuum, ~ 100 Torr with 0.1-0.2 scfh gas flow for inert gas flowthrough, moderated by a vacuum switch-controlled solenoid valve and rotary vane roughing pump).

The furnace temperature is then slowly increased to the sublimation temperature of the source material (generally 300-400°C) and a temperature gradient of up to $\pm 50^\circ\text{C}$ is applied relative to the middle zone. The temperatures are selected such that light impurities and the high purity crystalline material sublime in the hottest zone. The middle zone temperature allows the high purity crystalline material to deposit; light impurities deposit at the coolest end of the furnace. A schematic of this process is shown in Figure 1-6. The entire purification process can take several days, with high pressure flowthrough purifications generally taking less time than high vacuum. After the process is complete, the high purity crystals are collected and added to clean tubes as the source material for an additional purification cycle, if desired.

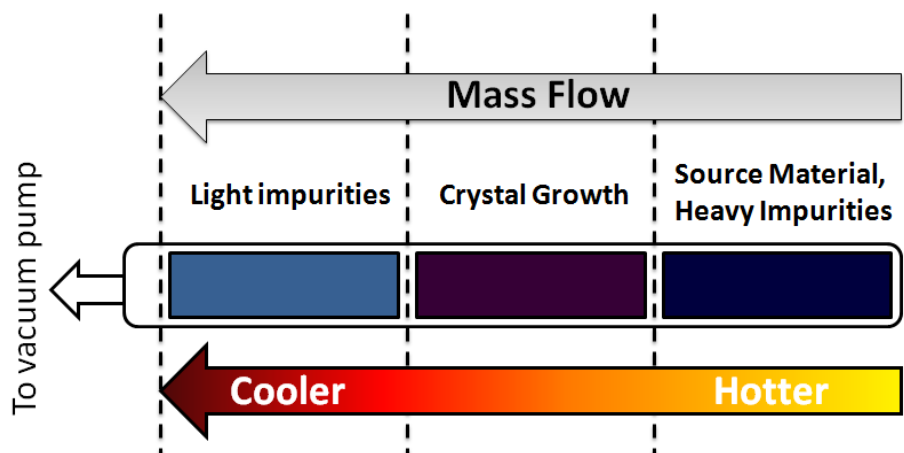


Figure 1-6. Gradient zone sublimation, with colors approximating that of CuPc during high vacuum purification.

1.4.2 Vacuum Thermal Evaporation

Vacuum thermal evaporation (VTE) is the preferred method for growing thin films of organic small molecules. Polymers are ill-suited to VTE, as they decompose at temperatures lower than their evaporation temperature. The size and complexity of VTE systems can vary greatly. A simple VTE system is shown in Figure 1-7, consisting of source material holders (“boats”), a quartz crystal monitor and shutter to accurately control film thickness, and a shadow mask to pattern the substrate.

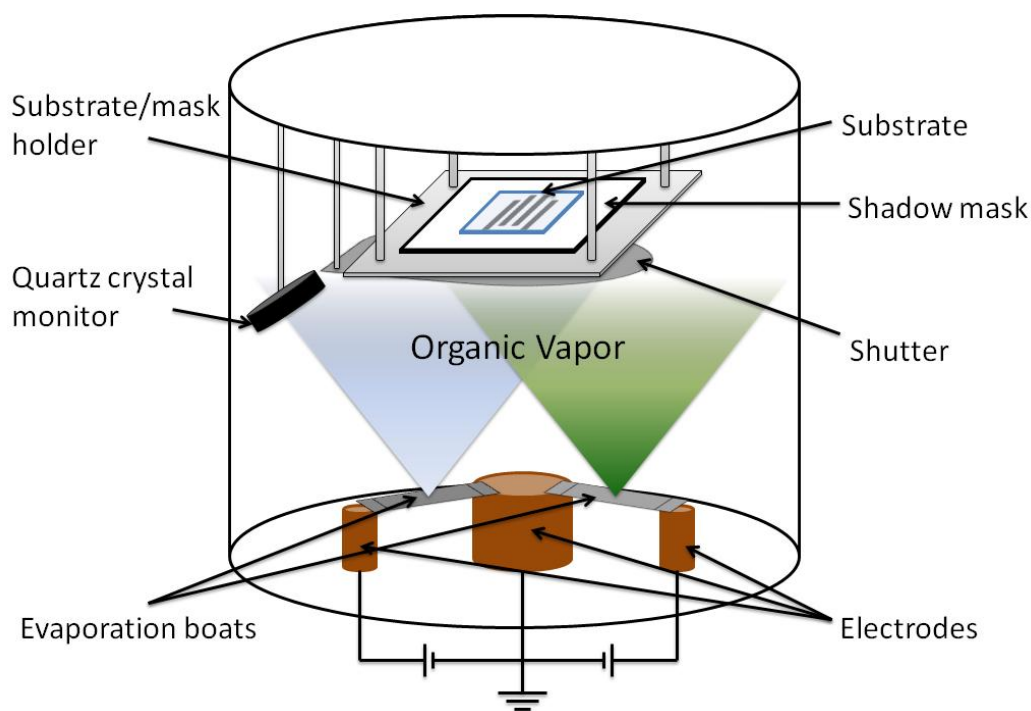


Figure 1-7. A representative vacuum thermal evaporation (VTE) system. The entire chamber is held at 10^{-6} to 10^{-7} Torr during evaporation.

The source-to-mask distance in the primary chamber used for this work is approximately 20 cm. A large source-to-mask distance results in less efficient source material usage due to a smaller fraction of the molecular beam impacting the substrate,

but will improve the uniformity of the layer thicknesses across multiple substrates. Additionally, the substrate platter can be rotated to increase film thickness uniformity.

The source materials are loaded into boats made from refractory metals (i.e. tungsten, molybdenum, tantalum) or insulating crucibles (i.e. boron nitride, aluminum oxide, quartz). The system is evacuated to high vacuum ($< 10^{-6}$ Torr) and the boats are resistively heated to the evaporation (or sublimation) temperature of the source material. To increase uniformity in the molecular beam, the boats can be designed to act as a point source.

The evaporated molecules exhibit ballistic transport behavior after exiting the boat, with the mean free path of each molecule determined according to³³

$$MFP = \frac{k_B T}{\sqrt{2} \cdot P_{dep} \cdot \pi d^2},$$

where k_B is Boltzmann's constant, T is the temperature of the molecular flux, P_{dep} is the pressure in the deposition chamber, and πd^2 is the collision area between molecules, assuming that all molecules are spherical. In a typical high vacuum VTE system MFP is much greater than h , the source-to-mask distance. This means that molecules can be assumed to follow a straight line between the source and the substrate without any collisions in between to alter their path, making geometric analysis of the mask and resulting feature size simple to determine. The feature resolution limit p of the system is

$$p \approx \frac{(s + 2t)l}{2h}$$

where s is the substrate-to-mask separation, h is the source-to-mask distance, t is the thickness of the mask, and l is the width of the source. As shown in Figure 1-8, divergent beams from the source, mask thickness, and substrate separation create a

shadowing effect that increases the feature size beyond the mask aperture. Slightly increased feature size must be accounted for when calculating efficiencies to report accurate values, but is generally not a concern in large area organic photovoltaic devices. During deposition, the film thickness and deposition rate are monitored with a calibrated quartz crystal microbalance. A properly calibrated system can achieve average film thicknesses less than one nanometer (i.e. a partial monolayer), allowing for detailed investigation of organic film growth behavior³⁴.

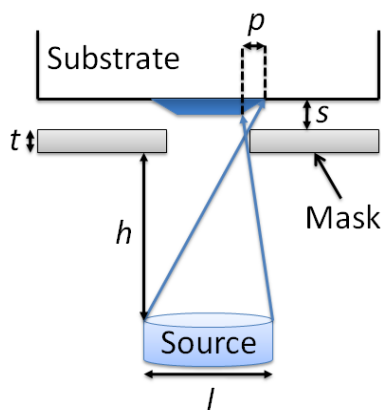


Figure 1-8. Diagram of shadow mask geometry.

VTE has several advantages, offering high quality film deposition without the expense of a molecular beam epitaxy system, the ability to deposit metals, organics, and some inorganic dielectrics in the same system, very fine thickness control, and the capability to deposit complex, multilayer structures. Additionally, VTE is a preferred route for doping, as multiple crystal monitors can be used to precisely measure the rates of coevaporated materials. Doping has not found widespread use in organic photovoltaic devices, but organic light emitting devices rely extensively on it. VTE is not suitable for all applications, however – it cannot process polymers and materials with

low decomposition temperatures, and a large percentage of the source material is wasted. Still, it is a mainstay technique for the fabrication of small molecule organic electronics devices.

1.4.3 Spin Coating

As discussed in the previous section, polymers and other materials with decomposition temperatures less than their evaporation temperatures cannot be processed with vacuum thermal evaporation. Instead, these materials are processed using solution-based methods, the most common laboratory technique being spin coating. Spin coating is an inexpensive method to achieve uniform thin films with a defined thickness from a wide variety of starting solutions. It is a well established technique, with the most familiar industrial application being photoresist application for photolithography in inorganic microelectronic device fabrication and patterning.

There are four stages to the process:

1. Solution deposition,
2. Spin-up/acceleration,
3. Spin-off, and
4. Solvent evaporation.

In step (1), the source solution is added to the substrate. There are few constraints on the solution, save that an excessive amount of solution is deposited onto the substrate and it must be able to flow. The solution should also be free of dust and other particulates, as these can lead to defects in the final film. In the second step, the substrate is accelerated (either gradually or rapidly) to a final desired spin speed (typically several thousand revolutions per minute). Centrifugal forces create a wave front in the solution and it flows to the edge of the substrate. In the third stage, excess

solution is cast off the edge of the film and a uniform thickness is achieved based on a balance of the centrifugal force from acceleration and the solution viscosity. The film then dries in the final stage as excess solvent evaporates. The spin coating process is diagrammed in Figure 1-9.

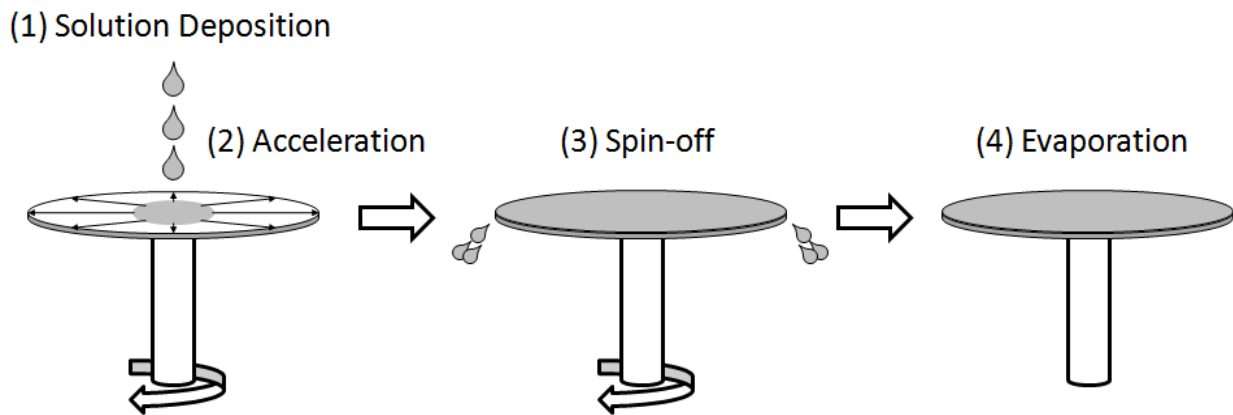


Figure 1-9. Stages of spin coating.

The final film thickness is dependent on the initial solution concentration, acceleration rate, solvent evaporation rate, and final spin speed, making fine thickness control and repeatability possible. However, because films are initially deposited in the liquid state, multilayer structures are difficult to process unless underlying layers are not compatible with upper layer solvents. Otherwise, the underlying layers will redissolve and mix with the new layer. Also, metal electrodes must still be processed in vacuum after the polymer layer is deposited, though solution-processed electrodes are currently under investigation³⁵⁻³⁷. Additionally, a large proportion of material is lost during the spin-off stage making this a relatively expensive technique from a material usage standpoint. While spin coating is ultimately limited as a production-scale method due to

wasted source material and limited substrate diameter, its low equipment cost and simplicity make it the standard laboratory technique for solution-processed devices.

1.4.4 Emerging Techniques

While vacuum evaporation and spin coating are the primary techniques used for device fabrication in this work, there are a myriad of other techniques that are gaining increasing interest for industrial-scale production and laboratory-scale investigation. Foremost amongst these techniques is inkjet printing, a solution-processed technique that offers high-throughput fabrication and non-lithographic patterning as small as 5 μm , depending on substrate preparation^{38,39}. Inkjet printing has very little overspray and is therefore much less wasteful than most other solution-based methods. However, there are challenges to overcome: ink formulation is difficult, and nozzle alignment is extremely important to pattern small features.

Spray deposition is another alternative solution-based fabrication method that is highly compatible with high-throughput processing and large deposition areas⁴⁰⁻⁴². The spray is either formed within an atomizer or pumped in liquid form to an ultrasonic nozzle. After the spray is formed it is guided by an inert gas flow to the substrate. Because the solution arrives at the substrate as micrometer-diameter droplets, a prime challenge in spray deposition is achieving uniform, high-quality films.

The main competitor to VTE for small molecule deposition is organic vapor phase deposition (OVPD)^{33,43}. In OVPD, materials are evaporated in boats or effusion cells under an inert gas atmosphere. The resulting molecular beam is directed towards the substrate by an inert carrier gas flow. This method uses source materials more efficiently than VTE, but deposition rates are sensitive to pressure, temperature, and

flow rate, making OVPD more difficult to control. A related technology is organic vapor jet printing (OVJP), a hybrid between OVPD and inkjet printing, where organic vapor is fed through a printing nozzle via an inert carrier gas, making patterning possible without shadow masking⁴⁴⁻⁴⁶.

1.5 Common Organic-Based Devices

Organic semiconductors have been successfully applied to a wide variety of electronic devices. The following section is a brief overview of the two main organic optoelectronic device types: photovoltaics and light emitting devices.

1.5.1 Organic Photovoltaics

Efficient OPV devices were first demonstrated in 1986 by Tang with a ~1% efficient bilayer heterojunction consisting of copper phthalocyanine and a perylene derivative⁴⁷. Since the introduction of this architecture, rapid advancements have been made in both basic scientific understanding and device performance. Through the understanding and development of new active layer materials and optimization of device architectures, state-of-the-art OPVs now have efficiencies of over 8%⁴⁸. Processing technology has also evolved to the point that commercial production and market viability are increasing. Some examples of OPV products are shown in Figure 1-10, highlighting their main advantage over inorganic PV modules: they are lightweight, flexible, and produced using roll-to-roll processing. These advantages make OPVs an excellent source for integration into building materials and everyday objects for portable power generation, such as clothing. OPVs can also be made to mimic natural shapes, such as leaves, for aesthetically pleasing or concealed installation.

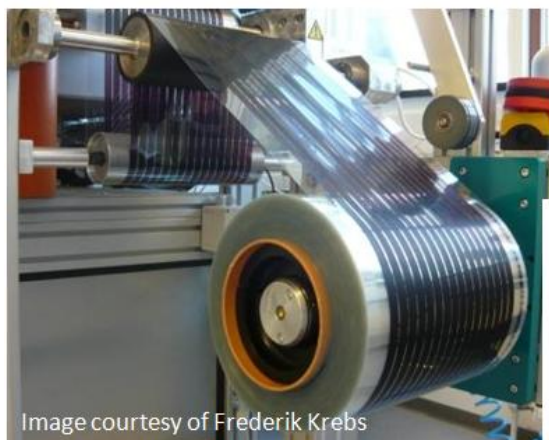


Image courtesy of Konarka, Inc.

Figure 1-10. Examples of organic photovoltaic devices. Clockwise from the far left: roll-to-roll production line of polymer OPVs, leaf-shaped flexible OPVs, and a commercially available OPV module, Power Plastic by Konarka, Inc.

This work has focused on two areas of organic photovoltaics research: Chapter 5 concerns how free charge carriers move within the device after exciton dissociation; Chapter 6 discusses the impact that controlled light propagation has on device performance, with the goal of demonstrating practical enhancement techniques to push efficiencies towards commercially desirable values.

For a detailed history of organic photovoltaics and a discussion of device operation principles, the reader is referred to Chapter 2. Proper measurement system calibration and device characterization techniques are discussed in Chapter 3.

1.5.2 Organic Light Emitting Devices

To date, organic light emitting devices (OLEDs) have found the widest commercial acceptance within the field of organic electronics. In many ways, OLEDs operate as the reverse of OPVs – charges are funneled into a light emitting organic material to form an exciton, which then recombines to emit light. The color of light is dependent on the optical gap of the emitting molecule.

While organic electroluminescence has been known since the 1960s⁴⁹, practical OLEDs were not realized until 1987 with the demonstration of a bilayer heterojunction of a hole-transporting layer of N, N'-bis(naphthalen-1-yl)-N,N'-bis(phenyl)-benzidine (NPB) and an electron-transporting layer of aluminum tris(8-hydroxyquinoline) (Alq3)⁵⁰. In this device, holes and electrons are efficiently transported to the heterojunction interface by their respective layers, and exciton formation and recombination occurs within the Alq3 layer to emit green light. The electron-to-photon conversion efficiency was approximately 1% at a driving voltage of less than 10 V, substantial improvements over previous technology.

The largest jump in OLED performance came with the introduction of heavy-metal complex phosphorescent emitters, which enable radiative recombination of triplets via spin-orbit coupling²³. As discussed in Section 1.3.3, the triplet to singlet ratio in organic materials is 3:1, and radiative recombination of the triplet state is forbidden. The heavy metal atoms permit the singlet and triplet exciton states to mix, allowing all excitons to contribute to light emission. Phosphorescent OLEDs have demonstrated ~100% internal quantum efficiency²⁴⁻²⁶.

OLEDs have rapidly matured into a commercially viable technology for active-matrix displays, promising greater efficiency, flexibility, and truer color reproduction than

liquid crystal technology. A second application area is in solid-state white lighting, with many laboratories demonstrating highly efficient, true white devices. Several commercially available and prototype applications are shown in Figure 1-11.



Figure 1-11. Examples of commercial OLED products. Clockwise from top left: 15" television (LG Display), large area white light OLED panel (Fraunhofer IPMS), semitransparent automobile heads-up display (NeoView KOLON/Hyundai), and a 6.5" flexible active matrix OLED display (Samsung SDI).

1.6 Research Scope

There are two main topics to the results presented here: first, understanding and controlling the behavior of charge carriers within organic optoelectronic devices by modifying the heterojunction architecture and second, increasing performance by

controlling the interaction of incident light with the device. Chapters 1 and 2 provide background information to aid in the reader's understanding of the current field of organic electronics, particularly organic photovoltaics. Chapter 3 describes the experimental measurement methods and characterization of device performance, including the introduction to a novel characterization technique developed for use in Chapter 5.

The subsequently presented research is heavily related to understanding optical behavior within the device active area. Therefore, Chapter 4 describes two different optical simulation techniques, Monte Carlo ray optics and transfer matrix wave optics. In addition to the mathematical underpinnings of these methods, example results are presented to demonstrate the potential of each technique and describe some specific aspects of their implementation for this work.

Chapter 5 explores the correlations between optical field, charge carrier motion, and heterojunction architecture in organic photovoltaic devices. Synchronous photocurrent detection was used to directly measure the photocurrent contribution from a variety of devices and a detailed qualitative model is presented to explain the observed behavior. The model is then extended further to explain optical field dependence and provide evidence for field-assisted dissociation of excitons in bilayer OPVs.

Optical management is the topic of Chapter 6. Transparent, stamped microlens arrays were used to increase performance in a wide range of organic photovoltaic devices. Their macro-scale optical behavior and geometric effects on enhancement were probed using Monte Carlo ray optics simulations and modified transfer matrix

wave optics simulations were applied to understand the effect of microlens arrays on the internal optical field. In both cases, qualitative and quantitative agreements with experimental results were obtained.

Chapter 7 discusses organic bifunctional optoelectronic devices (BFDs). BFDs can operate as either an OPV or an OLED, but the optimal designs of these two device types are in opposition. Namely, OLEDs funnel charge carriers into the center of the device for recombination and light emission, whereas OPVs are designed to quench excitons and efficiently remove photogenerated charge carriers from the device interior. This places unique design constraints on BFDs, which were explored. Ultimately, significant redesign of BFDs is required to maintain reasonable performance in both operation modes. Finally, Chapter 8 summarizes the results of this research and offers possible routes of further investigation.

CHAPTER 2 INTRODUCTION TO ORGANIC PHOTOVOLTAIC DEVICES

2.1 Basic Concepts

The conventional silicon photovoltaic device is over half a century old and has established itself as a promising clean, alternative energy source. While these devices offer high power conversion efficiencies, their total cost per watt is still too high to be competitive with non-renewable resources due to expensive source materials, processing costs, and installation restrictions. A push has been made recently to develop so-called “Class III” photovoltaic devices, which would offer electricity at less than \$1/watt⁵¹. Extremely high-performance compound semiconductors and inorganic thin film devices are two examples of Class III technology; a third, and the focus of this work, is organic-based photovoltaics (OPVs).

Organic materials hold several intrinsic advantages over inorganics, among them processability on inexpensive substrates using high-throughput methods, intrinsic flexibility and mechanical robustness, and low source material cost. These beneficial characteristics have generated a huge amount of scientific interest, and performance has steadily increased from a reported value of 1% in 1986 to over 8% today^{47,48}. This chapter will describe the basic operation of organic photovoltaic devices and the history of their development, along with the current major avenues of investigation for increased performance.

Before this, it will be beneficial to the reader to understand the parameters used to quantify OPV performance. Figure 2-1 shows the current-voltage (J-V) characteristics of a representative device. Three curves are depicted: the dark current, characteristic

of a typical diode, the photocurrent, the current generated by the device under illumination, and the total current, the summation of the dark and photocurrents. Because the dark current is always present, it is common to not consider the photocurrent as a separate component as it is difficult to directly measure.

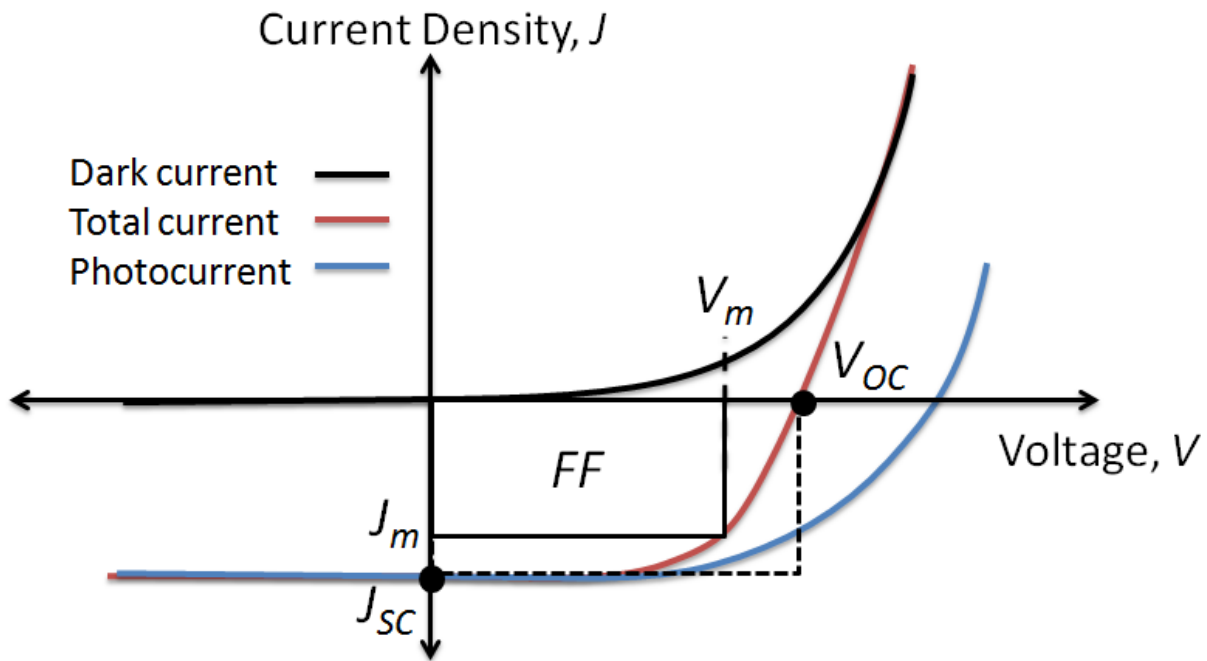


Figure 2-1. Current-voltage characteristics of a representative photovoltaic device.

Two points indicated on the current and voltage axes are the short-circuit current density, J_{SC} , the photocurrent generated at zero applied bias, and the open-circuit voltage, V_{OC} , the point at which the summation of the photo and dark currents equals zero. Also indicated are the current and voltage at the maximum power point, $P_m = |J_m V_m|$, within the power-generating fourth quadrant (where $V < V_{OC}$).

The fill factor (FF) is the ratio of the measured maximum power to the ideal maximum power and is representative of the “squareness” of the total current curve, such that

$$FF = \frac{J_m V_m}{J_{sc} V_{oc}}$$

An ideal fill factor will therefore be unity. Modern optimized OPV devices have $FF \leq 0.7$ ⁴⁸. The metric of greatest interest is the total power conversion efficiency, defined as

$$\eta_p = \frac{J_{sc} V_{oc} FF}{P_0}$$

where P_0 is the incident power intensity. A final parameter of interest is the external quantum efficiency (EQE), a ratio of the number electron generation to incident photons at a certain wavelength,

$$\eta_{EQE} = \frac{I_{sc}/q}{P_0/\lambda hc}$$

with q as the elementary charge, h as Planck’s constant, and c as the speed of light.

The details of measuring quantum efficiency are presented in Chapter 3.

Photovoltaic devices can be represented by an equivalent circuit, shown in Figure 2-2. The equivalent circuit contains an ideal diode in parallel with a current source, representing the photocurrent generation within the device. There are two resistors that are additionally present – the series resistance, R_s , which represents the intrinsic electrical resistance of the organic semiconducting layers and contact resistances, and

the shunt resistance, R_{sh} , a parallel resistance that represents leakage between the electrical contacts.

From this circuit, an expression for the current-voltage relationship can be developed, known as the Shockley equation:

$$J = J_s \left\{ \exp \left[\frac{q(V - JR_s)}{nkT} \right] - 1 \right\} + \frac{V - JR_s}{R_{sh}} + J_{ph}$$

where J_s is the saturation current density of the diode, n is the diode ideality factor, k is Boltzmann's constant, and T is the temperature. From this relationship, it is clear that J is maximized when R_s is minimized and R_{sh} is maximized. Increases in R_s are associated with decreased FF and J_{SC} ; decreased values of R_{sh} reduce FF and V_{OC} . The principle components of an OPV are also shown in Figure 2-2. The specific mechanisms of operation and materials selection criteria for these layers will be discussed in Section 2.3.1.

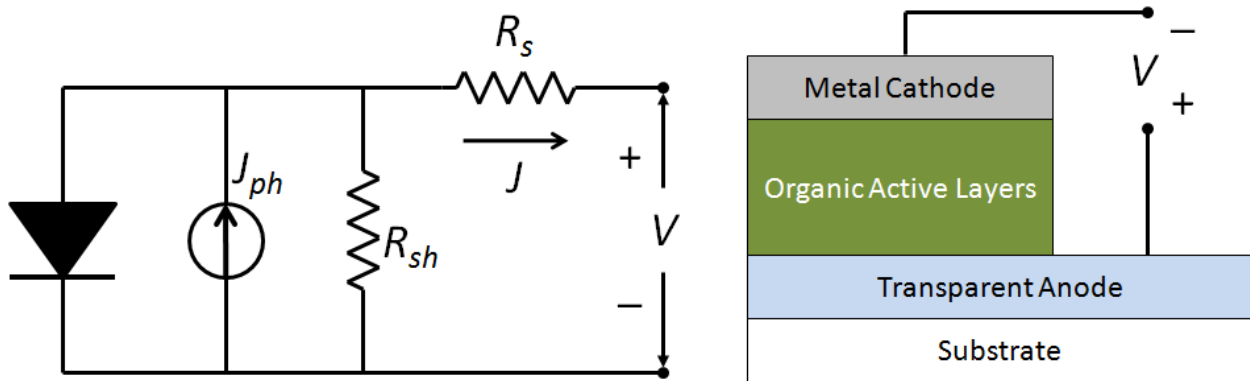


Figure 2-2. Equivalent photovoltaic device circuit and typical schematic of an organic photovoltaic device.

For an ideal photovoltaic device ($R_s = 0$, $R_{sh} = \infty$), the photocurrent is directly proportional to the incident power and remains a constant value regardless of the

magnitude of P_0 . The open circuit voltage is defined as the voltage at which the total current $J = 0$, or

$$V_{OC} = \frac{nkT}{q} \ln \left[\frac{J_{ph}}{J_s} + 1 \right],$$

giving V_{OC} a logarithmic dependence on J_{ph} and, therefore, on P_0 . Assuming no loss mechanisms, η_p should increase logarithmically with incident power due to the increase in V_{OC} and the constant value of J_{SC}/P_0 .

In an actual device, there are loss mechanisms. The series and shunt resistances are finite values, reducing FF , J_{SC} , and V_{OC} from their ideal values. Additionally, bimolecular recombination increases with free carrier concentration (and, therefore, illumination intensity), causing the J_{SC}/P_0 ratio to reduce with increased illumination intensity according to¹⁸

$$R_{BM} = \gamma(np - n_i p_i) \propto np$$

$$\gamma = \frac{q}{\epsilon_0} (\mu_n + \mu_p)$$

Therefore, the highest value of η_p for a given OPV device is obtained at an incident power intensity where the increase in V_{OC} is greater than the decrease in J_{SC}/P_0 due to bimolecular recombination.

2.2 Overview and History

While the photovoltaic effect has been observed in organic materials dating back to 1959⁵², modern efficient organic photovoltaic devices emerged in the 1980s with the introduction of the bilayer heterojunction architecture. Prior to this advancement, OPVs were inefficient Schottky diodes that relied on the strong electric field near a metal

electrode-organic interface to split the photogenerated exciton and create free charge carriers^{53,54}. This is intrinsically inefficient, as excitons can be quenched at the metal interface and exciton dissociation only occurs in a narrow band near the electrode, wasting a large percentage of absorbed photons. In an organic heterojunction, excitons are instead split apart by the energy level offsets at the heterojunction interface.

A notable early success in bilayer OPV devices was reported by Harima, *et al.* in 1984⁵⁵. By combining the electron-transporting material 5,10,15,20-tetra(3-pyridyl)porphyrin (TPyP) and the hole transporting material zinc phthalocyanine (ZnPc) they observed a roughly thirty times increase in photocurrent compared to a reference single layer ZnPc Schottky device. Power conversion efficiency under weak, 430 nm monochromatic illumination was ~2%, but poor exciton transport behavior limited performance. Additionally, photocurrent contribution was limited to the TPyP layer.

The true breakthrough in OPV device performance, with a power conversion efficiency under simulated AM2 solar illumination of nearly 1%, was reported by Ching Tang in 1986⁴⁷, a nearly ten-fold increase over earlier efforts. Tang used a hole-transporting layer of copper phthalocyanine (CuPc) and an electron-transporting layer of 3,4,9,10-perylene tetracarboxylic-bis-benzimidazole (PTCBI). This architecture shows photocurrent contribution from both layers, improving photocurrent generation and spectral response.

The Tang cell became the archetype for future OPV devices. It had four components: an electron-transporting/electron-accepting layer (PTCBI), a hole-transporting/electron-donating layer (CuPc), a transparent high work function electrode (indium tin oxide, or ITO) and a low work function electrode (silver). Convention has

respectively named these layers the acceptor, donor, anode, and cathode. The selection of these materials must follow certain guidelines for an efficient cell: the anode and cathode should correspondingly have Ohmic contact with the donor and acceptor, and the heterojunction formed between the donor and acceptor must have energy level offsets great enough to efficiently dissociate excitons from both materials. This is the key advantage that Tang's cell had over Harima's TPyP/ZnPc device. The TPyP/ZnPc interface can only dissociate TPyP excitons, but the CuPc/PTCBI interface can dissociate both CuPc and PTCBI excitons. Additionally, the donor and acceptor can either be deposited as neat layers, to form a planar (or bilayer) heterojunction or mixed together to form a mixed (or bulk) heterojunction.

2.3 Operation Principles

2.3.1 Basic Processes

Before discussing the steps taken to improve upon Tang's results and reach the current world record efficiency of 8.3%^{5,48}, it is beneficial to describe the basic operation of an OPV device. There are four primary, sequential processes (Figure 2-3) that must occur in order to extract power from an OPV⁵⁶:

- Photon absorption (exciton generation)
- Exciton diffusion
- Charge transfer (exciton dissociation)
- Charge collection

As there are efficiencies associated with each of these processes, the overall quantum efficiency of a photovoltaic device can be summarized as the product of its constituents,

$$\eta_{EQE} = \eta_A \eta_{ED} \eta_{CT} \eta_{CC}$$

Or, the latter three processes can be considered as their own product, the internal quantum efficiency, reducing the quantum efficiency to:

$$\eta_{EQE} = \eta_A \eta_{IQE}$$

Thinking of device efficiency in these terms can be advantageous; absorption and internal quantum efficiency are inherently opposed in most organic systems.

The first process, light absorption, is characterized by an optical absorption length of $1/\alpha$, where α is the wavelength dependent absorption coefficient of the material. Typical values of α for organic materials are 10^4 to 10^5 cm^{-1} , leading to absorption lengths of at least 100 nm. The absorption spectra for several photovoltaic materials are shown in Figure 2-4.

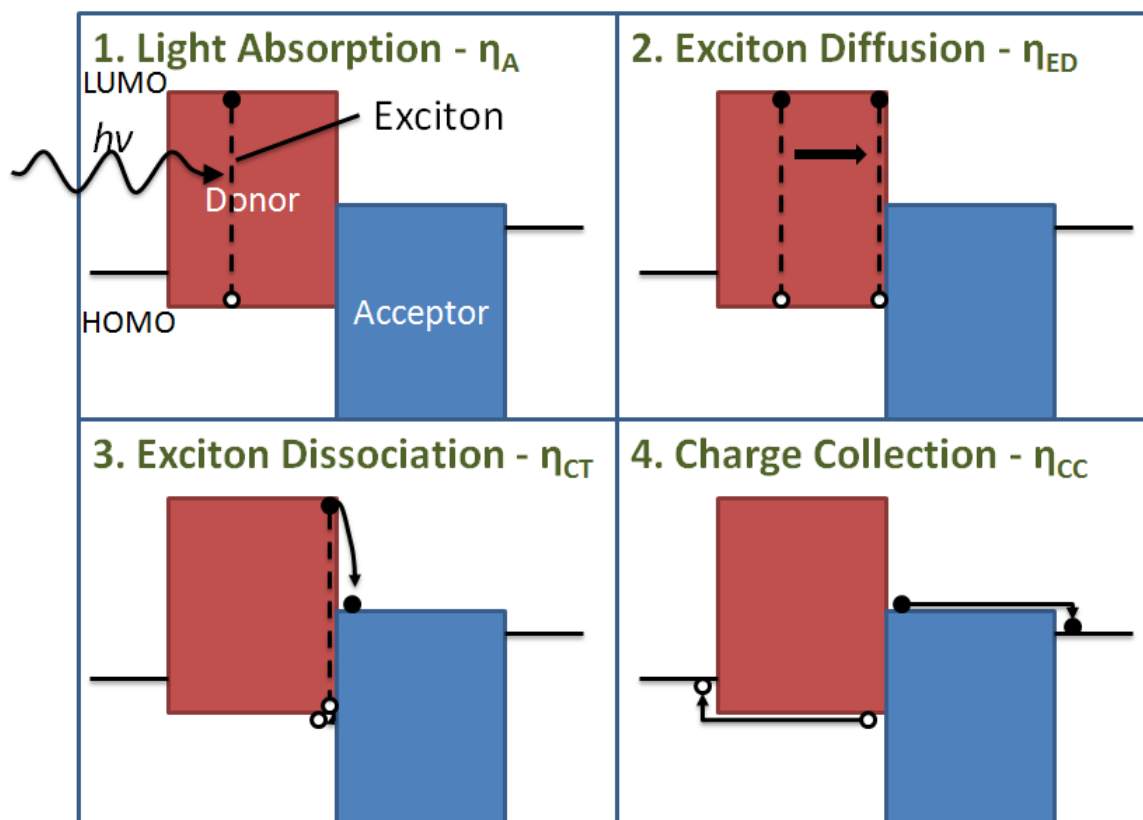


Figure 2-3. Basic processes in power generation in a bilayer organic photovoltaic device.

The donor and acceptor materials should be chosen to maximize absorption across the visible spectrum. Tang's choices of CuPc and PTCBI only absorb strongly between 500-700 nm. Recent advances have been realized by incorporating small bandgap materials to increase near-infrared absorption, such as lead phthalocyanine (PbPc) and new conjugated polymers, as discussed in Section 2.4.1.

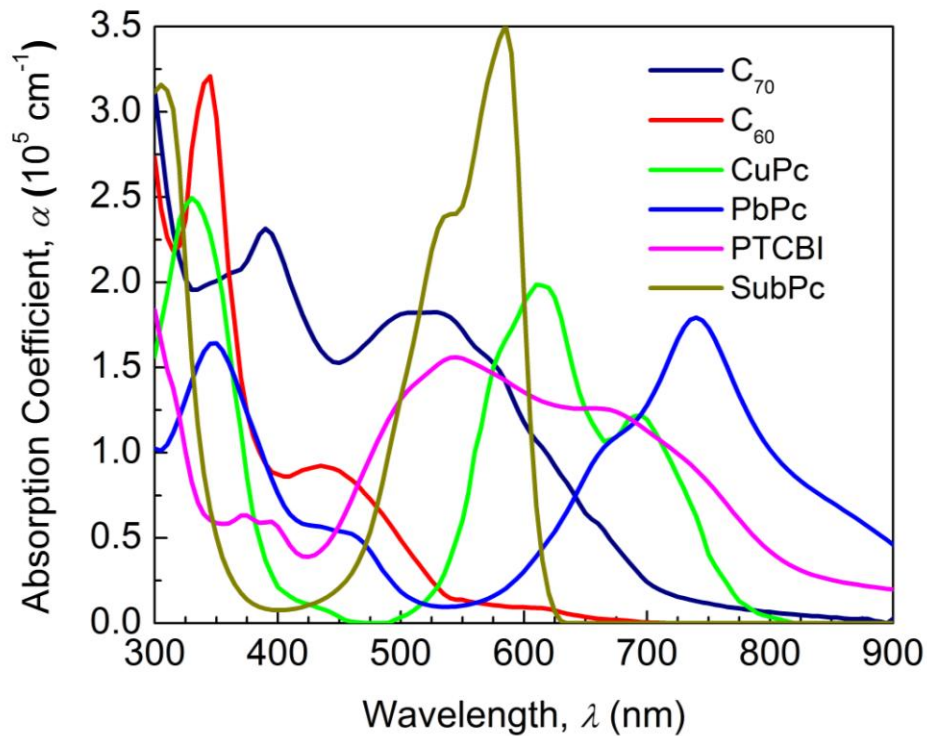


Figure 2-4. Optical absorption spectra for several organic photovoltaic materials, calculated from extinction coefficient data measured with spectrographic ellipsometry.

Upon absorption, an exciton, or bound electron-hole pair, is formed within the material, with a typical binding energy of 0.1 – 1 eV¹⁸. Excitons are mobile particles, and will diffuse within the organic material, characterized by the exciton diffusion length

$l_{ex} = \sqrt{D_{ex}\tau}$, with D_{ex} as the diffusivity and τ as the exciton lifetime. Most organic

material exciton diffusion lengths are on the order of 10 nm²⁷⁻²⁹. The smaller exciton diffusion length relative to the optical absorption length in most organic materials results in $\eta_{ED} \ll 1$ for bilayer heterojunctions that are thick enough to absorb a substantial proportion of the incident light. Bulk heterojunction devices do not have this limitation.

While the exciton is present and mobile within the active layer, two basic processes can occur. First, the exciton can recombine, either within the organic layer after a certain time τ has elapsed or at a metal-organic interface; this will reduce η_{ED} . Otherwise, the exciton will be dissociated by either the electric field or at the heterojunction interface. Schottky-type OPVs rely on field-assisted dissociation, but as the field required to efficiently dissociate an exciton is quite large, $\sim 10^5$ to 10^6 V/m^{1,57}, this process is typically ignored in organic heterojunction devices. Charge generation is assumed to occur solely through dissociation at the organic heterojunction interface, where it is energetically favorable for the bound exciton to split and have the free electron and hole reside on different molecules (electron on the acceptor, hole on the donor). In other words, the separation between the donor HOMO and acceptor LUMO is greater than the binding energy of the exciton¹. The exciton dissociation process is exceedingly fast, on the order of a few hundred femtoseconds⁵⁸. In a properly designed heterojunction, the charge transfer efficiency η_{CT} is taken as unity. The HOMO and LUMO levels for several common OPV donor and acceptor materials are shown in Figure 2-5.

After dissociation the photogenerated charges are able to move to their respective electrodes (holes to the anode, electrons to the cathode) for collection and power generation in the external circuit. This process can be highly efficient in bilayer devices,

where the heterojunction interface separates free electrons and holes. Since bimolecular recombination is dependent on the product of the number of free electrons and holes np , this is not a large loss mechanism in a bilayer device away from the heterojunction interface. In a bulk heterojunction device, free electrons and holes have a significant spatial overlap while moving towards their respective collection electrodes. Thus, the np product is large, recombination is significant, and $\eta_{CC} \ll 1$ is typical.

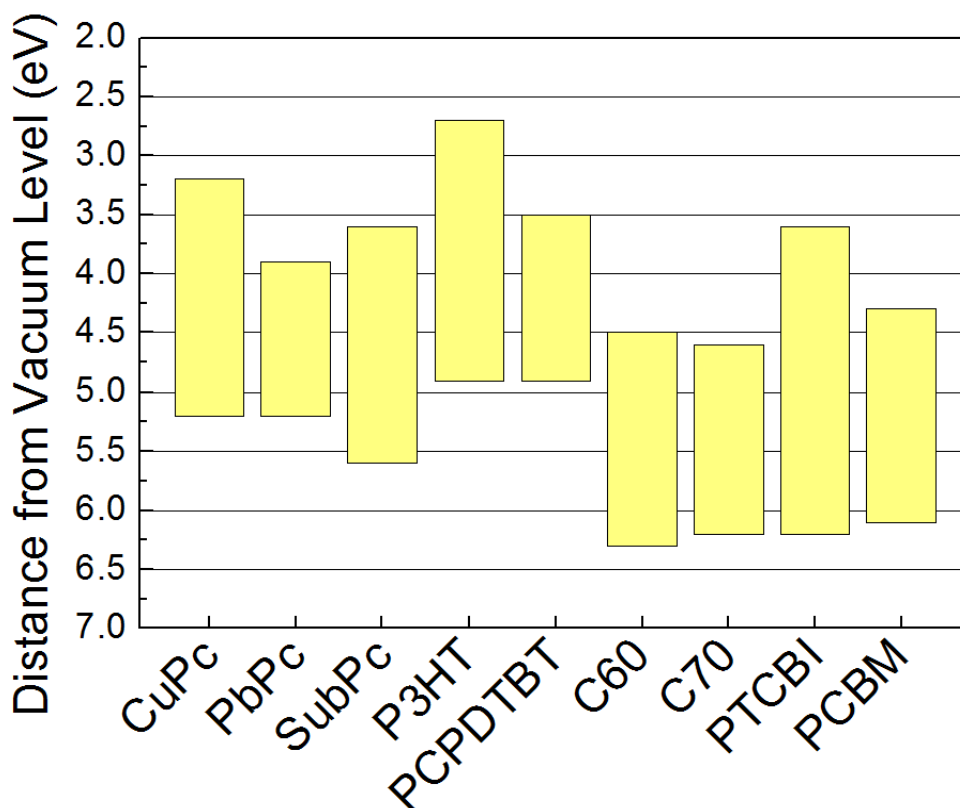


Figure 2-5. HOMO and LUMO energy levels for several common OPV materials. Donors: CuPc, PbPc, SubPc, P3HT, and PCPDTBT. Acceptors: C₆₀, C₇₀, PTCBI, and PCBM.

2.3.2 Fundamental Limitations

As discussed in the previous section, one of the greatest obstacles to efficient OPVs is the fundamental tradeoff between photon absorption and internal quantum

efficiency. In almost all relevant organic materials, the optical absorption length $1/\alpha$ (>100 nm) is greater than the effective exciton diffusion length (~ 10 nm) and charge collection length (< 100 nm). Thus, the optical absorption efficiency η_A is inherently opposed with either the exciton diffusion or charge collection efficiencies η_{CC} and η_{ED} , depending on the device architecture and active layer materials. In general, bilayer heterojunction devices are limited by η_{ED} due to their single plane of exciton dissociation; bulk heterojunction devices are limited by poor charge collection because of strong bimolecular recombination and poor charge transport morphologies related to segregation of the constituent donor and acceptor materials.

Because of these limitations, many avenues have been investigated to ameliorate the tradeoff between η_A and η_{IQE} . These are reviewed in the next section.

2.4 Progress in Organic Photovoltaic Device Performance

There have been two primary avenues to improve the performance of OPVs: developing and incorporating new active layer materials and designing and optimizing device architectures and morphologies. A third route, optical management, has been sparsely reported in the literature but has shown promise. While there are many processes in the operation of an OPV that can be improved, the predominant trend has been towards alleviating the fundamental tradeoff between η_A and η_{IQE} . The following sections are an overview of notable examples of improved device performance for small molecule and polymer OPVs. In Section 2.4.4, enhancements from improved optical management are highlighted.

2.4.1 Small Molecule Organic Photovoltaic Devices

The earliest successful OPV devices almost exclusively consisted of small molecules. Following Tang's 1% cell, it was realized that a primary limitation was the efficiency of exciton dissociation and charge generation. Several architectural changes were introduced to attempt to remedy this. First, the planar-mixed heterojunction, a sandwich of a mixed donor-acceptor layer between two neat donor and acceptor layers, was developed to attempt to balance exciton dissociation efficiency (in the mixed layer) with charge transport and collection efficiency (in the neat, planar layers).

While early efforts showed marked improvement in photocurrent generation and J_{SC} , there were large decreases in fill factor that were attributed to poor morphology within the mixed layer^{59,60}. The poor mixed layer morphology can be overcome by controlling the phase segregation of the coevaporated materials³⁴, typically by thermal annealing or deposition on hot substrates. Increased crystallinity and phase segregation result in large surface roughness and poor device performance due to pinhole leakage pathways^{61,62}, but annealing after deposition of the metal cathode constrains film reorganization during annealing, preventing pinholes and increased roughness while still allowing for internal phase segregation⁶³.

A cartoon of an ideal nano-phase segregated morphology is shown in Figure 2-6. In the unoptimized case, there is a large interface area for exciton dissociation, but poor conducting pathways lead to recombination and reduced charge collection efficiency. In the ideal phase segregated case, free carriers have easy transport routes to their collection electrodes, increasing η_{CC} . From these findings, the planar-mixed architecture has become a highly efficient choice for small molecule OPVs⁶⁴⁻⁶⁷.

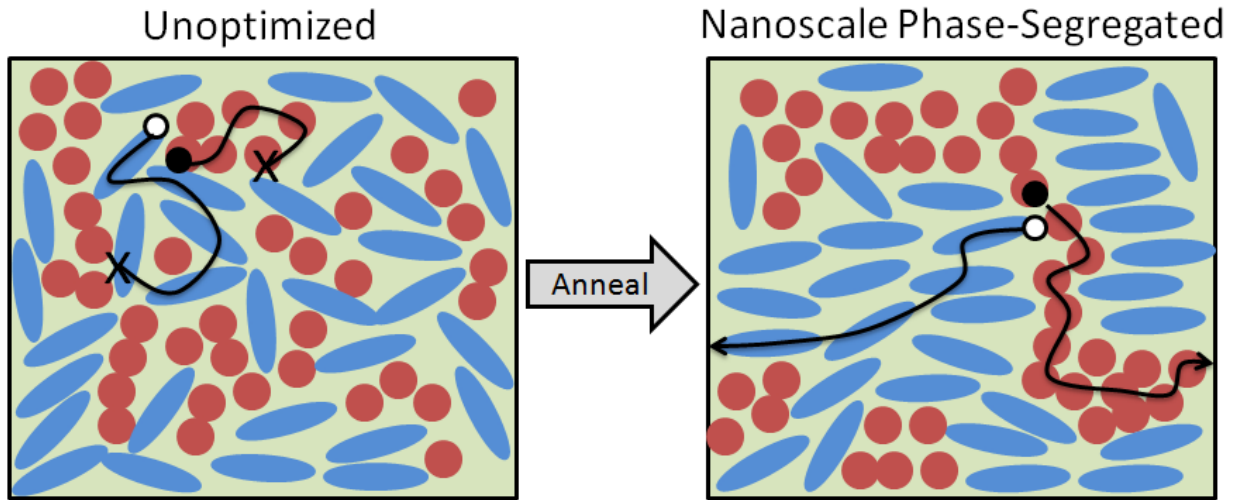


Figure 2-6. Representations of unoptimized and nanoscale phase-segregated bulk heterojunction OPV microstructures with two constituent materials. An example of charge carrier transport is shown for each.

A second ideal architecture for small molecule OPVs is the so-called interdigitated heterojunction architecture (Figure 2-7). Here, neat pillars of donor and acceptor form a regularly-spaced heterojunction with spacing on the order of the exciton diffusion length.

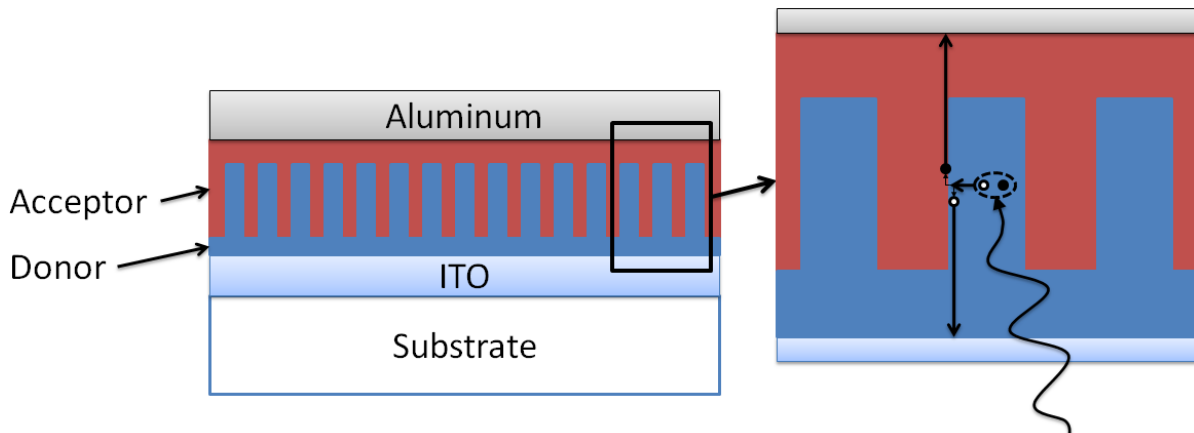


Figure 2-7. Ideal interdigitated heterojunction for organic photovoltaics.

Thus, very high exciton diffusion and charge collection efficiencies are possible. However, forming this structure on the nanoscale is quite challenging. The typical route taken is to form pillars of one material by either glancing-angle deposition⁶⁸⁻⁷¹ of small molecules or synthesis of inorganic nanorods⁷² and infilling with a solution-processed molecule or polymer to complete the heterojunction.

Another prominent architectural feature in small molecule OPVs is the addition of a thin electron transporting layer between the acceptor and cathode that prevents exciton quenching at the electrode/organic interface²⁹. 2,9-dimethyl-4,7-diphenyl-1,10-phenanthroline, i.e. bathocuproine (BCP), is used as the exciton blocking layer for the small molecule devices in this work.

The greatest increases in small molecule device performance have come from in incorporation of advanced active layer materials, to increase exciton diffusion length, open-circuit voltage, or incident photon absorption. Early advances were made by changing the acceptor from PTCBI, with a short exciton diffusion length of ~3 nm, to C₆₀, with a diffusion length on the order of 40 nm²⁹. Additionally, C₆₀ has strong absorption at short wavelengths, offering better coverage of the solar spectrum than PTCBI when paired with metal phthalocyanines. Even better spectral coverage and device performance is obtained with C₇₀, which has strong absorption through the blue and green wavelength regions⁷³. C₆₀ and C₇₀ are the current standard small molecule acceptor materials.

Most material advances have resulted in new electron donors. Compared to the archetypal CuPc used by Tang, various metal and metal-chloride phthalocyanines (Pcs) (tin Pc (SnPc), lead Pc (PbPc), chloroaluminum Pc (ClAlPc), and chloroindium Pc

(ClInPc)) with red-shifted absorption into the near infrared have been incorporated⁷⁴⁻⁸⁰. To extend absorption further into the infrared and improve charge transport properties, the metal Pc layer can be deposited on a thin, highly ordered templating material to encourage preferential molecular alignment⁸¹. This is especially beneficial for PbPc, to increase the ratio of triclinic phase to monoclinic phase^{79,82}. The predominate crystal phase is also of importance in ClInPc, which requires solvent annealing to increase near-infrared absorption⁸³.

Alternately, the donor layer can be chosen to maximize the open-circuit voltage by minimizing the reverse saturation dark current J_S ⁸⁴. The most prominent of these materials is boron subphthalocyanine chloride, SubPc. With a $V_{OC} > 1$ V and $\eta_P > 3\%$, SubPc has become a standard donor layer in high-efficiency bilayer OPVs⁸⁵⁻⁸⁸. Enhancement in V_{OC} has also been observed in zinc pthahlocyanine (ZnPc) synthesized such that the deposited films have reduced concentrations of electronic defect states, decreasing J_S ⁸⁹.

Currently, the highest efficiency small molecule OPV is a tandem cell (Section 2.4.3) produced by Heliatek GmbH using proprietary red, green, and blue absorbers for a power conversion efficiency of 8.3%^{5,48}.

2.4.2 Polymer-Based Organic Photovoltaic Devices

As was the case for small molecule OPVs, early π -conjugated polymer devices were single-layer Schottky diodes with universally terrible performance made from polythiophene⁹⁰, polyacetylene⁹¹, or polyvinylenes^{92,93}. The first appreciable performance was observed in bilayer devices made with a polymer donor of poly(2-methoxy-5-(2'-ethyl-hexyloxy)-1,4-phenylene vinylene) (MEH-PPV) and a thermally

evaporated C₆₀ acceptor^{94,95}. Eventually, a functionalized derivative of C₆₀, [6,6]-phenyl C₆₁-butyric acid methyl ester (PC₆₁BM or, more commonly, PCBM) was incorporated and has remained the standard acceptor, though some modern high efficiency devices use PC₇₁BM, a functionalized derivative of C₇₀⁹⁶. Virtually all other material work on polymer OPVs has focused on optimizing the donor.

The first class of donor polymers to show strong performance was the poly(1,4-phenylene-vinylene)s (PPVs), specifically (MEH-PPV)⁹⁷ and poly(2-methoxy-5-(3,7-dimethyloctyloxy)-1,4-phenylene-vinylene) (MDMO-PPV)^{98,99}. These early devices had high quantum efficiency under low intensity light that rolled off drastically as the illumination intensity increased, evidence of strong bimolecular recombination and poor film morphology. Sariciftici demonstrated the importance of morphological control and interface modification in polymer OPVs. Films cast from solutions of either chlorobenzene or toluene were compared and a strong correlation between reduced aggregation and improved device performance was observed⁹⁸. Further, modifying the cathode interface with LiF induces a strong interface dipole and increases charge extraction. This, combined with a hole extraction and film planarization layer of poly(3,4-ethylenedioxythiophene):poly(styrenesulfonate) (PEDOT:PSS) resulted in a device efficiency of 3.3%, comparable to the best small molecule devices of the day¹⁰⁰.

The most widespread donor polymer to date has been poly(3-hexylthiophene) (P3HT), replacing the PPVs as the archetypal choice. The absorption spectrum of P3HT is slightly red-shifted compared to MEH-PPV or MDMO-PPV, allowing it to absorb a greater portion of the solar spectrum and generate a larger photocurrent. Extensive studies on the morphology of P3HT:PCBM films to generate an ideal nanoscale phase-

segregated structure has increased their efficiency to 5-6%¹⁰¹⁻¹⁰⁴. This underscores the value of morphological control in OPVs. Additionally, it is now understood that the structural regularity and molecular weight of the donor polymer are important¹⁰⁵⁻¹⁰⁷.

Improved donor materials have followed two routes, both relying heavily on synthesis. The first is to develop low bandgap materials with absorption edges shifting to the near-infrared. Attempts to increase the conjugation length of P3HT¹⁰⁸ or change the thiophene subgroup to the more electronegative selenophene^{109,110} were successful in reducing the band gap, but ultimately did not improve performance over that of P3HT.

A more successful approach is to design new polymers with electron-rich and electron-poor (i.e. donor-acceptor) constituents¹¹¹⁻¹¹³. From the wide variety of synthesized polymers, a few will be highlighted here. The first, poly[2,6-(4,4-bis-[2-ethylhexyl]-4H-cyclopenta[2,1-b;3,4-b]-dithiophene)-alt-4,7-(2,1,3-benzothiadiazole)] (PCPDTBT), has a greatly red shifted absorption spectrum (with peak absorption observed under 825 nm illumination) and has found widespread adoption in the research community^{114,115}.

A larger band gap polymer, poly[*N*-9''-hepta-decanyl-2,7-carbazole-alt-5,5-(4',7'-di-2-thienyl-2',1',3'-benzothiadiazole)] (PCDTBT) has a higher V_{OC} than P3HT-based cells due to a lower HOMO level, resulting in less energy loss upon charge separation¹¹⁶. Heeger has reported a 6% efficient device using PC₇₁BM that has almost 100% internal quantum efficiency under monochromatic green illumination¹¹⁷.

The final materials to be discussed are fluorinated donor-acceptor polymers, one of which, poly(benzo[1,2-b:4,5-b']dithiophene)-(5,6-difluoro-4,7-dithien-2-yl-2,1,3-benzothiadiazole) (PBnDt-DTffBT), was used in Chapter 6. By incorporating the

strongly electronegative fluorine atoms into a common 2,1,3-benzothiadiazole acceptor subgroup, the HOMO level is reduced and interchain interaction is increased due to a more rigid aromatic structure¹¹⁸. Devices made in conjunction with PBCM are greater than 7% efficient, among the few reports to reach this value^{119,120}.

As of writing, the highest efficiency polymer OPV is a proprietary donor-acceptor blend reported by Konarka, Inc. with an efficiency of 8.3%⁴⁸.

2.4.3 Tandem Organic Photovoltaic Devices

Given the inherent tradeoff between η_A and η_{IQE} in most organic systems, one possible mediation route is to stack multiple devices with high η_{IQE} in series. This arrangement is referred to as a “tandem” device and is responsible for the highest efficiency inorganic photovoltaics^{48,121} by allowing greater coverage of the solar spectrum with different materials in the constituent subcells. This same concept can also be applied to organic materials, incorporating, for example, blue and green absorbers in the cell proximate to the cathode (“back cell”) and red and blue absorbers in the cell proximate to the anode (“front cell”). Even without the additional spectral coverage, simple tandem cells can increase performance by doubling the output voltage of the structure. For photovoltaic cells in tandem, the current can be taken as the lowest of the subcell currents and the voltage as the sum of the subcell voltages, i.e. a two-cell tandem would have $J = \min(J_1, J_2)$ and $V = V_1 + V_2$, where 1 and 2 denote the individual subcells.

A tandem organic photovoltaic has a notable architectural requirement that single junction cells lack – the carrier recombination zone (CRZ) that connects the subcells. In the CRZ, photogenerated electrons and holes from the front and back cells,

respectively, and recombine. Most of the development in tandem OPVs has focused on this region. The first tandem devices utilized a 15 nm-thick semitransparent layer of gold, which has high conductivity but blocks a large proportion of incident light¹²².

Yakimov and Forrest presented a better CRZ made from high conductivity small molecule layers embedded with a vacuum deposited 0.5 nm-thick (nominal) layer of silver nanoparticles¹²³. At these dimensions the nanoparticles do not absorb a significant amount of light and can even enhance the optical field at certain wavelengths due to plasmonic effects¹²⁴. This interlayer was used in ~2.5% efficient CuPc/PTCBI-based devices and a 5.7% efficient tandem based on planar-mixed CuPc/C₆₀ devices, both records for those materials^{66,123}.

Tandem devices based on polymer subcells are much more difficult to fabricate than those built from small molecules. Specifically, the front cell must be either not be soluble in or completely protected from (via the CRZ) the solvent used in processing the back cell. Therefore, polymer cells can either be used as the front cell with a vacuum-deposited small molecule back cell^{125,126}, or the CRZ can be engineered to isolate the front cell using nanoparticle or solvent-resistant organic layers¹²⁷⁻¹³⁰.

Regardless of the material choices, the architecture of a tandem OPV is highly complex compared to a single junction cell. Figure 2-8 shows a typical architecture for a two-cell tandem OPV and the optical field optimized for CuPc/C₆₀ planar-mixed subcells⁶⁶. Optimizing both the charge transport properties and optical fields in the front and back cells is a non-trivial task. Typically, the back cell is situated in the first blue-green interference peaks and the CRZ thickness is such that the front cell is in the in the

first green-red interference peak, or into the second blue region, depending on the absorption spectra of the organic layers.

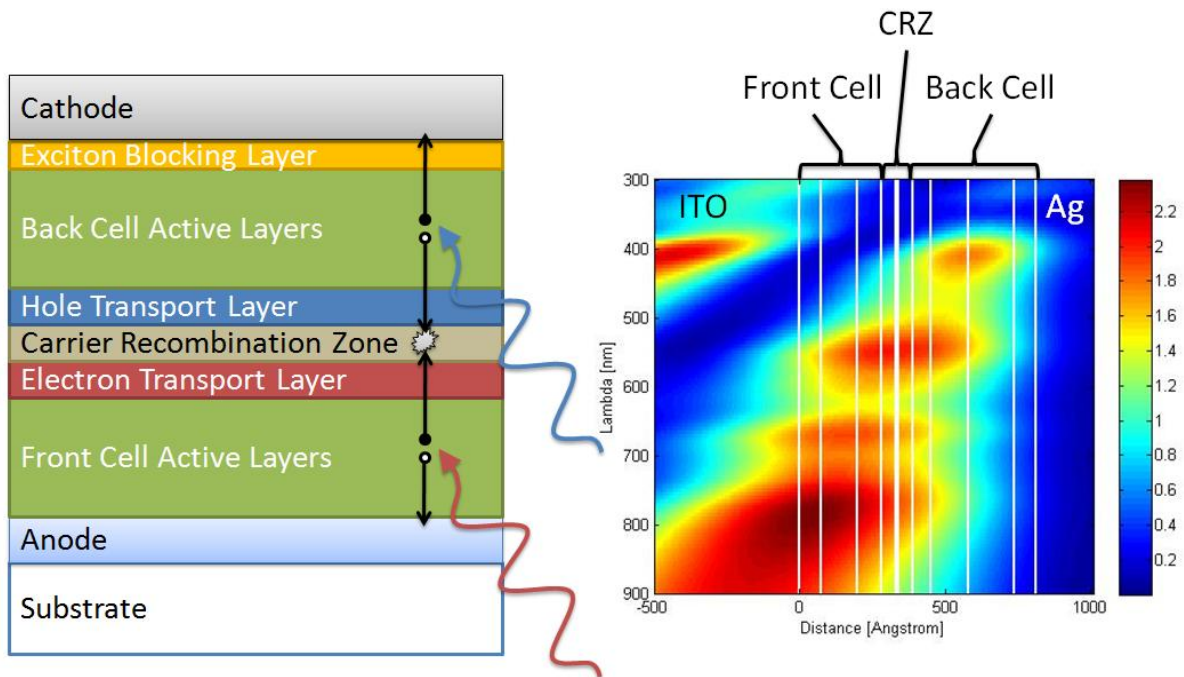


Figure 2-8. Typical device structure and optical field plot for a tandem organic photovoltaic device. The optical field is calculated for front and back cells of planar-mixed CuPc/C₆₀ heterojunction, with optimized thicknesses⁶⁶.

2.4.4 Optical Management

The previous sections discussed changes in active layer materials and device architectures to increase efficiency. History has certainly borne out that these are valid improvement routes, but a third approach, optical management, has been relatively ignored. Instead of altering the internal components of a device, changes can be made to alter how the entire device (substrate and active layers) interacts with incoming light. This is accomplished by altering the substrate geometry. Non-geometric enhancements, including luminescent concentrating layers¹³¹ and plasmon-enhanced

absorption^{124,132-134}, can also be considered optical management but will not be discussed further.

Figure 2-9 shows three examples of changes to substrate geometry to increase absorption by forcing light to pass through the active layer multiple times.

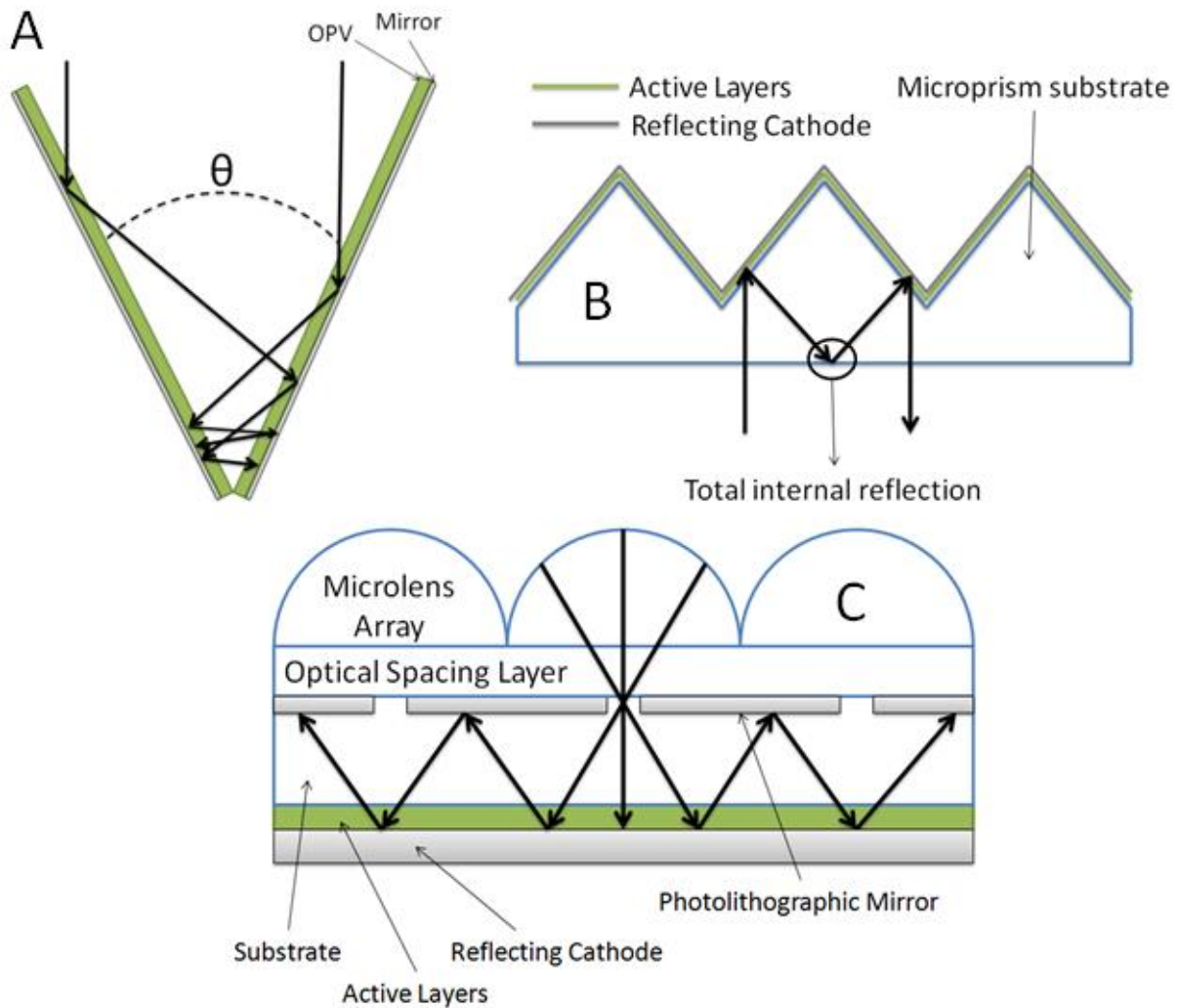


Figure 2-9. Three previous examples of optical enhancement techniques. A) V-aligned solar cells for enhanced light trapping¹³⁵⁻¹³⁷. B) OPVs produced on microprism substrates, to induce total internal reflection¹³⁸. C) A mirror-and-microlens light trap: a metalized layer is deposited with gaps at the microlens focal point to admit light^{139,140}.

Figure 2-9A shows two substrates in a V-pattern to form a light trap¹³⁵⁻¹³⁷. Light that enters is funneled deeper into the trap, passing through the active layers multiple times. Further, this trap will cause multiple reflections at almost all incident angles, though a large portion of the total active area will be shaded as the illumination angle changes. Figure 2-9B details a device fabricated on a prism-shaped substrate such that light reflecting off of the cathode will undergo total internal reflection at the substrate/air interface, returning for two more potential passes through the active layer¹³⁸. The prismatic features in this case are on the order of 100 μm ; other textured substrates have been used with much smaller features intended to serve as diffraction gratings^{141,142}. Finally, Figure 2-9C shows a complex structure consisting of a microlens array that focuses incoming light through gaps in a photolithographically patterned metal layer that forms a reflecting cavity with the cathode; subsequent reflections have a very small probability of escaping, in theory greatly increasing absorption^{139,140}.

These examples are ultimately ill-suited for use in commercial OPVs, where low processing cost, large device areas, and high throughput are required. A geometric substrate modification that meets these criteria, soft lithographically stamped microlens arrays, is presented in Chapter 6.

CHAPTER 3 ORGANIC OPTOELECTRONIC DEVICE CHARACTERIZATION

3.1 Chapter Overview

The proper measurement of optoelectronic device performance is key to ensure valid results that are directly comparable to those within the scientific community at large¹⁴³. This includes correct design and installation of characterization systems and equipment, control of systematic measurement errors, and redundant calibrations. As this work is largely focused on OPVs, the lion's share of this chapter is devoted to the specifics of their characterization. The background and calibration of a simulated solar light source are discussed in Section 3.2.1, along with the most prevalent OPV characterization technique, current-voltage (J-V) measurement. Section 3.2.2 covers another common characterization method, quantum efficiency, both external (EQE) and internal (IQE). Finally, Section 3.2.3 introduces synchronous photocurrent detection, a novel technique used extensively in Chapter 5.

The bifunctional photovoltaic and light emitting devices investigated in Chapter 7 require characterization of their emission efficiencies; therefore, the principles of OLED characterization are briefly presented in Section 3.3.

3.2. Organic Photovoltaics

3.2.1 Calibration, Spectral Mismatch, and Current-Voltage Measurement

A supreme concern in proper OPV characterization is the quality of the simulated solar light source in comparison to the reference solar spectrum. The typical reference solar spectrum is currently defined by the ASTM International G173-03 standard¹⁴⁴,

which specifies the optical power ($\text{Wm}^{-2}\text{nm}^{-1}$) at regular intervals from the ultraviolet (280 nm) to infrared (4000 nm) wavelengths at precise irradiance angles over the contiguous United States (37° tilt relative to the equator). The actual spectra are calculated¹⁴⁵⁻¹⁴⁷ using several assumptions, the most significant of which is the absolute air mass of 1.5, for a solar zenith angle of $48^\circ 19'$. There are three reference spectra included in the G173-3 standard: extraterrestrial, global, and direct (Figure 3-1A).

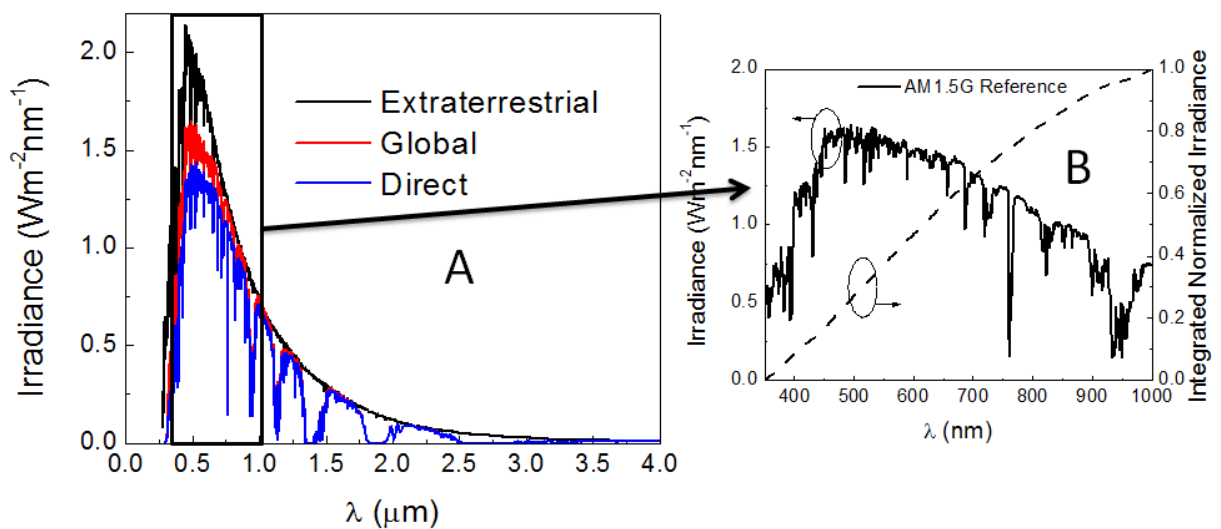


Figure 3-1. Reference solar spectra. A) Reference Air Mass 1.5 spectra from the ASTM G173-3 standard. B) AM1.5 Global spectrum with the normalized integrated optical intensity within visible wavelengths.

The extraterrestrial spectrum does not include absorption by the atmosphere and other effects and is not used for this work. The direct spectrum includes only the light that is directly incident on the 37° surface, while the global spectrum additionally includes light diffused by the atmosphere; the latter is used for the calibrations presented here. The unit “sun” is used to define the light intensity of the solar source. Since the total integrated power in the global spectrum is $\sim 100 \text{ mW/cm}^2$, one sun is

defined as this value. Figure 3-1B shows the AM1.5G (global) spectrum within the visible region, from 350 to 1000 nm, and integrated irradiance values across this wavelength range.

The devices characterized in this work were measured under illumination from a 150W Xe-arc bulb with a parabolic rear reflector to increase irradiance. The Xe-arc bulb has strong UV emission, so an AM1.5G filter is used to remove some of this light from the spectrum. The incident power intensity was measured using a certified Si reference cell with an active area of 0.9 cm².

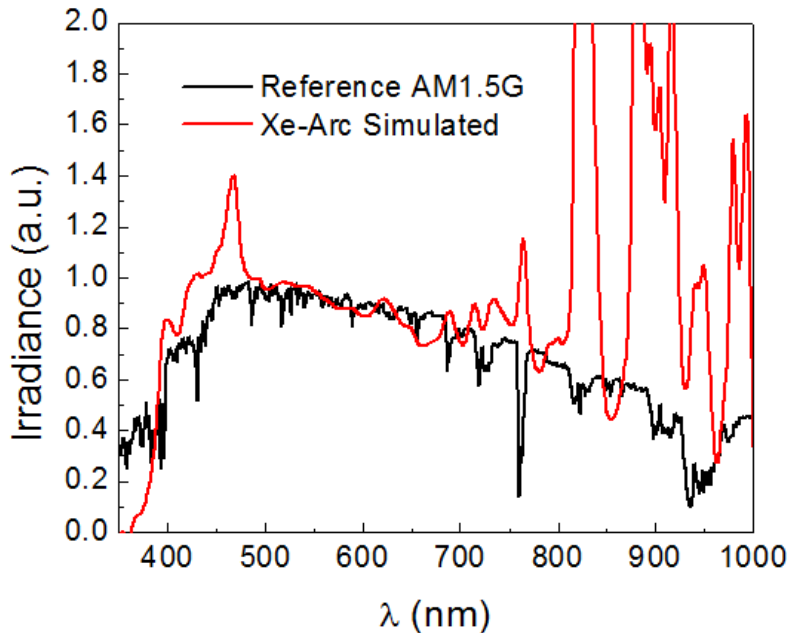


Figure 3-2. Reference AM1.5 Global and simulated Xe-arc lamp spectra. Data is normalized to 495 nm for comparison.

Because the simulated solar light spectrum, even with the AM1.5G filter, does not exactly match the reference spectrum (Figure 3-2) and organic materials have different absorption spectra compared to the Si detector, a spectral mismatch factor M is used to adjust the measured intensity, according to

$$M = \frac{\int_{\lambda_1}^{\lambda_2} E_R(\lambda) S_R(\lambda) d\lambda \int_{\lambda_1}^{\lambda_2} E_S(\lambda) S_T(\lambda) d\lambda}{\int_{\lambda_1}^{\lambda_2} E_R(\lambda) S_T(\lambda) d\lambda \int_{\lambda_1}^{\lambda_2} E_S(\lambda) S_R(\lambda) d\lambda},$$

where E_R is the reference spectral intensity, E_S is the simulated source intensity, S_R is the responsivity of the Si reference cell, and S_T is the responsivity of the OPV under consideration. Each function should be integrated over the spectral response range of the test cell. Note that a KG1 standardized colored glass filter has been added to the Si reference cell to reduce its long-wavelength absorption, giving it better spectral responsivity agreement with organic materials.

Despite the difference in spectral irradiance between the solar simulator and reference spectrum, most OPVs have a mismatch close to unity in this system. The final, corrected optical intensity value is taken as

$$I_{test,std} = \frac{I_{ref,std} I_{test,source}}{I_{ref,source} M}$$

where “std” and “source” are the AM1.5G standard reference spectrum and Xe-arc source spectrum, respectively, and “ref” and “source” are correspondingly the Si reference cell and the test OPV device. The spectral mismatch factor M for several different organic material systems in this characterization setup is shown in Table 3-1.

Table 3-1. Spectral mismatch factor M for various devices

	P3HT:PCBM	CuPc/C ₆₀	ZnPc/C ₆₀	SubPc/C ₆₀	PBnDt-DTffBT:PCBM
M	0.98	0.99	1.01	0.98	0.98

The typical arrangement of the solar simulator and associated optical components for a J-V measurement are shown in Figure 3-3. Neutral density filters are used to adjust the incident power P_0 from 0.1 sun to greater than 1 sun. The testing pocket is placed at a position calibrated to be 1 sun intensity under a certain filter combination using the Si reference cell with an assumed mismatch factor of unity. The intensity at this position can be adjusted slightly to account for variability in the spectral mismatch factors and lamp age by varying the lamp driving power (to 150 ± 5 W).

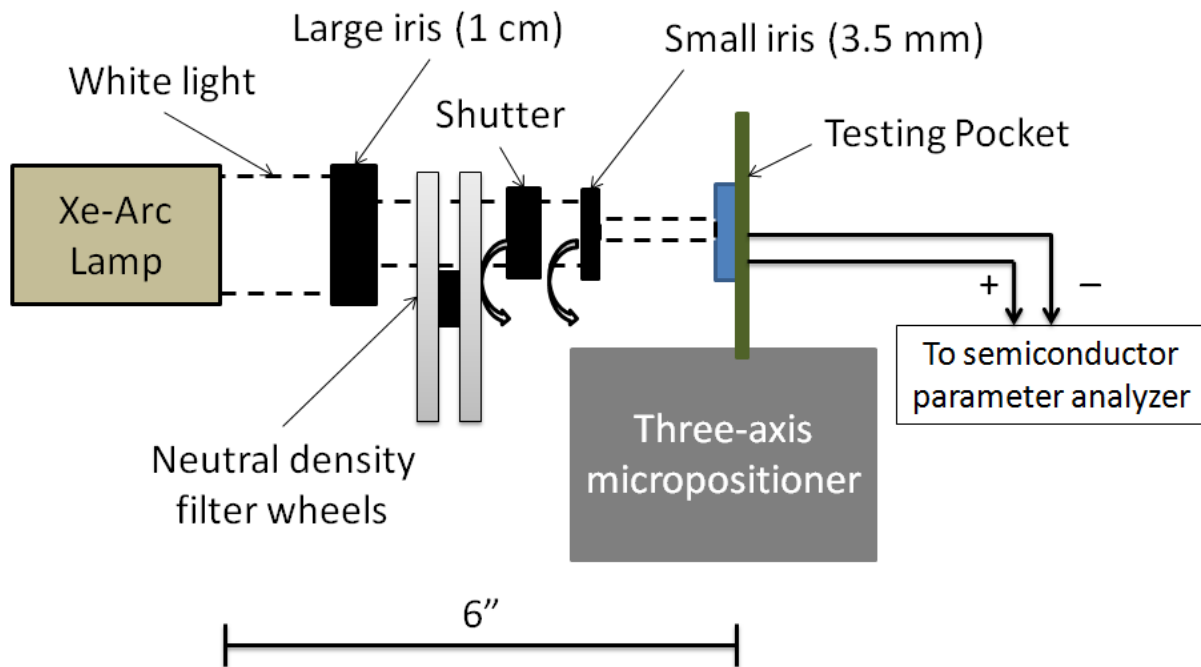


Figure 3-3. Arrangement of the solar simulator and associated optical components.

In this arrangement, multiple irises are used to isolate a specific area of the larger generated beam to increase beam uniformity. Small area devices are measured with the final, small iris in place; this iris can be flipped out of the optical path to illuminate larger areas. Unfortunately, the Xe-arc bulb and parabolic reflector combination still

results in significant variations across the final ~4 mm diameter spot. Figure 3-4 details the variability in power intensity across the final spot, represented as the short-circuit current generated from the Si reference cell through a pinhole opening.

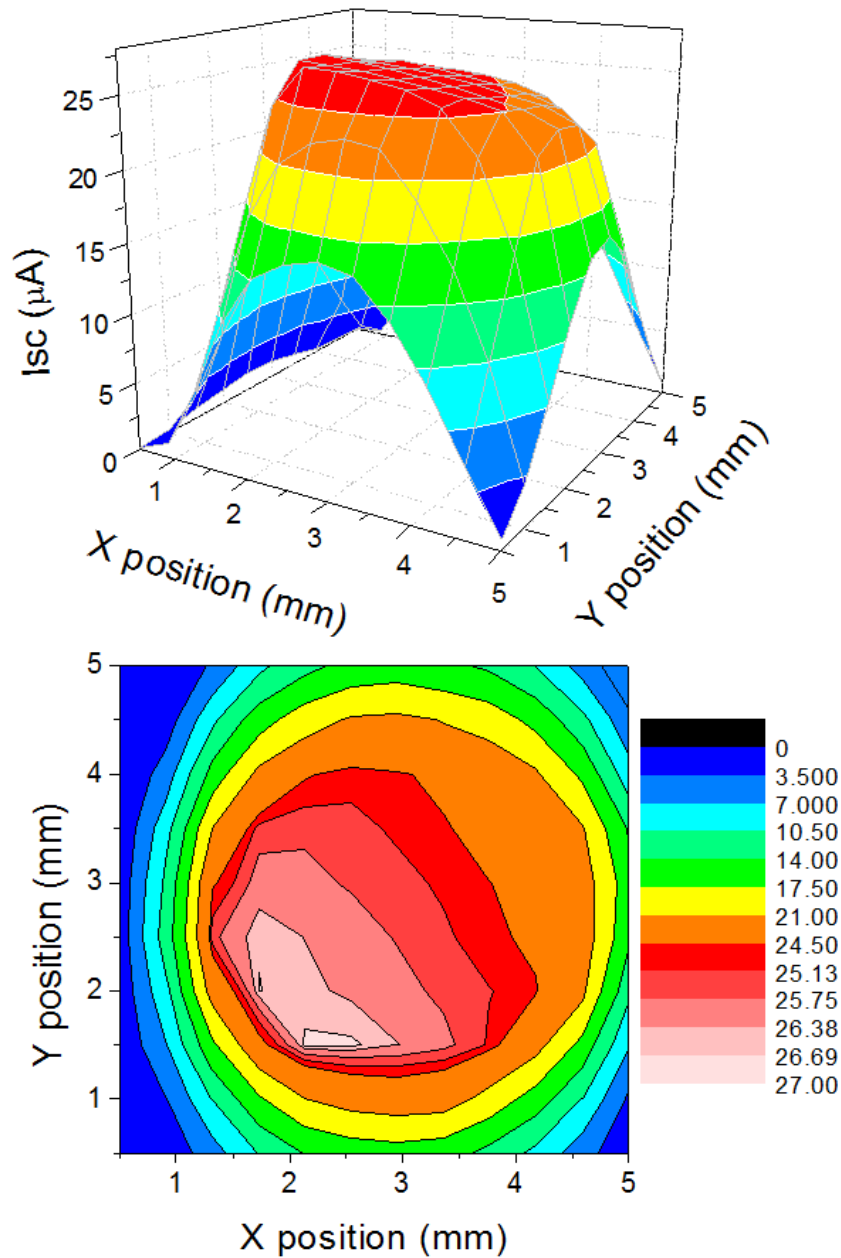


Figure 3-4. Optical intensity distribution over a calibrated 100 mW/cm^2 white light beam, measured as a function of current from a Si reference cell using a pinhole aperture.

There is an obvious region of high intensity near (2 mm, 2 mm), with intensity decreasing drastically toward the spot edge. While the total intensity over the spot size in this instance is $\sim 100 \text{ mW/cm}^2$, extra care must be taken to account for this when measuring devices with an active area different from the standard 0.04 cm^2 .

The current-voltage characteristics are measured using an Agilent 4155C semiconductor parameter analyzer, which both biases the test OPV and measures the current output. For dark current measurements, a shutter is used to block the white light beam and the test pocket is covered with a blackout cloth to ensure a light-free environment. Typically, double scans are used to detect any hysteresis in device performance, which can be indicative of charge trapping or other electronic defects within the device active layer. For illuminated scans, the relevant photovoltaic performance parameters (short-circuit current (J_{SC}), open-circuit voltage (V_{OC}), and the maximum power point (P_{max})) are averaged from the two individual scans.

3.2.2 Quantum Efficiency

A second vital technique to assess and compare OPV performance is quantum efficiency measurement. The quantum efficiency is calculated in one of two ways: the external quantum efficiency (EQE), a representation of the number of electrons collected per number of photons incident on a device, and the internal quantum efficiency (IQE), the ratio of electrons collected per absorbed photon. EQE is also known as the internal photon-to-electron conversion efficiency, IPCE. The quantum efficiency measurement system is shown in Figure 3-5, conforming to the ASTM E1021 testing standard¹⁴⁸.

EQE is typically measured across the visible spectrum to show the full spectral response of an OPV. A quartz tungsten halogen (QTH) lamp feeds white light into a monochromator, where diffraction gratings are used to split the white light into a low intensity ($1-10 \mu\text{W}/\text{cm}^2$) monochromatic beam of the desired wavelength. From there, the diverging monochromatic beam is collimated and chopped by a mechanical blade to create an alternating signal. The beam is then collimated and chopped by a mechanical blade to create an alternating signal. The beam is then condensed by another lens onto either the test device or, for incident power measurement, a calibrated Si photodetector.

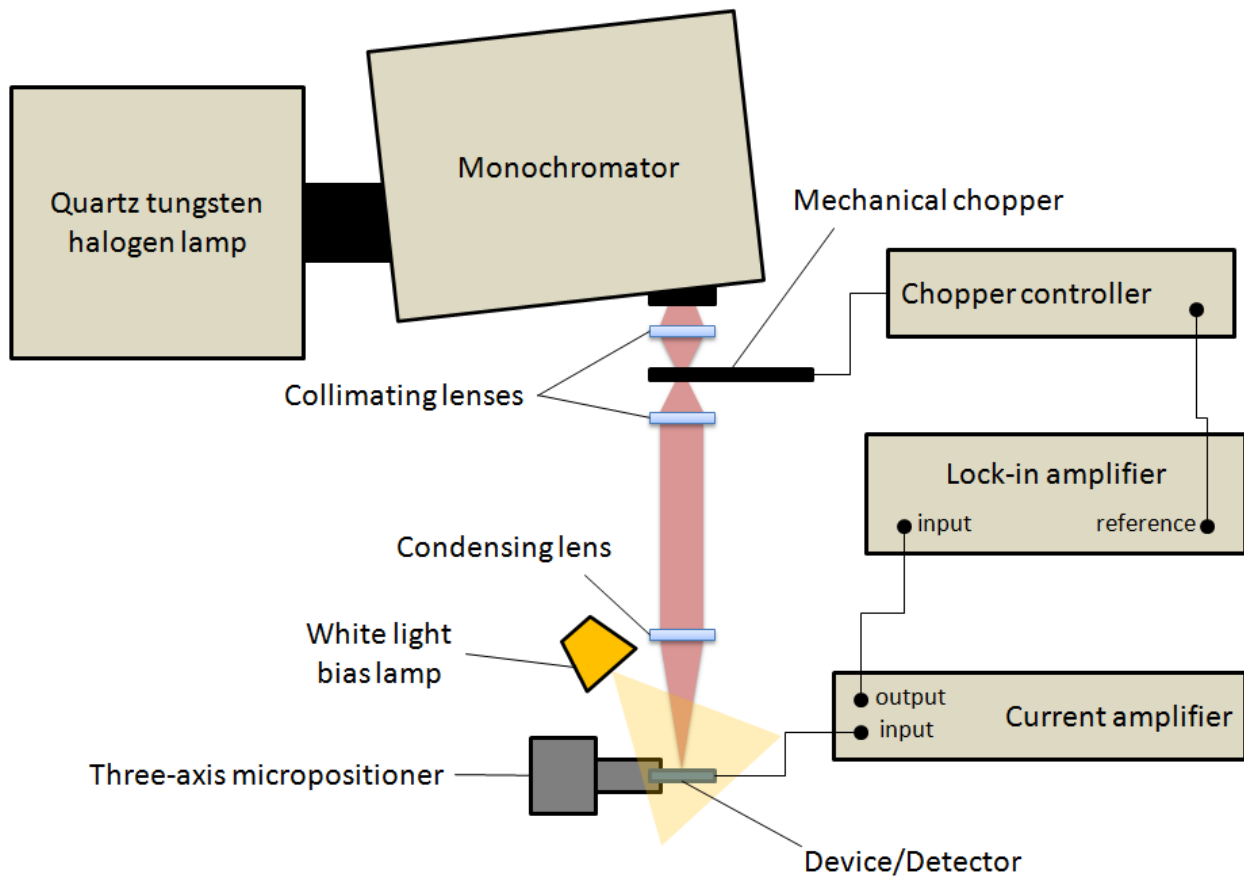


Figure 3-5. External quantum efficiency characterization system based on the ASTM E1021 standard.

The test device is also illuminated by non-chopped white light of typically 0.5-1 sun intensity to mimic the optical and electrical field within a device measured under one sun conditions in the J-V characterization system. The photocurrent is routed through a current amplifier to increase the signal/noise ratio, and then input into a lock-in amplifier. The lock-in amplifier uses the reference frequency from the chopper controller to isolate the current component that comes solely from the chopped monochromatic light. The EQE is then calculated as

$$EQE(\lambda) = \frac{hc}{q\lambda} \cdot \frac{I_T(\lambda)}{I_D(\lambda)/R_D(\lambda)} = IQE(\lambda) \cdot \eta_A(\lambda)$$

where c is the speed of light, h is Planck's constant, q is the elementary charge, $I_T(\lambda)$ is the lock-in-measured photocurrent from the test OPV, $I_D(\lambda)$ is the Si photodetector current, and $R_D(\lambda)$ is the responsivity of the reference detector. To calculate IQE, the absorption efficiency $\eta_A(\lambda)$ is taken into account. Ideally, the monochromatic beam should be slightly smaller than the device itself. If the beam is larger than the device area, the incident power $I_D(\lambda)/R_D(\lambda)$ must be adjusted to account only for the power incident on the device area (this adjustment is used in Chapter 6 to measure EQE under large area monochromatic illumination). The EQE spectrum for a rubrene/C₆₀ (35/25 nm) device is shown in Figure 3-6. The short-circuit current under reference 100 mW/cm² AM1.5G illumination can also be calculated from EQE data, via

$$J_{SC} = \int_{\lambda_1}^{\lambda_2} \frac{q\lambda}{hc} EQE(\lambda) S(\lambda) d\lambda$$

where $S(\lambda)$ is the reference AM1.5G power intensity. If both the EQE and J-V measurement systems are calibrated correctly, the difference between the integrated

and experimental J_{SC} values should be minor. For the example rubrene/ C_{60} device, the mismatch is approximately 3%, indicating acceptable agreement between the two systems and proper calibration.

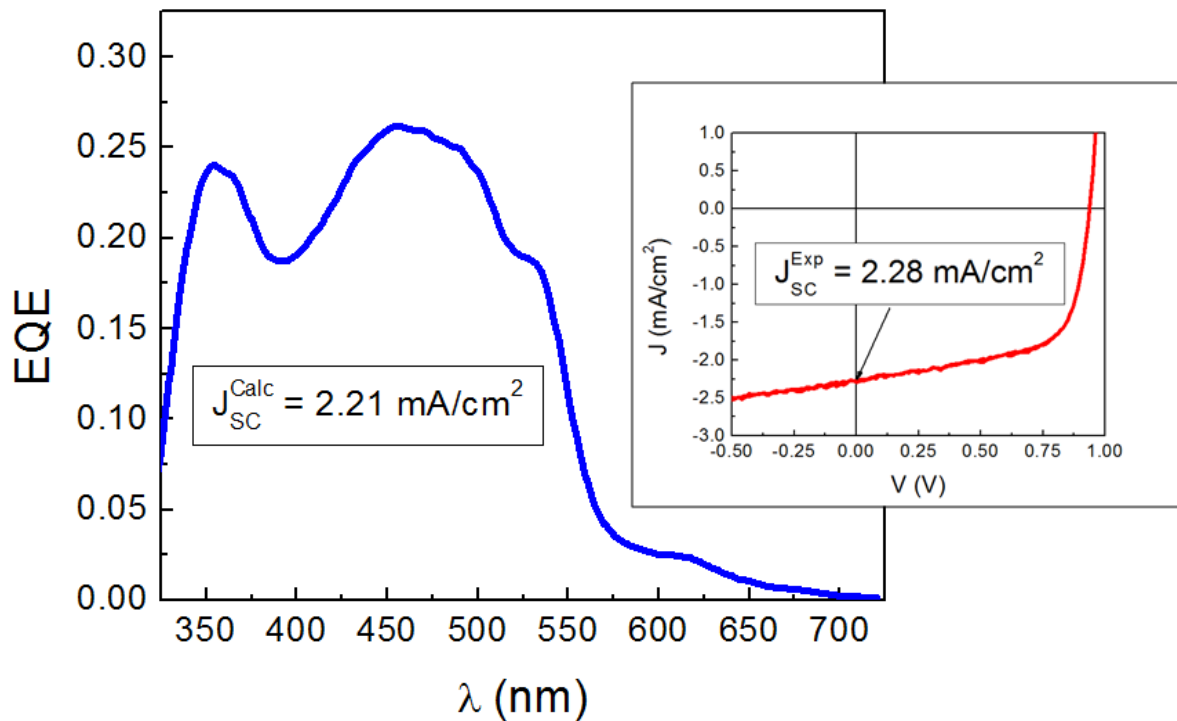


Figure 3-6. External quantum efficiency spectrum and current-voltage curve for a rubrene/ C_{60} (35/25 nm) device. The EQE-calculated and experimentally measured short-circuit currents are indicated.

3.2.3 Synchronous Photocurrent

Synchronous photocurrent detection is a novel technique developed and used extensively for this work. The basic characterization setup is the same as for an EQE measurement (Figure 3-5), with the light source either being monochromatic or simulated solar illumination. However, a bias is applied across the device by the current amplifier. The bias is swept from negative to positive (typically to +1 V) to reconstruct

the photocurrent component of the total current curve. The measurement can be performed under chopped simulated solar illumination to obtain a photocurrent curve of a directly comparable magnitude to the total and dark currents, as in Figure 3-7A for a 20 nm zinc phthalocyanine (ZnPc)/40 nm C₆₀ bilayer device. Note that this demonstrates how the photocurrent curve dominates total current from $V = -1$ V to $V \approx 0.25$ V. The dark current dominates the total current at larger forward biases, as expected.

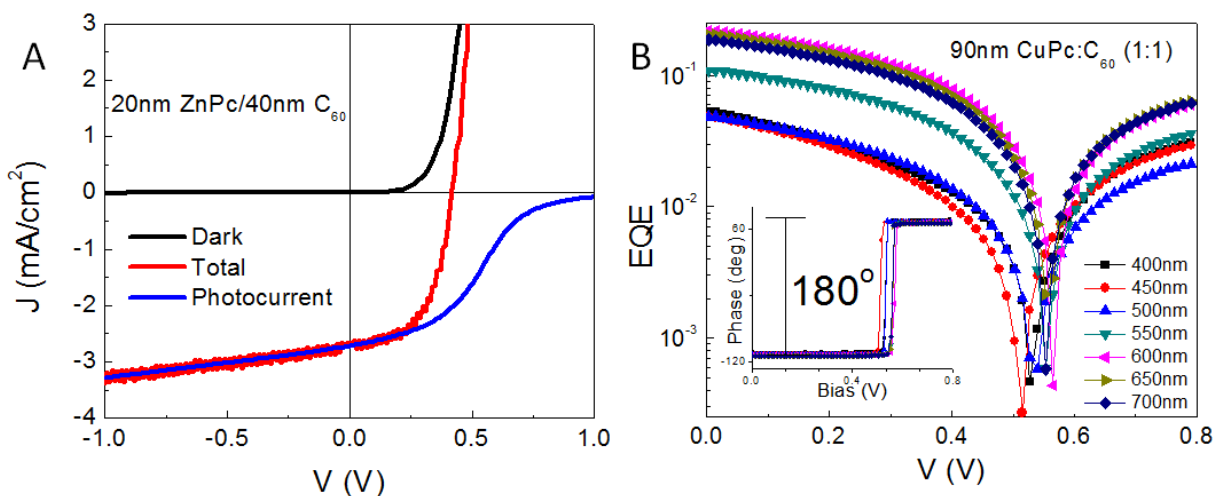


Figure 3-7. Example photocurrent data. A) Dark, total, and photocurrents of a 20 nm ZnPc/40 nm C₆₀ bilayer device under simulated solar illumination. B) Photocurrent measured under monochromatic illumination of various wavelengths for a 90 nm CuPc:C₆₀ (1:1 by weight) mixed heterojunction device. Inset: phase information recorded from the lock-in amplifier.

The more common usage is under monochromatic illumination, to study the photocurrent behavior as a function of wavelength (Figure 3-7B). In this configuration, a strong white light bias (ideally 100 mW/cm², but device instability at large voltages can necessitate lower intensities to reduce measurement error) is applied to create a representative electrical field across the active layers of the test OPV. Additionally, the

white light bias spectrum should be matched with the absorption spectrum of the device. For example, the spectra of three different bias lamps are shown in Figure 3-8, along with the absorption spectra of CuPc, C₆₀, and PbPc.

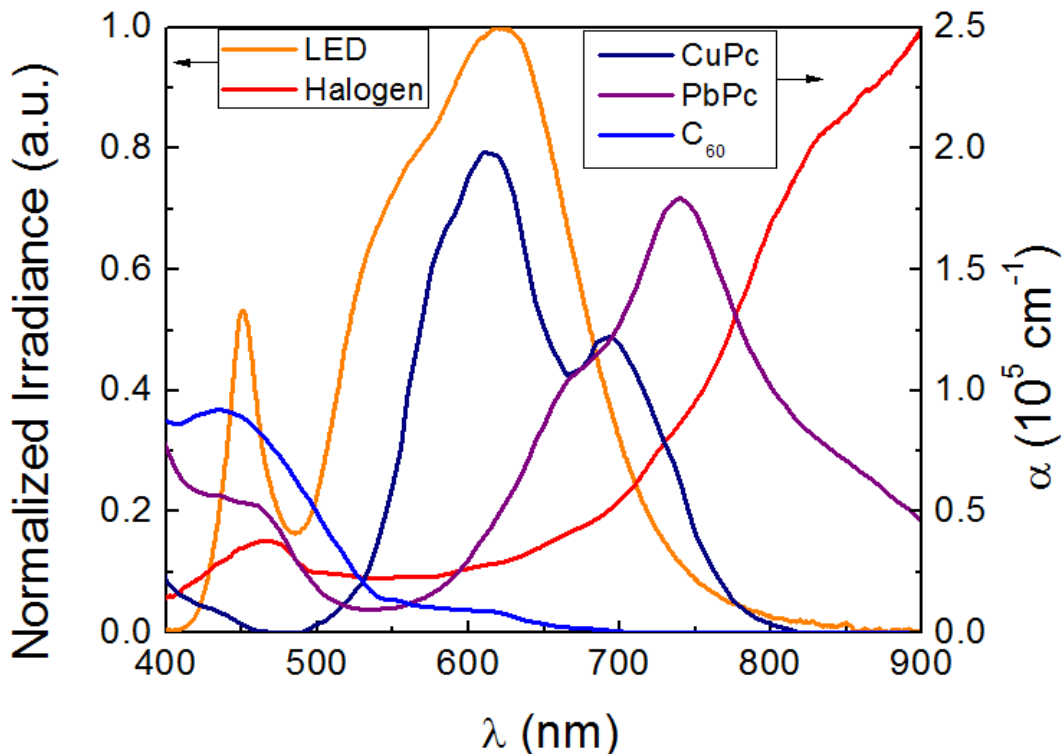


Figure 3-8. Irradiance spectra of two different white light bias lamps compared to the absorption spectra of three representative OPV materials within the visible region.

The LED lamp irradiance spectrum is closely matched to the absorption peaks of CuPc ($\lambda = 600\text{-}700\text{ nm}$) and C₆₀ ($\lambda = 450\text{ nm}$), making it a suitable choice for that material system. PbPc, however, absorbs at longer wavelengths ($\lambda > 700\text{ nm}$) and is not matched well with the LED lamp spectrum. The halogen lamp is a better choice for PbPc to better mimic the AM1.5G conditions. The halogen lamp also demonstrates spectral match with CuPc and C₆₀. Precaution must be taken to cool the OPV when

using a halogen bulb due to its large heat output; extra heat will degrade the device over the course of the measurement.

As the bias is increased across the test OPV during testing, the magnitude of the photocurrent can decrease by several orders of magnitude. This rapidly decreases the signal-to-noise ratio of the measurement. To compensate, a longer integration constant (300 ms or 1 s), greater noise filtering within the lock-in amplifier, and much longer hold times (~7 time constants) compared to an EQE measurement are used. Scan times can range from one to three hours depending on the number of wavelengths considered, necessitating device encapsulation to minimize degradation during this period. Measurement times can be reduced by varying the integration constant and hold time based on the magnitude of the photocurrent signal.

Refer to Chapter 5 to see synchronous photocurrent measurements applied to study photocarrier generation and transport behavior based on OPV heterojunction design and for other purposes.

3.3 Organic Light Emitting Diodes

Complete characterization of an OLED encompasses the measurement of current-voltage performance, luminance, and emission spectra. From these characteristics the luminous, power, and quantum efficiencies are determined.

The emission spectrum is measured using a spectrometer (Ocean Optics JAZ), which accepts light through a 400 μm optical fiber. The incoming light is split with a diffraction grating and reflected onto a charge-coupled device (CCD) array which is configured to correlate response from each pixel with a specific wavelength. In addition

to photon count measurements, the system is calibrated with a reference tungsten halogen light source for absolute power measurement.

Current-voltage and luminance characteristics are measured using the system depicted in Figure 3-9.

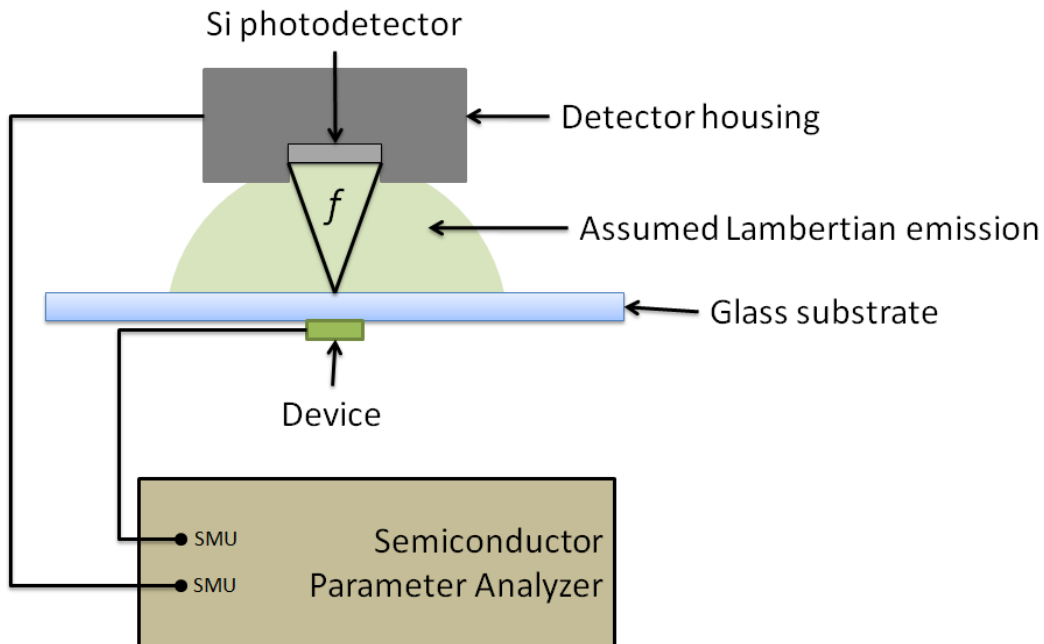


Figure 3-9. OLED current-voltage and luminance characterization system.

The most important assumption made in this characterization system is that the OLED emission pattern is Lambertian, or equal in intensity in the forward direction regardless of the solid angle¹⁴⁹. In reality, there are slight deviations from Lambertian emission, and any type of optical structure designed to increase light outcoupling will alter the emission pattern^{150,151}.

The system is initially calibrated using a commercial luminance meter to determine a conversion factor α between the actual luminance L and the measured

detector photocurrent I_{det} . The value of α is obtained by curve fitting of L vs. I_{det} over a representative luminance range. Additionally, α depends on the spectral response of the photodetector and a geometric factor f , the fraction of the total emitted light that the detector can observe. By assuming that the emission spectrum of the device is constant regardless of driving voltage, f is calculated as

$$f = \frac{\phi_0}{A\pi\alpha} \cdot \frac{\int g(\lambda)S(\lambda)d\lambda}{\int S(\lambda)R(\lambda)d\lambda}$$

where $g(\lambda)$ is the normalized photopic response (responsivity of the human eye in bright light) curve with a peak value $\phi_0 = 683 \text{ lm/W}^{152}$, $S(\lambda)$ is the device emission spectrum, $R(\lambda)$ is the detector responsivity, and A is the device area. Typically, the emission spectra of different devices are ignored in the calculation of f , making it dependent only on the geometry of the measurement system, such as detector area and distance from the device.

With the geometric factor, emission spectrum, I_{det} , and the device driving current I_D known, the luminous efficiency η_L , power efficiency η_P , and external quantum efficiency η_{EQE} can be readily calculated,

$$\eta_L = \frac{LA}{I_D} = \frac{AI_{det}\phi_0}{\pi f I_D} \cdot \frac{\int g(\lambda)S(\lambda)d\lambda}{\int S(\lambda)R(\lambda)d\lambda},$$

$$\eta_P = \frac{\pi}{V} \cdot \eta_L,$$

$$\eta_{EQE} = \frac{qI_{det}}{hc f I_D} \frac{\int \lambda S(\lambda)d\lambda}{\int S(\lambda)R(\lambda)d\lambda}$$

where h is Planck's constant, c is the speed of light, and q is the elementary charge. Ideally, the emission spectrum $S(\lambda)$ should be measured at a variety of voltages to account for any changes as the driving conditions change. Note also that the method of calculating f only accounts for forward emission, ignoring waveguided and back-reflected emission; an integrating sphere can be used to account for these components¹⁵².

CHAPTER 4 OPTICAL SIMULATION OF ORGANIC PHOTOVOLTAIC DEVICES

4.1 Monte Carlo-Based Ray Optics Modeling

The propagation of light can be represented in two ways: as a ray with an origin point and a direction or as a wave traveling with a certain frequency, wavelength, and direction. Because the wavelength of a visible light photon is less than 1 μm , optical simulations at larger dimensions than this can be suitably approximated by treating the light wave as a ray. At dimensions near or less than the wavelength of light, the governing equations of ray optics are not an accurate approximation and the wave nature of light must be taken into account. For the purposes of this work, Monte Carlo ray optics simulations were used to primarily examine the geometric effects of optical structures on light propagation behavior, not model the behavior of light within the active layer itself. In the realm of organic devices, ray optics have primarily been used for studying light extraction in light emitting diodes^{150,153}, but there have been applications in photovoltaics research^{154,155}.

At macroscopic scales, the equations that govern the behavior of light are well known. Transmission and reflection probabilities are calculated via the Fresnel equations, which are dependent on the polarization of the incident light ray (either parallel or perpendicular to the incident plane, respectively notated as *p*-polarization and *s*-polarization), the indices of refraction of the media under consideration, and the incident angle of the light ray relative to the interface surface normal. A simple diagram denoting the relationship between the incident angle θ_i , the reflected angle θ_r , and the

transmitted angle θ_t as light moves from one medium into a second (with a higher refractive index) , is shown in Fig. 4.1.

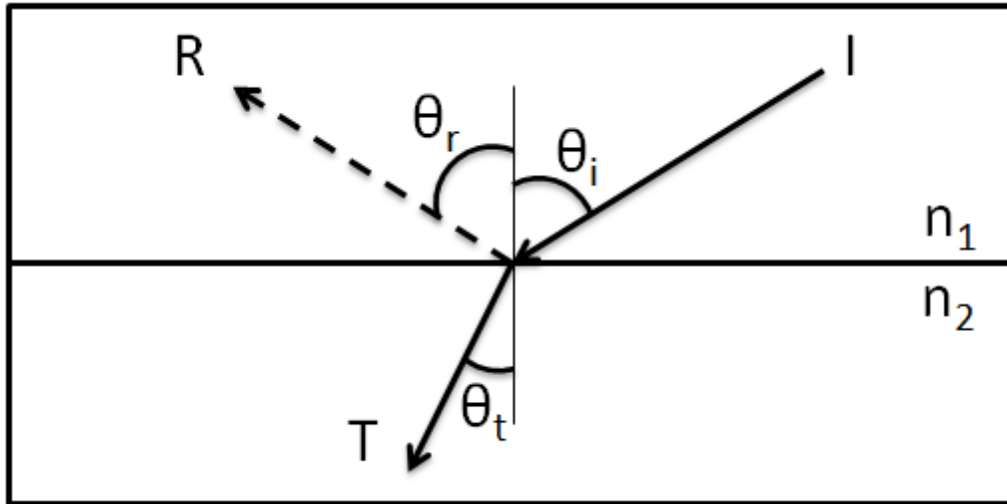


Figure 4-1. Schematic diagram of light propagation via ray optics. Note that $n_2 > n_1$ in this situation.

The relative proportions of R and T are calculated using the Fresnel equations,

$$R_s = \left[\frac{n_1 \cos \theta_i - n_2 \cos \theta_t}{n_1 \cos \theta_i + n_2 \cos \theta_t} \right]^2$$

$$R_p = \left[\frac{n_1 \cos \theta_t - n_2 \cos \theta_i}{n_1 \cos \theta_i + n_2 \cos \theta_t} \right]^2$$

Where n is the refractive index and the angles θ_i and θ_t are referenced to the surface normal as shown in Figure 4-1. The transmittance angle can be calculated using Snell's law,

$$\frac{\sin \theta_1}{\sin \theta_2} = \frac{n_2}{n_1}$$

This relationship can then be used to reduce the Fresnel equations to functions of n and θ_i ,

$$R_s = \left[\frac{n_1 \cos \theta_i - n_2 \sqrt{1 - \left(\frac{n_1}{n_2} \cos \theta_i\right)^2}}{n_1 \cos \theta_i + n_2 \sqrt{1 - \left(\frac{n_1}{n_2} \cos \theta_i\right)^2}} \right]^2$$

$$R_p = \left[\frac{n_1 \sqrt{1 - \left(\frac{n_1}{n_2} \cos \theta_i\right)^2} - n_2 \cos \theta_i}{n_1 \sqrt{1 - \left(\frac{n_1}{n_2} \cos \theta_i\right)^2} + n_2 \cos \theta_i} \right]^2$$

For nonpolarized light, the total reflection and transmission coefficients are then taken as:

$$R = \frac{R_s + R_p}{2} = 1 - T$$

With this, the proportions of an incoming light ray with intensity I that have been reflected (R) and transmitted (T) at the interface between two media with differing refractive indices can be readily calculated. The final component from Figure 4-1, θ_r , is simply θ_i – only the direction of the ray changes, not its angle relative to the interface normal. Practical implementation of these equations in a computer simulation can take two forms: first, a recursive algorithm that starts with a single ray with a set incident intensity, which is then split into two components at the first interface, reflected and transmitted, with the relative intensities of those two rays calculated using the above formulations. Those rays are then further split into reflected and transmitted components at the next interface they encounter, and so on.

The second approach relies on simulating a large number of rays to generate a statistically valid distribution of reflected and transmitted rays at each interface, where

the number of rays reflected is proportional to the Fresnel-calculated R value. For example, the calculated R value for normally-incident light on an air-glass interface (with refractive indices of 1 and 1.5, respectively) is approximately 0.04. The first method would take a single ray with intensity 1.00 and split it into a transmitted ray with an intensity of 0.96 and a reflected ray with intensity of 0.04. The second method would generate 100 rays, 4 of which would be reflected and 96 of which would be transmitted without any change in intensity. This is considered a Monte Carlo-type simulation method.

The latter approach has been implemented. The following discussion contains details of the specific implementations of the basic ray optics method, and how that technique has been adapted to work with microlens arrays, with the necessary refinements to give quantitatively significant results. The results of this simulator are used extensively in Chapter 6.

4.1.1 Basic Implementation Scheme

A basic ray optics simulator of planar layers must perform several functions:

1. Create a simulated stack of several layers and remember their locations in space (layer start/end coordinates) and refractive indices
2. Generate rays with a randomized origin and desired vector
3. Calculate the intersection point of the ray with the next layer based on the ray's position, vector, and the coordinates of the next layer interface
4. Perform Fresnel calculations to determine the reflection and transmission probabilities
5. Determine whether the ray will reflect or transmit at the interface
6. Calculate new vectors after either reflection or transmission

7. Repeat steps 2 through 6 until the ray will no longer interact with the simulated stack due to reflection away from the layers, transmission through all layers, or absorption within a layer
8. Accurately track the behavior of the ray, and whether it was absorbed, transmitted, or reflected
9. Repeat steps 2 through 8 for a large number of rays.

A flow chart describing this process is shown in Figure 4-2.

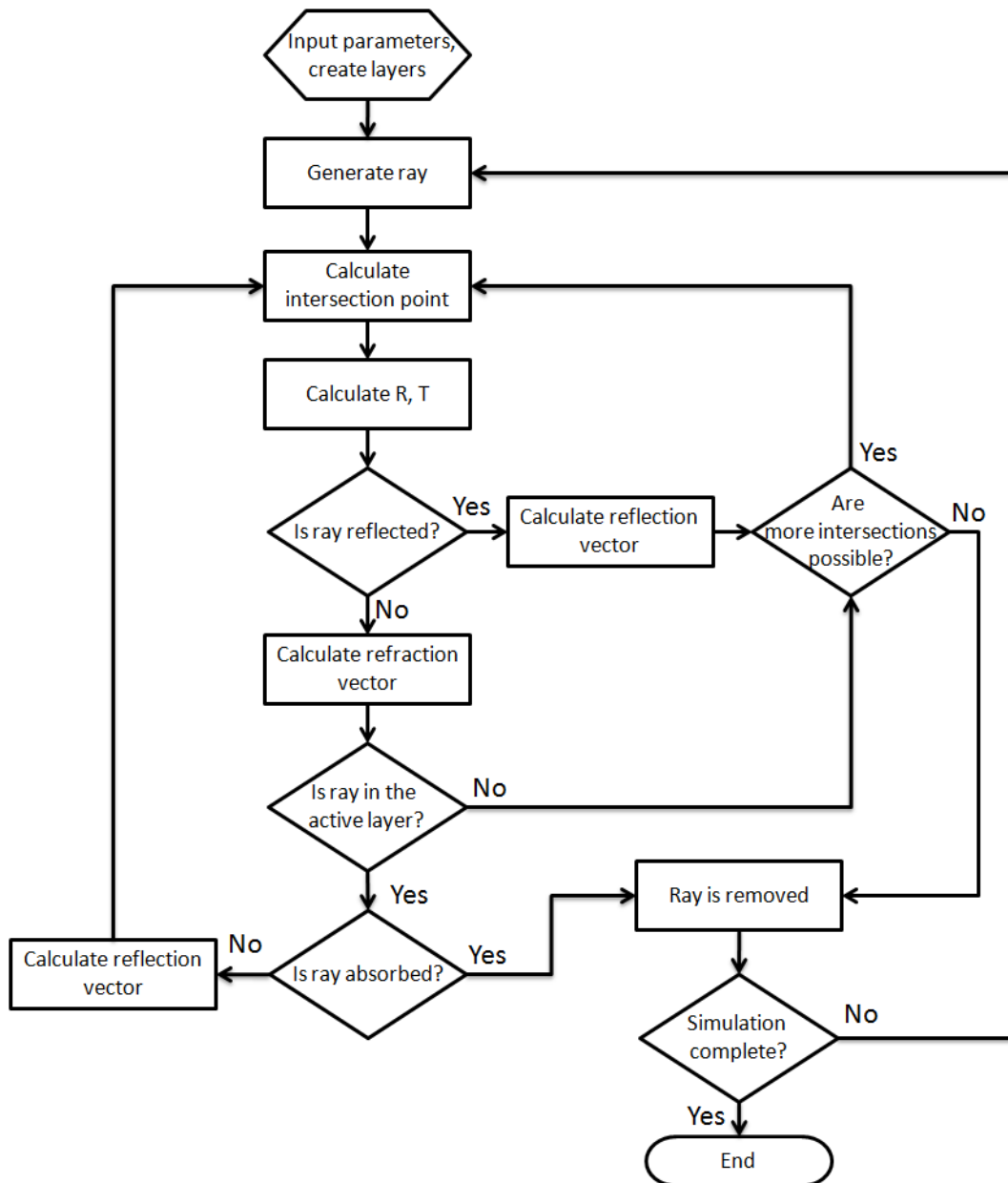


Figure 4-2. Simplified flow chart of a Monte Carlo ray optics simulator.

For a system composed of purely planar layers, the implementation and mathematics of the simulator are straightforward. A basic simulated stack of planar layers is shown in Figure 4-3, with the different device, substrate, and illumination areas indicated. The “device” is created by defining a region that functions as a mirror on the back side of the active layer; the rest of the active layer is taken as adjacent to air, so rays can be lost by transmitting through the entire stack.

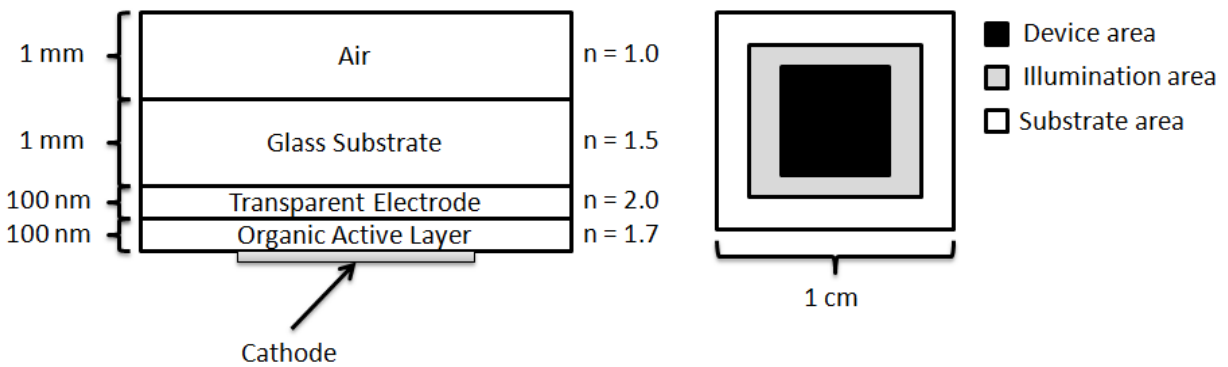


Figure 4-3. Typical simulated stack. Note that layer thicknesses are not to scale.

The intersection point between the ray and the next planar layer is a simple projection onto the layer. After the Fresnel reflection and transmission coefficients, R and T , are determined, a random number within the set $[0,1]$ is obtained; if the random number is less than or equal to R , the ray is reflected and a new vector is calculated according to:

$$\mathbf{d}_{\text{reflect}} = \mathbf{d} + 2(\mathbf{n} \cdot (-\mathbf{d}))\mathbf{n},$$

where \mathbf{d} is the direction vector of the ray, and \mathbf{n} is the surface normal. Otherwise, the ray is transmitted through the interface and the new refracted vector is:

$$\mathbf{d}_{\text{refract}} = \mathbf{d} \left(\frac{n_1}{n_2} \right) + \left[\left(\frac{n_1}{n_2} \right) (\mathbf{n} \cdot (-\mathbf{d})) - \sqrt{1 - \left(\frac{n_1}{n_2} \right)^2 (1 - (\mathbf{n} \cdot (-\mathbf{d}))^2)} \right],$$

where n_1 and n_2 are the refractive indices of the layers involved.

Eventually, the ray will transmit to the organic active layer, where it can be absorbed according to the Beer-Lambert law $A = 1 - e^{-\alpha d}$, where α is the wavelength-dependent absorption coefficient and d is the path length of light within the layer. Similarly to the determination mechanism for reflection and transmission, if a randomly generated number is less than or equal to A , the ray is absorbed. This calculation is performed whenever the ray is within the active layer. Should the ray not be absorbed on a first pass, there are subsequent opportunities for absorption on additional passes. If the ray is outside of the device area, Fresnel calculations are performed to determine if the ray is reflected or transmitted at the organic/air interface; within the device area, the ray is reflected off of the cathode back into the active layer, absorption calculations are repeated, and the simulation cycle continues.

Several parameters are tracked during the simulation for later analysis, among them the number of rays absorbed in the device area, absorbed outside of the device area, reflected upon initial interaction with the stack, reflected at any other point in the simulation, and transmitted through the stack. Additional tracked quantities include the ray pathlength through the active layer, initial generation point (inside or outside of the device area) and wavelength of each absorbed ray.

4.1.2 Simulation of Optical Structures

The basic simulator framework is suitable for a stack that contains non-planar layers, such as arrays of pyramids or hemispherical microlenses, but significant care must be taken to properly describe the interaction around the non-planar optical structure. This takes several forms:

1. Correct initialization of the simulated optical structure layer, with the flexibility to accommodate a variety of structures, such as microlens arrays with different contact angles, packing factors, and lens diameters.
2. Determination of whether the next intersection will be with a planar layer or the optical structure
3. Accurate calculation of ray intersection points with the optical structure
4. Error checking to ensure interaction with only one optical structure, in the case of an array of features

For the purposes of this section, the optical structure is a convex hemispherical microlens array unless otherwise noted. The typical simulated device structure is shown in Figure 4-4, with typical layer thicknesses and indices of refraction indicated.

Note that the layer thicknesses are not to scale.

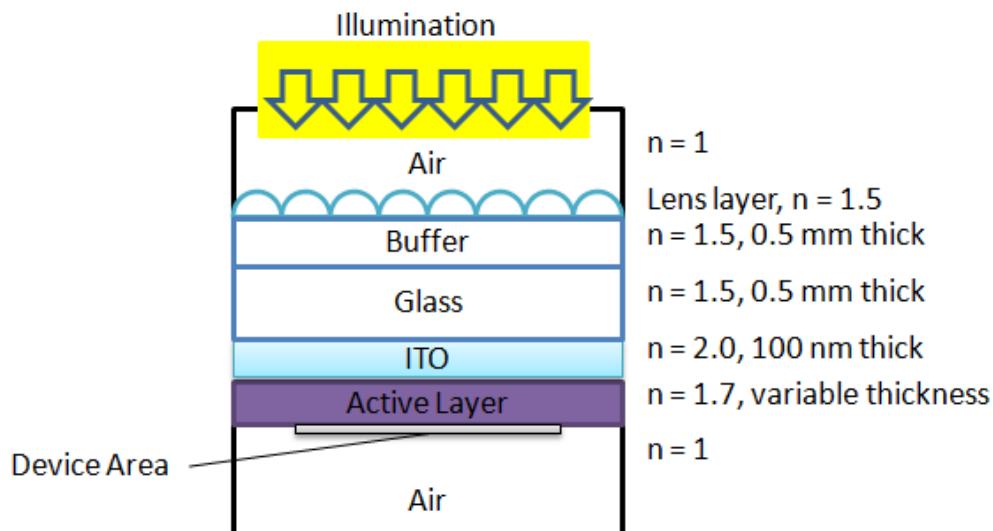


Figure 4-4. Typical simulated device structure with a convex microlens array.

Proper simulation of the lens geometry is crucial. For a convex hemispherical microlens array with a contact angle of 90° , a sphere is first created at a desired height within the structure – the midpoint of the sphere is placed at the interface between air and the buffer layer, leaving a perfect hemisphere above and below the interface. The sphere is then repeated in space to simulate the array. Two different packing factors are considered (Figure 4-5), a square array and a close-packed hexagonal array. Image files are generated by recording the coordinates at every point the ray interacts with the structure; the resulting coordinate file is output and viewed using Visual Molecular Dynamics (VMD)¹⁵⁶.

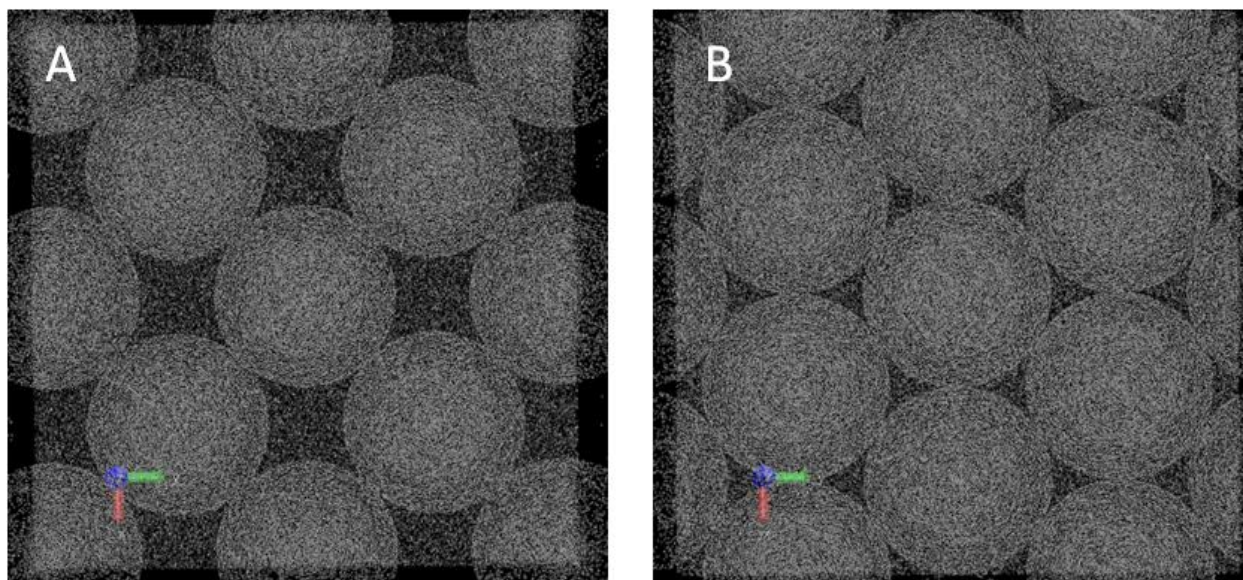


Figure 4-5. Simulated microlens arrays. A) square and B) hexagonal close-packed (right) arrays of 1 mm diameter, 90° contact angle convex lenses (visualized using VMD¹⁵⁶).

With the full array simulated, the concavity of the array is defined by disallowing interactions between the ray and sphere below (for convex arrays) or above (for concave arrays) the air/buffer interface. To simplify later calculations, the center point

of each lens is saved during array generation. The lens array can either be created to fill the entire defined array area or as a small array that is spatially shifted to catch rays as they approach an intersection with the lens layer. The former approach is computationally expensive but simple to program; the latter requires additional care to accurately shift the array but vastly decreases expense and simulation time. The latter approach was used in this simulator.

Simulation of different contact angles was also required. Figure 4-6 illustrates the shifting process to create a lens with a contact angle less than 90°. First, a 90° lens is made by the previously described process. Then, the lens is shifted a distance of $r \cos(\theta)$ into the buffer layer, where r is the radius of the sphere and θ is the desired contact angle. The array is then generated by either using the original sphere radius to leave gaps between the individual lenses, or by using the new lens radius

$r_{cap} = \sqrt{h_{cap}(2r - h_{cap})}$ to create a close-packed array.

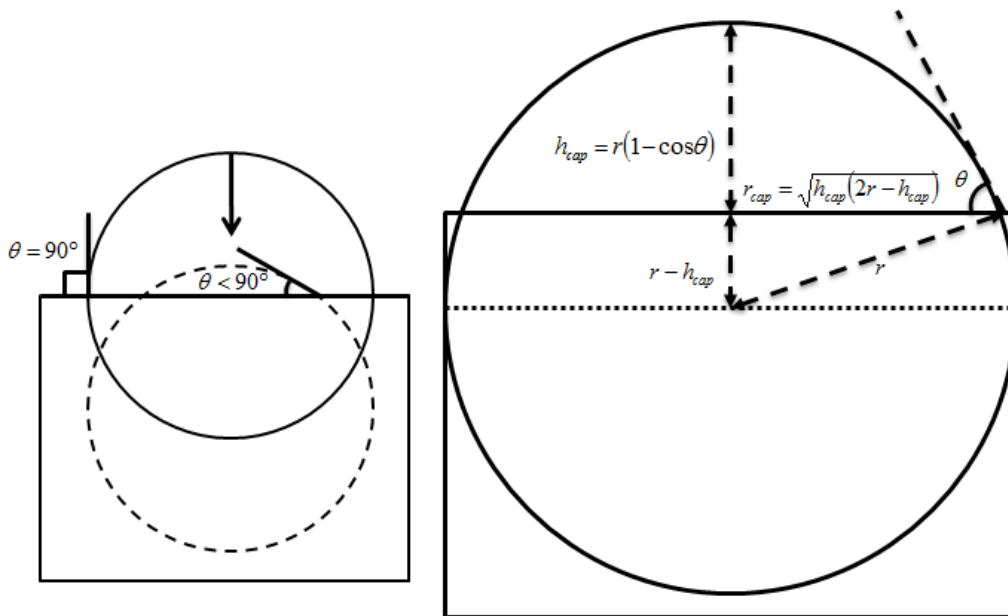


Figure 4-6. Concept and mathematical details to simulate lenses of different contact angles.

Close-packed arrays were used to isolate the effect of contact angle. Images of 90° and 30° hexagonally close-packed arrays generated from 1 mm spheres are shown in Figure 4-7, visualized with VMD. The images appear semi-transparent because the coordinate files are generated from a finite number of interactions.

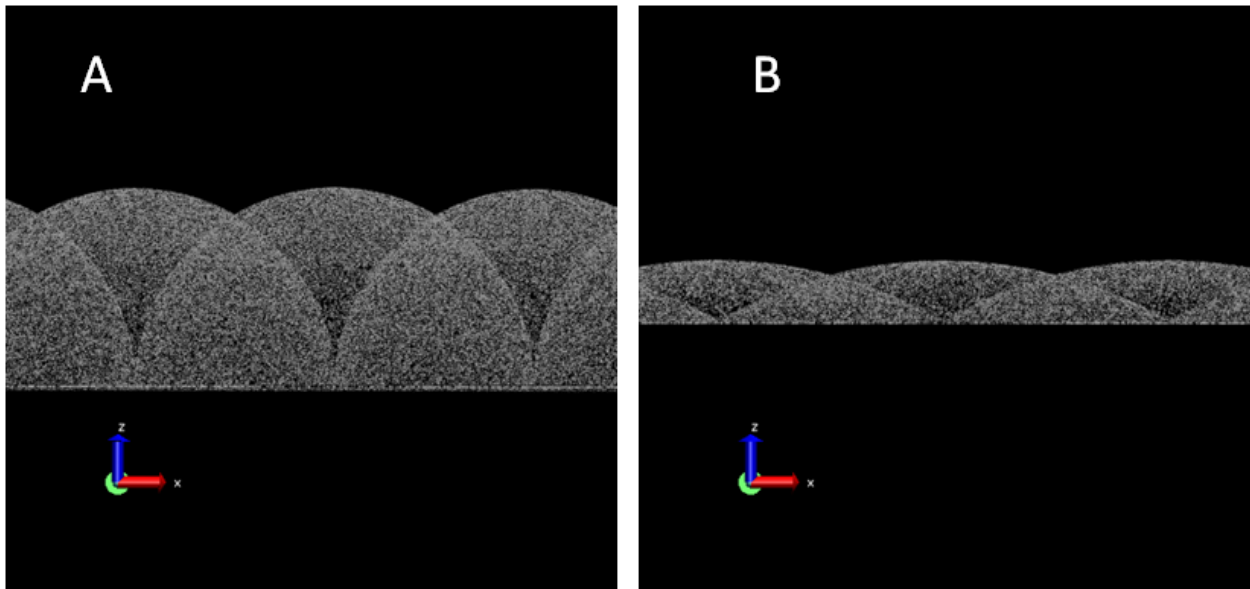


Figure 4-7. Simulated lens arrays with contact angles of 90° and 30° (visualized with VMD¹⁵⁶).

With the array properly created, the next concern is accurately defining interactions between the ray and the lens layer. Whenever there is a chance that the ray will intersect with the lens array an intersection point is sought; if no valid intersection is found, the next interaction surface is planar and the ray is projected to the next planar interface and Fresnel reflection and transmission calculations are performed.

The translation distance required along a ray's direction to intersect a point on a sphere is a quadratic relation, calculated as

$$At^2 + Bt + C = 0,$$

$$A = \mathbf{d} \cdot \mathbf{d},$$

$$B = 2(\mathbf{s} \cdot \mathbf{d}) - 2(\mathbf{c} \cdot \mathbf{d}),$$

$$C = (\mathbf{s} \cdot \mathbf{s}) + (\mathbf{c} \cdot \mathbf{c}) - 2(\mathbf{c} \cdot \mathbf{s}) - r^2,$$

Where \mathbf{d} is the ray direction, \mathbf{s} is the ray origin, \mathbf{c} is the sphere center point, and r is the sphere radius. If the quantity $B^2 - 4AC$ is negative, no valid intersection exists between the ray and the sphere. In a convex array, the only allowed solutions are positive values of t such that the intersection point \mathbf{rd} is above the basal plane of the lens array. This calculation is repeated for all lenses in the array and the smallest positive value of t is taken as the correct intersection point. If no suitable positive value of t exists within the array the intersection is treated as a planar.

After an appropriate intersection point is calculated, the local surface normal of the lens at the intersection point is calculated for use in the Fresnel transmission and reflection calculations, and the ray is either reflected or refracted according to the previous equations.

4.1.3 Quantitative Significance and Verification

Since this simulator is intended to show the effect that optical structures have on a real photovoltaic device additional steps must be taken to ensure that the data is quantitatively significant. First, elementary hand calculations can be compared with simulated results to check that rays are being generated in an appropriately random manner across the specified area and that the simulator's calculated reflection coefficient behaves appropriately for an air-glass ($n = 1.5$) interface (Figure 4-8A), and that ray generation occurs in an appropriately random manner (Figure 4-8B).

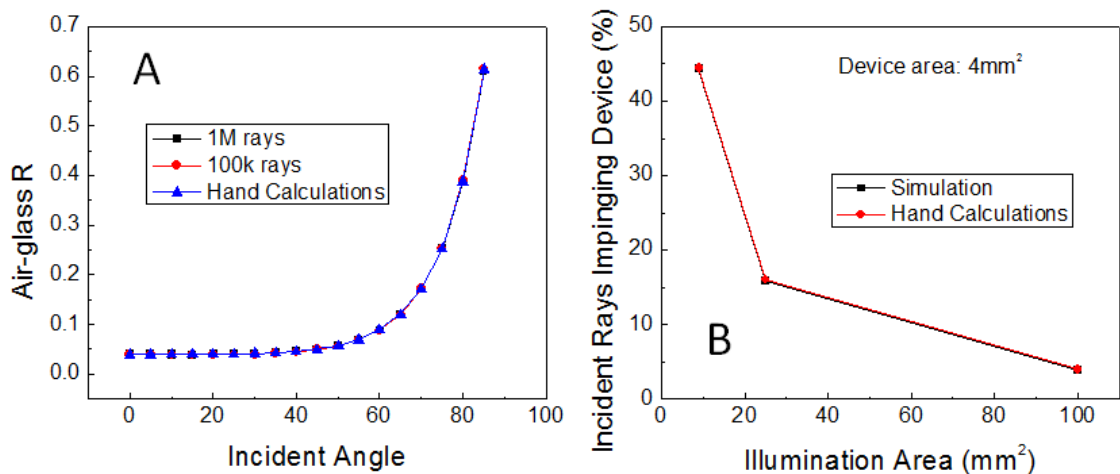


Figure 4-8. Verification of basic simulator functions. A) Calculated Fresnel reflection coefficients as a function of incident angle. B) Verification of randomized ray location generation.

To better approximate and analyze the absorption characteristics induced in real organic photovoltaic devices, the organic active layer is assigned wavelength-dependent absorption coefficients and rays are assigned wavelength values to mimic the wavelength distribution of light in the reference AM 1.5G solar spectrum¹⁴⁴. Absorption coefficients were derived from extinction coefficient values measured using spectroscopic ellipsometry according to $\alpha = 4\pi k/\lambda$. The absorption coefficients and simulated AM 1.5G spectra are shown in Figure 4.9.

The simulated AM 1.5G spectrum is created by first normalizing individual wavelength photon counts to the total photon count within the reference spectrum, then generating a random number. The ray is defined as having wavelength λ if the random number R satisfies

$$\sum_0^{\lambda-1} G < R \leq \sum_0^{\lambda} G,$$

where \mathbf{G} is the list of ordered, normalized photon counts. As shown in figure 4-9, close reproduction of the reference spectrum is obtained with a simulation of only one hundred thousand rays.

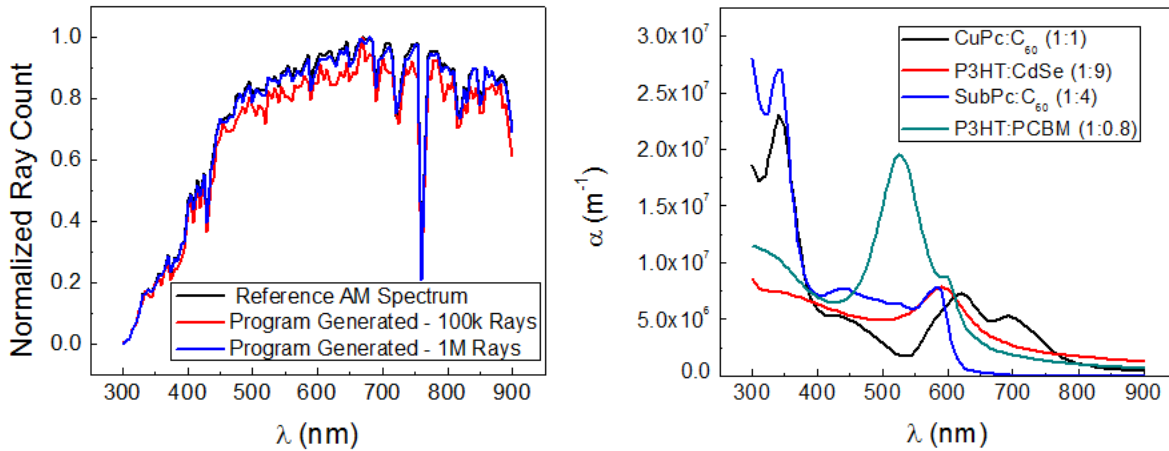


Figure 4-9. Simulated air mass 1.5G solar spectrum and active layers absorption coefficients for various material systems.

Increasing the ray count to one million gives an almost exact reproduction. Combining an accurate simulated spectrum with realistic absorption values gives a fairly accurate reproduction of solar cell absorption. Finally, periodic boundary conditions (PBCs) are enforced using the array area as a boundary, allowing the device to be effectively infinite (device area = array area) or isolated (device area \ll array area). Simulated absorption spectra and the results of various geometric arrangements are discussed extensively in Chapter 6.

4.2 Transfer Matrix Wave Optics

4.2.1 Concept

For dimensions near and less than the wavelength of visible light, ray optics methods are not suitable to describe the behavior of light. In OPVs, active layer thicknesses are on the order of 100 nm, and are typically adjacent to a highly reflective surface, the thermally evaporated metal cathode. In the area close to a reflective surface, incident and reflected light waves will constructively and destructively interact, creating areas of high and low optical intensity.

The emergent optical interference patterns can have a profound effect on OPV performance. In bilayer devices, thicknesses should be optimized to center regions of high optical intensity near the heterojunction interface, ensuring that a large proportion of generated excitons are dissociated at the interface. Mixed heterojunction devices do not have this requirement, but regions of strong optical absorption should be centered within the active region to maximize photocurrent generation. This can be accomplished by either increasing the layer thickness or, if charge carrier transport lengths or film morphologies limit how thick the active layer can be made, adding an optical spacer between the cathode and active layer. Additionally, tandem OPVs require extensive optical design to balance photocurrent between the front and back cells to maximize efficiency⁶⁶.

In all of these cases, transfer matrix optical simulations are a computationally efficient, robust method to examine optical interference effects in planar stacks of optical media. Here, the transfer matrix method of Pettersson¹⁵⁷ and Peumans¹ is implemented. This approach calculates the optical field within a series of planar layers and then determines the resulting exciton generation and photocurrent output from the

device, along with calculating properties such as reflection, transmission, and device absorption. The following section is a summary of the derivation of this method, which has been implemented in numerous studies^{27,66,79,158-163}.

4.2.2 Optical Field Calculation

Given the assumptions that all layers are uniform and isotropic with parallel, flat interfaces (for convention, the interface normals are taken to be parallel to the x direction within the simulation), and that the incident light can be described by planar waves, a basic formulation emerges. At any point within the system, the electric field can be described with two components, one of which is propagating in the positive x direction and one in the negative x direction. Each interface within the stack can therefore be described by a 2x2 matrix,

$$I_{ij} = \frac{1}{t_{ij}} \begin{bmatrix} 1 & r_{ij} \\ r_{ij} & 1 \end{bmatrix}$$

where r_{ij} and t_{ij} are the complex Fresnel reflection and transmission coefficients at each interface. This work only considers s-polarized light, with the electric field perpendicular to the plane of incidence, giving Fresnel coefficients of:

$$r_{ij} = \frac{q_i - q_j}{q_i + q_j}$$

and

$$t_{ij} = \frac{2q_i}{q_i + q_j},$$

with

$$q_i = \tilde{n}_i \cos \theta_i = \sqrt{\tilde{n}_i^2 - \eta_0^2 \sin^2 \theta_0},$$

where \tilde{n}_i is the complex refractive index of layer i , η_0 is the refractive index of air (1.0), and θ_0 is the angle of incidence on the stack. Within each layer, the propagation is described by a layer matrix

$$L_j = \begin{bmatrix} e^{-i\xi_j d_j} & 0 \\ 0 & e^{-i\xi_j d_j} \end{bmatrix},$$

where d_j is the thickness of layer j and

$$\xi_j = \frac{2\pi}{\lambda} q_j.$$

The quantity $\xi_j d_j$ is also known as the phase thickness, a representation of how much the phase of an incident light wave is changed by passing through that layer. This has important ramifications for interference, as shifts in the phase will change the spatial locations of constructive and destructive interference. Ultimately, the electric fields at each end of a system of m planar layers must be related by a transfer matrix \mathbf{S} , as in

$$\begin{bmatrix} E_0^+ \\ E_0^- \end{bmatrix} = \mathbf{S} \begin{bmatrix} E_{m+1}^+ \\ E_{m+1}^- \end{bmatrix}.$$

\mathbf{S} is itself calculated according to

$$\mathbf{S} = \begin{bmatrix} S_{11} & S_{12} \\ S_{21} & S_{22} \end{bmatrix} = \left(\prod_{v=1}^m I_{(v-1)v} L_v \right) \cdot I_{m(m+1)}.$$

The transmission and reflection coefficients for the entire structure can be describe with elements of the total transfer matrix \mathbf{S} ,

$$r = \frac{E_0^-}{E_0^+} = \frac{S_{21}}{S_{11}},$$

$$t = \frac{E_{m+1}^+}{E_0^+} = \frac{1}{S_{11}}.$$

This is allowed by realizing that light incident at upon the first layer propagating in the positive x direction will have no component propagating in the negative x direction at layer $m+1$, making $E_{m+1}^- = 0$. Thus, the reflection and transmission coefficients follow a logical formulation; the proportion of reflected light is the ratio of negatively propagating light to positively propagating light at the first layer, and the transmitted light is the ratio of positively propagating light at the final layer to positively propagating light at the first layer. The absorption of the multilayer stack is calculated according to $A = 1 - T - R$, where the transmittance and reflectance are respectively calculated as

$T = |t|^2 \tilde{n}_{m+1} / \tilde{n}_0$ and $R = |r|^2$. This can be further modified to remove the reflections at the air/substrate and substrate/multilayer interfaces, leaving only the reflection and transmission (and, therefore, absorption) through the multilayer stack itself^{1,164}. This form is

$$R' = \frac{R^* + R - 2R^*R}{1 - R^*R},$$

$$T' = \frac{T^*T}{1 - R^*R},$$

where

$$R^* = \left| \frac{1 - \tilde{n}_0}{1 + \tilde{n}_0} \right|^2,$$

$$T^* = \eta_0 \left| \frac{2}{1 + \tilde{n}_0} \right|^2.$$

The transmission, reflection, and absorption ($A' = 1 - T' - R'$) for a multilayer stack of ITO/CuPc/C₆₀/BCP/Ag (150/20/40/8/100 nm) calculated using this method is shown in Figure 4-10. As expected, there is very little transmission through the structure (given the metal cathode), giving absorption and reflection an inverse relationship.

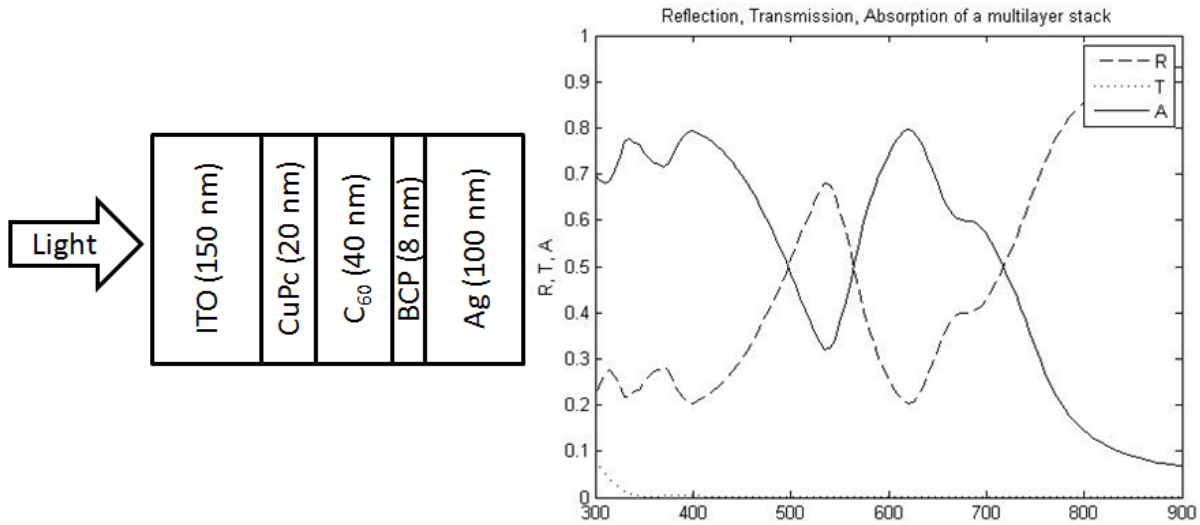


Figure 4-10. Calculated transmission, absorption, and reflection of a multilayer CuPc/C₆₀ structure.

This is a fine situation to look at the behavior of the system as a whole, but the desired outcome is the calculation of the optical field within the system's constituent layers, necessitating a modification of the total system matrix to

$$\mathbf{S} = \mathbf{S}'_j L_j \mathbf{S}''_j.$$

Now, each layer can be dealt with by its own transfer matrix, according to

$$\begin{bmatrix} E_0^+ \\ E_0^- \end{bmatrix} = \mathbf{S}'_j \begin{bmatrix} E_j^+ \\ E_j^- \end{bmatrix},$$

with

$$\mathbf{S}'_j = \begin{bmatrix} S'_{j11} & S'_{j12} \\ S'_{j21} & S'_{j22} \end{bmatrix} = \left(\prod_{v=1}^{j-1} I_{(v-1)v} L_v \right) \cdot I_{(j-1)j}.$$

Here, E_j^+ and E_j^- refer to the left hand boundary of layer j . A similar rewriting based on S''_j gives terms for the right hand boundary of layer j ,

$$\begin{bmatrix} E_j^{''+} \\ E_j^{''-} \end{bmatrix} = \mathbf{S}''_j \begin{bmatrix} E_{m+1}^+ \\ E_{m+1}^- \end{bmatrix},$$

with

$$\mathbf{S}''_j = \begin{bmatrix} S''_{j11} & S''_{j12} \\ S''_{j21} & S''_{j22} \end{bmatrix} = \left(\prod_{v=j+1}^m I_{(v-1)v} L_v \right) \cdot I_{m(m+1)}$$

Within this framework, reflection and transmission coefficients for layer j can be defined from both the right- and left hand directions in terms of elements of their respective partial system matrices:

$$r'_j = \frac{S'_{j21}}{S'_{j11}},$$

$$r''_j = \frac{S''_{j21}}{S''_{j11}},$$

$$t'_j = \frac{1}{S'_{j11}},$$

$$t''_j = \frac{1}{S''_{j11}}.$$

Next, a transmission coefficient that relates the incident wave to the wave propagating within layer j in the positive x direction at the interface of layers j and $(j - 1)$ can be derived using the above equations as

$$t_j^+ = \frac{E_j^+}{E_0^+} = \frac{t_j'}{1 - r_{j-}' r_j'' \cdot e^{i2\xi_j d_j}},$$

where $r_{j-}' = -S'_{j12}/S'_{j11}$. The negative- x propagating component can also be determined,

$$t_j^- = \frac{E_j^-}{E_0^+} = \frac{t_j' r_j'' \cdot e^{i2\xi_j d_j}}{1 - r_{j-}' r_j'' \cdot e^{i2\xi_j d_j}} = t_j^+ r_j'' \cdot e^{i2\xi_j d_j}.$$

These last two equations can be used to describe the electric field at any distance x away from the interface of layers j and $(j-1)$, provided that $0 \leq x \leq d_j$. In terms of the incident forward-propagating wave, the final solution is

$$E_j(x) = E_j^+(x) + E_j^-(x) = \left[t_j^+ e^{i\xi_j x} + t_j^- e^{-i\xi_j x} \right] E_0^+ = t_j^+ \left[e^{i\xi_j x} + r_j'' e^{-i\xi_j (2d_j - x)} \right] E_0^+.$$

The optical field at position x is proportional to $|E_j(x)|^2$. The total energy absorbed at a position x per second is given by

$$Q_j(x) = \frac{1}{2} c \varepsilon_0 \alpha_j \eta_j |E_j(x)|^2,$$

where c is the speed of light, ε_0 is the permittivity of free space, and α_j is the absorption coefficient of light within layer j . This is a quantity of great interest in OPV device simulation, as it represents the time-averaged absorption of light and (assuming a 100% photon-to-exciton conversion) exciton generation. Substituting the expression for $E_j(x)$ into this yields

$$Q_j(x) = \alpha_j I_0 \left(\frac{\eta_j}{\eta_0} |t_j^+|^2 \right) \left[e^{-\alpha_j x} + \rho_j''^2 \cdot e^{-\alpha_j (2d_j - x)} + 2\rho_j'' \cdot e^{-\alpha_j d_j} \cos\left(\frac{4\pi\eta_j}{\lambda} (d_j - x) + \vartheta_j'' \right) \right],$$

where I_0 is the incident light intensity and ρ_j'' and d_j'' are, respectively, the absolute value and the argument of r_j'' .

It is now clear that the energy absorbed at any position x within a layer j in a structure of planar layers is proportional to the summation of three components (from left to right inside of the bracketed portion of the proceeding equation): incident light propagating in the positive x direction, reflected light propagating in the negative x direction, and interference between these two waves.

While there are numerous reflecting interfaces inside of a typical device structure, the primary reflecting surface is the metal cathode. Thus, the regions of high intensity are closely related to the distance from this surface, with peaks coming at distances of $(2m+1)\lambda/4n$, where $m = 0, 1, 2, \dots$ is the integer order of interference. The proportional optical fields $I_j(x) = |E_j(x)|^2$ of two different structures, ITO (150 nm)/CuPc (20 nm)/C₆₀ (40 nm)/BCP (8 nm)/Ag (100 nm) and ITO (150 nm)/CuPc:C₆₀ (1:1) (60 nm)/BCP (8 nm)/Ag (100 nm) are shown in Figure 4-11.

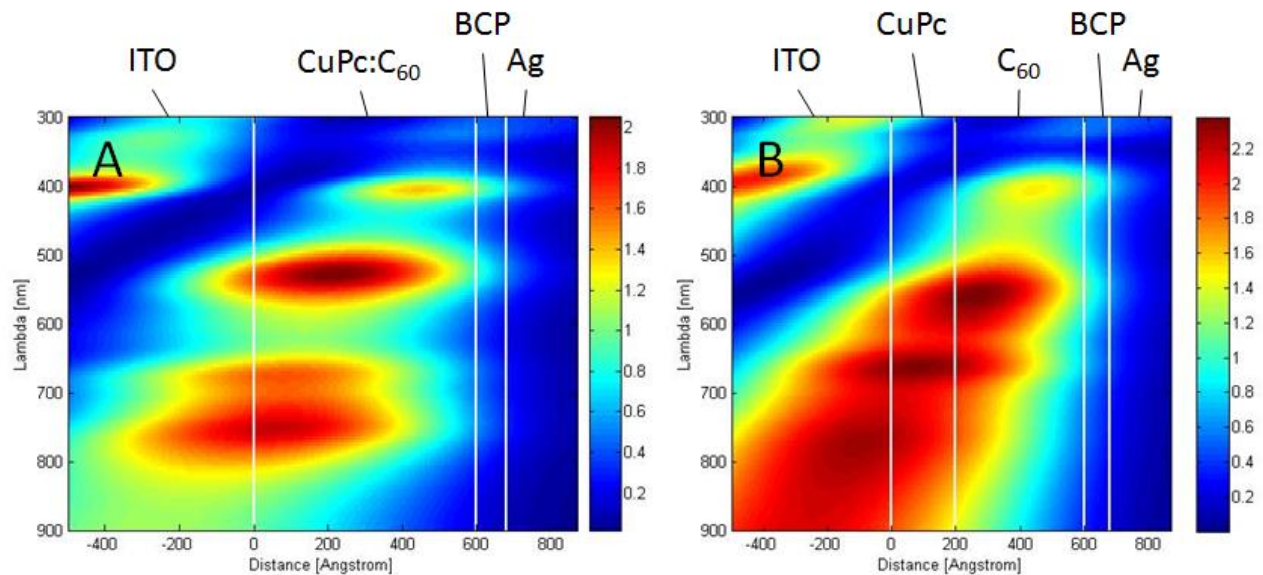


Figure 4-11. Transfer matrix-calculated optical fields. Both A) 1:1 (by weight) mixed and B) planar heterojunction CuPc/C₆₀ architectures are shown.

While there are differences between the optical fields within the bilayer and mixed devices, the general trend of $\lambda/4n$ remains true in either case; shorter wavelengths have intensity peaks closer to the cathode and the regions of high intensity for longer wavelengths are further away. In the case of the bilayer device, it is highly desirable to maximize the absorption and photocurrent in each layer by ensuring that regions of high intensity fall within the absorption band of the proper material and close to the heterojunction interface to maximize exciton diffusion efficiency. This can either be solved mathematically by computing the photocurrent generation from the optical field, or can be qualitatively shown by

$$G_j(x) \propto |E_j(x)|^2 \cdot \alpha_j(x),$$

where G is the photon absorption/exciton generation rate, E is the electric field intensity, and α is the wavelength-dependent absorption coefficient. The resulting exciton generation plots for two different bilayer structures, CuPc/C₆₀ 20/40 nm and 40/80 nm, are shown in Figure 4-12.

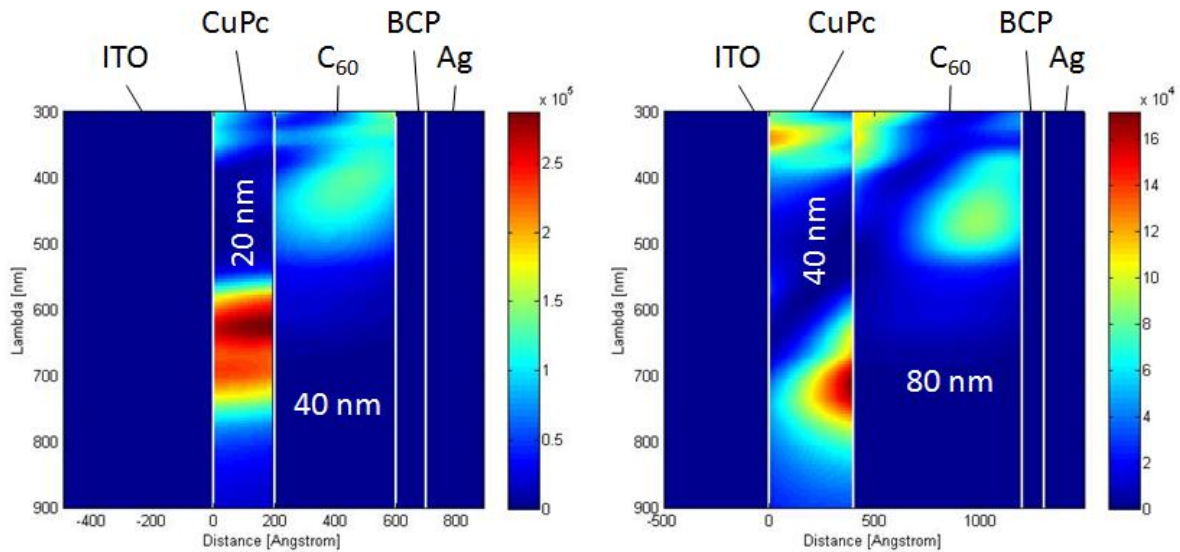


Figure 4-12. Exciton generation plots in two different bilayer CuPc/C₆₀ devices.

The discontinuities in the absorption field come from the different absorption spectra in each layer. Absorption in this model is only assumed to occur in the active layers. Examination of Figure 4-12 gives a good qualitative feel for the resulting device performance. In the case of a 20/40 nm bilayer, there is strong optical intensity in both CuPc and C₆₀ near the heterojunction interface and the layers are reasonably thin, which will maximize charge collection. In a 40/80 nm thick device, however, the heterojunction interface has been moved away from the bulk of exciton generation in C₆₀, the maximum intensity of absorption in CuPc has been decreased, and the layers are now much thicker, limiting charge collection efficiency. It is therefore reasonable to conclude that 20/40 nm is a preferred architecture over 40/80 nm. While this approach is fine for qualitative analysis, quantitative evaluations are needed for more accurate optimization.

4.2.3 Photocurrent Calculation

With the calculated photon absorption/exciton generation field $Q(x)$ already known, a steady-state diffusion equation can be constructed and solved for each layer that is defined as a contributor to the photocurrent (i.e. donor and acceptor),

$$D_j \tau_j \frac{\partial^2 \rho}{\partial x^2} - \rho + \tau_j \frac{\lambda Q_j(x)}{hc} = 0$$

Where D_j and τ_j are respectively the exciton diffusivity and lifetime within layer j and ρ is the exciton density at position x . Since a properly designed Type-II D-A heterojunction and metal electrodes serve as perfect quenching/dissociation site for excitons, boundary conditions of $\rho = 0$ can be set at these locations. Solving for the exciton diffusion current at the location of the D-A interface with this condition gives

$$J_j = qD_j \left. \frac{\partial \rho}{\partial x} \right|_{x=x_{DA}} .$$

The quantum efficiency is found by normalizing the current to the incident power,

$$\eta_{EQE}^j = \frac{2J_j / q}{c\epsilon_0 |E_0^+|^2} .$$

The total current for the cell is then computed by summing the individual quantum efficiencies of each layer and integrating with respect to the AM1.5G spectrum, outputting the one-sun photocurrent regardless of the incident power intensity.

Revisiting the previous CuPc/C₆₀ structure, the optimum value for C₆₀ thickness can be calculated as 40 nm, in agreement with qualitative predictions (Figure 4-13).

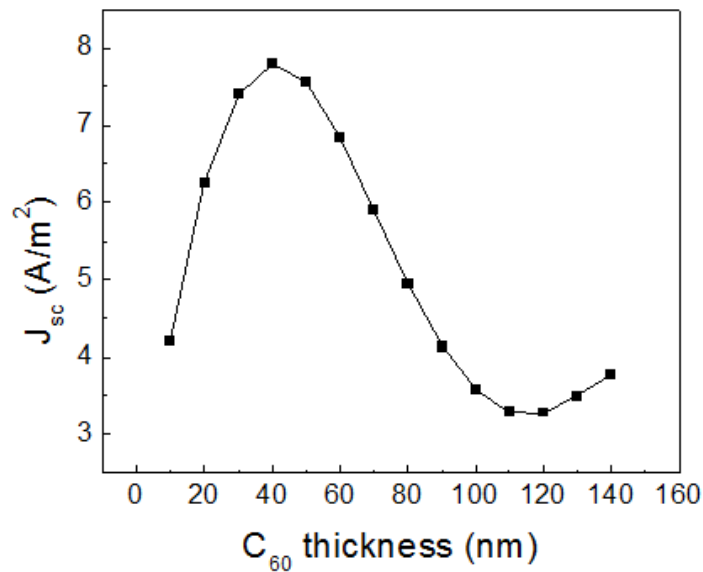


Figure 4-13. Transfer-matrix calculated short circuit current in a 20 nm CuPc/ x nm C₆₀ device.

Note that this presumes no loss from both the exciton dissociation efficiency η_{CT} and the charge collection efficiency η_{CC} , which results in an overestimation of short-circuit current. Corrections can be made if values for charge collection length and dissociation efficiency are known by modifying the current generation equation to

$$J_j = \eta_{CC}\eta_{CT}qD_j \left. \frac{\partial \rho}{\partial x} \right|_{x=x_{DA}}$$

$$\eta_{CC} = \exp\left(\frac{x_{DA} - x_{CC}}{l_{CC}}\right)$$

Where $x_{DA} - x_{CC}$ is the distance from the dissociation interface to a charge collecting interface (i.e. anode or cathode) and can vary based on charge carrier type, and l_{CC} is the charge carrier collection length. This is especially suitable for bulk heterojunction devices, where charge collection losses can be substantial.

The transfer matrix method has been used extensively in Chapters 5 and 6 to explore the relationship between optical field and photocurrent behavior.

4.3 Review of Optical Simulation Techniques

In this Chapter, the reader was presented with the theoretical background, practical implementation, and capabilities of two different optical simulation techniques, Monte Carlo ray optics and transfer matrix wave optics. Both Chapters 5 and 6 use these techniques to analyze OPVs.

Ray optics simulations are used extensively in Chapter 6 to investigate the geometric dependence of microlens arrays on absorption enhancement. This technique is readily implemented and is suitable for a variety of optical structures. The basic

governing equations and iteration scheme were described. The Monte Carlo framework makes the program easily customizable and suitable for recording many different aspects of ray behavior. To obtain quantitatively significant data, rays are generated to fit the simulated AM1.5G solar spectrum and the active layer mimics the absorption characteristics of real materials.

In Section 4.2, the transfer matrix method for wave optics simulation was explained. This method is appropriate for simulating the optical field, including interference patterns that emerge within a stack of planar layers. The optical field can then be used to calculate absorption and, with certain assumptions, the short circuit current in an OPV; this is useful to quickly optimize layer thicknesses in complex structures without the expense of device fabrication. Transfer matrix calculations are used in Chapter 5 to correlate photocurrent behavior with the internal optical field in a variety of devices. In Chapter 6, a slightly modified calculation is used to approximate the behavior of devices with and without microlens arrays.

CHAPTER 5

PHOTOCURRENT GENERATION AND TRANSPORT BEHAVIOR IN ORGANIC PHOTOVOLTAIC DEVICES

5.1 Overview

Despite significant advances in device performance, there are still fundamental questions regarding the nature of photocurrent generation and transport in organic photovoltaic devices. In this chapter, the novel technique of synchronous photocurrent detection is used to study the impact of device architecture and thickness on charge transport behavior (Section 5.2). Transfer matrix optical simulations are then used to correlate measured photocurrent characteristics and the optical field within the device active layers (Section 5.3). Finally, exciton dissociation behavior in bilayer OPVs is qualitatively described using a combination of optical simulation and synchronous photocurrent detection.

5.2 Effect of Heterojunction Architecture

OPV device architectures can take several different forms. The three most common small-molecule based architectures are (1) bilayer or planar, with neat layers of donor and acceptor and a single heterojunction interface, (2) bulk or mixed, where the donor and acceptor are uniformly mixed, creating dissociation interfaces throughout the active layer, and (3) planar-mixed, where neat layers of donor and acceptor sandwich a mixed layer in an attempt to maximize photocurrent generation without compromising charge extraction. A schematic of these three architectures is shown in Figure 5-1.

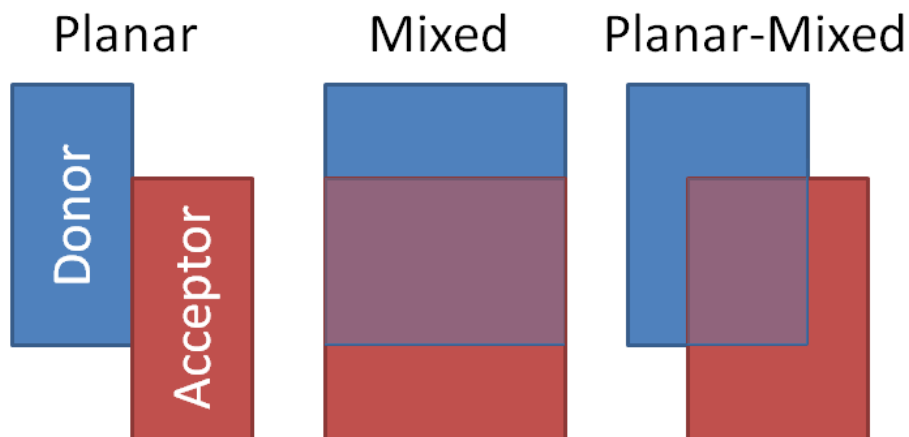


Figure 5-1. Three different small molecule device architectures.

The different placement of heterojunction interfaces in each of these architectures will have a significant impact on the locations of photocarrier generation. In a planar device, exciton dissociation will only efficiently occur at one plane within the active layers (discounting any effect of field-assisted exciton dissociation). Free charge carriers in this device therefore come only from the heterojunction interface. In a mixed device, charge generation will be more uniform throughout the active layer due to the abundance of readily available exciton dissociation interfaces (neglecting the effect of optical interference for the time being). A planar-mixed device is a hybrid between these two extremes: strong locations of carrier generation at the donor/mixed and mixed/acceptor interfaces with uniform generation inside the mixed portion of the active layer.

Based on this surface analysis, the movement of photogenerated charge carriers will differ due to the large variability in generation location and the charge transport characteristics of each architecture. A planar heterojunction will act as charge blocking

interface, causing carrier pileup. For example, electrons in a bilayer CuPc/C₆₀ device can move freely from CuPc to C₆₀ but have a large energy barrier (~1 eV) preventing movement from C₆₀ to CuPc^{29,165}. This arrangement should cause a concentration gradient to emerge pointing away from the interface, strongly influencing the diffusion motion of charge carriers.

To probe this behavior, devices consisting of an electron donor of CuPc and an electron acceptor of C₆₀, archetypical small molecule OPV materials, were studied. All devices were fabricated on glass substrates prepatterned with a tin-doped indium oxide (ITO) anode (15 Ω/□ sheet resistance) using vacuum thermal evaporation (Section 1.4.2). Before deposition, the substrates were sonicated in successive solutions of surfactant, deionized water, acetone, and isopropanol to remove any residual debris from the ITO surface. Finally, substrates were exposed to a UV-ozone treatment for 15 minutes to destroy any remaining organic particles and increase the work function of ITO for better hole extraction^{166,167}.

The planar heterojunction devices have a 20 nm-thick CuPc donor layer and a 40 nm-thick C₆₀ acceptor layer. Planar-mixed devices were a sandwich structure of CuPc/CuPc:C₆₀ (1:2 by weight)/C₆₀ (10 nm/20 nm/30 nm). Mixed heterojunction devices had varying active layer thicknesses (60 to 120 nm) and mixing ratios. All devices were finished with an 8 nm-thick exciton blocking layer of BCP and an aluminum cathode. CuPc was purified using high-vacuum gradient-zone sublimation (Section 1.4.1) prior to use; high purity C₆₀ and BCP were used as purchased.

The devices were characterized according to the techniques described in Chapter 3. All photocurrent measurements were performed under a white light bias of

approximately one sun (100 mW/cm^2) with a monochromatic beam intensity on the order of $1\text{-}10 \text{ }\mu\text{W/cm}^2$, conforming to ASTM standards¹⁴⁸. In synchronous photocurrent detection, three components are fed to the lock-in amplifier: dark current, photocurrent from the white light bias, and periodically varying photocurrent from the mechanically chopped monochromatic light. The last is the parameter of interest. Experimental results will be presented primarily as external quantum efficiency (EQE), calculated as

$$\eta_{EQE}(V, \lambda) = \frac{hc}{q\lambda} \frac{J_{ph}(V, \lambda)}{P_0(\lambda)}$$

where V is the applied voltage bias, λ is the incident monochromatic wavelength, and h , c , and q are Planck's Constant, the speed of light, and the elementary charge, respectively. The only difference between the photocurrent quantum efficiency and a standard EQE measurement is the voltage applied across the device. Under forward bias, the ITO anode is connected to the positive terminal, and positive current is referenced as positive when it flows from the anode to the cathode.

Photocurrent characteristics for three different architectures (planar, planar-mixed, and mixed 1:1 (by weight) CuPc:C₆₀) at $\lambda = 650 \text{ nm}$ are shown in Figure 5-2. In Figure 5-2A, the planar and planar-mixed devices show monotonic decreases in photocurrent as bias is increased, from $\eta_{EQE} > 10\%$ at $V = 0 \text{ V}$ to $< 0.05\%$ at $V = 1 \text{ V}$. Beyond $V = 1 \text{ V}$ data was unreliable due to overloading and noise in the measurement system. The mixed HJ device shows markedly different behavior. There is a steady decrease in η_{EQE} until it reaches a minimum value at $V \approx 0.55 \text{ V}$. After this point η_{EQE} begins to increase. Shown in the inset of Figure 5-2A is the phase recorded by the lock-in amplifier. While there is no change for the planar or planar-mixed devices (excepting noise at high biases), there is a 180° shift in the mixed device phase at the same voltage where η_{EQE}

is at a minimum. This indicates that the direction of photocurrent changes at this voltage, i.e. it changes from negative to positive at a specific zero-photocurrent voltage V_0 . In the planar and planar-mixed devices the photocurrent stays negative regardless of the voltage.

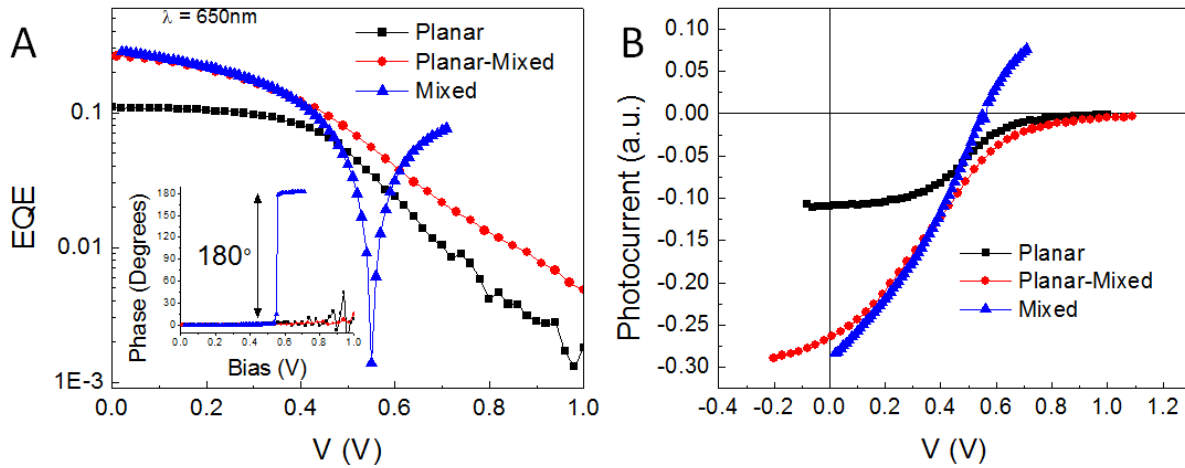


Figure 5-2. Example photocurrent characteristics for three different device architectures. A) Raw data (inset: lock-in amplifier phase). B) Phase-adjusted photocurrent characteristics.

This behavior can be explained by examining the relative behavior of the drift and diffusion components of the photocurrent. The photocurrent at any point in the active layer can be simply defined as a summation of the drift and diffusion subcomponents,

$$J_e = q \left(n \mu_e E + D \frac{dn}{dx} \right)$$

where μ_e is the electron mobility, q is the elementary charge, E is the local electric field, D is the electron diffusivity and n is the number of electrons. A similar equation can be written for holes, making the total photocurrent $J_{ph} = J_e + J_h$. Drift occurs as carriers are swept by the electric field; diffusion acts to reduce concentration gradients.

Figure 5-3 diagrams the relative contributions of drift and diffusion at small forward biases (or at the short circuit or negative biases), where the internal electric field points from the cathode to the anode, in planar and mixed architectures. The behavior of planar-mixed devices is qualitatively identical to planar and will therefore not be included in further discussions.

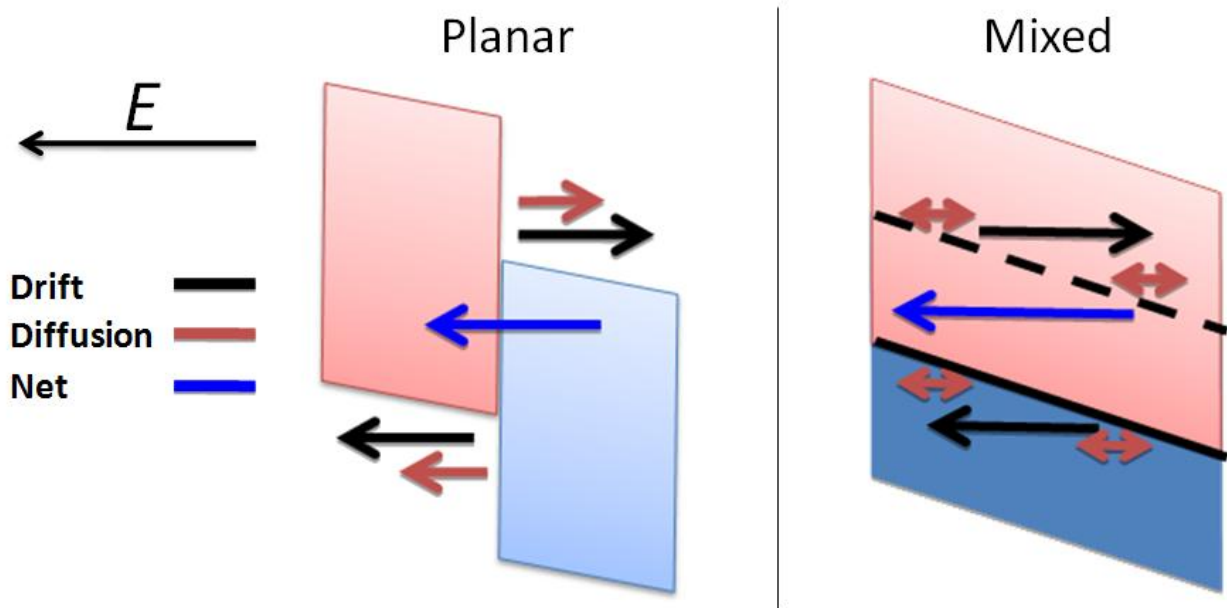


Figure 5-3. Relative contributions of drift and diffusion currents to the net photocurrent at small forward biases for two different device architectures. The direction of the internal electric field is indicated.

This is the standard operating condition of an OPV device. In the planar device, all charges are generated at the heterojunction interface. After dissociation, the internal electric field is able to sweep charges towards the electrodes for collection, giving a negative drift current. The diffusion current is also negative due to the concentration of charges at the dissociation interface, but it will be a minor contributor compared to drift. The internal electric field is continually sweeping charges away from the interface, reducing the concentration gradient and driving force for diffusion. The net photocurrent

for a planar device is therefore negative. In a mixed device, the lack of a singular heterojunction interface to block charge movement simplifies things. Charges will freely move with the electric field, giving a negative drift current. There is additionally no concentration gradient across the width of the active layer, reducing the diffusion photocurrent. This also leads to a negative net photocurrent.

The situation changes greatly when the forward bias is increased enough to overcome the built-in field across the active layer, depicted in Figure 5-4.

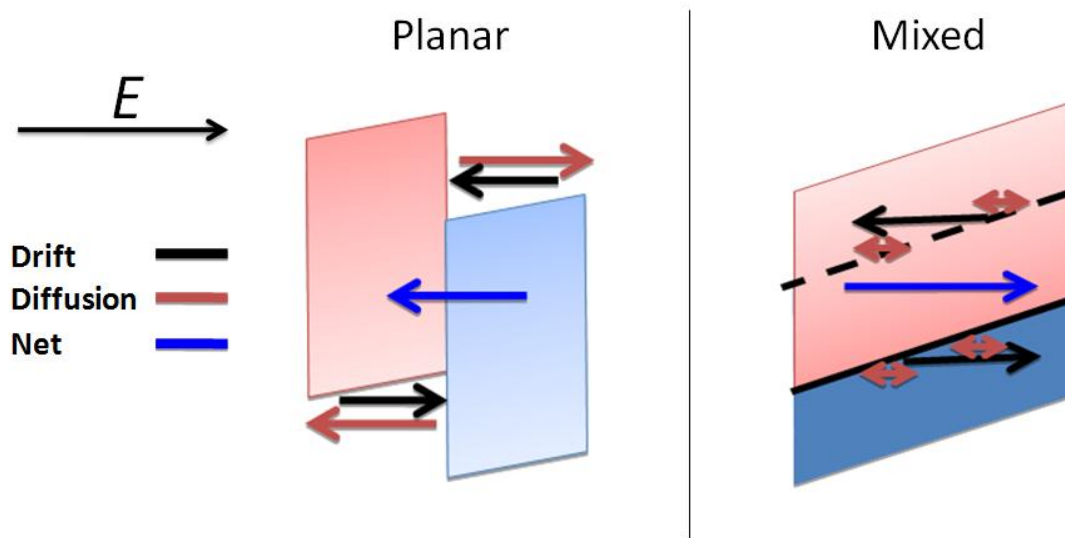


Figure 5-4. Relative contributions of drift and diffusion currents to the net photocurrent at large forward biases for two different device architectures. The direction of the internal electric field is indicated.

The planar device has very different behavior at large forward biases. Now, the internal electric field will sweep charge carriers towards the heterojunction interface, greatly increasing the concentration gradient. This will in turn increase the diffusion current to a sufficiently large value to maintain a negative net photocurrent regardless of the applied bias. The experimentally measured photocurrent curves show a steady decrease as the forward bias is increased. Two mechanisms are identified to explain

this. First, defect states exist within the band gap in these materials that can act as charge recombination centers. As the bias is increased and the concentration of electrons and holes increases the recombination current will increase accordingly, decreasing the driving force for diffusion. Second, an increased forward bias will cause sharper band bending within the active layer, increasing the efficiency of thermionic-assisted tunneling across the heterojunction interface and allowing the positive drift current to correspondingly increase.

There is no great change in the relative contributions of drift and diffusion in the mixed device; diffusion is still a minor constituent of the total photocurrent and drift dominates due to the lack of charge blocking interfaces. However, the drift current has changed direction with the electric field, making the total photocurrent positive. This explains the 180° phase shift and subsequent increase in photocurrent amplitude experimentally measured. This explanation infers that the experimental zero-photocurrent voltage V_0 must occur at a forward bias with a negligible internal electric field. A detailed study of the origin of V_0 and its wavelength dependence is covered in the Section 5.3.

5.3 Wavelength-Dependent Photocurrent Behavior in Mixed Heterojunction Devices

Section 5.2 explained the general relationship between the drift and diffusion components of the total photocurrent with respect to device architecture. One of the important conclusions to arise from this concerns mixed heterojunction devices; namely, the internal electric field must be negligible at the experimentally measured V_0 voltage because drift dominates the total photocurrent. Note that Figure 5-2 only presents one

wavelength of incident monochromatic light (650 nm). If V_0 is solely dependent on the internal electric field direction and drift current, there should be no difference between inversion voltages at different wavelengths. As Figure 5-5 shows, this is not true.

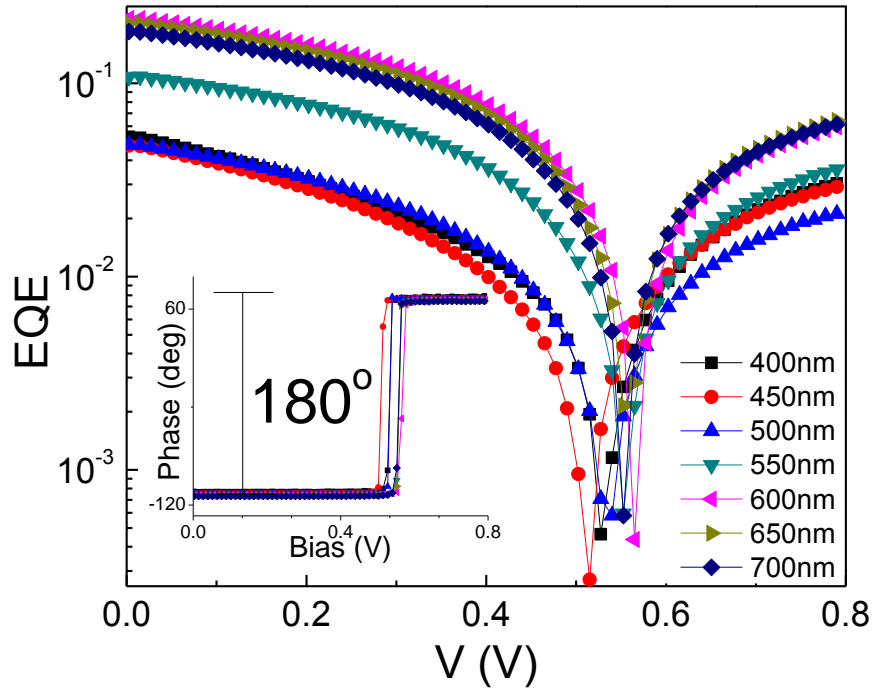


Figure 5-5. Photocurrent measurements of a 90 nm 1:1 CuPc:C₆₀ device at various wavelengths. Lock-in amplifier phase is inset.

In fact, V_0 falls at a wide range of voltages. There is also no obvious dependence of V_0 with respect to wavelength, i.e. the shortest and longest wavelengths (400 and 700 nm) do not correspond to the smallest and largest inversion voltages. Further, the order and magnitude of inversion voltages change with the active layer thickness. In a 90 nm thick 1:1 CuPc:C₆₀ device (Figure 5-6A), the minimum inversion voltage is ~0.52 V with 450 nm illumination. Increasing the active layer thickness to 120 nm (Figure 5-

6B) decreases the minimum inversion voltage to ~ 0.45 V, now with 500 nm light; V_0 at 450 nm illumination is ~ 0.48 V.

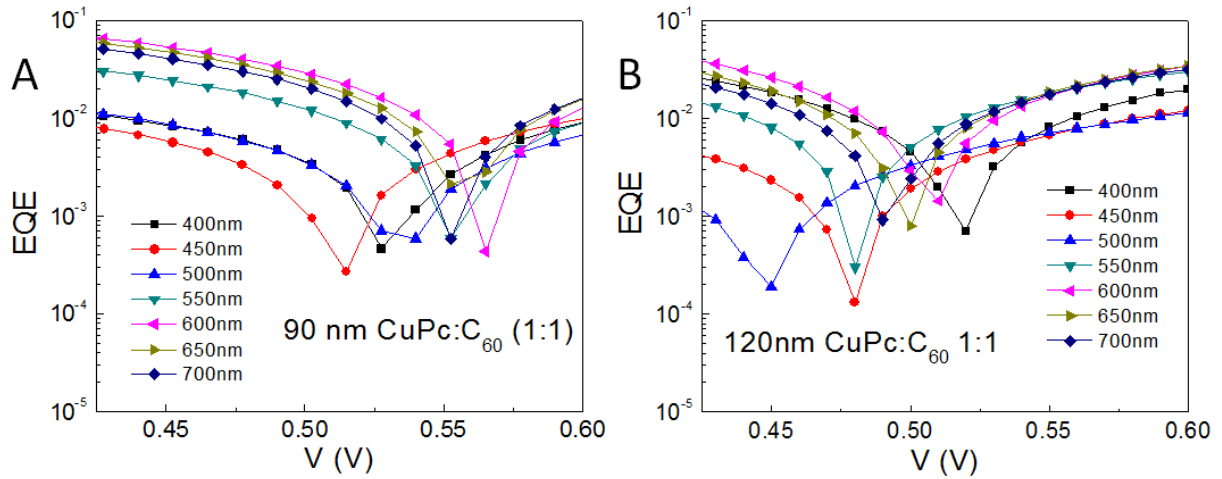


Figure 5-6. Measured photocurrent values for two different mixed layer thicknesses at different wavelengths. A) 90 nm CuPc:C₆₀ (1:1 by weight). B) 120 nm CuPc:C₆₀ (1:1 by weight).

To gain a clearer picture, linear interpolation of the measured photocurrent spectra near the inversion voltage can give a more precise value for V_0 at each wavelength. Figure 5-7 shows the resulting curves for three different layer thicknesses (60, 90, and 120 nm) of 1:1 CuPc:C₆₀ devices measured at 10 nm wavelength increments from 350 to 750 nm. After processing, it is clear that V_0 shows a definite relationship to wavelength. To explain the wavelength dependence, the details of carrier generation within the active layer must be studied. This is readily accomplished with transfer-matrix optical simulations to replicate the optical field within the device, taking into account interference between incident and reflected light from the cathode (refer to Section 4.2.2 for details on transfer matrix optical field calculations). At a 1:1 weight

ratio CuPc and C₆₀ mix homogenously¹⁰, making it suitable to approximate charge carrier generation with optical intensity.

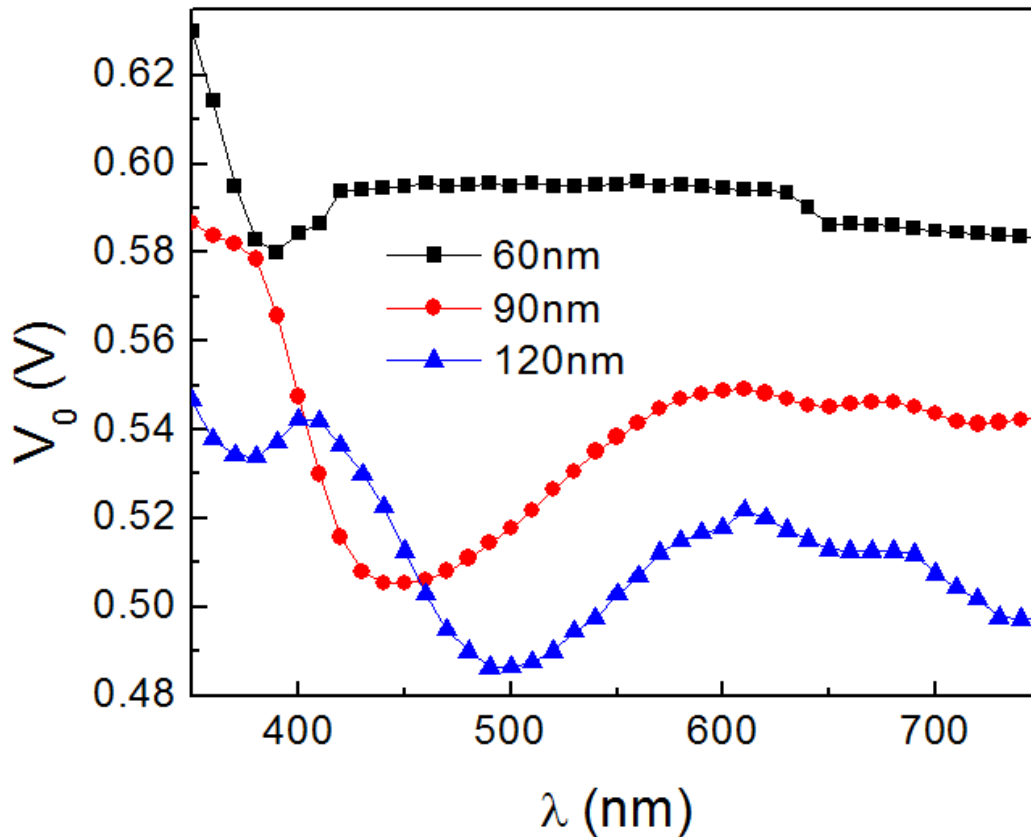


Figure 5-7. V_0 vs. wavelength for three different CuPc:C₆₀ (1:1) layer thicknesses.

Figure 5-8 shows the calculated carrier generation fields $G_j(x) = |E_j(x)|^2 \cdot \alpha_j(x)$ for three different active layer thicknesses, 60, 90, and 120 nm. Also shown is a reproduction of Figure 5-7 for comparative purposes. The weighted average centers of charge generation x_c for each wavelength are shown in white on the transfer matrix plots. The values of x_c at each wavelength show a clear relationship to the optical interference patterns formed within the active layer. Interference patterns in an OPV

result in peak intensity values at an approximate distance of $(2m + 1)\lambda/4n$ away from the reflecting metal cathode, since it is the primary reflecting surface in the system. For example, in the 90 nm-thick device, the maximum optical intensity/carrier generation at $\lambda \geq 450$ nm shifts away from the cathode with the as wavelength increases; x_c undergoes a similar shift. However, at $\lambda \leq 400$ nm, a second-order interference peak emerges proximate to the anode, shifting x_c closer to the ITO/organic interface. The average location of charge carrier generation is closest to the cathode at $\lambda \approx 440$ nm.

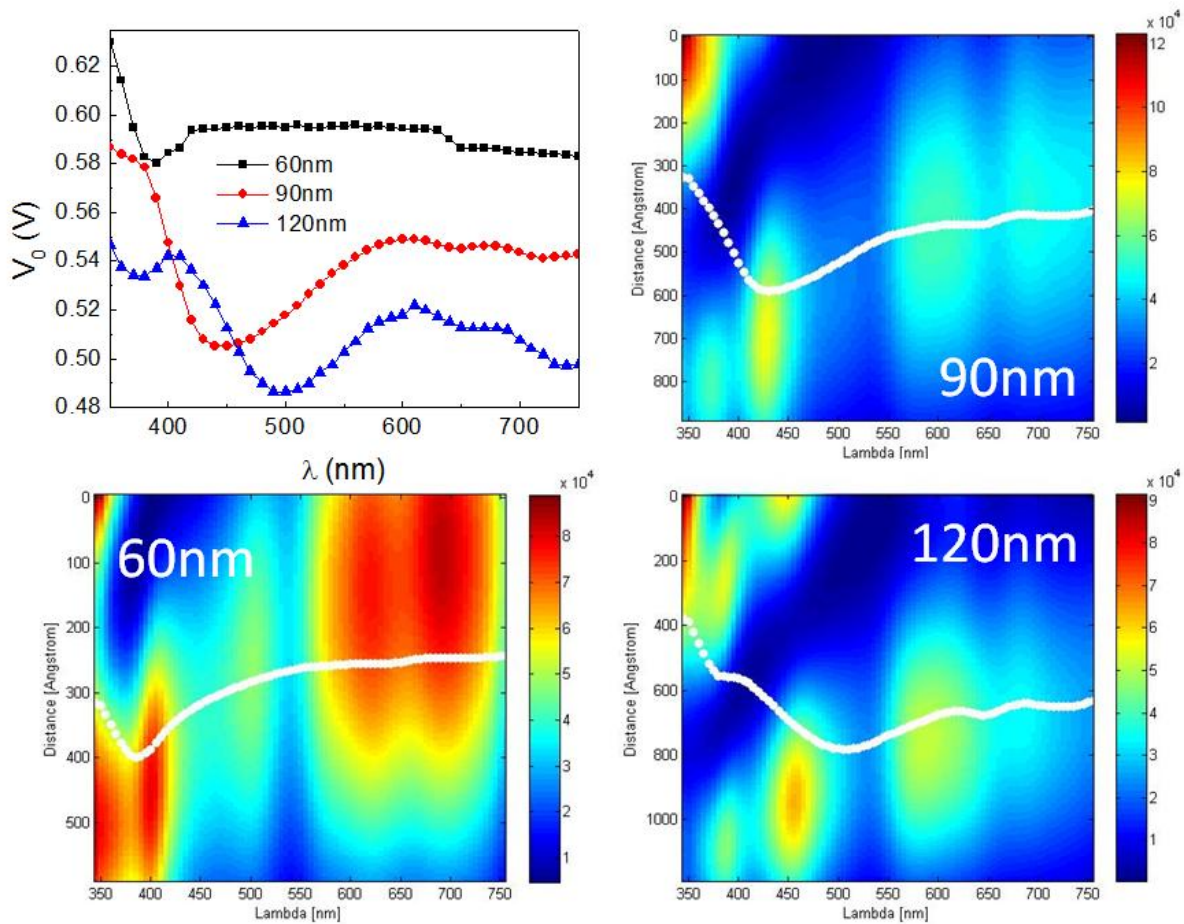


Figure 5-8. Experimental V_0 vs. wavelength data and transfer matrix-calculated charge generation fields for three different CuPc:C₆₀ (1:1) active layer thicknesses. The weighted center of charge generation is shown in white on the transfer matrix plots. The ITO/organic interface is at the top of the plots; organic/cathode is at the bottom.

The observed correlation between V_0 and x_c is attributed to the diffusion current in these devices. In a CuPc:C₆₀ (1:1) mixed film, the hole mobility ($\sim 10^{-5}$ cm²/Vs) is approximately three orders of magnitude lower than the electron mobility ($\sim 10^{-2}$ cm²/Vs)¹⁰. Therefore, charge extraction from the active layer will be limited by hole transport. When holes are generated close to the cathode, the corresponding hole diffusion current is low; holes must travel a long distance to reach the anode. Since the total diffusion current is reduced, a smaller positive drift current (and smaller forward bias) is required to reach a zero-photocurrent value. In contrast, if x_c is close to the anode, the diffusion current will be large, resulting in a larger V_0 . A comprehensive device model is needed to fully understand this relationship.

One simple verification of this model is to examine the effect of device thickness on V_0 . A thicker active layer will require charge carriers to diffuse over a longer distance for collection, reducing the diffusion component of the photocurrent. In effect, V_0 will be reduced across the entire visible spectrum. Figure 5-9 shows a plot of V_0 vs. wavelength for three different poly(3-hexylthiophene) (P3HT): [6,6]-phenyl C₆₁-butyric acid methyl ester (PCBM) (1:0.8 weight ratio) bulk heterojunction OPVs. The thickness is varied from ~ 80 nm for a 1000 rpm, 18 mg/mL device to >150 nm for a 1000 rpm, 36 mg/mL active layer.

The thicker devices show universally reduced V_0 voltages, reducing from ~ 0.82 V in a 1000 rpm, 18 mg/mL device to ~ 0.70 V in the thickest device, 1000 rpm, 36 mg/mL. These results add more support to the earlier conclusions regarding diffusion current and inversion voltage.

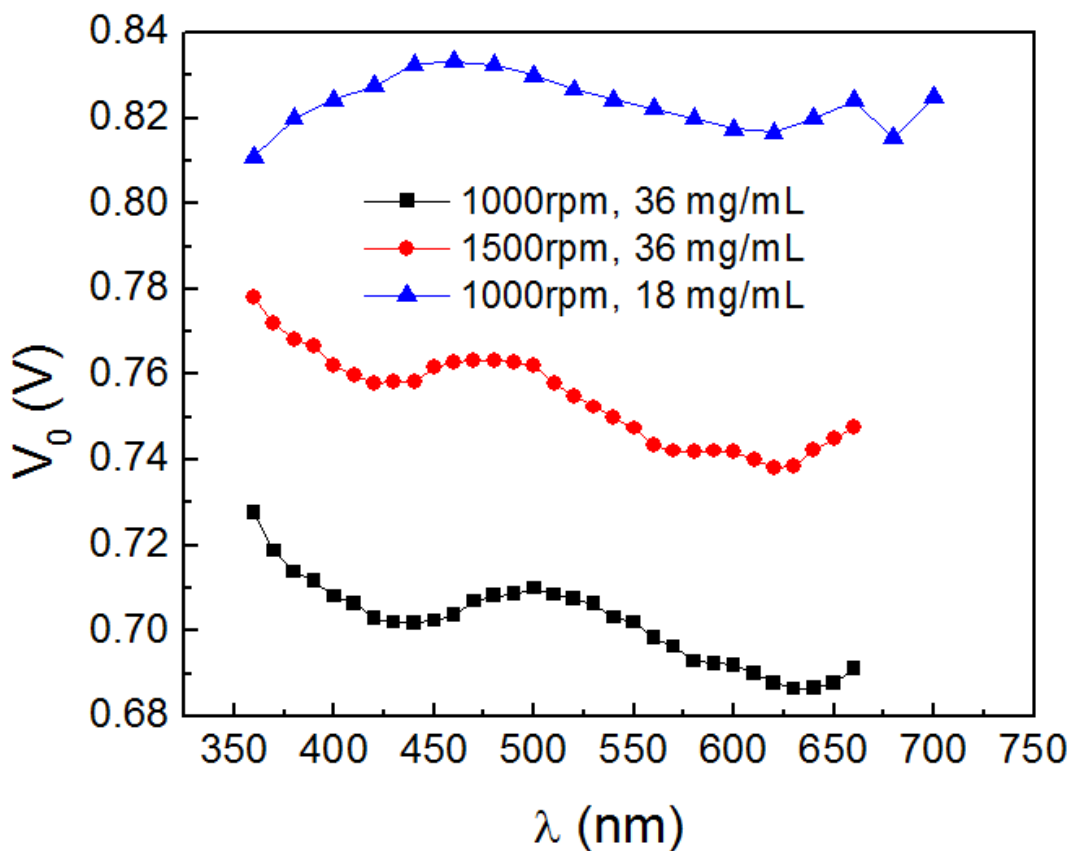


Figure 5-9. V_0 vs. wavelength for three different P3HT:PCBM devices.

5.4 Exciton Dissociation Behavior in Bilayer Organic Photovoltaics

The photocurrent behavior presented in Section 5.2 outlined the general relationship between drift and diffusion currents in typical bilayer OPV devices. In a 20 nm CuPc/40 nm C_{60} device the photocurrent remains negative up to the limits of the measurement setup (Figure 5-10A). However, increasing the CuPc donor thickness from 20 nm to 40 nm introduces inversion at some wavelengths, as shown in Figure 5-10B. Specifically, the 40 nm/40 nm device has inversion under 350, 400, 550, 600, 650, and 700 nm monochromatic light and no inversion under 450 and 500 nm illumination.

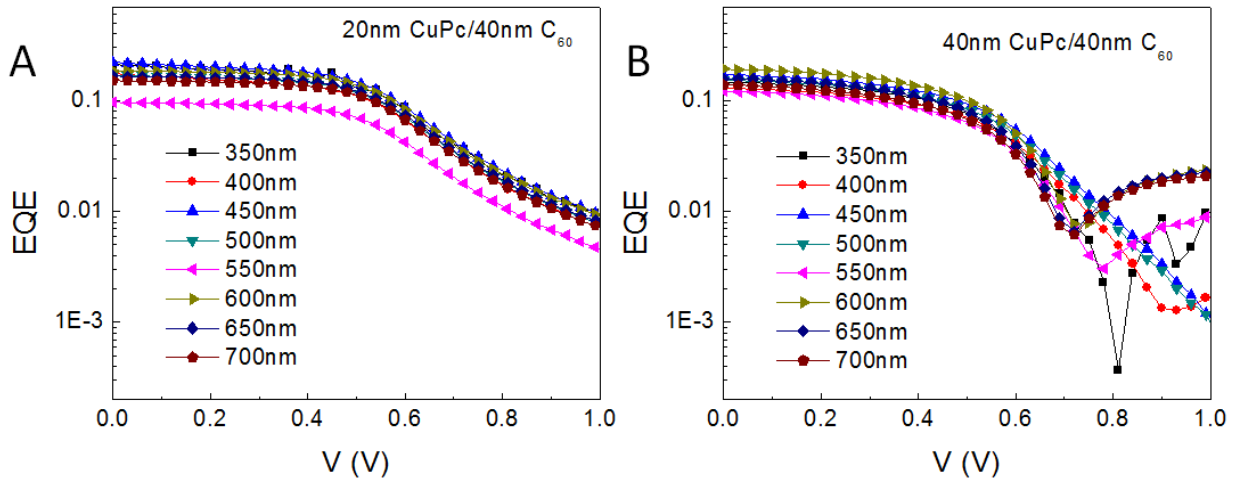


Figure 5-10. Measured photocurrent characteristics for planar heterojunction devices at different wavelengths. A) 20 nm/40 nm CuPc/C₆₀. B) 40 nm/40 nm CuPc/C₆₀.

There is no obvious correlation between the absorption spectrum of CuPc and the inversion voltages, as inversion occurs at short wavelengths in addition to 600-700 nm. Other variations in active layer thickness show different patterns of inversion. For further analysis, transfer matrix simulations were used to examine a relationship between optical absorption and inversion (and the lack thereof). The results for three different thickness combinations are shown in Figure 5-11.

The transfer matrix plots in Figure 5-11 are representative of exciton generation, not carrier generation. The weighted average centers of exciton generation are shown in white on each transfer matrix plot. Note that the experimental V_0 plots have a much wider range of inversion voltages in a single devices than the bulk heterojunction devices presented in Section 5.3. Additionally, the plateau from 450-500 nm presented in the 40 nm/40 nm device does not represent inversion. Instead, it is the voltage at

which the minimum value is observed for each wavelength; since inversion is not observed, this is the maximum voltage scanned in the system.

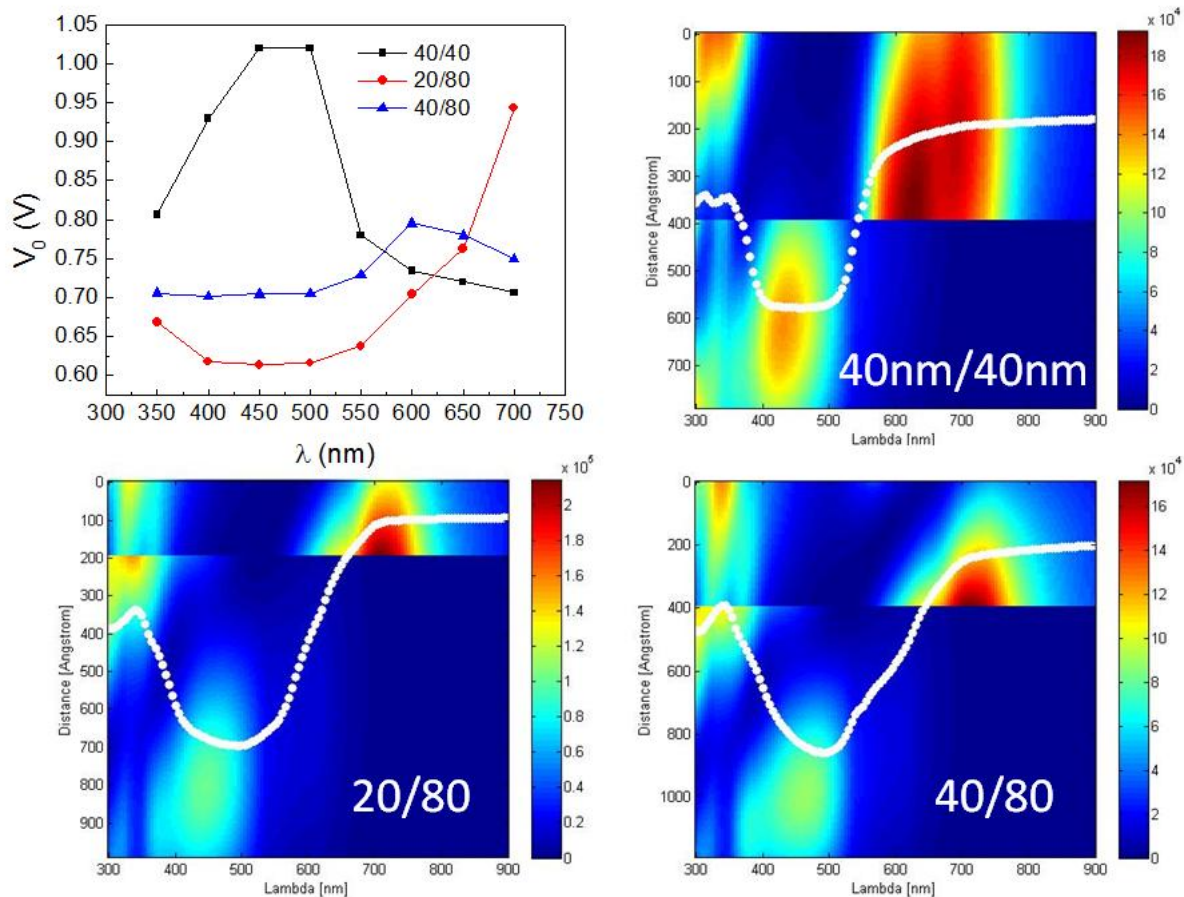


Figure 5-11. Transfer matrix optical simulations for three different bilayer devices. Also shown are experimentally calculated V_0 values. The weighted average centers of exciton generation are shown in white.

There is no clear correlation between the direct exciton generation fields and the measured inversion voltage plots, as there was for bulk heterojunction devices. Since exciton generation and diffusion occurs in distinct layers in a bilayer device as opposed to a mixed medium in a bulk heterojunction device, it is important to take the exciton diffusion length into account. The exciton diffusion length in C_{60} is much longer than in

CuPc (40 nm vs. 10 nm)^{1,66}; this is why C₆₀ layers can be thicker than phthalocyanine layers and still show decent internal quantum efficiencies. A more useful analysis is presented in Figure 5-12B, where the center of exciton generation has been adjusted to show the distance from the heterojunction interface in terms of exciton diffusion length.

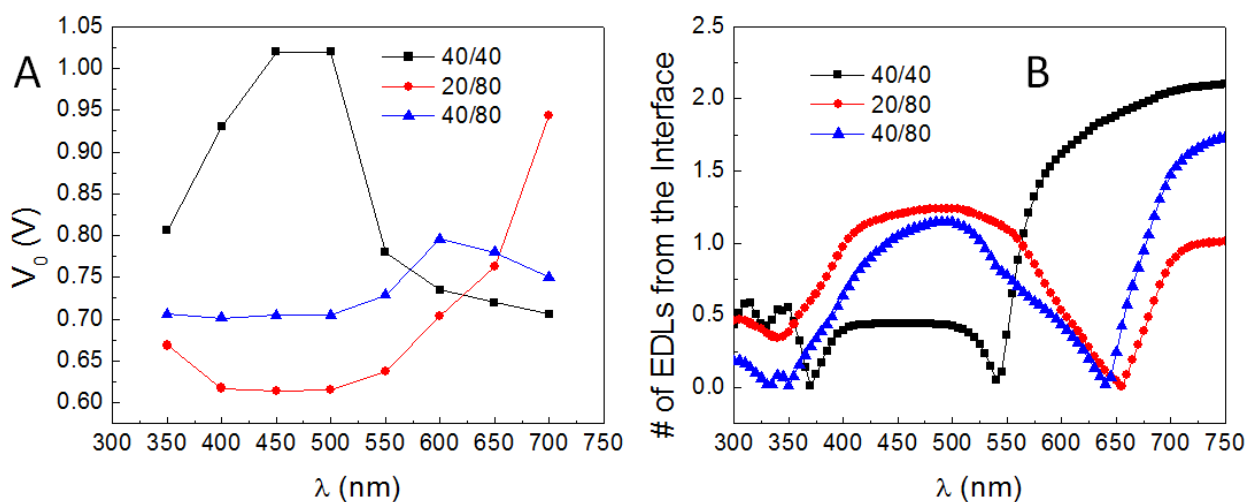


Figure 5-12. Inversion voltage and exciton generation profiles for CuPc/C₆₀ planar devices with different thicknesses. A) Experimentally measured V_0 values. B) Transfer-matrix calculated average exciton generation distance from the heterojunction interface.

A relationship emerges upon analysis of this figure in comparison to the experimental V_0 values. If excitons are on average generated close to the heterojunction interface, the inversion voltage is large, or there is no inversion. As exciton generation moves further from the interface, the inversion voltage decreases. Since the percentage of interface-dissociated excitons will increase as the average generation location moves closer to the heterojunction, there is a correlation between increased interface-dissociated excitons and increased inversion voltage.

All excitons have a chance of being dissociated by the electric field within the device, instead of at the heterojunction interface. This is generally ignored as a contributor to photocurrent, since it is an extremely inefficient and minor contributor compared to interface dissociation. However, at large forward biases the photocurrent resulting from interface dissociation will be limited to the diffusion component. This can be overcome by drift of carriers generated by field-assisted dissociation, where charges will not be blocked by the interface. The drift, diffusion, and net photocurrent for two different excitons created in the donor layer, one dissociated by the interface and one by the electric field, are diagrammed in Figure 5-13 for a device at a large forward bias.

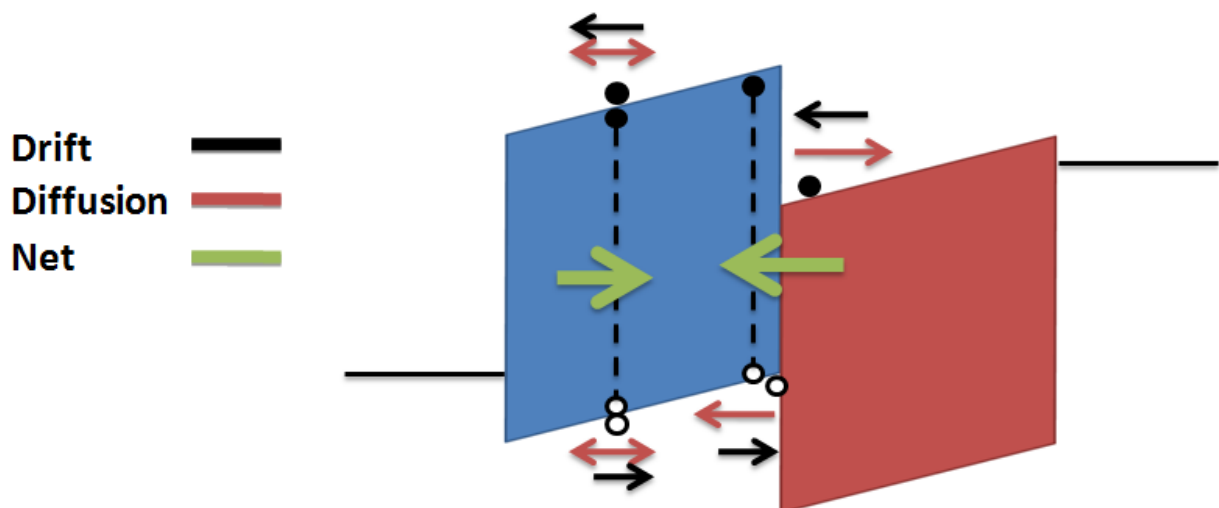


Figure 5-13. The drift, diffusion, and net photocurrent for excitons dissociated by either the interface or the electric field. The internal electric field is representative of a device at a large forward bias.

The first exciton is created close to the interface and dissociated by the heterojunction. This results in carrier pileup at the heterojunction interface and an increased diffusion current, as explained in Section 5.2. The net photocurrent from

interface dissociated excitons will be negative, but with a small magnitude due to the thicker active layers, which reduce the long-range concentration gradient.

The exciton created far from the interface has very different characteristics. When it dissociates, it will introduce a hole into the donor HOMO and an electron into the LUMO. The lack of a strong concentration gradient away from the heterojunction interface will reduce to diffusion component of photocurrent. Because the electron is no longer blocked by the heterojunction interface and has a clear path to the anode, the drift current will instead be primary component of net photocurrent from the field-dissociated exciton. Thus, the net photocurrent from the field-dissociated excitons will be positive. In this model, inversion will appear under illumination from a certain wavelength if the positive field-assisted drift current is larger than the negative interface-dissociated diffusion current.

While this model is internally consistent and agrees well with experimental results, more study is needed to quantify the significance of field-assisted exciton dissociation and its contributions of drift and diffusion photocurrent. Potential future research opportunities are discussed in Chapter 8.

5.5 Review

In this Chapter, the charge generation and transport processes in OPVs were probed to gain a better understanding of fundamental device processes. A synchronous photocurrent detection method was developed to isolate the contribution of photogenerated current at different wavelengths and applied device biases.

First, the photocurrent characteristics of thin bilayer and planar-mixed heterojunction devices were explored, and the photocurrent was found to always remain

negative. As the photocurrent results from both the drift and diffusion motion of photocarriers, a model using the relative magnitudes of these two components was developed. At small forward biases, the drift current dominates in these architectures as the built-in field sweeps charges away from the interface. When the bias is increased sufficiently and the direction of the internal electric field reverses, carriers are instead swept towards the heterojunction interface, where the large energy band offsets result in carrier pileup. The increased concentration gradient leads to an increase in the diffusion current, and the photocurrent therefore remains negative, but at a much smaller magnitude as leakage pathways create a small positive current that increases with the applied bias.

The lack of charge transport barriers in a mixed heterojunction device causes the drift current to dominate at almost all applied biases. At large forward biases, the internal electric field and drift current direction will reverse and become positive when the applied bias overcomes the built-in field. However, at a certain narrow applied bias range the internal electric field will be negligible, enabling the diffusion current to dominate. The specific voltages where photocurrent inversion occurs were found to be highly correlated to the average charge carrier generation location within the active layer, as determined using transfer matrix wave optics calculations.

Additional studies provided evidence that field-assisted exciton dissociation can be an important contributor to photocurrent under some conditions. In contrast to most bilayer heterojunction devices, where photocurrent is persistently negative, devices with thicker donor or acceptor layers display photocurrent inversion at certain wavelengths. Comparisons between the calculated optical field and measured inversion voltages

reveal a relationship between the proximity of exciton location relative to the dissociation interface and increased inversion voltage. Because there is no change in the heterojunction interface, this suggests that field-assisted exciton dissociation is introducing free charge carriers past the heterojunction interface, where they create a positive drift current.

Ultimately, the characteristics observed here require more qualitative evaluation and simulation. The insights into photocarrier behavior from this study can be used to develop and verify the results of an advanced device simulator. In Chapter 8, the basic framework of the simulator is introduced and discussed, along with a proposed implementation scheme.

CHAPTER 6 OPTICAL MANAGEMENT IN ORGANIC PHOTOVOLTAIC DEVICES

6.1 Introduction and Background

In the search for clean, renewable energy sources, photovoltaics (PVs) have emerged as a strong contender. Most of the existing PV technologies rely on inorganic active layer materials, such as crystalline silicon or III-V compound semiconductors like GaAs. While these materials have excellent power conversion efficiencies, they are prohibitively expensive for widespread adoption. Thin-film inorganic technologies like CdTe and $\text{CuIn}_x\text{Ga}_{(1-x)}\text{Se}_2$ (CIGS) are supplanting legacy technologies, but expense and mechanical robustness remain intrinsic issues with inorganic materials. OPVs offer a promising alternative. They offer mechanical durability, inexpensive, light weight modules and are compatible with economical, high-throughput production techniques. With recent power conversion efficiencies exceeding 8%, performance is close to the values for market acceptance.

Most of the efforts in increasing performance have focused on synthesizing new active layer materials, optimizing processing techniques and conditions, and developing new device architectures, little work has been expended investigating potential enhancements from manipulating the coupling of incident light into the active layer.

Regardless of the method taken, the primary goal is to ameliorate the fundamental tradeoff between light absorption and internal quantum efficiency in OPVs. The external quantum efficiency is defined by these two terms, $\eta_{EQE} = \eta_A \eta_{IQE}$. The internal quantum efficiency (IQE) itself has three subcomponents, the charge collection efficiency, charge transfer efficiency, and exciton diffusion efficiency, so $\eta_{IQE} = \eta_{ED} \eta_{CT} \eta_{CC}$.

The charge transfer efficiency η_{CT} is approximately unity in a properly designed OPV heterojunction and will not be considered further. The other two components vary with architecture. In a bilayer heterojunction, exciton diffusion efficiency η_{ED} falls off quickly with increased layer thickness. As a benefit, however, the thinner, neat layers that results have favorable charge transport properties and η_{CC} is high. A bulk heterojunction has the opposite issue – η_{ED} is considered to be unity due to the intermixing of the two materials and the resulting ubiquitous heterojunction interface; however, poor internal morphologies and phase separation disrupt charge transport and collection, decreasing η_{CC} .

In either case, the simplest method to increase IQE without altering the active layer material is to decrease layer thickness. However, this has a deleterious effect on light absorption, which can be described by the Beer-Lambert Law for a ray-optics based system,

$$\eta_A \propto 1 - \exp(-\alpha d)$$

where α is the wavelength-dependent absorption coefficient and d is the path length of light through the active layer (typically taken as the layer thickness). Given this, there are two ways to increase light absorption without increasing the active layer thickness: increase the absorption coefficient, which would require a different active layer material, or increase the path length in the layer. The first option is ultimately desirable but requires considerable time and expense for synthesis and reoptimization of processing parameters; the second can be accomplished by manipulating how light interacts with and propagates within the active layer.

There have been few reports in the literature of optical designs that accomplish this in OPVs. Among them are using prism-shaped substrates to induce total internal reflection¹³⁸, V-aligned solar cells^{135,136}, and a patterned mirror-and-lens light trap^{139,140}. While these are certainly effective methods to increase light absorption, they are incompatible with high-throughput, inexpensive processing techniques, or cannot be implemented effectively with large area, production-scale devices.

The solution presented here is a transparent microlens array (MLA) applied to the light-incident surface of the device using a soft lithographic stamping technique. When light strikes a MLA, two advantageous processes will occur (Figure 6-1).

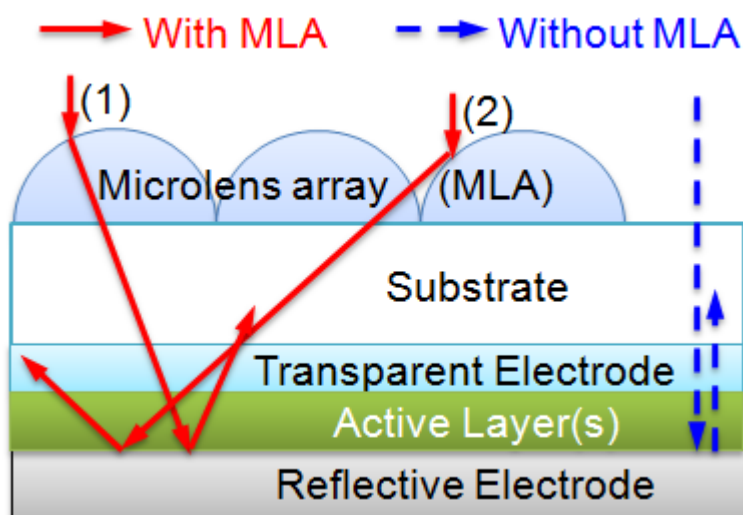


Figure 6-1. Schematic diagram of light interaction and path length through the active layer in a device with and without a microlens array (MLA). 1) Refraction of light due to the curved lens surface. 2) Reflection of incident light into a neighboring feature.

Without a MLA, the path length of light is just the layer thickness t_a for normal-incident light. Should the light not be absorbed on the first pass, it will reflect off the cathode and pass through the layer again with the same path length, and then be lost to

the device. With a MLA, the situation is greatly changed. Figure 6-1 process (1) illustrates an incident light ray refracted by the non-normal surface of the lens. The refraction will add an additional angular component to the light ray, increasing the path length to $t_a / \cos \theta$, where θ is the angle relative to the surface normal; the degree of refraction is dependent on the specific angle of impact at the lens surface.

Since the reflection coefficient will increase with the impact angle, at some angle a substantial percentage of the incident light will be reflected at the lens/air interface. The periodic structure of the microlens array becomes advantageous in this situation, as the incident light can be reflected into a neighboring feature at an angle that is now favorable for transmission (process (2), Figure 6-1). In either case, the path length has been increased and the absorption probability will accordingly rise without any changes to the active layer.

Further, because this is an optical effect based on interaction of incident light with a textured substrate, path length enhancements are present regardless of the active layer material. In the subsequent sections, the performance of small molecule, polymer, and inorganic quantum dot/polymer hybrid devices will be detailed for various architectures (Section 6.3). There are also numerous geometric effects on enhancement performance, which are probed using a ray optics simulation package (Chapter 4) in Section 6.4, along with experimental results. The effects of optical field shifts in these devices upon application of a MLA are described in Section 6.5. Finally, Section 6.6 describes device architectures and characteristics that are favorable for MLA enhancement.

6.2 Microlens Array Fabrication

Since the primary advantages of OPVs over conventional PV technology are their flexibility and inexpensive processing the MLA must be compatible with these characteristics. The MLAs fabricated for this work were produced from a poly(dimethylsiloxane) (PDMS) stamp patterned using convective-capillary self-assembly of 100 μm polystyrene microspheres. The convective-capillary self-assembly method is a low-cost, repeatable laboratory-scale technique to achieve high quality, large area (3 in²), close-packed microsphere monolayers¹⁶⁸. To form the close-packed monolayers, polystyrene microspheres in aqueous solution are dropped onto a silicon wafer. The wafer is then tilted to introduce convective flow of microspheres to the liquid-air interface. As the water evaporates, capillary forces pull the microspheres together into a hexagonal close-packed array. Other techniques to form arrays, including inkjet-printed lenses¹⁶⁹, liquid crystal droplets¹⁷⁰, the melting of self-assembled polymer microspheres¹⁷¹, and photolithographic techniques^{172,173}, either cannot make arrays of sufficient quality, are too expensive, or are incompatible with high-throughput processing..

The subsequent steps in mold fabrication are shown in Figure 6-2. After a monolayer of desired size is assembled (6-2A), PDMS precursors are added in a 10:1 weight ratio of polymer to curing agent and poured onto the monolayer. The PDMS is then thermally cured in a vacuum oven for 2 hours at $\sim 60^{\circ}\text{C}$ and the cured polymer is removed from the silicon substrate, leaving a polymer mold with the polystyrene microspheres embedded (Figure 6-2B). The spheres are removed from the PDMS surface with a scotch-tape liftoff technique, leaving behind a concave mold (Figure 6-2C). The mold fabrication process is identical to the method used in previous reports of

light outcoupling enhancements in organic light emitting diodes using microlens arrays^{174,175}.

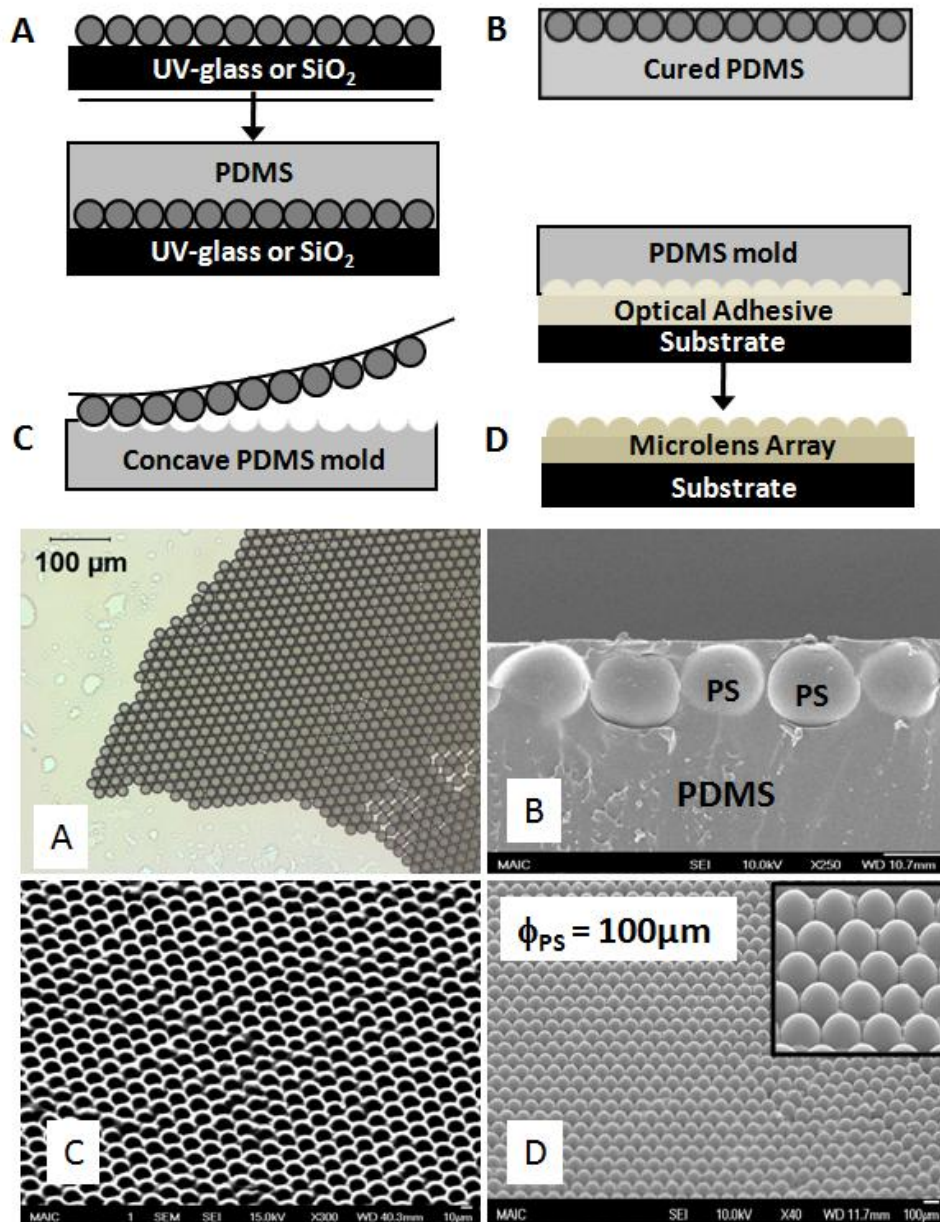


Figure 6-2. Processing steps in microlens array fabrication. A) Convective-capillary self-assembly of polystyrene microspheres and addition of poly(dimethylsiloxane) (PDMS) precursors. B) PDMS after curing, with polystyrene microspheres embedded. C) Removal of microspheres with scotch-tape liftoff, leaving behind a concave mold. D) Addition of optical adhesive to concave mold and application to substrate, and the resulting array after mold removal. Image courtesy of S.-H. Eom, parts reprinted with permission¹⁷⁴.

To form a MLA on the substrate, optical adhesive (Norland Optical Adhesive #63) is added to the mold and brought into contact with the substrate. After allowing time for the optical adhesive to spread and infill the microlens pattern (approximately three minutes), 365 nm UV light is shone through the mold for three minutes to cure the adhesive. The mold is then gently removed, leaving behind a convex array (Figure 6-2D). This process can be repeated several dozen times with a single mold before it fails due to UV-induced embrittlement and degradation. The resulting lenses have contact angles of $(85 \pm 5)^\circ$ and a high packing factor. The cured adhesive has a refractive index of ~ 1.56 , closely matched to the glass substrate, and is highly transparent past 360 nm.

The lens application procedure typically requires exposing the organic layers to UV light while the optical adhesive cures, which can induce slight degradation in photovoltaic performance. This can be circumvented for thermally evaporated devices by prefabricating arrays on the substrate prior to active layer deposition, but no satisfactory laboratory-scale workaround was found for solution-processed devices.

6.3 Enhancement Characteristics

When a MLA is added to a device there are noticeable increases in both short circuit current (J_{SC}) and power conversion efficiency (η_P), with the majority of the η_P increase attributed to enhancement in J_{SC} . There are only minor enhancements in the open circuit voltage (V_{OC}) and fill factor (FF) corresponding to a higher photocurrent relative to dark current. The current-voltage (J-V) characteristics for a thermally evaporated bilayer boron subphthalocyanine chloride (SubPc)/C₆₀ (12/40 nm) device with an 8 nm-thick BCP exciton blocking layer are shown in Figure 6-3, along with

external quantum efficiency response across the visible spectrum. Note that all devices in this study were fabricated on indium tin oxide (ITO) coated glass substrates that were successively cleaned in a solution of Tergitol surfactant, deionized water, acetone, and isopropanol, then exposed to a UV-ozone environment for 15 minutes prior to organic layer deposition.

With the MLA, J_{SC} is significantly increased from $(5.4 \pm 0.2) \text{ mA/cm}^2$ from $(4.6 \pm 0.1) \text{ mA/cm}^2$, approximately 17% enhancement. Combined with minimal increases in V_{OC} and FF , η_P also increases from $(3.1 \pm 0.1)\%$ to $(3.7 \pm 0.1)\%$, a 20% increase. The device active area is approximately 2 mm x 2 mm, and a large area 2.25 cm² rear reflector is used to simulate the geometric characteristics of a large device. Exact device areas were measured using optical microscopy. The methodology and justification for using a rear reflector is explained fully in Section 6.5.

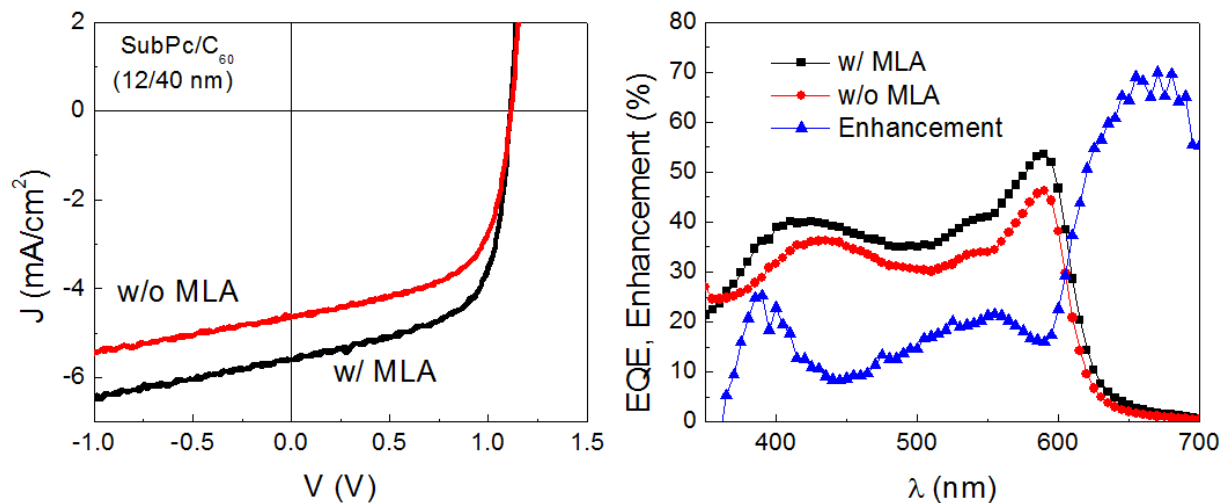


Figure 6-3. Current-voltage and external quantum efficiency characteristics of a SubPc/C₆₀ (12/40 nm) device with and without a microlens array (MLA). Relative enhancement is indicated across the visible spectrum.

Comparing the external quantum efficiency spectra of the device with and without a MLA shows that the enhancement is present across all wavelengths, though it is not constant. In general, the observed enhancement is greater in regions where absorption is relatively weak (e.g. $\lambda > 620$ nm) and smaller at wavelengths where the absorption is strong (e.g. at $\lambda \sim 575$ nm, the peak of SubPc absorption). This is in agreement with predictions from the Beer-Lambert law. For instance, a hypothetical 50% increase in the optical path length will result in only a 15% increase in η_A if 60% of the light is initially absorbed; if only 10% is absorbed initially, the increase in η_A is 46%. The reduced EQE of the device with a lens array near 350 nm is caused by absorption of the microlens material. We also observe a slight shift in the EQE spectrum with and without a lens array (most observable in the slight blueshift of the peak near 425 nm), attributed to an optical field shift within the active layer. The origin and ramifications of the optical field shift are discussed in Section 6.4.

One of the most attractive features of MLAs is that their enhancement mechanisms are universal and work with a wide variety of active layer materials. Significant enhancements have been realized for very high efficiency polymer:fullerene cells (Figure 6-4) and polymer-nanocrystal hybrid cells (Figure 6-5).

High efficiency polymer devices with an active layer of 1:1 by weight poly(benzo[1,2-b:4,5-b']dithiophene)-(5,6-difluoro-4,7-dithien-2-yl-2,1,3-benzothiadiazole) (PBnDT-DTffBT):[6,6]-phenyl-C₆₁-butyric acid methyl ester (PCBM)¹³⁷ show enhancements of η_P from $(6.2 \pm 0.3)\%$ to $(7.0 \pm 0.4)\%$, a relative increase of approximately 13%.

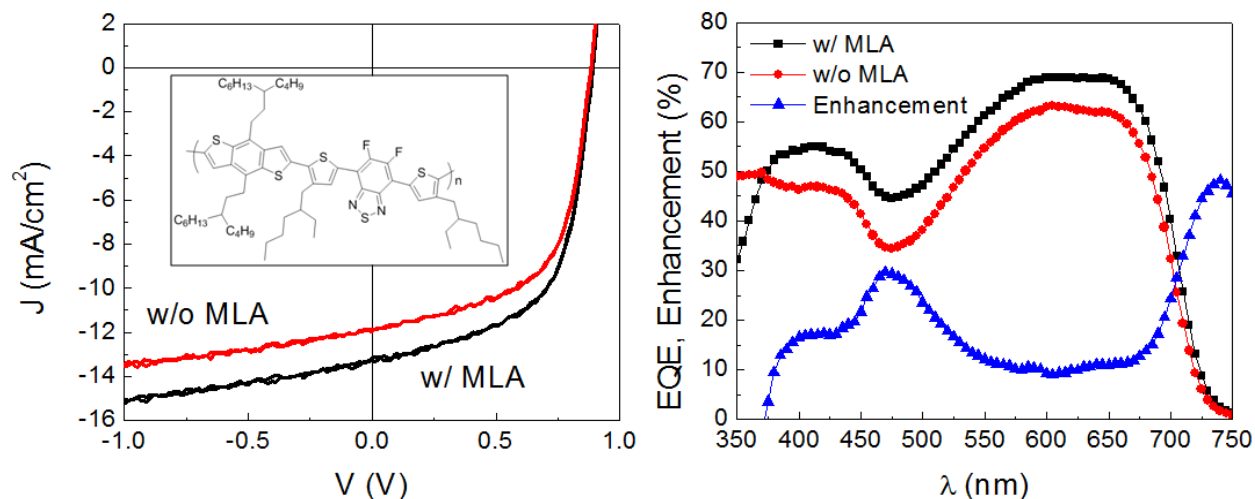


Figure 6-4. Current-voltage and quantum efficiency characteristics for a high efficiency PBnDT-DTffBT:PCBM OPV. Inset: PBnDT-DTffBT molecular structure.

As with the SubPc/C₆₀ bilayer devices, a correlation between strong EQE/absorbance and reduced enhancement is observed in the EQE spectra. PBnDT-DTffBT and PCBM were dissolved in dichlorobenzene and spin coated at ~120°C on top of a 40 nm-thick PEDOT:PSS layer, and then solvent annealed for 12 hours prior to thermal deposition of a 1 nm-thick LiF interfacial electron extraction layer and an aluminum cathode.

Hybrid PV cells with active layers consisting of the low-gap polymer poly[2,6-(4,4-bis-(2-ethylhexyl)-4H-cyclopenta[2,1-b;3,4-b']dithiophene)-alt-4,7-(2,1,3-benzothiadiazole)] (PCPDTBT) and CdSe nanoparticles^{176,177} (~7 nm diameter) in a 9:1 (by weight) ratio were spin coated from a 9:1 chloroform:pyridine solution, then annealed at 150°C for 30 minutes prior to aluminum cathode deposition. Devices with a solution-processed ZnO nanoparticle-based electron transport/optical spacing layer

show a 18% increase in η_P ; those without ZnO have a 32% increase (Figure 6-5). The ZnO was spin coated from an ethanol solution and annealed at 85°C for 15 minutes.

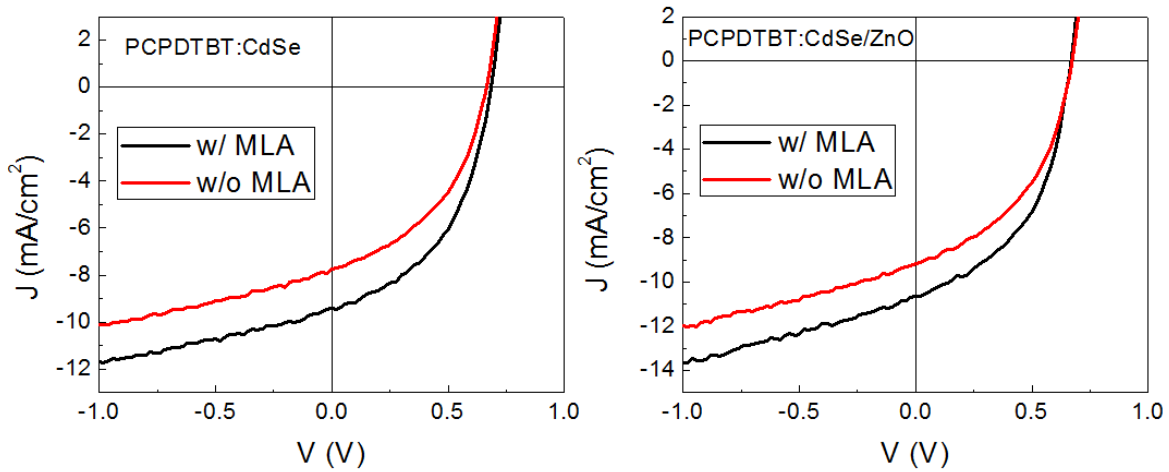


Figure 6-5. Current-voltage characteristics of hybrid PCPDTBT:CdSe polymer:inorganic nanoparticle devices with and without a ZnO optical spacing layer.

Hybrid devices are noteworthy in that their increases in η_P are substantially greater than the enhancements in J_{SC} . Devices without ZnO have a much greater enhancement in η_P due to significant increases in fill factor of $(6 \pm 1)\%$ and $(3 \pm 1)\%$ in V_{OC} . For comparison, the device without ZnO only has increases of $(3 \pm 3)\%$ in fill factor and negligible increases in V_{OC} . This is attributed to the increased dark current in devices without ZnO. The higher dark current limits FF and V_{OC} by beginning to dominate the photocurrent at lower voltages. Therefore, the increased photocurrent induced by the microlens array therefore has a greater effect on these devices than on a device that is not limited in this manner. The performance metrics for several different device architectures and active layer materials are summarized in Table 6-1.

Table 6-1. Performance characteristics for several different device architectures and active layer materials with and without microlens arrays (MLAs).

Architecture	J_{SC} (mA/cm ²)		Enhancement (%)	η_P (%)		Enhancement (%)
	w/o MLA	w/ MLA		w/o MLA	w/ MLA	
SubPc/C ₆₀ (1)	4.6 ± 0.2	5.4 ± 0.3	17	3.1 ± 0.2	3.7 ± 0.2	19
SubPc /C ₆₀ (2)	1.5 ± 0.1	2.3 ± 0.1	53	0.9 ± 0.1	1.4 ± 0.1	56
P3HT:PCBM (1)	9.2 ± 0.5	10.5 ± 0.5	14	3.4 ± 0.2	3.9 ± 0.2	15
P3HT:PCBM (2)	5.9 ± 0.3	7.4 ± 0.4	25	1.9 ± 0.1	2.4 ± 0.1	26
PCPDTBT:CdSe (1)	9.1 ± 0.5	10.3 ± 0.5	13	2.8 ± 0.1	3.3 ± 0.2	18
PCPDTBT:CdSe (2)	7.5 ± 0.4	9.0 ± 0.5	20	2.2 ± 0.1	2.9 ± 0.2	32
PBnDT-DTffBT:PCBM	11.8 ± 0.6	13.1 ± 0.7	11	6.2 ± 0.3	7.0 ± 0.4	13

SubPc/C₆₀ (1): 12 nm SubPc/40 nm C₆₀
 SubPc/C₆₀ (2): 12 nm SubPc/80 nm C₆₀
 P3HT:PCBM (1): 100 nm mixed layer thickness, no ZnO optical spacing
 P3HT:PCBM (2): 100 nm mixed layer thickness, 45 nm ZnO
 PCPDTBT:CdSe (1): 85 nm mixed layer thickness, 20 nm ZnO
 PCPDTBT:CdSe (2): 85 nm mixed layer thickness, no ZnO
 PBnDT-DTffBT:PCBM: 140 nm mixed layer thickness.

6.4 Optical Field Optimization

6.4.1 Bilayer Heterojunction Devices

It was noted in the previous section that the EQE spectrum of a SubPc/C₆₀ bilayer OPV exhibits a slight blueshift at shorter wavelengths in addition to the expected increases from MLA-enhanced absorption. This is consistent with changing optical interference patterns within the device active layer.

Under normal illumination, regions of high optical intensity will emerge at distances of $(2m+1)\lambda/4n$ away from the cathode/organic interface, where $m = 0, 1, 2, \dots$ is the integer order of interference between the incoming wave and the reflected wave off of the cathode. The location of the intensity peak is related to the phase shift that the

reflected wave undergoes as it travels through the organic layers. Each layer therefore has a certain phase thickness, defined as

$$t_{\psi} = \frac{2\pi d_i \tilde{n}_i \cos \theta_i}{\lambda}$$

where \tilde{n}_i is the complex refractive index of the layer θ_i is the angle of wave propagation through the layer, d_i is the layer thickness, and λ is the wavelength of light. Therefore, if the angle of incidence is increased, the phase shift is correspondingly altered and the locations of constructive and destructive interference will move further away from the cathode. This effect can be modeled using transfer-matrix optical simulations¹⁵⁷ by making the key assumption that the MLA-refracted light can be modeled as non-normal incidence light on a series of planar layers.

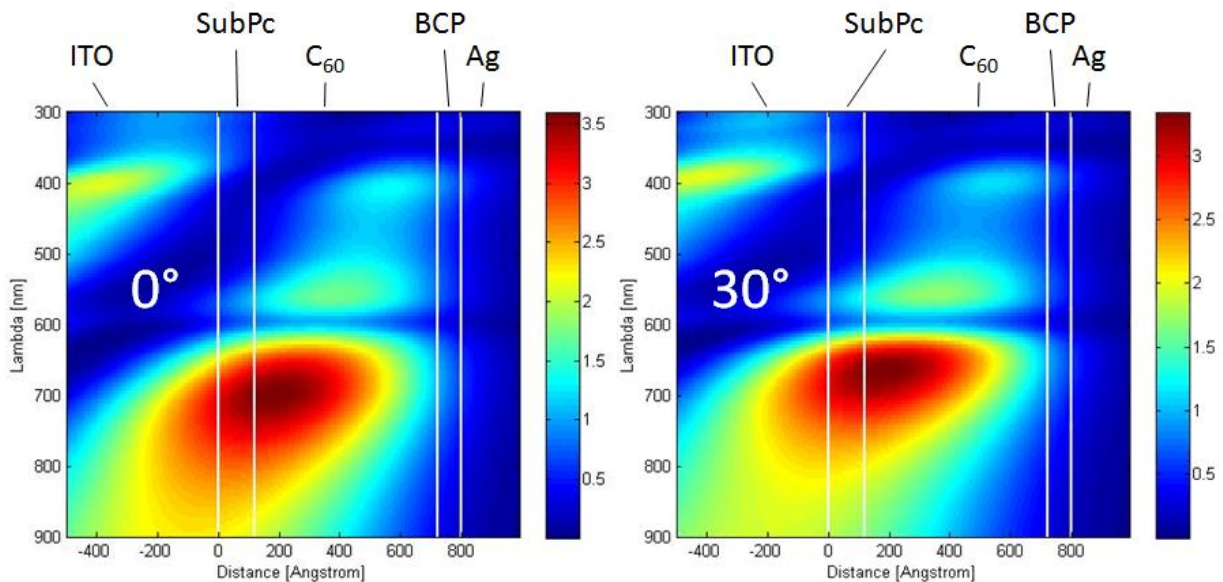


Figure 6-6. Calculated optical fields for SubPc/C₆₀ (12/60 nm) OPVs at normal (0°) and 30° incidence.

Figure 6-6 shows the calculated optical field intensities within a SubPc/C₆₀ (12/60 nm) bilayer OPV for normal (0°) and 30° incidence. The effects of the phase thickness

shift are most observable in the altered intensity profile at $\lambda > 700$ nm and the intensity tail bleeding into the SubPc layer at $\lambda \approx 575$ nm with 30° incidence.

Since 60 nm is larger than the optimized C_{60} thickness (40 nm) for SubPc devices, shifting the 575 nm high intensity region into the SubPc layer has significant ramifications, as the maximum SubPc absorption occurs in this wavelength region. This suggests that the optimum device thickness for a device under normal illumination is not necessarily the optimum thickness for a device with a MLA.

The optical field shift has a significant effect on bilayer devices, where carrier generation can be highly dependent on the location of optical intensity peaks relative to the heterojunction interface, especially as strongly-absorbed wavelengths are moved in and out of a layer. Figure 6-7 shows this situation for a SubPc/ C_{60} device (12 nm/y nm), where the C_{60} thickness is varied to serve as an optical spacing layer. When the device has a thinner C_{60} layer, relative enhancements in J_{SC} and η_P are less than a device with a thicker layer. For example, a 40 nm C_{60} layer has an enhancement of 19% in η_P ; this rises to 56% when the C_{60} thickness is increased to 80 nm. With an 80nm thick active layer, the optical field within the SubPc layer under normal incidence is not optimized – specifically, the SubPc absorption maximum at 575 nm is still predominantly within the C_{60} layer. By adding the MLA and inducing the optical field shift, this intensity region is pushed into the SubPc region, greatly increasing the photocurrent generation from that layer. The inset of Figure 6-7 shows the transfer matrix-calculated EQE response within the SubPc layer at normal (0°) and 30° incidence. The optical field shift in this case is extremely favorable, significantly increasing response near the SubPc absorption peak.

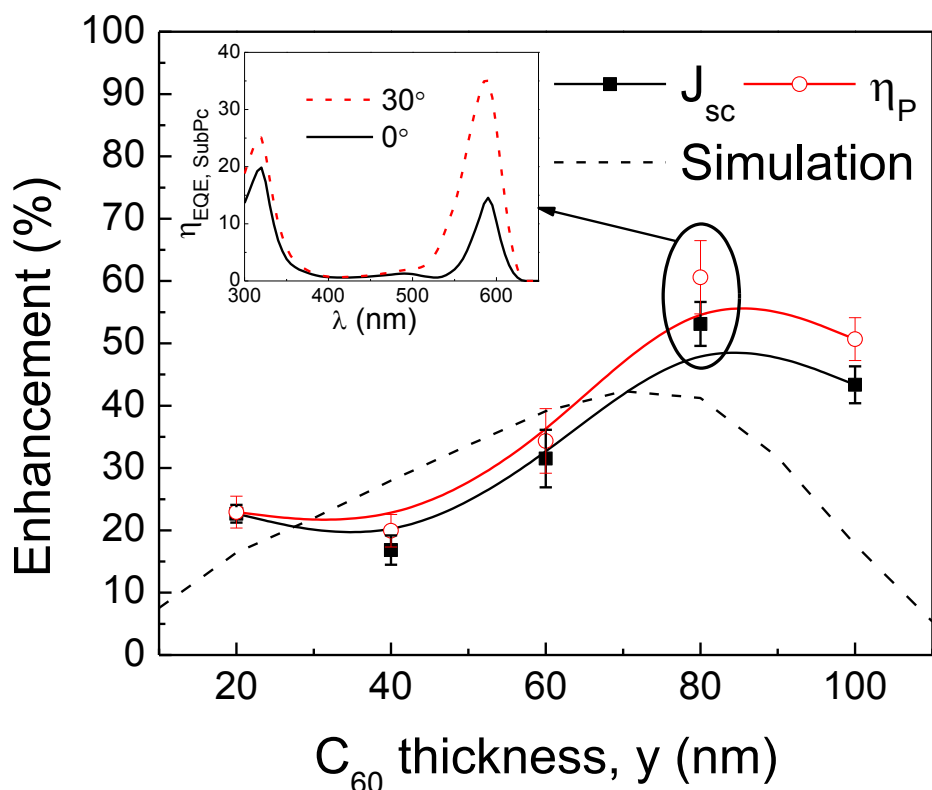


Figure 6-7. Effect of varied C_{60} thickness on J_{SC} and η_P enhancement for a SubPc/ C_{60} (12/ y nm) device with and without a microlens array. The results of transfer matrix simulations are also shown. Inset: calculated quantum efficiency response within the SubPc layer for $y = 80$ nm at normal (0°) and 30° incidence, showing the effect of the optical field shift.

Figure 6-7 also shows calculated enhancements in short-circuit current using transfer matrix simulations; these are in general agreement with the experimental data. To obtain qualitatively significant data the calculated currents for several different incident angles must be averaged together, as a MLA does not equally refract all light to a single incident angle. Monte Carlo ray optics simulations were used to obtain a proper angular distribution.

The details of the ray optics simulator are explained in Chapter 4. To determine the angular distribution, SubPc: C_{60} (1:4 by weight) active layers of various thicknesses

were simulated with 90° contact angle, 100 μm lens arrays. The device, lens array, and illumination areas were treated as infinite by applying periodic boundary conditions. Mixed films were used in place of bilayer SubPc/C₆₀ films for computational simplicity. To correlate results, the total active layer thicknesses were compared (i.e. 20 nm SubPc:C₆₀ is comparable to 12 nm SubPc/10 nm C₆₀). Whenever a ray is absorbed its path length through the active layer is recorded; the incident angle was back-calculated from the ratio of path length to film thickness. Figure 6-8 shows the incident angle distributions for absorbed rays in thin (20 nm) and thick (120 nm) SubPc:C₆₀ devices.

The results follow expectations from the Beer-Lambert law. For a very thin device, the proportion of light absorbed with an increased path length will be more significant. In a thicker device, a substantial percentage of light with no angular component will already be absorbed, making the relative contributions at with longer path lengths less significant.

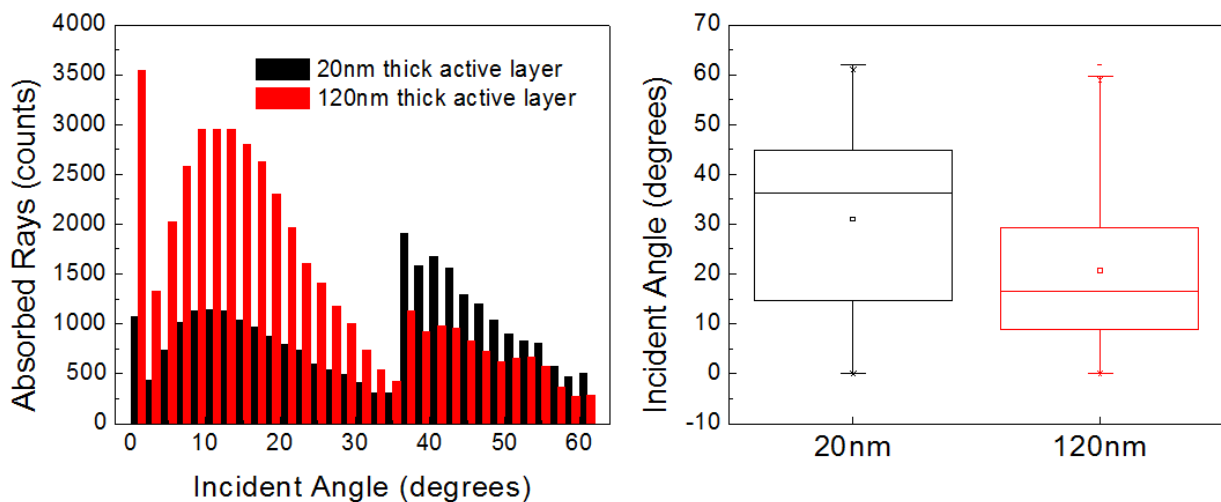


Figure 6-8. Distributions of light incident angle upon the active layer in SubPc:C₆₀ (1:4 by weight) films calculated by ray optics simulations.

From these results, the relative contributions for rays sorted into five different angle bins (with bin centers of 9.6°, 22.4°, 35.2°, 48°, and 60.8°) are calculated and used to weight the short-circuit current values calculated using transfer matrix simulations. While this is an adequate method to approximate the relative enhancements with and without a MLA using the transfer matrix method, a more rigorous implementation is needed for full quantitative simulations.

While the relative enhancements increase with C_{60} thickness due to the favorable optical shift, the total efficiency does not. Because a thicker C_{60} layer will also reduce η_{ED} and η_{CC} , the optimum C_{60} thickness with a MLA remains at the same value as that of a bare device, 40 nm (Figure 6-9). A dedicated electron transport/optical spacing layer could circumvent this issue.

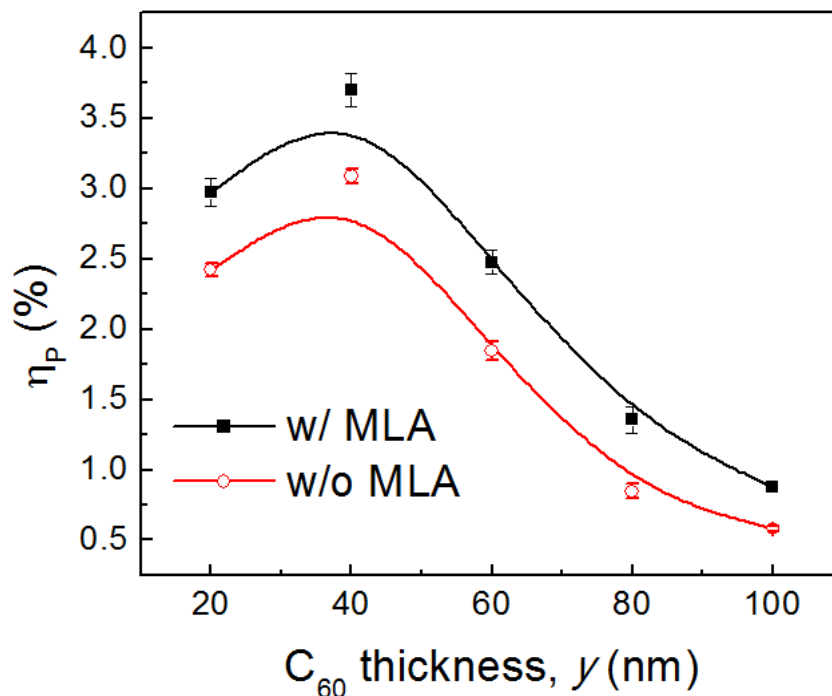


Figure 6-9. Power conversion efficiency η_p for SubPc/ C_{60} (12/ γ nm) with and without a microlens array (MLA).

6.4.2 Bulk Heterojunction Devices

The optical field shift has a different impact on bulk heterojunction devices, where exciton dissociation is not limited to a single plane within the active layer. Instead, the shift can move optical intensity peaks out of the active layer entirely, negating any benefit from enhanced path length. For example, the enhancements in a poly(3-hexylthiophene (P3HT):PCBM (1:0.8 by weight) device with varying active layer thicknesses show two distinct trends, depending on whether the device is semi-transparent (and therefore removed from the optical interference effect) or conventional, with a reflecting metal cathode (Figure 6-10).

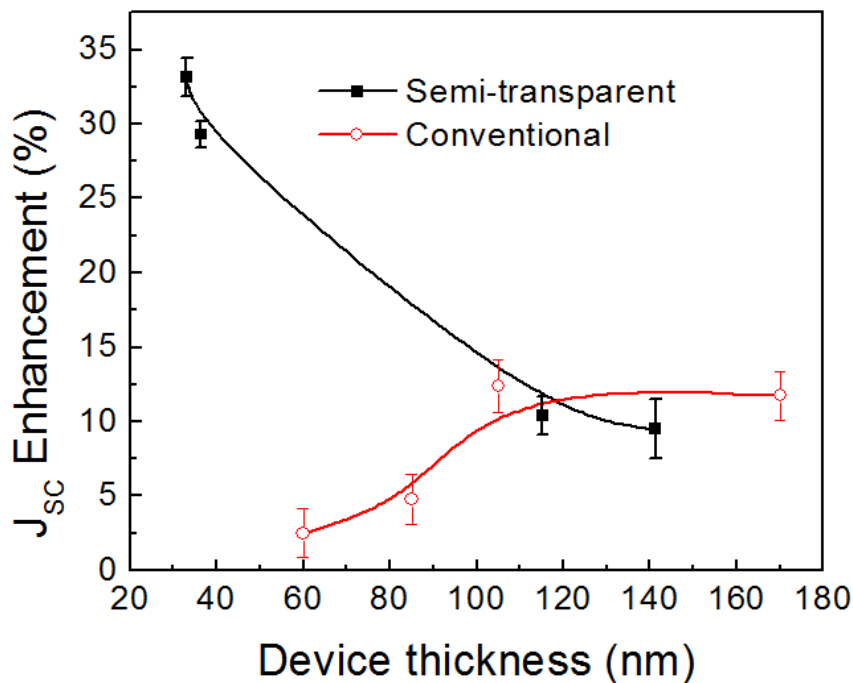


Figure 6-10. Short-circuit current enhancements for P3HT:PCBM bulk heterojunction devices with and without a microlens array. Conventional devices have a reflecting metal cathode; semi-transparent devices have a cathode of ITO/ZnO and a vacuum-deposited trilayer anode of MoO₃/Au/MoO₃.

The conventional device has an anode of tin-doped indium oxide (ITO) and a vacuum-deposited aluminum cathode. The semi-transparent device, however, has an electron-selective cathode of ITO/ZnO nanoparticles and a vacuum-deposited anodic trilayer electrode^{178,179} of MoO₃/Au/MoO₃ (3/10/40 nm). An aluminum-coated piece of glass is attached to the top of the semi-transparent device with optical adhesive to still give a reflecting back surface, but as the reflecting surface's location is removed from the active layer, strong interference patterns will not emerge and govern the optical field within the device. Instead, ray optics approximations are appropriate. In both cases, the P3HT:PCBM active layer was spun coat from a 1:0.8 (by weight) chlorobenzene solution and annealed inside a nitrogen-filled glovebox.

The measured enhancement for the semi-transparent device therefore closely follows predictions from the Beer-Lambert law, that the increase in path length is exponentially more significant as the active layer thickness decreases. A 140 nm-thick device has current enhancements of ~10%, while an active layer thickness less than 35 nm yields enhancements above 30%.

In a conventional device, the opposite is true – enhancement monotonically decreases with the active layer thickness. In a thin device, the optical shift introduced by the MLA begins to move strongly absorbed wavelengths out of the active layer, negating any additional benefit from increased path length. Enhancements vary from ~12% for a 170 nm-thick device to a negligible 3% with a 60 nm-thick active layer.

As with the bilayer device, however, the optical field shift can be understood and compensated for to increase enhancements. In this case, a solution-processed ZnO nanoparticle^{177,180-182} layer can be added as an electron transport/optical spacing layer

between the cathode and the active layer, decoupling layer thickness and position within the optical field. Now, the optical field shift can have one of two effects, based on ZnO thickness. First, (considering only the first order interference peaks) it can shift short wavelength intensity peaks out of the ZnO layer and into the active layer. Second, longer wavelength peaks can be moved out of the active layer.

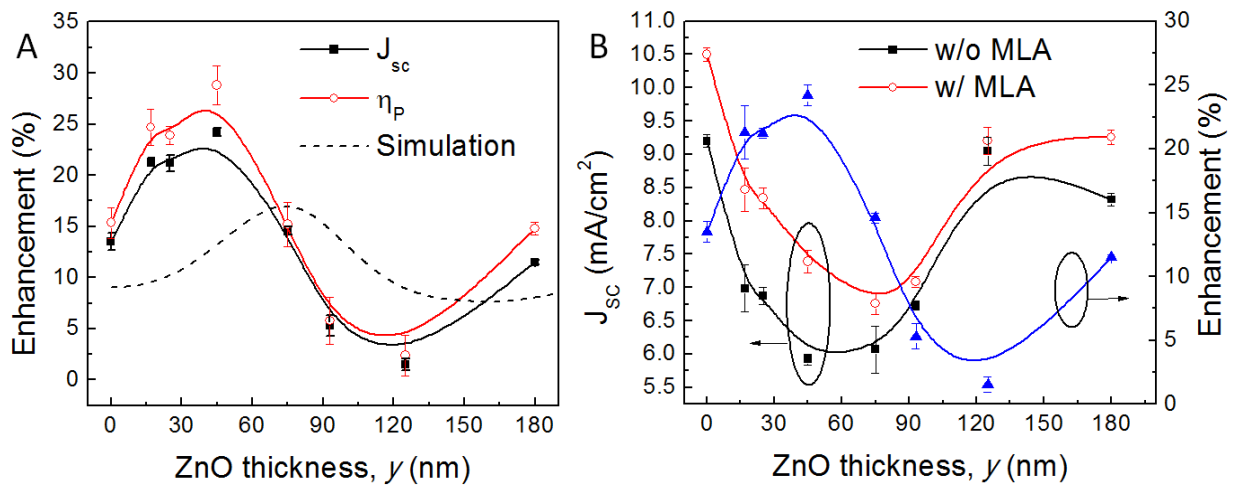


Figure 6-11. Effect of ZnO optical spacer thickness on mixed P3HT:PCBM devices. A) Enhancements in short-circuit current and power conversion efficiency for P3HT:PCBM/ZnO (100/ γ nm) devices. The transfer matrix-calculated enhancements are also shown. B) Comparison of short-circuit current with and without a microlens array and the relative enhancement.

When the ZnO thickness in a P3HT:PCBM is varied, a periodic oscillation of J_{sc} emerges, roughly following the spacing of optical intensity peaks (Figure 6-11B). Starting with an optimized P3HT:PCBM layer thickness of 100 nm, the highest observed values of J_{sc} are present for ZnO thicknesses γ of 0 and ~130 nm, which corresponds well to the expected spacing between the first and second optical intensity peaks for $\lambda = 500$ nm, in the middle of the P3HT:PCBM absorption region according to the $(2m+1)\lambda/4n$ relationship (assuming $n = 1.8$, the first intensity peak occurs ~70 nm away

from the cathode). The minimum in optical intensity will occur between the intensity peaks, i.e. at ~105 nm away from the cathode, explaining the observed minimum in J_{SC} with a 45 nm thick ZnO optical spacer (the experimentally measured maxima and minima will vary from the calculation due to the wide band of P3HT:PCBM absorption).

The relative enhancements in J_{SC} and η_P (Figure 6-11A) also vary according to the optical intensity profile. The greatest enhancement is observed when the optical intensity within the active area is weak ($y = 45$ nm) and the optical field shift works positively, moving high intensity regions into the active layer; J_{SC} is increased by ~24%. Conversely, a negligible enhancement of ~1% is measured when the optical field is already favorable for device performance ($y = 130$ nm) and the optical field shift moves strongly absorbed intensity regions out of the active area. When there is no ZnO ($y = 0$) enhancements are still modest at ~13% in J_{SC} , as the high intensity regions are not completely shifted out of the active layer. The transfer matrix-calculated enhancement values in Figure 6-11A are in very rough qualitative agreement with experiment, first showing increased enhancement and then reducing as ZnO thickness increases, but the experimentally observed characteristics are not effectively reproduced. This underscores the need for more rigorous modeling to fully understand and exploit the optical shift.

6.5 Geometric Effects

Microlens arrays introduce several dependencies on the geometric relationship between the illumination, device, and lens array areas. These effects arise because the arrays diverge light in a periodic pattern over the illumination area. The even dispersion creates the favorable characteristic that enhancements increase with device area as

loss mechanisms reduce. The effect of device area on J_{SC} enhancement for SubPc/C₆₀ (12/60 nm) bilayer devices is shown in Figure 6-12 for both large area illumination and device area illumination.

Considering a device where the illumination area is equal to the device area, a portion of light near the edge of the device is refracted and diverted outside of the active area. With small, laboratory scale devices, the perimeter length is relatively long compared to the total device area and a large proportion of incident light will be lost. As the device active area becomes larger, the proportion of light lost around the edges decreases accordingly.

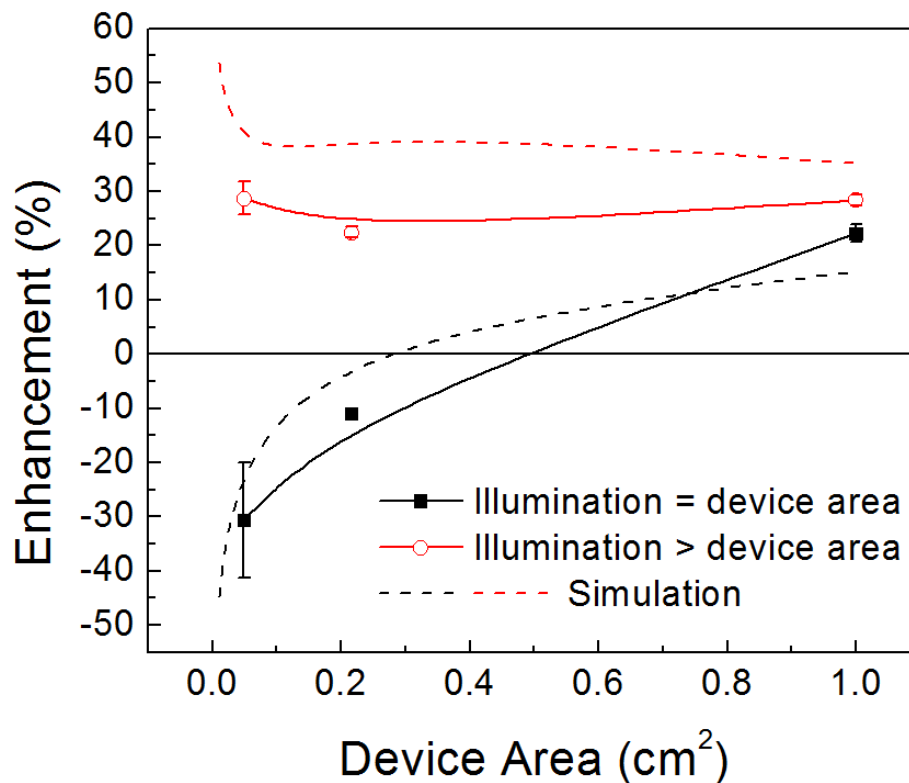


Figure 6-12. Effect of device active area on relative enhancement with SubPc/C₆₀ (12 nm/60 nm) devices. Devices were either illuminated with a beam ~2" in diameter (large area illumination) or masked off so only the active area was exposed to light (device area illumination). Ray optics-simulated absorption enhancement in a 70 nm SubPc:C₆₀ (1:4) device is included.

Extending the concept, an infinitely large device would not exhibit this effect. Lost light can be partially compensated for by making the illumination area larger than the device area, where light can be incoupled from outside of the device area.

This effect has important ramifications for production-scale devices. In the laboratory, device areas are typically kept small for ease of fabrication and characterization. Commercial devices, however, need to be as large as possible to maximize power generation and minimize module cost. Any optical enhancement technique should accordingly be compatible with large areas, as MLAs are.

Also shown in Figure 6-12 are calculated absorption enhancements using Monte Carlo ray optics simulations (simulation methodology is described in Chapter 4) for large (20 mm x 20 mm) and device area illumination with a lens array area of 100 mm x 100 mm. The simulated enhancements agree very well with experimental results, both qualitatively and quantitatively. For this reason, studies of lens geometry and relative array, device, and illumination areas were simulated rather than performed experimentally.

The first point of investigation is the relationship between device area and illumination area. Figure 6-13A shows the relative absorption enhancements for two simulated 70 nm SubPc:C₆₀ (1:4) devices with either 1 mm² or 1 cm² active areas. The illumination area was varied in each case, and the enhancement is plotted as a function of the device area to illumination area ratio. The array width was set at 100 times the device width in each case to mimic completely isolated devices. When the device area is small, there is a significant increase in enhancement when the illumination area is changed from one to four times the device area, rising from a decrease in absorption of

80% to no enhancement. Increasing the illumination area to 100 times the device area gives an absorption enhancement of 25%.

For the large 1 cm² device, there is a much more gradual increase in enhancement as the illumination area changes, rising from 11% for equal device and illumination areas to 48% when the illumination-to-device area ratio is 100. This underscores the importance of perimeter loss for different device sizes. Since the smaller device has much more significant leakage around the device edge, compensation by increasing the illumination area has a much more significant effect.

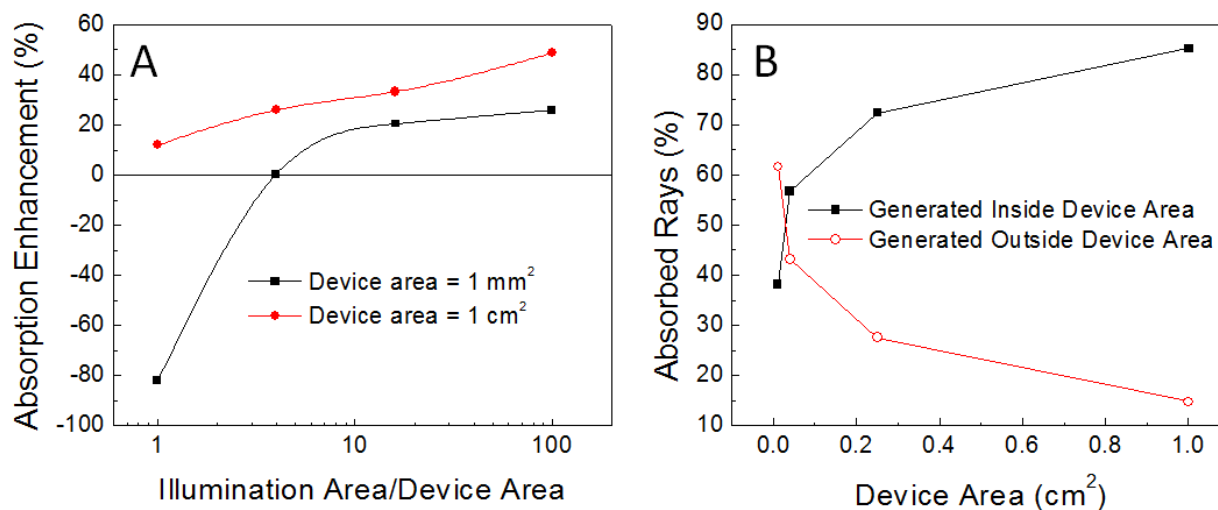


Figure 6-13. Simulation results of different geometric arrangements. A) Absorption enhancement vs. device area/illumination area for SubPc:C₆₀ (1:4 by weight, 70 nm active layer thickness) devices of either 1 mm² or 1 cm² device area. B) Percentage of absorbed rays sorted by generation location for different device sizes (illumination area = 20 mm x 20 mm, array area = 100 mm x 100 mm).

The perimeter effect can also be examined by comparing the generation locations of absorbed rays as a function of device area (Figure 6-13B). When the device area is small (1 mm²), less than 40% of the absorbed rays are initially generated outside of the

device area, demonstrating how significant light leakage around the device perimeter is with a small area device. As the device area increases, the percentage of intra-device generated absorbed rays increases monotonically to ~85% in a 1 cm² device. The behavior as area increases closely follows the experimental data in Figure 6-12, indicating that light leakage is the primary loss mechanism.

Because the enhancements of small area devices are compromised by light leakage, the experimental results presented in Section 6.3 and Section 6.4 are small area devices with a large area aluminum rear reflector to mimic the geometric arrangement of a large area device. The reflector is insulated from the cathode by a ~100 nm-thick spin coated layer of Cytop fluoropolymer; the Cytop layer is cured in a high vacuum environment prior to aluminum deposition. This situation is analogous to sampling a 2 mm x 2 mm area in a 2.25 cm² device.

The amount of reflecting area around a device has a marked impact on enhancement. This can be readily simulated by enforcing and varying periodic boundary conditions (PBCs) in the ray optics simulations. When PBCs are enforced, a box defined as the main simulation area is effectively surrounded by identical imaginary boxes on all borders. Should a ray exit from one side of box, and identical ray is created to enter from the opposite side, as if it came from a neighboring box. For these simulations, the periodic boundary area is taken as the array (or substrate) area.

In Figure 6-14, the device and illumination areas are held constant at 1 cm² and the array area (periodic boundary area) is varied to simulate an array of devices with various packing densities. When the array area and device area are the same size, the device area is effectively infinite since no light can be lost due to transmission through

the substrate (the cathode covers the entire simulated substrate area); calculated absorption enhancement is ~50% for a SubPc:C₆₀ (1:4, 70 nm) device. Enhancement falls exponentially with increasing device spacing, eventually decreasing to 15% with a device-to-device spacing of 180 mm. This has important implications for commercial photovoltaic modules, which are comprised of large arrays of smaller devices. With a sufficiently close-packed array, enhancements can approach the theoretical limit for an infinitely large device.

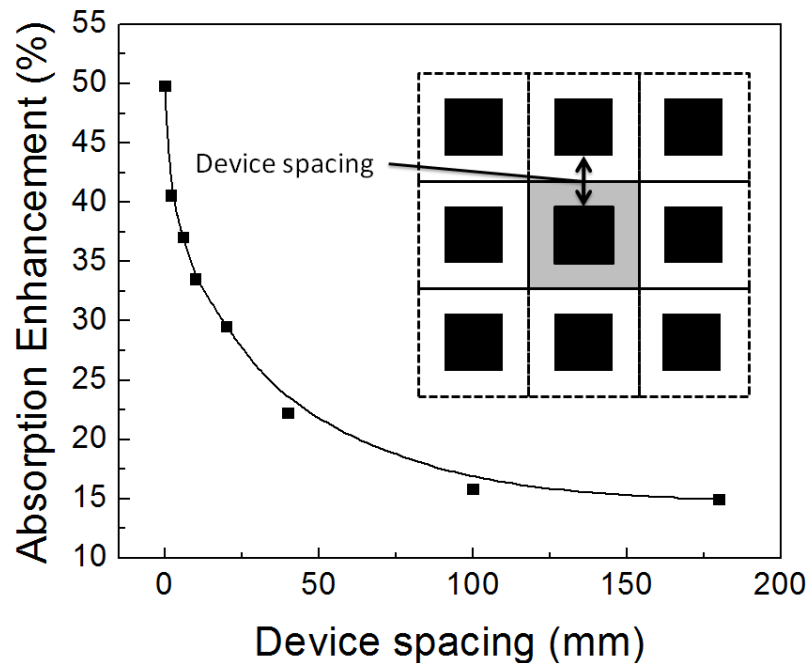


Figure 6-14. Effect of device spacing on simulated absorption enhancement in a 70 nm-thick SubPc:C₆₀ (1:4) device. Periodic boundary conditions are enforced with a variable periodic area to mimic device arrays with different device packing densities.

Independent of the relative sizes of the device, illumination, and substrate areas, the microlens geometry itself can affect the degree of enhancement. The two identified enhancement mechanisms, refraction and reflection, will be dominant at different

locations on the lens surface, based on the probability of transmission (considering only the initial ray-lens interaction for normally-incident light). Near the crown of the lens, the incident angle will be low enough to still have a high probability of transmission; refraction will dominate in this region. As the incident angle increases (i.e. as the intersection point moves from the crown to the base of the lens), reflection becomes a more significant component. By varying the contact angle θ of the simulated lens array (Figure 6-15) the relationship between incident angle and surface reflection can be probed.

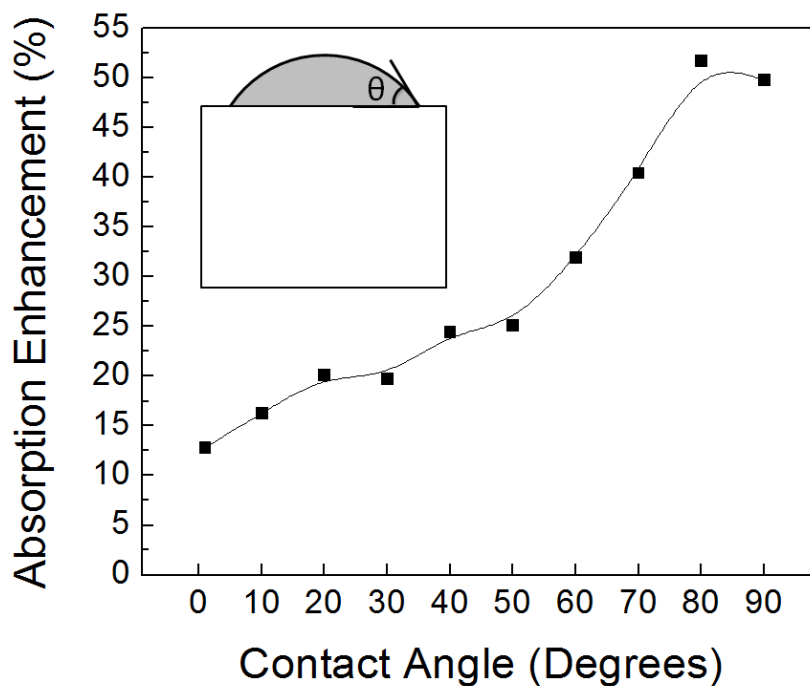


Figure 6-15. Effect of contact angle variations on simulated enhancements in 70 nm-thick SubPc:C₆₀ (1:4) films. Devices are treated as infinite using periodic boundary conditions.

The device, illumination, and substrate areas are treated as infinite in these simulations to isolate the effect of lens geometry on enhancement. Further, the MLA is

close-packed regardless of the contact angle, so the same non-planar surface is available in all cases. As shown in Figure 6-15, the simulated absorption enhancement in 70 nm-thick SubPc:C₆₀ (1:4) films decreases with the contact angle. The decrease is not strictly monotonic, however. The highest calculated enhancement of ~52% is obtained for $\theta = 80^\circ$. In a microlens with $\theta = 90^\circ$, rays incident near the lens base have an extremely high probability of reflection, but as the incident and reflection angles are equal, the path length increase will be negligible. When the contact angle is reduced slightly to 80° , these reflected rays will have a more significant angular deflection, increasing absorption enhancement. As the contact angle reduces further, the reflection mechanism first reduces due to a reduction in surface area that will allow a reflected ray to strike a neighboring feature; below $\theta = 45^\circ$ this mechanism does not occur. At smaller contact angles the degree of refraction of incident rays is decreased. Eventually, a close-packed array with $\theta = 1^\circ$ demonstrates an enhancement of only 12%.

Finally, an important performance metric for any optical enhancement technology is its performance versus the incident angle of illumination, as the solar illumination angle varies through the day for a photovoltaic module without a solar tracking system. Since OPVs are intended as a low-cost PV solution, expensive solar tracking systems are not desirable. To test the behavior of MLAs under variable illumination angle, 1 cm² SubPc/C₆₀ (12/40 nm) were fabricated and illuminated under uniform, ~5 mW/cm² white light. Two different illumination areas were considered: illumination area > device area (Figure 6-16A) and illumination area = device area (6-16B).

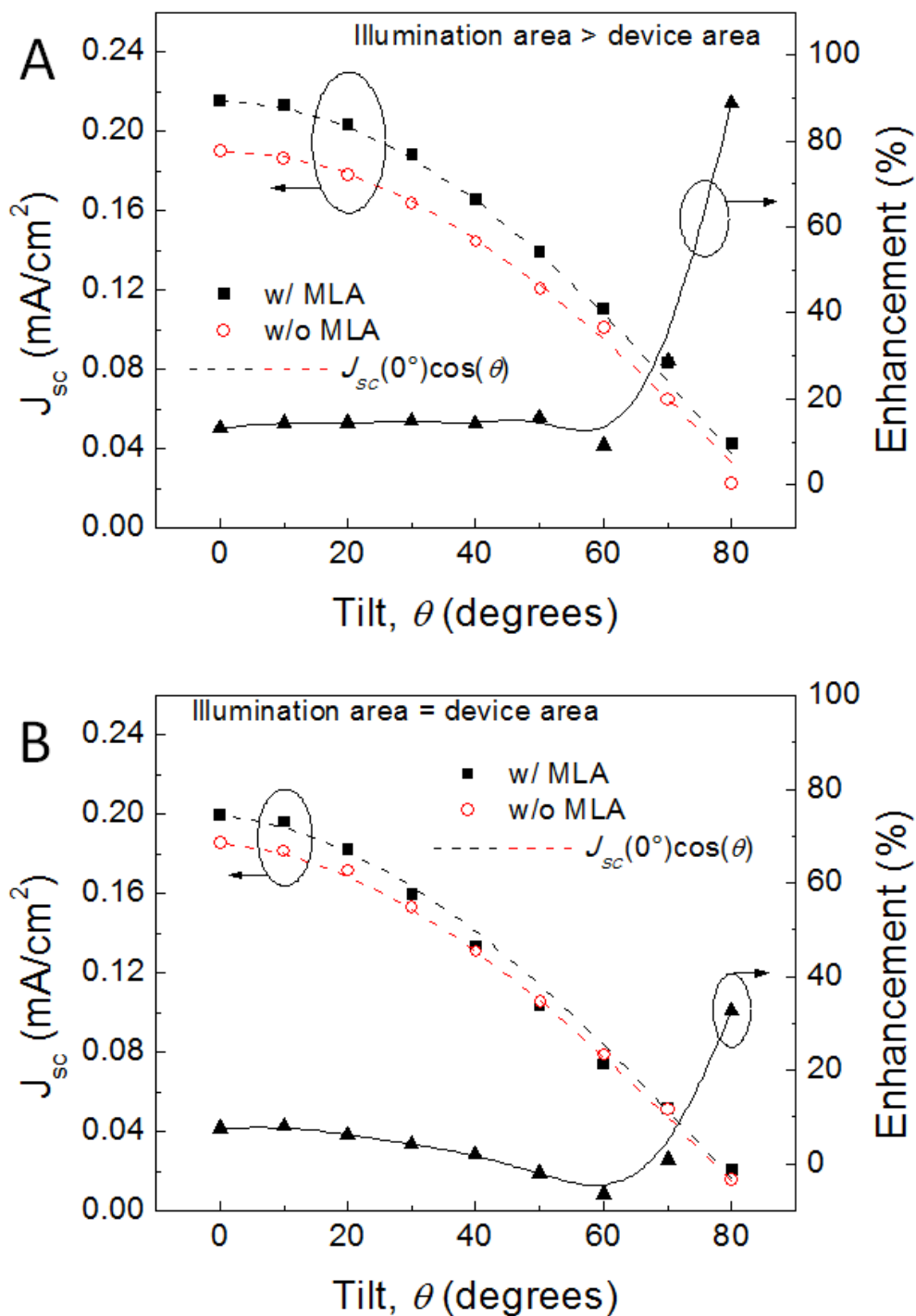


Figure 6-16. Performance of 1 cm² SubPc/C₆₀ (12/40 nm) devices under 5 mW/cm² white light illumination with a variable incident angle. A) Illumination area greater than device area. B) Illumination area equal to device area. Relative enhancements with and without a microlens array (MLA) are shown. Dashed lines are $\cos\theta$ predictions.

When the illumination area is much greater than the device area, there is a monotonic decrease in J_{SC} as the tilt angle θ is increased, closely following a predicted $J_{SC}(\theta) = J_{SC}(0^\circ) \cos \theta$ relationship. This suggests compensation between increased surface reflectivity and increased path length through the active layer due to angled illumination, allowing the change in illumination intensity to dominate. The relationship deviates at high angles for a device without a MLA as surface reflection dominates. With a MLA, the measured J_{SC} outperforms the $\cos \theta$ dependence. Enhancements are mostly constant for $\theta < 50^\circ$. However, it sharply increases from $\sim 15\%$ (when $\theta < 60^\circ$) to $\sim 90\%$ at $\theta = 80^\circ$. The drastic increase in enhancement for large incident angles is attributed to the curved microlens surface. The reflectivity of light in this region is highly sensitive to the exact incident angle. Consequently, the small changes in the surface normal due to lens curvature have a significant impact on the reflection probability and the MLAs reduce the reflection of very high angle incident light.

When the illumination and device areas are equal, the predicted $\cos \theta$ relationship is adjusted to account for the increase in shadowed device area and the same trends in J_{SC} reduction are observed. The relative enhancement behavior differs, however. It steadily decreases until $\theta = 60^\circ$, after which it increases sharply to $\sim 35\%$ at $\theta = 80^\circ$. The monotonic enhancement decrease when $\theta < 60^\circ$ is a byproduct of light leakage around the device perimeter, which will increase relative to a bare device with the increasing illumination angle. When the illumination area is much larger than the device area, the extra light lost is compensated by incoupling more light from outside of the active area.

6.6 Ideal Architectures for Enhancement

After testing several different architectures and active layer materials, general guidelines can be set forth for suitable candidate systems for microlens enhancement. Microlens arrays enhance the photocurrent generated by a device, allowing for either a larger J_{SC} or an equivalent J_{SC} with thinner device layers, which can have a beneficial effect on fill factor and reduced material usage when compared to a bare device of a set thickness. Additionally, the device must be limited by light absorption, as a device that already absorbs a substantial portion of the incident light will not benefit from additional path length.

An ideal material system will therefore have a relatively low J_{SC} and large V_{OC} . For example, SubPc/C₆₀, with V_{OC} in excess of 1.1 V and small baseline J_{SC} of 4.6 mA/cm² for an optimized device, fits this pattern and shows significant enhancement of ~20% in η_P for a 12 nm/40 nm system. Material systems that are constrained with low fill factors and open circuit voltages due to high dark currents can also have significant enhancements in these regions from the improved photocurrent component. The hybrid PCPDTBT:CdSe system (without ZnO) exemplifies this, with enhancement in J_{SC} of 20% and η_P enhancement of 32%.

Given these enhancement characteristics, tandem organic photovoltaic devices could be ideally suited for microlens arrays. These devices have high open circuit voltages and can be designed to capture different portions of the solar spectrum in the front and back cells, creating wide spectral regions suitable for absorption enhancement. Further, the carrier recombination zone can serve as a built-in optical spacing layer that can be tuned to exploit the optical field shift. There are significant

challenges in optimizing the optical field in a tandem device, however. Additional experiments must be performed to determine the suitability of MLAs for tandem devices.

6.7 Review

In this Chapter, soft-lithographically stamped microlens arrays were demonstrated to enhance power conversion efficiency enhancements of 10-60%. Enhancement is due to an increase in the average path length that light travels through the active layer, increasing the absorption probability without having to increase the active layer thickness, change the materials, or implement a more complicated heterojunction architecture. The path length is increased by refraction and reflection processes at the array-air interface due to the curved, periodic nature of the arrays.

Because the enhancement is due to light interaction with the air/substrate interface, it is applicable to all organic material systems. Small molecule, high efficiency polymer:fullerene, and hybrid inorganic nanoparticle/organic polymer systems all show enhancements. Dependencies of enhancement on the internal optical field intensity distribution were revealed and exploited to further increase enhancement by altering layer thicknesses and using optical spacers.

Further, Monte Carlo-based ray optics simulations were used to understand the geometric dependence of microlens array enhancements on device packing density, active area, and illumination area; enhancement increases with all of these. Finally, general guidelines were described for devices that are well-suited to enhancement from MLAs: high V_{OC} , low J_{SC} , and low dark current.

Because MLAs were demonstrated to have several properties that align with commercial device requirements: enhancement increases with area, it is present at all

incident angles, and soft lithography is compatible with roll-to-roll processing. For this reason, steps should be taken to complete development and commercialize this technology. In Chapter 8, several necessary steps and suggestions for further development are presented.

CHAPTER 7
BIFUNCTIONAL ORGANIC OPTOELECTRONIC DEVICES

7.1 Fundamentals of Organic Bifunctional Devices

One of the great advantages of organic semiconducting materials is their versatility. One niche application of this is a device that can function as either an OPV or an OLED based on operating conditions, dubbed here as a bifunctional organic optoelectronic device, or BFD. A BFD with respectable performance in both operating modes would have many different applications, but this has yet to be achieved.

Examples of BFDs in the literature have been sparse¹⁸³⁻¹⁹⁰, but two different trends have emerged, with device design either based off of an OPV or OLED architecture. Generally, an OLED-based BFD has respectable light emission performance but poor photovoltaic efficiency (typically only under UV illumination)^{186,187}. OPV-based BFDs are the opposite^{185,191}. This is due to the opposing operation principles of these two processes (Figure 7-1).

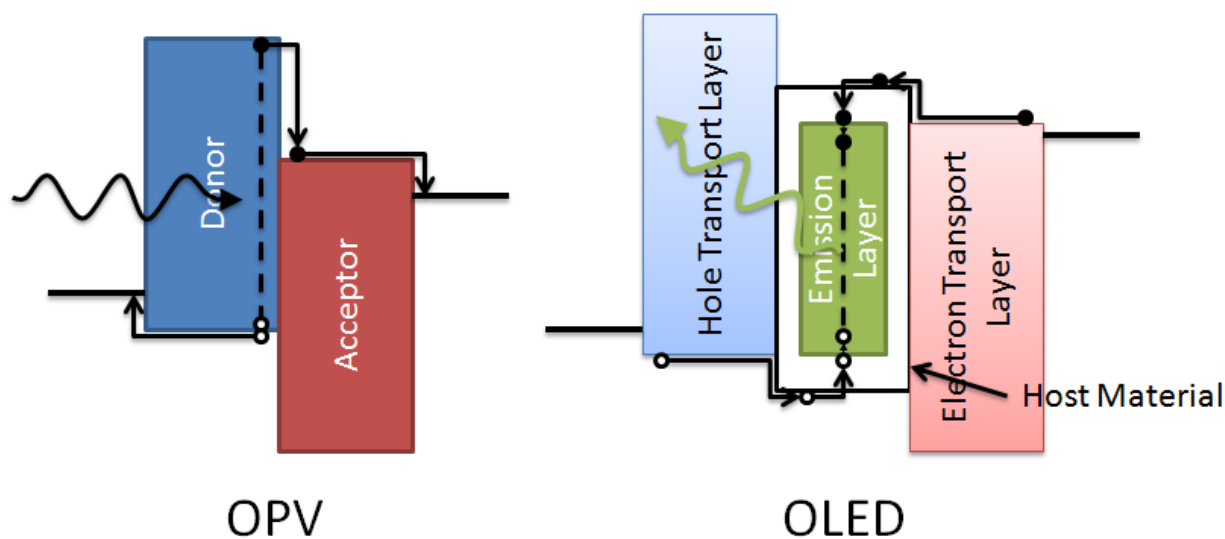


Figure 7-1. Basic OPVs and OLEDs device architectures, with charge carrier behavior diagrammed.

OLEDs are designed to efficiently move charge carriers from the electrodes into the interior of the device, where they recombine in an emitting layer. Conversely, OPVs are intended to efficiently quench photogenerated excitons in the interior of the device and move charge carriers to the electrodes without transport barriers. This is the primary tradeoff that must be overcome in BFDs to have appreciably efficient operation in both modes.

A promising architecture based on a 5,6,11,12-tetraphenylanthracene (rubrene)/C₆₀ heterojunction has been previously presented by Pandey and Nunzi¹⁸⁵. They report a large open circuit voltage of ~0.9 V (consistent with other bilayer rubrene/C₆₀ OPVs⁸⁴) and respectable photovoltaic performance. OLED efficiency was poor, but the turn-on voltage was ~1 V, half of the optical gap of the fluorescent rubrene emitting layer.

This architecture functions as a BFD for three reasons. First, there is no barrier to charge carrier extraction from the rubrene/C₆₀ interface, giving high OPV power conversion efficiency. Second, the rubrene/C₆₀ heterojunction can efficiently dissociate C₆₀ excitons, but cannot dissociate rubrene excitons. Thus, luminescence excitons are not immediately quenched after formation near the interface. Third, there is an Auger-assisted energy up-conversion process (Figure 7-2) that occurs at the interface, enabling electrons to overcome the large energy offset between the C₆₀ and rubrene LUMOs. This is responsible for the half-gap turn-on voltage. The Auger up-conversion process has also been observed in other organic and hybrid inorganic nanoparticle/organic polymer systems^{182,192}. There are three processes that can describe the Auger-assisted injection process for light emission:

1. Non-radiative recombination of an electron (in C_{60}) and a hole (in rubrene) across the heterojunction interface.
2. Transfer of the recombination energy to an electron in C_{60} , and excitation of that electron over the rubrene/ C_{60} energy barrier.
3. Recombination and light emission in rubrene.

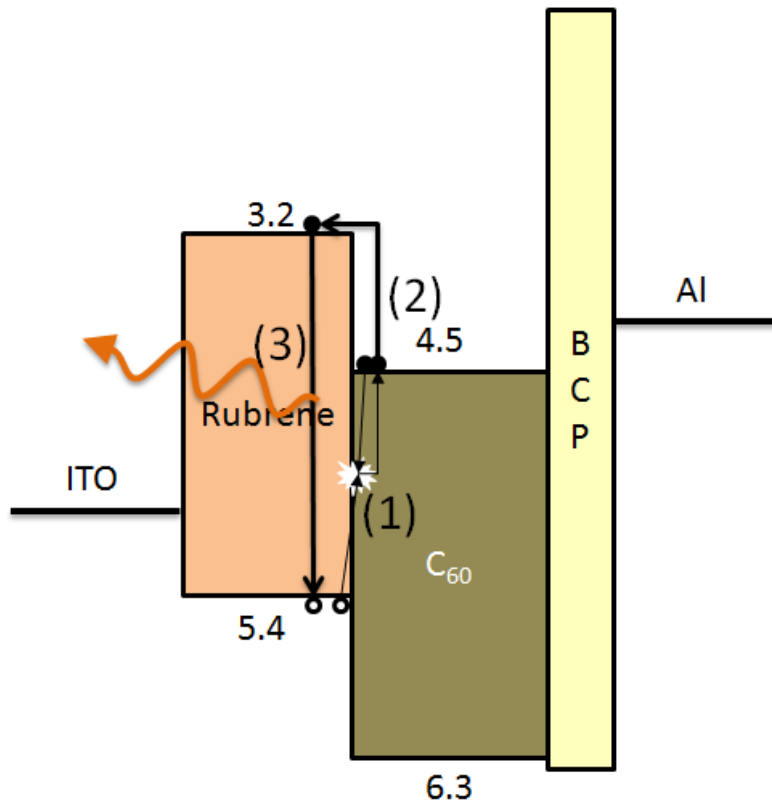


Figure 7-2. Auger up-conversion process for half-gap electroluminescence in rubrene/ C_{60} BFDs, with HOMO and LUMO energy levels indicated. 1) Non-radiative recombination across the interface. 2) Energy transfer to and excitation of an electron in C_{60} . 3) Recombination and light emission.

Without the up-conversion process, prohibitively large voltages would be required to excite electrons into the rubrene LUMO. Unfortunately, Auger recombination is an extremely inefficient excitation method. At best, half of the injected charge carriers are wasted in non-radiative recombination; in actuality, a larger percentage will be lost.

The rubrene/C₆₀ system has many opportunities for optimization to improve emissive efficiency while still maintaining respectable photovoltaic performance. This architecture was chosen as the starting point to increase total BFD efficiency.

7.2 Novel Device Architectures for Phosphorescent Bifunctional Devices

The large energy barrier to electron injection in a rubrene/C₆₀ BFD means that this will be limiting factor in OLED performance. Therefore, either the injection barrier must be lowered or more efficient use of whatever electrons are injected through the Auger process must be made. The former approach requires a change in the emissive/donor material, acceptor, or both. Because the rubrene/C₆₀ architecture already has several beneficial exciton energy properties and respectable performance as an OPV, this route was not taken. Instead, several different architectures and material systems were investigated to improve control of the BFD emissive properties and increase performance. Improved OLED performance was ultimately not realized, but greater control and understanding of exciton behavior in BFD devices was obtained.

There are several possible avenues to more efficiently use excitons in the donor/light emitting layer. First, rubrene is a fluorescent material and has inherently low emission efficiency; replacing it with a phosphorescent emitter should increase performance. Second, there is a possibility that electrons are traveling through the rubrene layer and escaping into the ITO anode before they form excitons.

The latter assumption can be quickly tested. Patterned indium tin oxide substrates were cleaned in successive baths of surfactant, deionized water, acetone and isopropanol, and then dried under a nitrogen flow. The substrates were then treated by UV-generated ozone, then a 40 nm-thick layer of poly(3, 4-

ethylenedioxythiophene):poly(styrenesulfonate) (PEDOT:PSS) was spin coated in air and annealed for 10 minutes at 140°C. Then, the substrate was placed in a high vacuum thermal evaporator and a 10 nm-thick electron blocking layer of N, N'-bis(naphthalen-1-yl)-N,N'-bis(phenyl)-benzidine (NPB), a 35 nm-thick rubrene emissive layer, a 40 nm-thick C₆₀ acceptor, a 8 nm-thick bathocuproine (BCP) exciton blocking layer, and an aluminum cathode were deposited (Figure 7-3A). Note that all other devices in this section were also thermally evaporated.

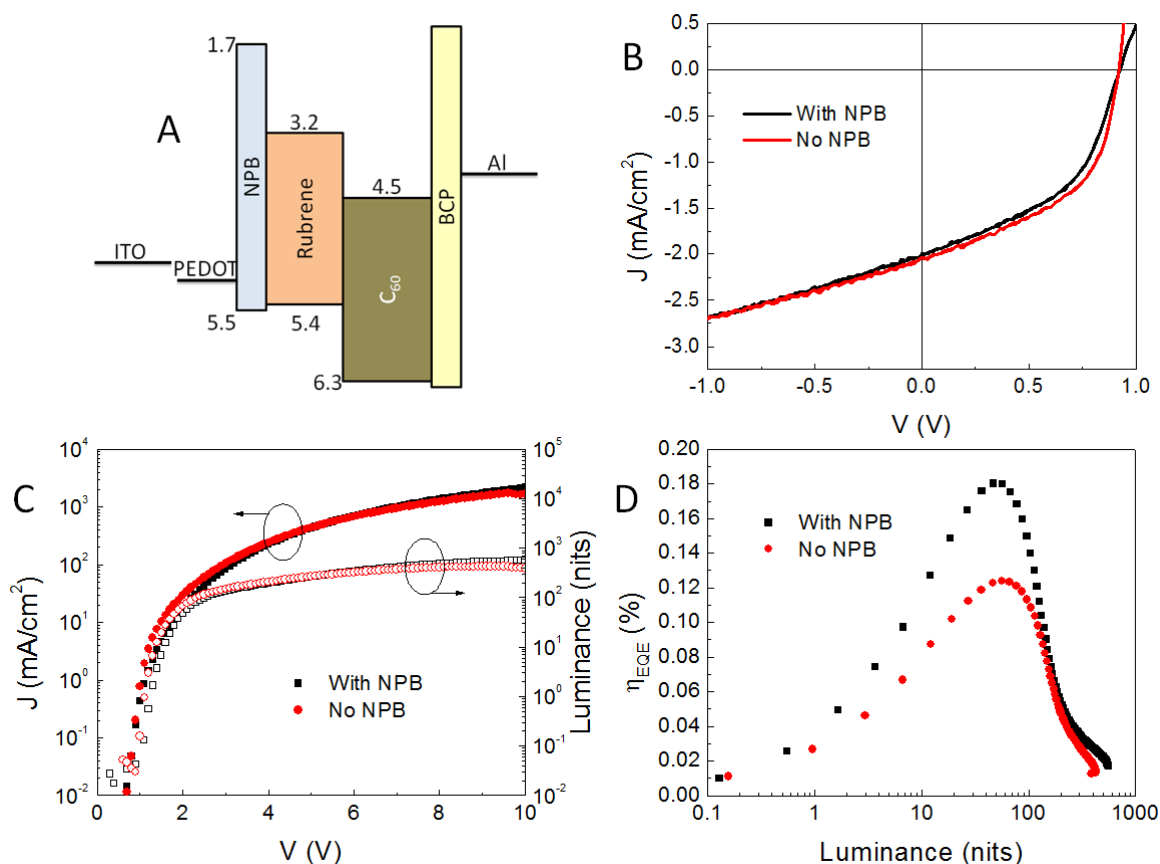


Figure 7-3. Effect of an NPB electron blocking layer on a rubrene/C₆₀ BFD. A) device architecture, with HOMO-LUMO energy levels. B) Current-voltage behavior under 1 sun illumination. C) Current-Luminance-Voltage characteristics. D) OLED external quantum efficiency.

The high LUMO level of NPB confines electrons within the rubrene layer, while its HOMO level is approximately the same as that of rubrene, so there should be a limited impact on hole transport and extraction and OPV efficiency. NPB will additionally serve as an exciton blocking layer to prevent quenching at the anode/organic interface.

The NPB electron confinement layer has almost no impact on photovoltaic performance, as anticipated. In both cases, the power conversion efficiency η_P is virtually the same, $\sim 0.9\%$, with only minor differences in fill factor (Figure 7-3B). When driven as an OLED, there is a large increase in quantum efficiency, from $\eta_{EQE} \approx 0.12\%$ without NPB to $\eta_{EQE} \approx 0.18\%$ with NPB at a brightness level of 50 nits (cd/m^2) (Figure 7-3D). While this is not the desired order-of-magnitude improvement, it indicates that there is some benefit to an electron blocking layer.

The remainder of this Section focuses on integrating phosphorescent emitters into a rubrene/ C_{60} BFD for more efficient use of injected electrons. Fluorescent emitters, such as rubrene, can only radiatively recombine singlet excitons. Phosphorescent emitters, however, can radiatively recombine triplet excitons, which are produced at a ratio of 3:1 versus singlets²⁰. Additionally, singlet excitons produced in a phosphorescent emitter are converted to triplets via spin-orbit coupling, allowing approximately 100% of generated excitons to contribute to light emission²³⁻²⁶.

Attempts to completely remove rubrene and replace it with the phosphorescent emitter platinum octaethylporphine (PtOEP) were not successful. PtOEP has similar HOMO-LUMO alignment to rubrene and PtOEP/ C_{60} heterojunctions result in respectable OPV performance⁸⁴. However, because PtOEP triplet excitons can be dissociated at the heterojunction interface, there is extremely inefficient light emission

from such a structure. Any excitons that form proximate to the interface will be dissociated back into free charge carriers. Further, neat PtOEP films exhibit strong triplet-triplet annihilation behavior, where two triplet excitons combine and create a singlet¹⁹³. Doping PtOEP into the wide bandgap host material 4,4'-N,N'-dicarbazole-biphenyl (CBP) to reduce triplet-triplet quenching does not improve BFD performance. The rubrene/C₆₀ heterojunction is therefore crucial: rubrene excitons are not efficiently dissociated at the interface, allowing for emissive recombination.

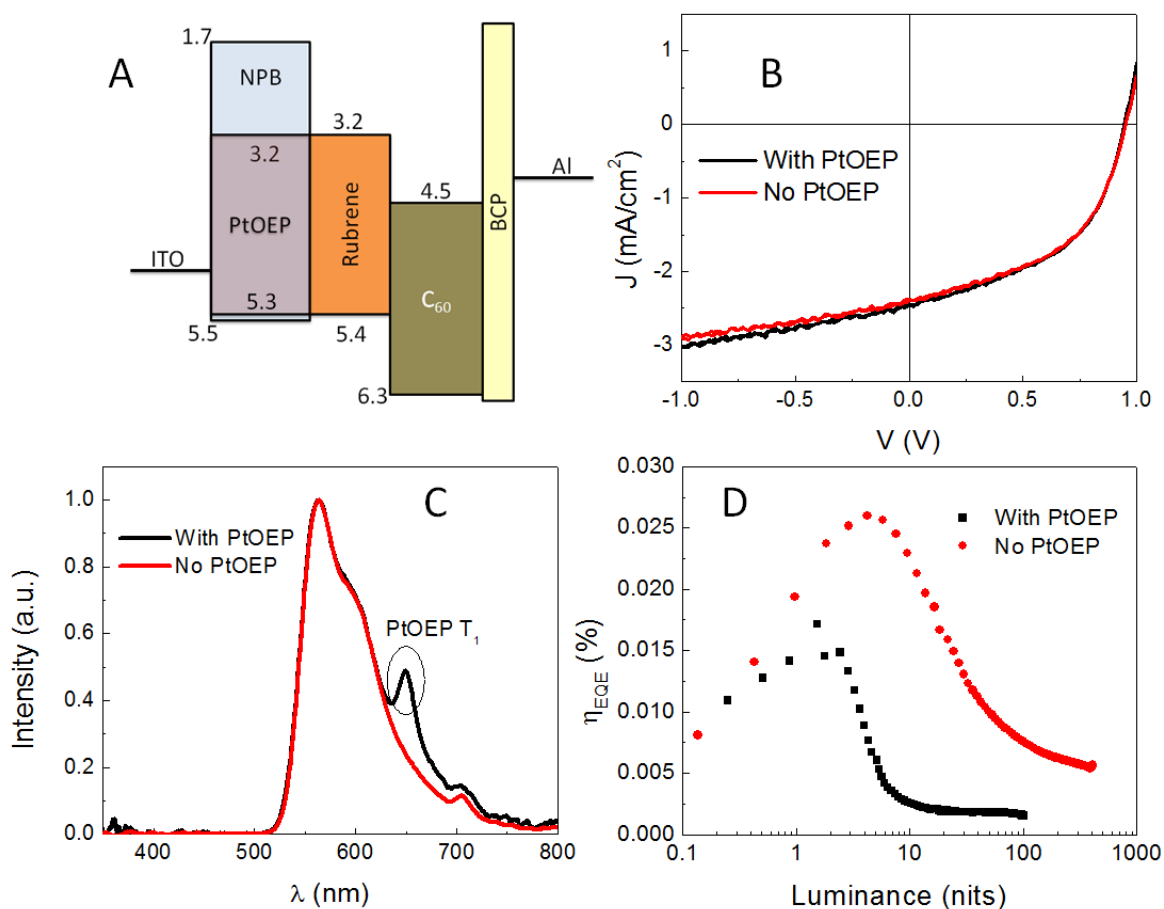


Figure 7-4. BFDs using a doped phosphorescent emissive layer. A) Basic phosphorescent BFD architecture and B) photovoltaic performance under 1 sun illumination. C) Emission spectra of BFDs with and without PtOEP doped into the NPB electron blocking layer. D) External quantum efficiency behavior for two representative devices.

A more successful approach is to place PtOEP immediately next to a thin electron injection layer of rubrene, which will isolate PtOEP triplets from immediate dissociation at the interface (Figure 7-4A). The resulting structure is ITO/x/rubrene/C₆₀/BCP/Al (20/10/40/8 nm, excluding the electrodes), where x is either neat NPB or NPB:PtOEP (10% by weight). In this architecture, there is no change in photovoltaic performance between devices with and without PtOEP (Figure 7-4B).

There is a slight alteration in the emission spectrum with the addition of PtOEP, as shown in Figure 7-4C, but the emission pattern is still predominately that of rubrene. Despite the addition of phosphorescent emission, total luminance and quantum efficiency actually decrease with the addition of PtOEP (Figure 7-4D). The reduced luminance is caused by energy transfer to the lowest energy state in the system, the rubrene triplet state, $T_{1, rub}$, enabled by the strong spin-orbit coupling behavior of PtOEP. Figure 7-5 shows a basic Jablonski diagram with the energy transfer pathways indicated.

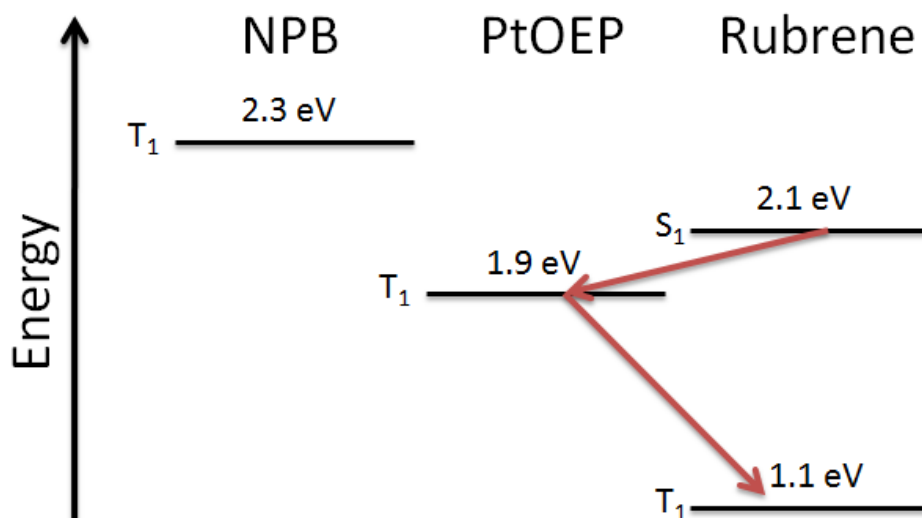


Figure 7-5. Jablonski diagram of exciton energies for a system containing NPB, PtOEP, and rubrene.

Because the triplet energy of PtOEP is in between the singlet and triplet energies of rubrene, phosphorescent emission from PtOEP will be quenched as excitons instead move to the non-emissive rubrene T_1 . One option to prevent this is to replace PtOEP with a different phosphorescent material with $T_1 > 2.1$ eV, such that the lowest energy state in the system would be the fluorescent rubrene singlet (once excitons are transferred to the rubrene S_1 state they are forbidden to move to the rubrene T_1 level)

One material that fits this requirement is the common green phosphorescent dopant *fac*-tris-(phenylpyridine) iridium ($\text{Ir}(\text{ppy})_3$), which exhibits ~ 2.4 eV T_1 emission. However, devices with and without 10% $\text{Ir}(\text{ppy})_3$ doping into NPB have no appreciable differences in either photovoltaic or light emitting performance (Figure 7-6). Either the LUMO level of $\text{Ir}(\text{ppy})_3$ is too high relative to rubrene (2.8 vs. 3.2 eV), limiting electron injection, or the $\text{Ir}(\text{ppy})_3$ T_1 -to-rubrene S_1 transition is quenching phosphorescent emission. In either case, this is not a viable option.

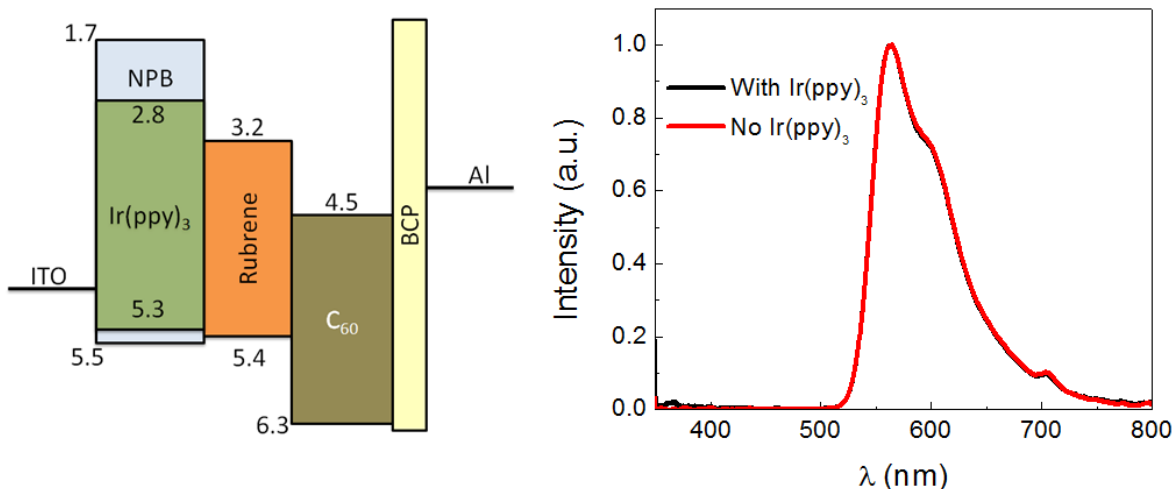


Figure 7-6. $\text{Ir}(\text{ppy})_3$ phosphorescent BFD architecture and emission spectra for devices with and without doping into NPB. No changes in performance were observed.

Instead of changing materials, a new architecture was developed to isolate PtOEP from rubrene to prevent exciton energy transfer to the non-emissive rubrene T_1 state. This is accomplished by inserting a thin neat layer of NPB between the doped PtOEP region and rubrene such that electrons can tunnel through to reach PtOEP but exciton energy transfer back to rubrene cannot occur. This architecture is depicted in Figure 7-7. In addition to the thin NPB layer between rubrene and PtOEP, an additional neat NPB layer is added to prevent quenching at the ITO/organic interface.

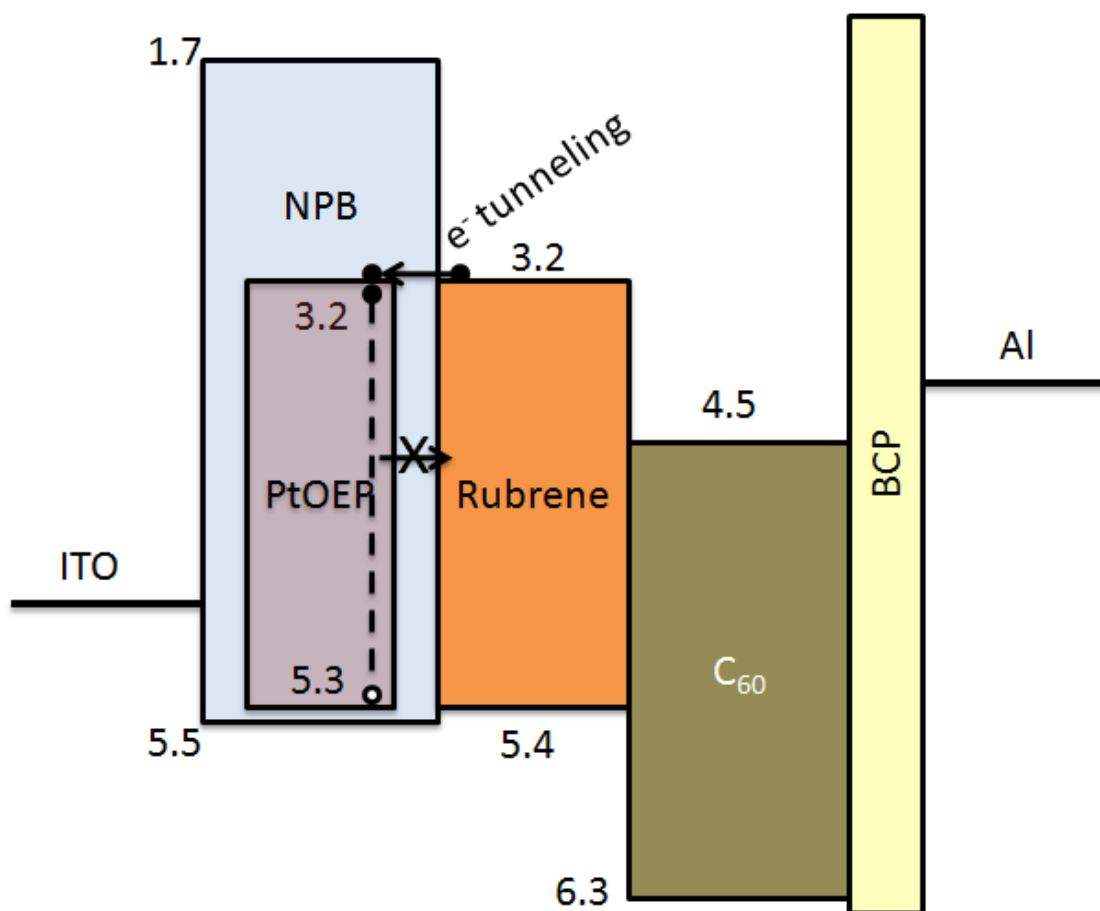


Figure 7-7. Adjusted phosphorescent BFD architecture. Thin NPB layers isolate excitons on PtOEP while still allowing electrons to tunnel into PtOEP for exciton formation.

The NPB blocking layer functions as an effective exciton barrier due to the short triplet-triplet exchange distance via the Dexter process, which has a typical range of a few nanometers (Section 1.3.3). Tunneling can occur at longer distances than this, making the layer both electron-permeable and exciton blocking. Figure 7-8A shows the photovoltaic performance under 1 sun illumination. There is no significant change as the NPB buffer thickness is altered, with power conversion efficiencies of approximately 1% for all structures.

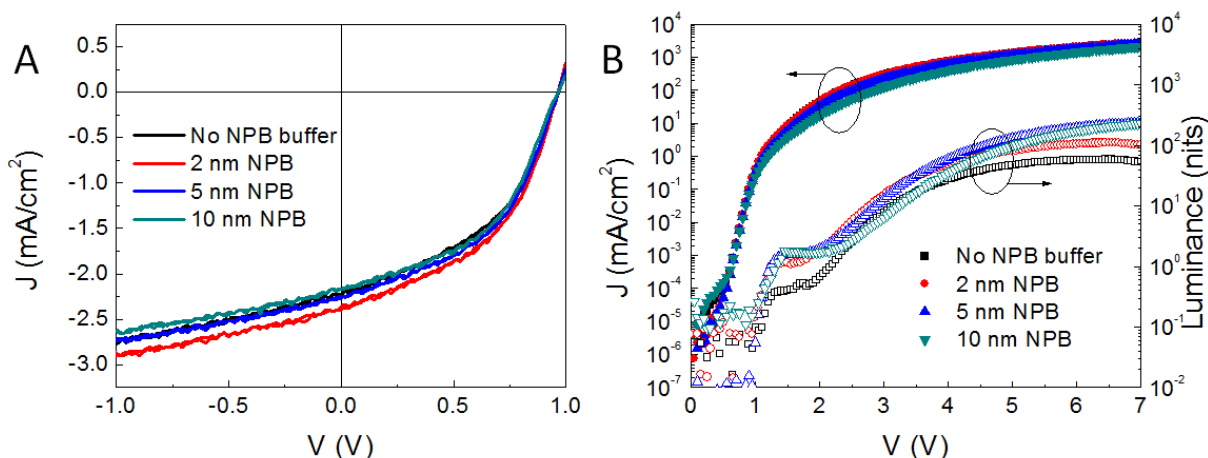


Figure 7-8. Photovoltaic and LJV characteristics of phosphorescent BFDs. A) Current-voltage characteristics of ITO/NPB/NPB:PtOEP (20%)/NPB/rubrene/C₆₀/BCP/Al (5/15/y/10/40/8 nm) devices under 1 sun illumination. B) Luminance-current-voltage characteristics.

While the injection behavior of each device is similar regardless of the NPB buffer layer thickness, devices with no buffer or a thin 2 nm-thick buffer have reduced luminance, indicating that quenching is an issue in these structures (Figure 7-8B). However, emission is predominately from the phosphorescent PtOEP T₁ state in these two devices, detailed in Figure 7-9A. Note that the PtOEP doping ratio is 20% in this structure, compared to 10% in the previous example (Figure 7-4C), giving increased

650 nm phosphorescent emission without a buffer layer. When the buffer layer thickness is increased to 5 nm and beyond, electron tunneling into the PtOEP layer is reduced and rubrene emission dominates.

However, the emissive efficiencies of these devices are all extremely low. A 2 nm-thick NPB buffer has predominately phosphorescent emission, but peak efficiencies are only $\eta_{EQE} = 0.024\%$, $\eta_{lum} = 0.04$ cd/A and power efficiency $\eta_P = 0.10$ lum/W at ~ 1 nit. For comparison, a fluorescent device with a 10 nm-thick buffer has $\eta_{EQE} = 0.022\%$, $\eta_{lum} = 0.06$ cd/A and power efficiency $\eta_P = 0.13$ lum/W at the same brightness.

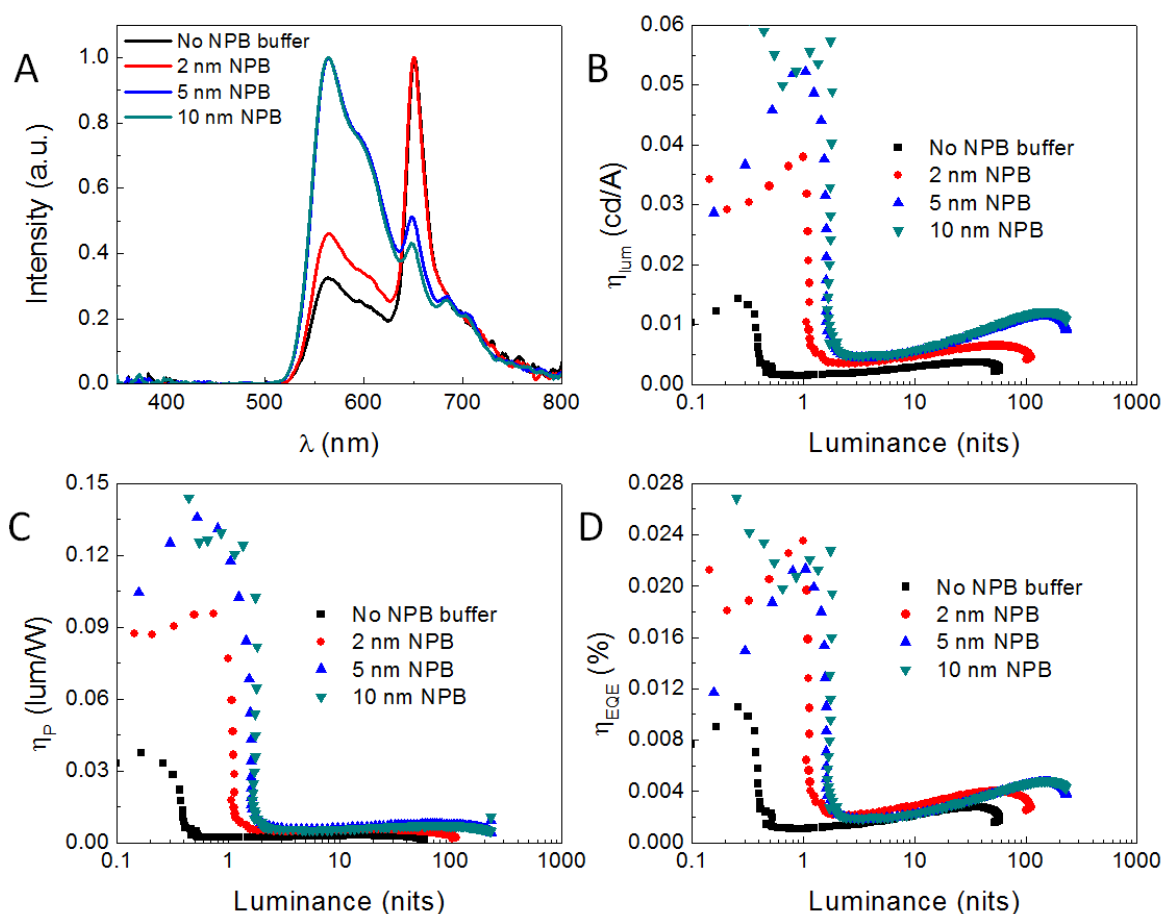


Figure 7-9. Light emitting characteristics of phosphorescent BFDs. A) Emission spectra for ITO/NPB/NPB:PtOEP (20%)/NPB/rubrene/C₆₀/BCP/Al (5/15/y/10/40/8 nm) devices, with B) luminous efficiency, C) power efficiency, and D) external quantum efficiency characteristics for the same devices.

Efficiencies roll off drastically for all structures at higher luminance levels. The comparable values of η_{EQE} indicate that phosphorescent emission is inherently more efficient, but the reduced luminance/increased quenching reduce efficiency. While the developed architecture is successful at isolating emission on PtOEP, the compromise between increased energy back transfer to non-emissive states and reduced electron tunneling prevent an increase in OLED performance.

Additional optimization attempts with this structure were not successful in appreciably increasing performance. It is promising that all of the experimental architectures maintained approximately equivalent photovoltaic performance, with power conversion efficiencies of approximately 1%, demonstrating good understanding and control of the requirements for efficient BFD photovoltaic characteristics. Ultimately, either a fundamental redesign of BFD architecture or the incorporation of new active layer materials is required to realize a device that has respectable efficiencies as both an OPV and an OLED.

7.3 Requirements for Efficient Bifunctional Device Design

Efficient BFDs are intrinsically difficult to achieve. As described in Figure 7-1, the operating mechanisms for power generation and light emission are inherently opposed. In Section 7.2, new device architectures were developed in an effort to shift emission to phosphorescent materials, but no real improvements in performance were seen. From this failure, however, several materials selection guidelines are now understood and can be described to support future advances in BFD performance and architecture development.

For respectable photovoltaic performance:

- No barriers to hole or electron transport away from the heterojunction/dissociation interface (high fill factor)
- Absorption over a large portion of the solar spectrum (high short circuit current)
- Reduced dark current (high open-circuit voltage).

For efficient light emission, the device requires:

- Reduced hole or electron injection barriers (depending on which side of the heterojunction has the light-emitting component)
- Isolation of emissive excitons from the heterojunction interface, or
- Inability of the heterojunction interface to dissociate emissive excitons
- A phosphorescent or high-efficiency fluorescent emitter, preferably doped into a wide bandgap material to improve emissive efficiency.

These necessities make materials selection extremely complex. Fullerenes, such as C₆₀ and C₇₀, have high electron mobility and perform well as an acceptor for photovoltaic applications, but their deep LUMO level creates a large barrier for charge injection into most emissive materials. Changing to other accepting materials, such as 3,4,9,10-perylene tetracarboxylic-bis-benzimidazole (PTCBI) or poly((9,9-dioctylfluorene)-2,7-diyl-alt-[4,7-bis(3-hexylthien-5-yl)-2,1,3-benzothiadiazole]-2',2''-diyl) (F8TBT), will reduce the injection barrier, but at the cost of reduced photovoltaic performance. F8TBT can actually function as either a donor or acceptor, depending on which materials it is paired with, making it a very versatile option¹⁹⁴. This research also made clear that fluorescent dopants are preferred to phosphorescent emitters. Phosphorescent materials allow energy transfer to non-emissive states, necessitating extra steps to isolate the emitter from materials with lower energy triplets.

In Chapter 8, a redesigned architecture is proposed that could reduce the necessary tradeoff between OPV and OLED performance using inorganic nanoparticles to selectively tune the electric field and potential energy barrier to electron injection at the heterojunction interface.

CHAPTER 8 CONCLUSIONS AND FUTURE WORK

8.1 Photocurrent Generation and Transport

In Chapter 5, the charge generation and transport processes in OPVs were explored using a novel characterization technique, synchronous photocurrent detection, to isolate the contribution of photogenerated current at different wavelengths and device biases. It was found that the device architecture and heterojunction structure have a significant impact on the resulting photocurrent behavior

In thin bilayer and planar-mixed heterojunction devices, the photocurrent always remains negative. At small forward biases, the drift current dominates in these architectures as the built-in field sweeps charges away from the interface to be collected at their respective electrodes. When the bias is increased sufficiently and the direction of the internal electric field is reversed, carrier pileup at the heterojunction interface due to the large charge transport barriers results in an increase in the diffusion current large enough to compensate for positive photocurrents created via leakage pathways at the interface. The photocurrent therefore remains negative, but at a much smaller magnitude.

The lack of charge transport barriers in a mixed heterojunction device causes the drift current to dominate at almost all applied biases. At large forward biases, the photocurrent direction reverses and becomes positive as the internal electric field switches directions relative to the built-in field. However, at a certain narrow applied bias range the internal electric field will be negligible, enabling the diffusion current to dominate. The distribution of charge carriers within the active layer then becomes

important, and correlations between the wavelength-dependent optical field and the inversion voltage (at which the photocurrent changes from negative to positive) were observed.

Additional studies were performed on bilayer devices with layer thicknesses larger than typical optimal values. While an optimized bilayer device has a persistent negative photocurrent, the thicker devices display photocurrent inversion at certain wavelengths. Correlation between the optical field and inversion voltage reveal a relationship between the proximity of exciton location relative to the dissociation interface and inversion voltage. Namely, exciton generation closer to the heterojunction interface is observed with increased inversion voltage. This indicates that field-assisted exciton dissociation, which can introduce free charge carriers past the heterojunction interface, becomes a significant contributor to photocurrent at large forward biases.

While these explanations agree qualitatively with experimental photocurrent behavior, there is a need for simulation of photocurrent behavior to quantitatively determine the relative contributions of the drift and diffusion current. This can be accomplished by combining the Gummel iteration method¹⁹⁵ with transfer matrix optical simulations to calculate electrical and optical field profiles, respectively. This approach has been applied to OPVs before^{158,196} as a basic device simulator for the optimization of device thickness and charge carrier mobility, not with the goal of examining photocurrent transport and behavior.

A basic implementation scheme would use the Gummel method to iteratively calculate the electric field, charge carrier distribution, and dark current profile within the device through manipulations of Poisson's equation. Then, transfer matrix simulations

are applied to determine the optical field profile within the device. From this, the total charge carrier profile can be determined by calculating absorption and exciton dissociation probabilities. The experimental technique of synchronous photocurrent detection can be approximated by moving a small amount of charge carriers for each wavelength (in proportion with the AM1.5G spectrum) and recording the amount of charge carriers that arrive at each electrode via either drift or diffusion. The total current curve can then be taken as the summation of the dark, drift, and diffusion currents. Finally, the experimentally determined photocurrent behavior provides an extra level of verification that previous simulation techniques have lacked. This approach to simulation should be highly accurate, and will enable holistic simulation of device behavior.

8.2 Optical Management in Organic Photovoltaic Devices

Most of the advancements in OPV performance have come through the synthesis of new active layer materials and development of new architectures. While important, these are expensive, time-consuming routes. In Chapter 6, a third improvement method was explored, optical management. Enhancements of 10-60% in power conversion efficiency were demonstrated using soft-lithographically stamped microlens arrays on the light-incident surface of the device. This serves to increase the average path length that light travels through the active layer, increasing the absorption probability without having to increase the active layer thickness, change the materials, or implement a more complicated heterojunction architecture. The path length is increased by refraction and reflection processes at the array-air interface.

This enhancement was demonstrated to be present regardless of the active layer materials. Small molecule, high efficiency polymer:fullerene, and hybrid inorganic nanoparticle/organic polymer systems all show enhancements. The degree of enhancement is strongly dependent on the optical intensity profile within the device. Microlens arrays change the direction of the incident light, which will alter the interference patterns in the active layers. This was exploited to increase the level of enhancement.

The geometric dependence of microlens array enhancement was also explored. Ray optics simulations revealed relationships between the device packing density, active area, and illumination area, with enhancement increasing as all of these factors increase. MLAs were demonstrated to have several properties that are matched with commercial device requirements: enhancement increases with area, it is present at all incident angles, and soft lithography is compatible with roll-to-roll processing. Finally, general guidelines were described for devices that are well-suited to MLA enhancement: high V_{OC} , low J_{SC} , and low dark current.

There are numerous steps that can be taken to further study optical management in OPVs. First, a robust simulation method that can accurately couple millimeter-scale substrate and lens dimensions with nanometer-scale device active layer thicknesses is needed. The separate transfer matrix and ray optics simulations presented in Chapters 4 and 6 are not suitable for complete simulation of MLAs, especially in understanding and predicting the change in optical interference patterns. One such method is a finite difference time-domain (FDTD) calculation¹⁹⁷. FDTD is based on numerical iteration of Maxwell's equations to calculate the electrical (optical) field at a series of mesh points in

space. A wide variety of mesh sizes can be accommodated within a single simulation, allowing simultaneous calculation of optical field propagation within the lens array and the device layers. Numerous commercial software packages are available.

Additional work should also be done to scale up MLA production techniques to speeds and yields suitable for a manufacturing environment. This will require installation of a small-scale roll-to-roll production line with a stamping-and-curing assembly or a system designed to imprint the MLA pattern directly into a plastic substrate using a heated mold. Though stamped-and-cured lens arrays were used in this work, a directly textured substrate should show the same enhancement characteristics provided that the microlens shape and packing factor are consistent between the two methods. The proposed suitability for commercial development makes demonstration of functioning, high-throughput, roll-to-roll-produced MLAs key.

MLAs can theoretically be adapted for use in inorganic thin-film PVs, such as CdTe or $\text{CuIn}_x\text{Ga}_{(1-x)}\text{Se}_2$. Because the refractive indices of these materials are much larger than in organic materials (i.e. $n > 2.5$ vs. $n \approx 1.7-1.8$) the lens array itself must be conducted out of a higher index material. As it is not practical to have a transparent polymer with $n > 2$, high-index inorganic nanoparticles (i.e. BaTiO_3) could be mixed with a conventional transparent polymer, such as optical adhesive, to increase the refractive index, since particles with diameters much less than the wavelength of light will only increase the effective refractive index, not scatter light. This method is limited by the processability and refractive index of the nanoparticles. Alternately, transparent inorganic materials could be used to form the MLAs, but this requires drastically different fabrication techniques compared to soft lithography stamping. Additionally,

because the MLA refractive index is now much larger, a low-index polymer could be placed on top of the MLA to serve as a graded index antireflection coating and an encapsulation layer.

A final proposed route is the development of textured rear reflectors for OPVs. In this case, the texture will be a microlens array in either a concave or convex orientation relative to the device, as shown in Figure 8-1.

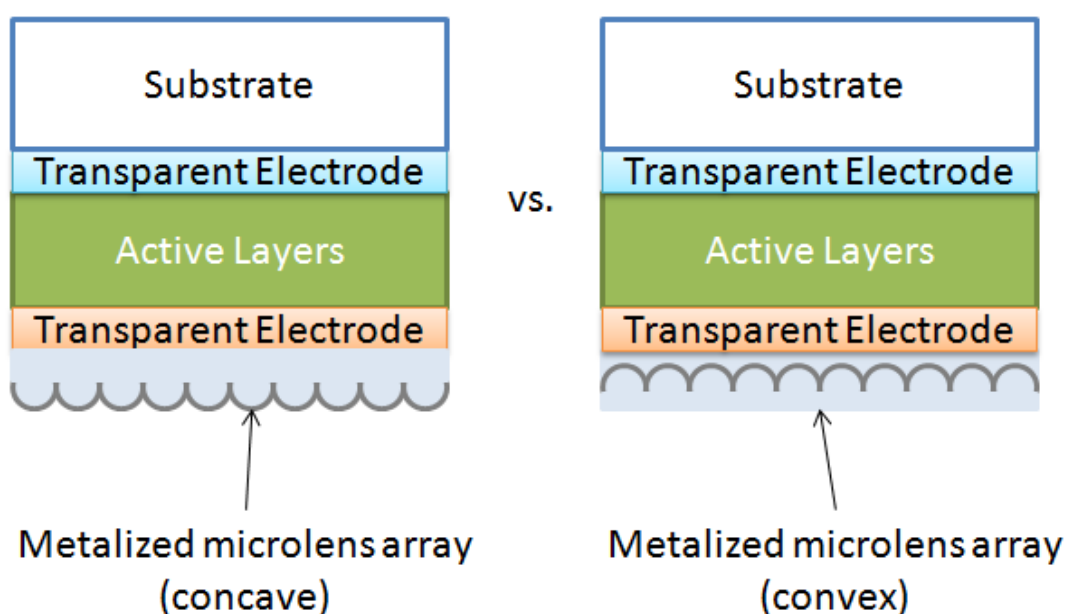


Figure 8-1. Device schematics for concave and convex microlens array rear reflectors. Light is first incident on the substrate in this geometry.

In this situation, the reflector will scatter light to both increase the average path length during subsequent passes through the active layer and induce total internal reflection for a portion of the reflected light. The effect could be further enhanced when combined with a MLA on the light incident surface. Preliminary investigations have shown that reflectors increase performance relative to a planar reflector by 5-10% in

polymer-based devices, and no statistically significant difference between concave and convex reflector geometries has been observed.

8.3 Bifunctional Organic Optoelectronic Devices

Chapter 7 concerns BFDs. These devices can function as either light emitting or power generating, depending on operating conditions. However, this presents a fundamental challenge. The operating mechanisms of OLEDs favor retaining charges in the interior of the device to maximize emissive recombination, while OPVs require efficient movement of charges from the interior dissociation interface to the electrodes. To ameliorate this tradeoff, a promising bilayer rubrene/ C_{60} architecture was modified to shift emission from rubrene (a fluorescent emitter) to PtOEP (a phosphorescent emitter) to make more efficient use of the electrons that are able to overcome the large injection barrier between rubrene and C_{60} . This proved to be a complicated task and revealed many design requirements for future bifunctional devices.

Initial attempts to simply replace rubrene with PtOEP were unsuccessful. While photovoltaic performance was respectable, PtOEP emission was quenched at the interface with C_{60} . Isolating PtOEP from C_{60} with a thin layer of rubrene enables phosphorescent emission, but energy transfer through PtOEP to the previously forbidden rubrene triplet state reduces total luminance and efficiency.

Finally, a novel architecture that isolates PtOEP from rubrene using a thin electron-permeable exciton blocking layer of NPB was developed. This was successful in inducing predominately phosphorescent emission, but the tradeoff between electron injection and exciton blocking limited total efficiency. Ultimately, substantial redesign is required to create an efficient BFD. This could either encompass better material

selection to lower injection barriers while still allowing for exciton dissociation, or radically different architectures, such as using inorganic nanoparticles to create favorable band bending for either OLED or OPV operation.

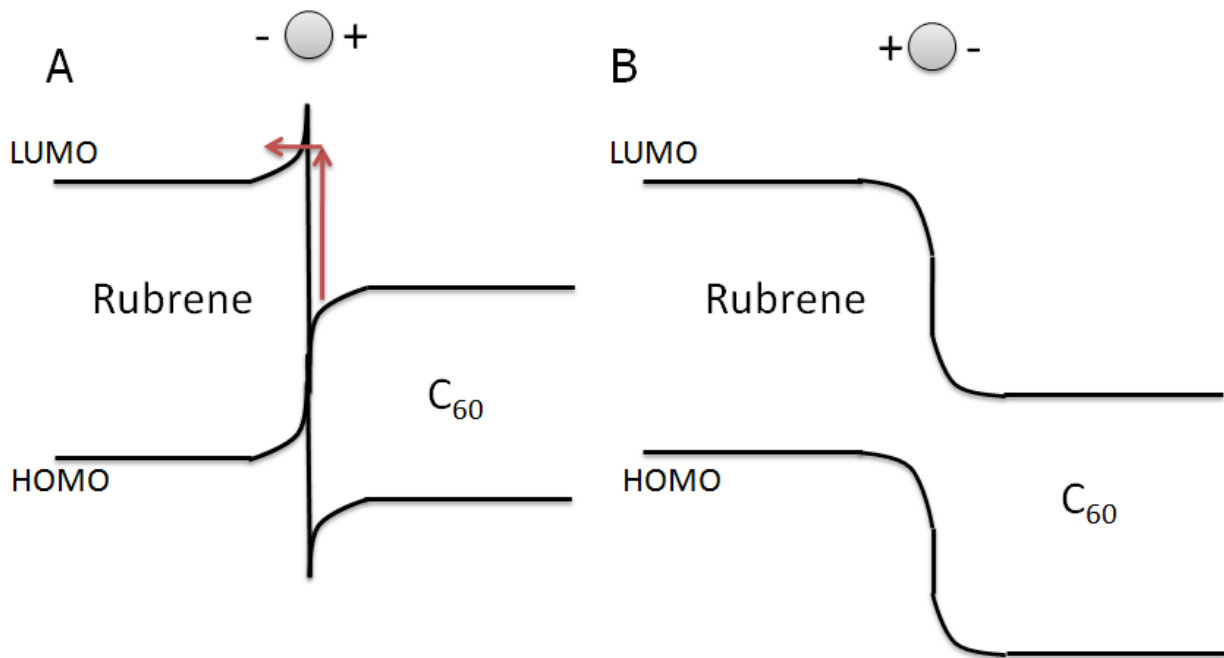


Figure 8-2. Schematic diagram of localized effects of ferroelectric nanoparticles polarization on the potential barrier for electron injection at a rubrene/ C_{60} interface. Ferroelectric nanoparticle polarization is shown above each set of band diagrams. A) Increased potential for thermionically-assisted tunneling electron injection due to the thinned barrier between C_{60} to rubrene, for OLED operation. B) Interfacial band diagram under opposite ferroelectric nanoparticle poling, for OPV operation.

Instead of relying solely on Auger-assisted injection, ferroelectric nanoparticles can be used to selectively induce band bending at the heterojunction interface and promote thermionic-assisted tunneling at a lower applied bias than is otherwise possible (Figure 8-2A). This arrangement should result in increased power efficiency and luminance from the device, as a greater amount of carriers is injected than would be otherwise. If the nanoparticles are polarized in the opposite direction (Figure 8-2B), the

altered interfacial electric field should help sweep charges away from the interface and towards the electrodes, a potential benefit for photovoltaic performance.

There are challenges in ferroelectric nanoparticle synthesis and incorporation at the interface. The nanoparticles must be small, to localize the induced electric field to the interface layers, but still large enough to allow significant polarization. There could also be different effects on band bending based on whether the nanoparticles are placed exactly at the interface, or slightly embedded into either of the layers.

An additional possibility is to isolate emission on inorganic quantum dots embedded in a solution-processed layer and electrically insulated by an encapsulating organic ligand. Previous studies have found that tunneling barriers can be tuned by the application of a large electric field, allowing charge carriers to move from an organic molecule to the inorganic nanoparticle¹⁹⁸. If the nanoparticles are dispersed in a bulk heterojunction OPV, the troublesome charge-blocking heterojunction interface would be removed. This could be an effective way to separate the OPV and OLED operation modes, but tuning the hole and electron tunneling barriers will be demanding.

BFDs are a revolutionary technology, but extensive investigation is required to realize their potential. The work presented here was a first step in understanding the material requirements for future development.

8.4 Afterword

In the past three decades, organic photovoltaic devices have emerged from a niche research topic to a prospective competitive technology in the photovoltaic marketplace. However, much work remains to make OPVs a viable alternative energy source. This dissertation presented two detailed studies to advance OPV technology:

first, investigation of photocurrent generation and transport behavior, including the development analytical techniques to enable future studies, and, second, a method to universally improve performance in OPVs by manipulating the behavior of incident light that is both inexpensive and compatible with a commercial production environment.

This study has also given insight into the necessary device characteristics and design requirements to fully exploit the optical enhancement effect, a promising avenue to push device efficiencies past 10%. Inexpensive, rugged, and high efficiency organic photovoltaics have the potential to revolutionize solar energy around the world and diligent research effort will realize this goal.

LIST OF REFERENCES

1. Peumans, P., Yakimov, A. & Forrest, S.R. Small molecular weight organic thin-film photodetectors and solar cells. *J. Appl. Phys.* **93**, 3693-3723 (2003).
2. Forrest, S.R. The path to ubiquitous and low-cost organic electronic appliances on plastic. *Nature* **428**, 911-918 (2004).
3. Shirota, Y. Organic materials for electronic and optoelectronic devices. *J. Mater. Chem.* **10**, 1-25 (2000).
4. Shaheen, S.E., Ginley, D.S. & Jabbour, G.E. Organic Based Photovoltaics: Toward Low-Cost Power Generation. *MRS Bull.* **30**, 10-19 (2005).
5. Xue, J. Perspectives on Organic Photovoltaics. *Polym. Rev.* **50**, 411 (2010).
6. Sun, Y. et al. Management of singlet and triplet excitons for efficient white organic light-emitting devices. *Nature* **440**, 908-912 (2006).
7. Scott, J.C. & Bozano, L.D. Nonvolatile Memory Elements Based on Organic Materials. *Adv. Mater.* **19**, 1452-1463 (2007).
8. Sundström, V. Femtobiology. *Annu. Rev. Phys. Chem.* **59**, 53-77 (2008).
9. Brütting, W. *Physics of organic semiconductors*. (Wiley-VCH: 2005).
10. Rand, B.P., Xue, J., Uchida, S. & Forrest, S.R. Mixed donor-acceptor molecular heterojunctions for photovoltaic applications. I. Material properties. *J. Appl. Phys.* **98**, 124902-7 (2005).
11. Bozano, L., Carter, S.A., Scott, J.C., Malliaras, G.G. & Brock, P.J. Temperature- and field-dependent electron and hole mobilities in polymer light-emitting diodes. *Appl. Phys. Lett.* **74**, 1132-1134 (1999).
12. Choulis, S.A. et al. High ambipolar and balanced carrier mobility in regioregular poly(3-hexylthiophene). *Appl. Phys. Lett.* **85**, 3890-3892 (2004).
13. Brenner, D.W. et al. A second-generation reactive empirical bond order (REBO) potential energy expression for hydrocarbons. *J. Phys.: Condens. Matter* **14**, 783-802 (2002).

14. Bisri, S.Z., Takenobu, T., Takahashi, T. & Iwasa, Y. Electron transport in rubrene single-crystal transistors. *Appl. Phys. Lett.* **96**, 183304 (2010).
15. de Boer, R.W.I., Gershenson, M.E., Morpurgo, A.F. & Podzorov, V. Organic single-crystal field-effect transistors. *Phys. Status Solidi A* **201**, 1302-1331 (2004).
16. Takeya, J. et al. Very high-mobility organic single-crystal transistors with in-crystal conduction channels. *Appl. Phys. Lett.* **90**, 102120 (2007).
17. Yamagishi, M. et al. High-mobility double-gate organic single-crystal transistors with organic crystal gate insulators. *Appl. Phys. Lett.* **90**, 182117 (2007).
18. Pope, M. & Swenberg, C.E. *Electronic Processes in Organic Crystals and Polymers*. (Oxford U: New York, 1999).
19. Sun, S.-S. & Sariciftci, N.S. *Organic Photovoltaics: Mechanisms, Materials, and Devices*. (CRC Press: Boca Raton, FL, 2005).
20. Baldo, M.A., O'Brien, D.F., Thompson, M.E. & Forrest, S.R. Excitonic singlet-triplet ratio in a semiconducting organic thin film. *Phys. Rev. B* **60**, 14422 (1999).
21. Baldo, M.A. & Forrest, S.R. Transient analysis of organic electrophosphorescence: I. Transient analysis of triplet energy transfer. *Phys. Rev. B* **62**, 10958 (2000).
22. Sokolik, I., Priestley, R., Walser, A.D., Dorsinville, R. & Tang, C.W. Bimolecular reactions of singlet excitons in tris(8-hydroxyquinoline) aluminum. *Appl. Phys. Lett.* **69**, 4168 (1996).
23. Baldo, M.A. et al. Highly efficient phosphorescent emission from organic electroluminescent devices. *Nature* **395**, 151-154 (1998).
24. Adachi, C., Baldo, M.A., Thompson, M.E. & Forrest, S.R. Nearly 100% internal phosphorescence efficiency in an organic light-emitting device. *J. Appl. Phys.* **90**, 5048 (2001).
25. Kawamura, Y. et al. 100% phosphorescence quantum efficiency of Ir(III) complexes in organic semiconductor films. *Appl. Phys. Lett.* **86**, 071104 (2005).
26. Williams, E.L., Haavisto, K., Li, J. & Jabbour, G.E. Excimer-Based White Phosphorescent Organic Light-Emitting Diodes with Nearly 100 % Internal Quantum Efficiency. *Adv. Mater.* **19**, 197-202 (2007).

27. Luhman, W.A. & Holmes, R.J. Investigation of Energy Transfer in Organic Photovoltaic Cells and Impact on Exciton Diffusion Length Measurements. *Adv. Funct. Mater.* **21**, 764-771 (2011).
28. Shaw, P.E., Ruseckas, A. & Samuel, I.D.W. Exciton Diffusion Measurements in Poly(3-hexylthiophene). *Adv. Mater.* **20**, 3516-3520 (2008).
29. Peumans, P. & Forrest, S.R. Very-high-efficiency double-heterostructure copper phthalocyanine/C₆₀ photovoltaic cells. *Appl. Phys. Lett.* **79**, 126-128 (2001).
30. Najafov, H., Lee, B., Zhou, Q., Feldman, L.C. & Podzorov, V. Observation of long-range exciton diffusion in highly ordered organic semiconductors. *Nat. Mater.* **9**, 938-943 (2010).
31. Forrest, S.R. Ultrathin Organic Films Grown by Organic Molecular Beam Deposition and Related Techniques. *Chem. Rev.* **97**, 1793-1896 (1997).
32. Karl, N. Organic Semiconductors: Purification and Crystal Growth. *Mol. Cryst. Liq. Cryst.* **171**, 157 (1989).
33. Shtein, M., Peumans, P., Benziger, J.B. & Forrest, S.R. Micropatterning of small molecular weight organic semiconductor thin films using organic vapor phase deposition. *J. Appl. Phys.* **93**, 4005 (2003).
34. Zheng, Y. et al. Computational and experimental studies of phase separation in pentacene:C₆₀ mixtures. *J. Vac. Sci. Technol. B* **27**, 169 (2009).
35. Krebs, F.C. All solution roll-to-roll processed polymer solar cells free from indium-tin-oxide and vacuum coating steps. *Org. Elec.* **10**, 761-768 (2009).
36. Wu, J. et al. Organic solar cells with solution-processed graphene transparent electrodes. *Appl. Phys. Lett.* **92**, 263302 (2008).
37. Lee, J.-Y., Connor, S.T., Cui, Y. & Peumans, P. Solution-Processed Metal Nanowire Mesh Transparent Electrodes. *Nano Lett.* **8**, 689-692 (2008).
38. Derby, B. Inkjet Printing of Functional and Structural Materials: Fluid Property Requirements, Feature Stability, and Resolution. *Annu. Rev. Mater. Res.* **40**, 395-414 (2010).
39. de Gans, B. -J, Duineveld, P.C. & Schubert, U.S. Inkjet Printing of Polymers: State of the Art and Future Developments. *Adv. Mater.* **16**, 203-213 (2004).

40. Green, R. et al. Performance of bulk heterojunction photovoltaic devices prepared by airbrush spray deposition. *Appl. Phys. Lett.* **92**, 033301-033301-3 (2008).
41. Vak, D. et al. Fabrication of organic bulk heterojunction solar cells by a spray deposition method for low-cost power generation. *Appl. Phys. Lett.* **91**, 081102 (2007).
42. Ishikawa, T., Nakamura, M., Fujita, K. & Tsutsui, T. Preparation of organic bulk heterojunction photovoltaic cells by evaporative spray deposition from ultradilute solution. *Appl. Phys. Lett.* **84**, 2424 (2004).
43. Baldo, M. et al. Organic Vapor Phase Deposition. *Adv. Mater.* **10**, 1505-1514 (1998).
44. Shtein, M., Peumans, P., Benziger, J.B. & Forrest, S.R. Direct, Mask- and Solvent-Free Printing of Molecular Organic Semiconductors. *Adv. Mater.* **16**, 1615-1620 (2004).
45. Shtein, M., Peumans, P., Benziger, J.B. & Forrest, S.R. Direct mask-free patterning of molecular organic semiconductors using organic vapor jet printing. *J. Appl. Phys.* **96**, 4500 (2004).
46. Sun, Y., Shtein, M. & Forrest, S.R. Direct patterning of organic light-emitting devices by organic-vapor jet printing. *Appl. Phys. Lett.* **86**, 113504 (2005).
47. Tang, C.W. Two-layer organic photovoltaic cell. *Appl. Phys. Lett.* **48**, 183-185 (1986).
48. Green, M.A., Emery, K., Hishikawa, Y. & Warta, W. Solar cell efficiency tables (version 37). *Prog. Photovolt: Res. Appl.* **19**, 84-92 (2011).
49. Dresner, J. Double injection electroluminescence in anthracene. *RCA Rev.* **30**, 322-334 (1969).
50. Tang, C.W. & VanSlyke, S.A. Organic electroluminescent diodes. *Appl. Phys. Lett.* **51**, 913 (1987).
51. Green, M.A. *Third Generation Photovoltaics*. (Springer-Verlag: Berlin, 2003).
52. Kallmann, H. & Pope, M. Photovoltaic Effect in Organic Crystals. *J. Chem. Phys.* **30**, 585 (1959).
53. Chamberlain, G.A., Cooney, P.J. & Dennison, S. Photovoltaic properties of merocyanine solid-state photocells. *Nature* **289**, 45-47 (1981).

54. Ghosh, A.K. & Feng, T. Merocyanine organic solar cells. *J. Appl. Phys.* **49**, 5982 (1978).
55. Harima, Y., Yamashita, K. & Suzuki, H. Spectral sensitization in an organic p-n junction photovoltaic cell. *Appl. Phys. Lett.* **45**, 1144-1145 (1984).
56. Blom, P.W.M., Mihailetschi, V.D., Koster, L.J.A. & Markov, D.E. Device Physics of Polymer:Fullerene Bulk Heterojunction Solar Cells. *Adv. Mater.* **19**, 1551-1566 (2007).
57. Popovic, Z.D., Khan, M.I., Atherton, S.J., Hor, A.-M. & Goodman, J.L. Study of Carrier Generation in Titanyl Phthalocyanine (TiOPc) by Electric-Field-Induced Quenching of Integrated and Time-Resolved Fluorescence. *J. Phys. Chem. B* **102**, 657-663 (1998).
58. Kraabel, B., McBranch, D., Sariciftci, N.S., Moses, D. & Heeger, A.J. Ultrafast spectroscopic studies of photoinduced electron transfer from semiconducting polymers to C₆₀. *Phys. Rev. B* **50**, 18543 (1994).
59. Hiramoto, M., Fujiwara, H. & Yokoyama, M. p-i-n like behavior in three-layered organic solar cells having a co-deposited interlayer of pigments. *J. Appl. Phys.* **72**, 3781 (1992).
60. Rostalski, J. & Meissner, D. Monochromatic versus solar efficiencies of organic solar cells. *Sol. Energy Mater. Sol. Cells* **61**, 87-95 (2000).
61. Geens, W., Aernouts, T., Poortmans, J. & Hadziioannou, G. Organic co-evaporated films of a PPV-pentamer and C60: model systems for donor/acceptor polymer blends. *Thin Solid Films* **403-404**, 438-443 (2002).
62. Wang, X.H., Grell, M., Lane, P.A. & Bradley, D.D.C. Determination of the linear optical constants of poly(9,9-dioctylfluorene). *Synth. Met.* **119**, 535-536 (2001).
63. Peumans, P., Uchida, S. & Forrest, S.R. Efficient bulk heterojunction photovoltaic cells using small-molecular-weight organic thin films. *Nature* **425**, 158-162 (2003).
64. Heremans, P., Cheyns, D. & Rand, B.P. Strategies for Increasing the Efficiency of Heterojunction Organic Solar Cells: Material Selection and Device Architecture. *Acc. Chem. Res.* **42**, 1740-1747 (2009).
65. Xue, J., Rand, B.P., Uchida, S. & Forrest, S.R. A Hybrid Planar-Mixed Molecular Heterojunction Photovoltaic Cell. *Adv. Mater.* **17**, 66-71 (2005).

66. Xue, J., Uchida, S., Rand, B.P. & Forrest, S.R. Asymmetric tandem organic photovoltaic cells with hybrid planar-mixed molecular heterojunctions. *Appl. Phys. Lett.* **85**, 5757-5759 (2004).
67. Yang, F. & Forrest, S.R. Photocurrent Generation in Nanostructured Organic Solar Cells. *ACS Nano* **2**, 1022-1032 (2008).
68. Zheng, Y., Bekele, R., Ouyang, J. & Xue, J. Interdigitated Bulk Heterojunction Organic Photovoltaic Cells With Aligned Copper Phthalocyanine Nanorods. *IEEE J. Sel. Top. Quantum Electron.* **16**, 1544-1551 (2010).
69. Zheng, Y., Bekele, R., Ouyang, J. & Xue, J. Organic photovoltaic cells with vertically aligned crystalline molecular nanorods. *Org. Elec.* **10**, 1621-1625 (2009).
70. Zheng, Y. & Xue, J. Organic Photovoltaic Cells Based on Molecular Donor-Acceptor Heterojunctions. *Polym. Rev.* **50**, 420 (2010).
71. Robbie, K. Advanced techniques for glancing angle deposition. *J. Vac. Sci. Technol. B* **16**, 1115 (1998).
72. Greene, L.E., Law, M., Yuhas, B.D. & Yang, P. ZnO-TiO₂ Core-Shell Nanorod/P3HT Solar Cells. *J. Phys. Chem. C* **111**, 18451-18456 (2007).
73. Pfuetzner, S., Meiss, J., Petrich, A., Riede, M. & Leo, K. Improved bulk heterojunction organic solar cells employing C₇₀ fullerenes. *Appl. Phys. Lett.* **94**, 223307 (2009).
74. Bailey-Salzman, R.F., Rand, B.P. & Forrest, S.R. Near-infrared sensitive small molecule organic photovoltaic cells based on chloroaluminum phthalocyanine. *Appl. Phys. Lett.* **91**, 013508 (2007).
75. Dai, J., Jiang, X., Wang, H. & Yan, D. Organic photovoltaic cells with near infrared absorption spectrum. *Appl. Phys. Lett.* **91**, 253503 (2007).
76. Kim, D.Y., Sarasqueta, G. & So, F. SnPc:C₆₀ bulk heterojunction organic photovoltaic cells with MoO₃ interlayer. *Sol. Energy Mater. Sol. Cells* **93**, 1452-1456 (2009).
77. Lunt, R.R. & Bulovic, V. Transparent, near-infrared organic photovoltaic solar cells for window and energy-scavenging applications. *Appl. Phys. Lett.* **98**, 113305 (2011).
78. Rand, B.P., Xue, J., Yang, F. & Forrest, S.R. Organic solar cells with sensitivity extending into the near infrared. *Appl. Phys. Lett.* **87**, 233508-233508-3 (2005).

79. Vasseur, K., Rand, B.P., Cheyins, D., Froyen, L. & Heremans, P. Structural Evolution of Evaporated Lead Phthalocyanine Thin Films for Near-Infrared Sensitive Solar Cells†. *Chem. Mater.* **23**, 886-895 (2011).
80. Xia, A.D. et al. Characteristics of heterojunction diode of C60/chloroindium phthalocyanine. *Solid State Commun.* **95**, 713-716 (1995).
81. Sullivan, P., Jones, T.S., Ferguson, A.J. & Heutz, S. Structural templating as a route to improved photovoltaic performance in copper phthalocyanine/fullerene (C60) heterojunctions. *Appl. Phys. Lett.* **91**, 233114-233114-3 (2007).
82. Iyechika, Y., Yakushi, K., Ikemoto, I. & Kuroda, H. Structure of lead phthalocyanine (triclinic form). *Acta Crystallogr., Sect. B: Struct. Sci* **38**, 766-770 (1982).
83. Wang, W., Placencia, D. & Armstrong, N.R. Planar and textured heterojunction organic photovoltaics based on chloroindium phthalocyanine (ClInPc) versus titanyl phthalocyanine (TiOPc) donor layers. *Org. Elec.* **12**, 383-393 (2011).
84. Perez, M.D., Borek, C., Forrest, S.R. & Thompson, M.E. Molecular and Morphological Influences on the Open Circuit Voltages of Organic Photovoltaic Devices. *J. Am. Chem. Soc.* **131**, 9281-9286 (2009).
85. Li, N., Lassiter, B.E., Lunt, R.R., Wei, G. & Forrest, S.R. Open circuit voltage enhancement due to reduced dark current in small molecule photovoltaic cells. *Appl. Phys. Lett.* **94**, 023307 (2009).
86. Mutolo, K.L., Mayo, E.I., Rand, B.P., Forrest, S.R. & Thompson, M.E. Enhanced Open-Circuit Voltage in Subphthalocyanine/C60 Organic Photovoltaic Cells. *J. Am. Chem. Soc.* **128**, 8108-8109 (2006).
87. Tong, X., Lassiter, B.E. & Forrest, S.R. Inverted organic photovoltaic cells with high open-circuit voltage. *Org. Elec.* **11**, 705-709 (2010).
88. Pandey, R. & Holmes, R.J. Graded Donor-Acceptor Heterojunctions for Efficient Organic Photovoltaic Cells. *Adv. Mater.* **22**, 5301-5305 (2010).
89. Fleetham, T.B. et al. Material dependence of the open-circuit voltage in zinc phthalocyanine-C60 organic photovoltaic cells. (*in submission*)
90. Glenis, S., Horowitz, G., Tourillon, G. & Garnier, F. Electrochemically grown polythiophene and poly(3-methylthiophene) organic photovoltaic cells. *Thin Solid Films* **111**, 93-103 (1984).
91. Kanicki, J. & Fedorko, P. Electrical and photovoltaic properties of trans-polyacetylene. *J. Phys. D: Appl. Phys.* **17**, 805-817 (1984).

92. Yu, G., Pakbaz, K. & Heeger, A.J. Semiconducting polymer diodes: Large size, low cost photodetectors with excellent visible-ultraviolet sensitivity. *Appl. Phys. Lett.* **64**, 3422-3424 (1994).
93. Marks, R.N., Halls, J.J.M., Bradley, D.D.C., Friend, R.H. & Holmes, A.B. The photovoltaic response in poly(p-phenylene vinylene) thin-film devices. *J. Phys.: Condens. Matter* **6**, 1379-1394 (1994).
94. Sariciftci, N.S., Smilowitz, L., Heeger, A.J. & Wudl, F. Photoinduced Electron Transfer from a Conducting Polymer to Buckminsterfullerene. *Science* **258**, 1474 -1476 (1992).
95. Sariciftci, N.S. et al. Semiconducting polymer-buckminsterfullerene heterojunctions: Diodes, photodiodes, and photovoltaic cells. *Appl. Phys. Lett.* **62**, 585-587 (1993).
96. Hummelen, J.C. et al. Preparation and Characterization of Fulleroid and Methanofullerene Derivatives. *J. Org. Chem.* **60**, 532-538 (1995).
97. Yu, G., Gao, J., Hummelen, J.C., Wudl, F. & Heeger, A.J. Polymer Photovoltaic Cells: Enhanced Efficiencies via a Network of Internal Donor-Acceptor Heterojunctions. *Science* **270**, 1789-1791 (1995).
98. Shaheen, S.E. et al. 2.5% efficient organic plastic solar cells. *Appl. Phys. Lett.* **78**, 841 (2001).
99. Wienk, M.M. et al. Efficient Methano[70]fullerene/MDMO-PPV Bulk Heterojunction Photovoltaic Cells. *Angew. Chem. Int. Ed.* **42**, 3371-3375 (2003).
100. Brabec, C.J., Shaheen, S.E., Winder, C., Sariciftci, N.S. & Denk, P. Effect of LiF/metal electrodes on the performance of plastic solar cells. *Appl. Phys. Lett.* **80**, 1288 (2002).
101. Ma, W., Yang, C., Gong, X., Lee, K. & Heeger, A.J. Thermally Stable, Efficient Polymer Solar Cells with Nanoscale Control of the Interpenetrating Network Morphology. *Adv. Funct. Mater.* **15**, 1617-1622 (2005).
102. Ma, W., Gopinathan, A. & Heeger, A.J. Nanostructure of the Interpenetrating Networks in Poly(3-hexylthiophene)/fullerene Bulk Heterojunction Materials: Implications for Charge Transport. *Adv. Mater.* **19**, 3656-3659 (2007).
103. Kim, Y. et al. A strong regioregularity effect in self-organizing conjugated polymer films and high-efficiency polythiophene:fullerene solar cells. *Nat Mater* **5**, 197-203 (2006).

104. Li, G. et al. High-efficiency solution processable polymer photovoltaic cells by self-organization of polymer blends. *Nat. Mater.* **4**, 864-868 (2005).
105. Leclerc, M., Diaz, F.M. & Wegner, G. Structural analysis of poly(3-alkylthiophene)s. *Die Makromolekulare Chemie* **190**, 3105-3116 (1989).
106. McCullough, R.D., Tristram-Nagle, S., Williams, S.P., Lowe, R.D. & Jayaraman, M. Self-orienting head-to-tail poly(3-alkylthiophenes): new insights on structure-property relationships in conducting polymers. *J. Am. Chem. Soc.* **115**, 4910-4911 (1993).
107. Koppe, M. et al. Influence of Molecular Weight Distribution on the Gelation of P3HT and Its Impact on the Photovoltaic Performance. *Macromolecules* **42**, 4661-4666 (2009).
108. Osaka, I. & McCullough, R.D. Chapter 3. Advanced Functional Regioregular Polythiophenes. *Design and Synthesis of Conjugated Polymers* (eds. M. Leclerc and J.-F. Morin) (2010).at <<http://onlinelibrary.wiley.com/doi/10.1002/9783527629787.ch3/summary>>
109. Ballantyne, A.M. et al. Understanding the Influence of Morphology on Poly(3-hexylselenothiophene):PCBM Solar Cells. *Macromolecules* **43**, 1169-1174 (2010).
110. Ballantyne, A.M. et al. Studies of Highly Regioregular Poly(3-hexylselenophene) for Photovoltaic Applications. *Adv. Mater.* **19**, 4544-4547 (2007).
111. Chen, J. & Cao, Y. Development of Novel Conjugated Donor Polymers for High-Efficiency Bulk-Heterojunction Photovoltaic Devices. *Acc. Chem. Res.* **42**, 1709-1718 (2009).
112. Boudreault, P.-L.T., Najari, A. & Leclerc, M. Processable Low-Bandgap Polymers for Photovoltaic Applications†. *Chem. Mater.* **23**, 456-469 (2011).
113. Kroon, R., Lenes, M., Hummelen, J.C., Blom, P.W.M. & de Boer, B. Small Bandgap Polymers for Organic Solar Cells (Polymer Material Development in the Last 5 Years). *Polym. Rev.* **48**, 531 (2008).
114. Peet, J. et al. Efficiency enhancement in low-bandgap polymer solar cells by processing with alkane dithiols. *Nat. Mater.* **6**, 497-500 (2007).
115. Peet, J., Senatore, M.L., Heeger, A.J. & Bazan, G.C. The Role of Processing in the Fabrication and Optimization of Plastic Solar Cells. *Adv. Mater.* **21**, 1521-1527 (2009).

116. Blouin, N., Michaud, A. & Leclerc, M. A Low-Bandgap Poly(2,7-Carbazole) Derivative for Use in High-Performance Solar Cells. *Adv. Mater.* **19**, 2295-2300 (2007).
117. Park, S.H. et al. Bulk heterojunction solar cells with internal quantum efficiency approaching 100%. *Nat Photon* **3**, 297-302 (2009).
118. Zhou, H. et al. Development of Fluorinated Benzothiadiazole as a Structural Unit for a Polymer Solar Cell of 7 % Efficiency. *Angew. Chem. Int. Ed.* **50**, 2995-2998 (2011).
119. Chen, H.-Y. et al. Polymer solar cells with enhanced open-circuit voltage and efficiency. *Nat Photon* **3**, 649-653 (2009).
120. Liang, Y. et al. For the Bright Future—Bulk Heterojunction Polymer Solar Cells with Power Conversion Efficiency of 7.4%. *Adv. Mater.* **22**, E135-E138 (2010).
121. Zhao, J., Wang, A. & Green, M.A. 24.5% Efficiency silicon PERT cells on MCZ substrates and 24.7% efficiency PERL cells on FZ substrates. *Prog. Photovolt: Res. Appl.* **7**, 471-474 (1999).
122. Hiramoto, M., Suezaki, M. & Yokoyama, M. Effect of Thin Gold Interstitial-layer on the Photovoltaic Properties of Tandem Organic Solar Cell. *Chem. Lett.* **19**, 327-330 (1990).
123. Yakimov, A. & Forrest, S.R. High photovoltage multiple-heterojunction organic solar cells incorporating interfacial metallic nanoclusters. *Appl. Phys. Lett.* **80**, 1667 (2002).
124. Rand, B.P., Peumans, P. & Forrest, S.R. Long-range absorption enhancement in organic tandem thin-film solar cells containing silver nanoclusters. *J. Appl. Phys.* **96**, 7519 (2004).
125. Janssen, A.G.F., Riedl, T., Hamwi, S., Johannes, H.-H. & Kowalsky, W. Highly efficient organic tandem solar cells using an improved connecting architecture. *Appl. Phys. Lett.* **91**, 073519 (2007).
126. Colmann, A., Junge, J., Kayser, C. & Lemmer, U. Organic tandem solar cells comprising polymer and small-molecule subcells. *Appl. Phys. Lett.* **89**, 203506 (2006).
127. Kim, J.Y. et al. Efficient Tandem Polymer Solar Cells Fabricated by All-Solution Processing. *Science* **317**, 222 -225 (2007).
128. Zhao, D.W. et al. Efficient tandem organic solar cells with an Al/MoO₃ intermediate layer. *Appl. Phys. Lett.* **93**, 083305 (2008).

129. Shrotriya, V., Wu, E.H.-E., Li, G., Yao, Y. & Yang, Y. Efficient light harvesting in multiple-device stacked structure for polymer solar cells. *Appl. Phys. Lett.* **88**, 064104 (2006).
130. Sista, S. et al. Highly Efficient Tandem Polymer Photovoltaic Cells. *Adv. Mater.* **22**, 380-383 (2010).
131. Currie, M.J., Mapel, J.K., Heidel, T.D., Goffri, S. & Baldo, M.A. High-Efficiency Organic Solar Concentrators for Photovoltaics. *Science* **321**, 226 -228 (2008).
132. Kim, S.-S., Na, S.-I., Jo, J., Kim, D.-Y. & Nah, Y.-C. Plasmon enhanced performance of organic solar cells using electrodeposited Ag nanoparticles. *Appl. Phys. Lett.* **93**, 073307 (2008).
133. Kulkarni, A.P., Noone, K.M., Munechika, K., Guyer, S.R. & Ginger, D.S. Plasmon-Enhanced Charge Carrier Generation in Organic Photovoltaic Films Using Silver Nanoprisms. *Nano Lett.* **10**, 1501-1505 (2010).
134. Tvingstedt, K., Persson, N.-K., Inganäs, O., Rahachou, A. & Zozoulenko, I.V. Surface plasmon increase absorption in polymer photovoltaic cells. *Appl. Phys. Lett.* **91**, 113514 (2007).
135. Rim, S.-B., Zhao, S., Scully, S.R., McGehee, M.D. & Peumans, P. An effective light trapping configuration for thin-film solar cells. *Appl. Phys. Lett.* **91**, 243501 (2007).
136. Tvingstedt, K., Andersson, V., Zhang, F. & Inganäs, O. Folded reflective tandem polymer solar cell doubles efficiency. *Appl. Phys. Lett.* **91**, 123514 (2007).
137. Zhou, Y., Zhang, F., Tvingstedt, K., Tian, W. & Inganäs, O. Multifolded polymer solar cells on flexible substrates. *Appl. Phys. Lett.* **93**, 033302 (2008).
138. Niggemann, M. et al. Functional microprism substrate for organic solar cells. *Thin Solid Films* **511-512**, 628-633 (2006).
139. Tvingstedt, K., Dal Zilio, S., Inganäs, O. & Tormen, M. Trapping light with micro lenses in thin film organic photovoltaic cells. *Opt. Express* **16**, 21608-21615 (2008).
140. Zilio, S.D., Tvingstedt, K., Inganäs, O. & Tormen, M. Fabrication of a light trapping system for organic solar cells. *Microelectron. Eng.* **86**, 1150-1154 (2009).

141. Cocoyer, C. et al. Implementation of submicrometric periodic surface structures toward improvement of organic-solar-cell performances. *Appl. Phys. Lett.* **88**, 133108 (2006).
142. Nalwa, K.S., Park, J.-M., Ho, K.-M. & Chaudhary, S. On Realizing Higher Efficiency Polymer Solar Cells Using a Textured Substrate Platform. *Adv. Mater.* **23**, 112-116 (2011).
143. Shrotriya, V. et al. Accurate Measurement and Characterization of Organic Solar Cells. *Adv. Funct. Mater.* **16**, 2016-2023 (2006).
144. ASTM Standard G173-03, 2008, Standard Tables for Reference Solar Spectral Irradiances: Direct Normal and Hemispherical on 37° Tilted Surface.
145. Gueymard, C.A. Parameterized transmittance model for direct beam and circumsolar spectral irradiance. *Sol. Energy* **71**, 325-346 (2001).
146. Gueymard, C.A. The sun's total and spectral irradiance for solar energy applications and solar radiation models. *Sol. Energy* **76**, 423-453 (2004).
147. Gueymard, C.A. *SMARTS2, A Simple Model of the Atmospheric Radiative Transfer of Sunshine: Algorithms and performance assessment*. **FSEC-PF-270-95**, (Florida Solar Energy Center/University of Central Florida: Cocoa, FL, 1995).
148. ASTM Standard E1021, Standard Test Method for Measuring Spectral Response of Photovoltaic Cells.
149. Kim, J.-S., Ho, P.K.H., Greenham, N.C. & Friend, R.H. Electroluminescence emission pattern of organic light-emitting diodes: Implications for device efficiency calculations. *J. Appl. Phys.* **88**, 1073 (2000).
150. Sun, Y. & Forrest, S.R. Organic light emitting devices with enhanced outcoupling via microlenses fabricated by imprint lithography. *J. Appl. Phys.* **100**, 073106 (2006).
151. Lee, J., Chopra, N. & So, F. Cavity effects on light extraction in organic light emitting devices. *Appl. Phys. Lett.* **92**, 033303 (2008).
152. Forrest, S.R., Bradley, D.D.C. & Thompson, M.E. Measuring the Efficiency of Organic Light-Emitting Devices. *Adv. Mater.* **15**, 1043-1048 (2003).
153. Chen, K.-Y., Hsiao, Y.-T., Lin, H.Y., Wei, M.-K. & Lee, J.-H. Partitioning pixel of organic light-emitting devices with center-hollowed microlens-array films for efficiency enhancement. *Opt. Express* **18**, 18685-18690 (2010).

154. Li, Y. et al. Origins of performance in fiber-based organic photovoltaics. *Appl. Phys. Lett.* **95**, 203503 (2009).
155. Peumans, P., Bulović, V. & Forrest, S.R. Efficient photon harvesting at high optical intensities in ultrathin organic double-heterostructure photovoltaic diodes. *Appl. Phys. Lett.* **76**, 2650 (2000).
156. Humphrey, W., Dalke, A. & Schulten, K. VMD - Visual Molecular Dynamics. *J. Mol. Graphics* **14**, 33-38 (1996).
157. Pettersson, L.A.A., Roman, L.S. & Inganäs, O. Modeling photocurrent action spectra of photovoltaic devices based on organic thin films. *J. Appl. Phys.* **86**, 487 (1999).
158. Sievers, D.W., Shrotriya, V. & Yang, Y. Modeling optical effects and thickness dependent current in polymer bulk-heterojunction solar cells. *J. Appl. Phys.* **100**, 114509-114509-7 (2006).
159. Stübinger, T. & Brütting, W. Exciton diffusion and optical interference in organic donor–acceptor photovoltaic cells. *J. Appl. Phys.* **90**, 3632 (2001).
160. Hoppe, H., Arnold, N., Sariciftci, N.S. & Meissner, D. Modeling the optical absorption within conjugated polymer/fullerene-based bulk-heterojunction organic solar cells. *Sol. Energy Mater. Sol. Cells* **80**, 105-113 (2003).
161. Scully, S.R. & McGehee, M.D. Effects of optical interference and energy transfer on exciton diffusion length measurements in organic semiconductors. *J. Appl. Phys.* **100**, 034907 (2006).
162. Hoppe, H., Arnold, N., Meissner, D. & Sariciftci, N.S. Modeling of optical absorption in conjugated polymer/fullerene bulk-heterojunction plastic solar cells. *Thin Solid Films* **451-452**, 589-592 (2004).
163. Gilot, J., Barbu, I., Wienk, M.M. & Janssen, R.A.J. The use of ZnO as optical spacer in polymer solar cells: Theoretical and experimental study. *Appl. Phys. Lett.* **91**, 113520 (2007).
164. Peumans, P. Erratum: “Small molecular weight organic thin-film photodetectors and solar cells” [*J. Appl. Phys.* 93, 3693 (2003)]. *J. Appl. Phys.* **95**, 2938 (2004).
165. Rand, B.P., Burk, D.P. & Forrest, S.R. Offset energies at organic semiconductor heterojunctions and their influence on the open-circuit voltage of thin-film solar cells. *Phys. Rev. B* **75**, 115327-11 (2007).
166. Kim, S.Y. Effect of ultraviolet–ozone treatment of indium–tin–oxide on electrical properties of organic light emitting diodes. *J. Appl. Phys.* **95**, 2560 (2004).

167. Sugiyama, K., Ishii, H., Ouchi, Y. & Seki, K. Dependence of indium–tin–oxide work function on surface cleaning method as studied by ultraviolet and x-ray photoemission spectroscopies. *J. Appl. Phys.* **87**, 295 (2000).
168. Malaquin, L., Kraus, T., Schmid, H., Delamarche, E. & Wolf, H. Controlled Particle Placement through Convective and Capillary Assembly. *Langmuir* **23**, 11513-11521 (2007).
169. Danzebrink, R. & Aegerter, M.A. Deposition of optical microlens arrays by ink-jet processes. *Thin Solid Films* **392**, 223-225 (2001).
170. Cheng, C.-C., Chang, C.A. & Yeh, J.A. Variable focus dielectric liquid droplet lens. *Opt. Express* **14**, 4101-4106 (2006).
171. Lu, Y., Yin, Y. & Xia, Y. A Self-Assembly Approach to the Fabrication of Patterned, Two-Dimensional Arrays of Microlenses of Organic Polymers. *Adv. Mater.* **13**, 34-37 (2001).
172. Möller, S. & Forrest, S.R. Improved light out-coupling in organic light emitting diodes employing ordered microlens arrays. *J. Appl. Phys.* **91**, 3324 (2002).
173. Chang, S.-I. & Yoon, J.-B. Shape-controlled, high fill-factor microlens arrays fabricated by a 3D diffuser lithography and plastic replication method. *Opt. Express* **12**, 6366-6371 (2004).
174. Eom, S.-H., Wrzesniewski, E. & Xue, J. Close-packed hemispherical microlens arrays for light extraction enhancement in organic light-emitting devices. *Org. Elec.* **12**, 472-476 (2011).
175. Eom, S.-H., Wrzesniewski, E. & Xue, J. Enhancing light extraction in organic light-emitting devices via hemispherical microlens arrays fabricated by soft lithography. *J. Photon. Energy* **1**, 011002 (2011).
176. Yang, J., Tang, A., Zhou, R. & Xue, J. Effects of nanocrystal size and device aging on performance of hybrid poly(3-hexylthiophene):CdSe nanocrystal solar cells. *Sol. Energy Mater. Sol. Cells* **95**, 476-482 (2011).
177. Qian, L. et al. Hybrid polymer-CdSe solar cells with a ZnO nanoparticle buffer layer for improved efficiency and lifetime. *J. Mater. Chem.* **21**, 3814 (2011).
178. Ji, W., Zhao, J., Sun, Z. & Xie, W. High-color-rendering flexible top-emitting warm-white organic light emitting diode with a transparent multilayer cathode. *Org. Elec.* **12**, 1137-1141 (2011).
179. Minami, T. Transparent conducting oxide semiconductors for transparent electrodes. *Semicond. Sci. Technol.* **20**, S35-S44 (2005).

180. Bera, D., Qian, L., Sabui, S., Santra, S. & Holloway, P.H. Photoluminescence of ZnO quantum dots produced by a sol-gel process. *Opt. Mater.* **30**, 1233-1239 (2008).
181. Zhou, H., Yang, L., Price, S.C., Knight, K.J. & You, W. Enhanced Photovoltaic Performance of Low-Bandgap Polymers with Deep LUMO Levels. *Angew. Chem. Int. Ed.* **49**, 7992-7995 (2010).
182. Qian, L. et al. Electroluminescence from light-emitting polymer/ZnO nanoparticle heterojunctions at sub-bandgap voltages. *Nano Today* **5**, 384-389 (2010).
183. Chen, L.L., Li, W.L., Li, M.T. & Chu, B. Bifunctional electroluminescent and photovoltaic devices using bathocuproine as electron-transporting material and an electron acceptor. *J. Lumin.* **122-123**, 667-670 (January).
184. Okada, H. et al. Organic Bifunctional Devices with Emission and Sensing Abilities. *Jpn. J. Appl. Phys.* **46**, 1328-1332 (2007).
185. Pandey, A.K. & Nunzi, J.-M. Rubrene/Fullerene Heterostructures with a Half-Gap Electroluminescence Threshold and Large Photovoltage. *Adv. Mater.* **19**, 3613-3617 (2007).
186. Wei, H. et al. White organic electroluminescent device with photovoltaic performances. *Appl. Surf. Sci.* **252**, 2204-2208 (2006).
187. Hong, Z.R., Lee, C.S., Lee, S.T., Li, W.L. & Shirota, Y. Bifunctional photovoltaic and electroluminescent devices using a starburst amine as an electron donor and hole-transporting material. *Appl. Phys. Lett.* **81**, 2878 (2002).
188. Narayan, K.S., Manoj, A.G., Nanda, J. & Sarma, D.D. Dual function hybrid polymer-nanoparticle devices. *Appl. Phys. Lett.* **74**, 871 (1999).
189. Sahu, S. & Pal, A.J. Multifunctionality of Organic Devices: Light Emission, Photovoltage Generation, and Photodetection. *J. Phys. Chem. C* **112**, 8446-8451 (2008).
190. Bernards, D.A., Flores-Torres, S., Abruña, H.D. & Malliaras, G.G. Observation of Electroluminescence and Photovoltaic Response in Ionic Junctions. *Science* **313**, 1416 -1419 (2006).
191. Ng, A.M.C., Djuricic, A.B., Chan, W.-K. & Nunzi, J.-M. Near infrared emission in rubrene:fullerene heterojunction devices. *Chem. Phys. Lett.* **474**, 141-145 (2009).

192. Pandey, A.K. & Nunzi, J.-M. Upconversion injection in rubrene/perylene-diimide-heterostructure electroluminescent diodes. *Appl. Phys. Lett.* **90**, 263508 (2007).
193. Baldo, M.A., Adachi, C. & Forrest, S.R. Transient analysis of organic electrophosphorescence. II. Transient analysis of triplet-triplet annihilation. *Phys. Rev. B* **62**, 10967 (2000).
194. McNeill, C.R. et al. Dual electron donor/electron acceptor character of a conjugated polymer in efficient photovoltaic diodes. *Appl. Phys. Lett.* **90**, 193506 (2007).
195. Gummel, H.K. A self-consistent iterative scheme for one-dimensional steady state transistor calculations. *IEEE Trans. Electron Devices* **11**, 455-465 (1964).
196. Mandoc, M.M., Koster, L.J.A. & Blom, P.W.M. Optimum charge carrier mobility in organic solar cells. *Appl. Phys. Lett.* **90**, 133504 (2007).
197. Yee, K. Numerical solution of initial boundary value problems involving Maxwell's equations in isotropic media. *IEEE Trans. Antennas Propag.* **14**, 302-307 (1966).
198. Ouyang, J., Chu, C.-W., Szmanda, C.R., Ma, L. & Yang, Y. Programmable polymer thin film and non-volatile memory device. *Nat. Mater.* **3**, 918-922 (2004).

BIOGRAPHICAL SKETCH

Jason Myers was born in 1985 in Kingsport, TN. During middle school, he moved to Miami, FL and finished his preparatory education there, graduating from Miami-Palmetto Senior High School in 2003, after which he was awarded a National Merit scholarship and enrolled at the University of Florida in Gainesville, FL. He completed his Bachelor of Science degree in Materials Science and Engineering *Summa cum Laude* in 2007 and remained for his doctoral studies in the same field, obtaining his M.S. in 2008.

In 2004, Jason joined Dr. Susan B. Sinnott's laboratory as an undergraduate research assistant investigating gaseous diffusion through branched carbon nanotube structures using molecular dynamics simulations. He was named the American Vacuum Society (AVS) Undergraduate Scholar of the Year in 2005 and presented his research at numerous conferences.

At the completion of his undergraduate degree, Jason shifted his efforts to experimental electronic devices and joined Dr. Jiangeng Xue's research group as an Alumni Fellow. His research focused on organic-based photovoltaic devices, with an emphasis on photocarrier motion and optical enhancements. His research has led to several refereed publications, numerous presentations at international conferences, and multiple United States patents. In 2010, he traveled to Kuala Lumpur, Malaysia as the United States representative in the Institute of Materials, Mining, and Minerals World Lecture Competition, winning the grand prize.

After receiving his doctorate in August 2011, Jason accepted a position with the Naval Research Laboratory in Washington, DC. He married his wife, Anne, in 2009.